

**POLITECNICO DI TORINO**



Master's degree course in Mechatronic Engineering

Master's Degree Thesis

**Development of attitude and trajectory  
control strategies for small satellites  
involved in rendez-vous and docking  
operations**

**Supervisors:**

Prof. Sabrina Corpino

Prof. Carlo Novara

Eng. Fabrizio Stesina

**Candidate:**

Simone Russo

Academic year 2020/2021

# Summary

1	Introduction.....	10
1.1	Rendezvous & Docking.....	11
1.2	Reference frame.....	13
1.3	SmallSats and CubeSat definition .....	13
1.4	Problem parameters .....	15
1.5	State of the art.....	16
1.6	MPC theoretical foundations.....	19
1.7	SMC theoretical foundations .....	23
2	Modelling and control design.....	26
2.1	Trajectory control – ideal conditions .....	27
2.2	Realistic model design.....	36
2.2.1	Plant, external disturbances and controllers design .....	37
2.2.1.1	Dynamics and kinematics .....	37
2.2.1.2	External disturbances.....	39
2.2.1.3	Orbit controller.....	41
2.2.1.4	Attitude controller.....	43
2.2.1.5	Results from simulations – realistic scenario 1 .....	44
2.2.2	Actuator models .....	51
2.2.2.1	Thrusters.....	51
2.2.2.2	Reaction wheels.....	57
2.2.3	Sloshing model.....	58
2.2.4	Results from simulations – realistic scenario 2 .....	62
3.	Robustness analysis.....	69
3.1	Montecarlo simulations.....	70
3.1.1	Montecarlo simulations: V-bar approach.....	72
3.1.1.1	Step 1.....	72
3.1.1.2	Step 2 .....	74
3.1.1.3	Step 3 .....	76
3.1.1.4	Step 4.....	78
3.1.1.5	Step 5 .....	80
3.1.1.6	Step 6 .....	82
3.1.1.7	Step 7 .....	84

3.1.1.8	Step 8 .....	86
3.1.1.9	Step 9 .....	88
3.1.1.10	Step 10 .....	90
3.1.2	Montecarlo simulations: R-bar approach.....	92
3.1.2.1	Step 1.....	92
3.1.2.2	Step 2.....	94
3.1.2.3	Step 3.....	96
3.1.2.4	Step 4.....	98
3.1.2.5	Step 5.....	100
3.1.2.6	Step 6.....	102
3.1.2.7	Step 7.....	104
3.1.2.8	Step 8.....	106
3.1.2.9	Step 9.....	108
3.1.2.10	Step 10.....	110
3.2	Controller refinement.....	112
4.	Off nominal conditions .....	122
4.1	Valve a closed .....	123
4.2	Valve a open .....	125
4.3	Valve b closed .....	127
4.4	Valve b open .....	129
4.5	Valve c closed .....	131
4.6	Valve c open.....	133
4.7	Valve d closed .....	135
4.8	Valve d open .....	137
4.9	Valve e closed .....	139
4.10	Valve e open .....	141
4.11	Valve f closed.....	143
4.12	Valve f open .....	145
4.13	Valve g closed .....	147
4.14	Valve g open .....	149
4.15	Valve h closed .....	151
4.16	Valve h open .....	153
5.	Conclusions.....	156

6. References ..... 157

7. Appendix – STK simulations..... 158

# List of figures

Figure 1: RVD overview .....	12
Figure 2: LVLH frame .....	13
Figure 3: receding horizon in MPC .....	19
Figure 4: internal architecture of MPC.....	22
Figure 5: phase portrait of sliding mode .....	24
Figure 6: CWH schematic .....	28
Figure 7: block schematic of the ideal closed loop system.....	31
Figure 8: state time response – ideal setup .....	33
Figure 9: zx relative position – ideal setup.....	34
Figure 10: zy relative position – ideal setup .....	34
Figure 11: relative velocity – ideal setup .....	35
Figure 12: input time response – ideal setup .....	35
Figure 13: block schematic of the realistic closed loop system.....	36
Figure 14: block schematic - rotational motion .....	37
Figure 15: block schematic - Euler moment equations.....	38
Figure 16: acceptance cone constraint .....	41
Figure 17: zx relative position - realistic scenario 1 .....	44
Figure 18: zx relative position (proximity detail) - realistic scenario 1 .....	44
Figure 19: zy relative position - realistic scenario 1 .....	45
Figure 20: zy relative position (proximity detail) - realistic scenario 1 .....	45
Figure 21: relative position 3d and acceptance cone – realistic scenario 1 .....	46
Figure 22: input time response - realistic scenario 1 .....	46
Figure 23: relative velocity time response - realistic scenario 1.....	47
Figure 24: angular velocity time response - realistic scenario 1.....	47
Figure 25: quaternions time response - realistic scenario 1.....	48
Figure 26: Drag torque time response - realistic scenario 1.....	48
Figure 27: Drag force time response - realistic scenario 1 .....	49
Figure 28: Magnetic field torque time response - realistic scenario 1 .....	49
Figure 29: Gravity gradient torque time response - realistic scenario 1 .....	50
Figure 30: Thrusters position .....	52
Figure 31: Thrusters setup 1 - block schematic .....	53
Figure 32: Simulink scope - thrust · mass [N·kg] in PWM-based setup .....	55
Figure 33: Thrusters setup 2 - block schematic .....	55
Figure 34: Valves characteristics .....	56
Figure 35: Simulink scope- realistic valve's behaviour (z-axis) .....	56
Figure 36: Simulink scope - misalignment torque [Nm] .....	57
Figure 37: reaction wheel model – y-axis example.....	58

Figure 38: sloshing mechanical model .....	61
Figure 39: Sloshing model - block schematic .....	61
Figure 40: Slosh disturbance torque [Nm] - Simulink scope.....	62
Figure 41: zx relative position - realistic scenario 2 .....	62
Figure 42: zx relative position (proximity detail) - realistic scenario 2 .....	63
Figure 43: zy relative position - realistic scenario 2 .....	63
Figure 44: zy relative position (proximity detail) - realistic scenario 2 .....	64
Figure 45: relative position 3d and acceptance cone – realistic scenario 2 .....	64
Figure 46: input time response - realistic scenario 2.....	65
Figure 47: relative velocity time response - realistic scenario 2.....	66
Figure 48: angular velocity time response - realistic scenario 2.....	66
Figure 49: quaternions time response - realistic scenario 2.....	67
Figure 50: quaternions time response – overshoot.....	67
Figure 51: angular velocity time response – overshoot.....	68
Figure 52: Relative position V-bar approach - Montecarlo 1.....	72
Figure 53: Time response plots in V-bar approach - Montecarlo 1 .....	73
Figure 54: Relative position V-bar approach - Montecarlo 2.....	74
Figure 55: Time response plots in V-bar approach - Montecarlo 2 .....	75
Figure 56: Relative position V-bar approach - Montecarlo 3.....	76
Figure 57: Time response plots in V-bar approach - Montecarlo 3 .....	77
Figure 58: Relative position V-bar approach - Montecarlo 4.....	78
Figure 59: Time response plots in V-bar approach – Montecarlo 4 .....	79
Figure 60: Relative position V-bar approach - Montecarlo 5.....	80
Figure 61: Time response plots in V-bar approach - Montecarlo 5 .....	81
Figure 62: Relative position V-bar approach - Montecarlo 6.....	82
Figure 63: Time response plots in V-bar approach - Montecarlo 6 .....	83
Figure 64: Relative position V-bar approach - Montecarlo 7.....	84
Figure 65: Time response plots in V-bar approach - Montecarlo 7 .....	85
Figure 66: Relative position V-bar approach - Montecarlo 8.....	86
Figure 67: Time response plots in V-bar approach - Montecarlo 8 .....	87
Figure 68: Relative position V-bar approach - Montecarlo 9.....	88
Figure 69: Time response plots in V-bar approach - Montecarlo 9 .....	89
Figure 70: Relative position V-bar approach - Montecarlo 10.....	90
Figure 71: Time response plots in V-bar approach - Montecarlo 10 .....	91
Figure 72: Relative position R-bar approach - Montecarlo 1.....	92
Figure 73: Time response plots in R-bar approach - Montecarlo 1 .....	93
Figure 74: Relative position R-bar approach - Montecarlo 2.....	94
Figure 75: Time response plots in R-bar approach - Montecarlo 2 .....	95
Figure 76: Relative position R-bar approach - Montecarlo 3.....	96

Figure 77: Time response plots in R-bar approach - Montecarlo 3 ..... 97

Figure 78: Relative position R-bar approach - Montecarlo 4..... 98

Figure 79: Time response plots in R-bar approach - Montecarlo 4 ..... 99

Figure 80: Relative position R-bar approach - Montecarlo 5..... 100

Figure 81: Time response plots in R-bar approach - Montecarlo 5 ..... 101

Figure 82: Relative position R-bar approach - Montecarlo 6..... 102

Figure 83: Time response plots in R-bar approach - Montecarlo 6 ..... 103

Figure 84: Relative position R-bar approach - Montecarlo 7..... 104

Figure 85: Time response plots in R-bar approach - Montecarlo 7 ..... 105

Figure 86: Relative position R-bar approach - Montecarlo 8..... 106

Figure 87: Time response plots in R-bar approach - Montecarlo 8 ..... 107

Figure 88: Relative position R-bar approach - Montecarlo 9..... 108

Figure 89: Time response plots in R-bar approach - Montecarlo 9 ..... 109

Figure 90: Relative position R-bar approach - Montecarlo 10..... 110

Figure 91: Time response plots in R-bar approach - Montecarlo 10 ..... 111

Figure 92: zx relative position - worst case scenario ..... 114

Figure 93: zx relative position (detail) - worst case scenario..... 115

Figure 94: zy relative position - worst case scenario ..... 115

Figure 95: zy relative position (detail) - worst case scenario..... 116

Figure 96: relative position 3d and acceptance cone on V\_bar - worst case scenario..... 116

Figure 97: input time response on V\_bar - worst case scenario ..... 117

Figure 98: relative velocity time response on V\_bar - worst case scenario ..... 117

Figure 99: xz relative position - worst case scenario ..... 118

Figure 100: xz relative position (detail) - worst case scenario..... 118

Figure 101: xy relative position - worst case scenario ..... 119

Figure 102: xy relative position (detail) - worst case scenario ..... 119

Figure 103: relative position 3d and acceptance cone on R\_bar - worst case scenario..... 120

Figure 104: input time response on R\_bar - worst case scenario..... 120

Figure 105: relative velocity time response on R\_bar - worst case scenario ..... 121

Figure 106: relative position - valve a closed..... 123

Figure 107: time responses - valve a closed ..... 124

Figure 108: relative position - valve a open ..... 125

Figure 109: time responses - valve a open ..... 126

Figure 110: relative position - valve b closed..... 127

Figure 111: time responses - valve b closed ..... 128

Figure 112: relative position - valve b open..... 129

Figure 113: time responses - valve b open ..... 130

Figure 114: relative position - valve c closed ..... 131

Figure 115: time responses - valve c closed..... 132

Figure 116: relative position - valve c open ..... 133

Figure 117: time responses - valve c open..... 134

Figure 118: relative position - valve d closed..... 135

Figure 119: time responses - valve d closed ..... 136

Figure 120: relative position - valve d open..... 137

Figure 121: time responses - valve d open ..... 138

Figure 122: relative position - valve e closed..... 139

Figure 123: time responses - valve e closed ..... 140

Figure 124: relative position - valve e open..... 141

Figure 125: time responses - valve e open ..... 142

Figure 126: relative position - valve f closed ..... 143

Figure 127: time responses - valve f closed ..... 144

Figure 128: relative position - valve f open..... 145

Figure 129: time responses - valve f open ..... 146

Figure 130: relative position - valve g closed..... 147

Figure 131: time responses - valve g closed ..... 148

Figure 132: relative position - valve g open..... 149

Figure 133: time responses - valve g open ..... 150

Figure 134: relative position - valve h closed..... 151

Figure 135: time responses - valve h closed ..... 152

Figure 136: relative position - valve h open..... 153

Figure 137: time responses - valve h open ..... 154

Figure 138: V-bar approach - LVLH frame..... 158

Figure 139: V-bar approach - zoom on SROC..... 159

Figure 140: R-bar approach..... 159

Figure 141: R-bar approach - zoom..... 160

# List of tables

Table 1: mass properties .....	15
Table 2: chaser orbital parameters .....	15
Table 3: MPC settings – ideal setup .....	32
Table 4: MPC settings - realistic scenario 1.....	43
Table 5: Valves activation criterion .....	51
Table 6: thrusters position abcd .....	52
Table 7: thrusters position efgh .....	52
Table 8: Reaction wheel parameters .....	57
Table 9: Tank and fluid parameters .....	60
Table 10: MPC 1 settings.....	113
Table 11: MPC 2 settings.....	113
Table 12: success rate - off nominal conditions.....	155

# Abbreviations

GNC	Guidance Navigation & Control
MPC	Model Predictive Control
SMC	Sliding Mode Control
SROC	Space Rider Observation CubeSat
RVD	Rendez-vous & Docking
LVLH	Local Vertical Local Horizontal
LTV	Linear Time Varying
LTI	Linear Time Invariant
LQR	Linear Quadratic Regulator
CAM	Collision Avoidance Manoeuvre
PWM	Pulse Width Modulation
CoM	Centre of Mass
MIMO	Multiple Inputs Multiple Outputs
SISO	Single Input Single Output

# ***1 Introduction***

Attitude and trajectory control represents a challenging task when it comes to space applications, first of all because of the intrinsic properties of the scenario, possible source of a high number of disturbances. Additional difficulties can arise in case strict constraints are imposed by the problem's requirements, as in the case of the project described in this thesis.

The scope of this work is focused on the design of an attitude and trajectory control system for a small sized satellite, so-called CubeSat, involved in a Rendezvous & Docking procedure, in the framework of the SROC mission developed by CubeSat Team Polito.

The approach employed to solve the problem is based on facing the main obstacles to be overcome, thus choosing among the best options in the design phase, in order to obtain the desired control performance and system behaviour. The said obstacles are, in detail:

- small size of the vehicle;
- high degree of required accuracy;
- internal and external disturbances;
- actuation.

A small size of the vehicle implies the necessity to limit the computational effort required by the control strategy as much as possible. On the other hand, the high degree of accuracy and the presence of disturbances suggest to use a real time control solution. High accuracy is required especially in terms of final approach velocity and position of the spacecraft, in order to ensure a safe docking between the vehicles. Internal disturbances are mostly due to thruster misalignments and to fuel sloshing, while noises coming from exterior are the ones related to environment properties: gravity gradient, Earth magnetic field, atmospheric drag. Given these

conditions, it is necessary to find a trade-off between the possible options, in order to satisfy all of them. The last main obstacle is actuation: even though this may be considered an issue related to the small size of the vehicle, it was chosen to outline it separately to give it the right amount of importance, as it can be identified as a key factor in the problem. In fact actuators, especially in such conditions, are characterised by physical limits due to e.g. available space, misalignments. It is of prior importance to tune the controllers in the best way to optimize actuator's actions.

It is quite evident how the control problem treated as follows is not trivial at all.

The thesis is articulated in four main chapters:

- the first one presents the project from a theoretical point of view, in order to give a general overview of the main topics involved;
- the second one describes both modelling phase (definition of plant, actuators, disturbances models) and controllers design.
- the third one is focused on simulation results obtained by exploiting the final model in uncertainty-based scenarios.
- The fourth one investigates the problem in off-nominal conditions, by considering a single failure scenario.

## ***1.1 Rendezvous & Docking***

Rendezvous & Docking (RVD) process consists of a sequence of phases, based on orbital manoeuvres and trajectories, allowing the chaser (active vehicle) to approach the target (passive vehicle), in order to gain structural connection between them. The chaser is equipped with a Guidance, Navigation & Control (GNC) system responsible of controlling the states of the vehicle in order to allow the entry into docking interface.

RVD is a complex process whose execution depends on various constraints, such as:

- launch and phasing trajectory strategy - the chaser must be brought to the same orbital plane of the target, which drifts with time, due to the oblateness of the Earth and multiple disturbances;
- operations in the vicinity of the target station - there is the necessity to define safety zones, hold points, approach corridors that should be inherently safe or, in alternative, it should be possible to execute a collision avoidance manoeuvre;
- onboard system requirements and constraints - requirements of sensors, antennas;
- synchronisation with Sun illumination conditions and crew work cycle - a good illumination condition is important for monitoring the docking/berthing status;
- communication link constraints.

A RVD mission can be divided into different phases:

- **launch** (and orbit injection);

- **phasing** (consists of reducing the phase angle between chaser and target, this kind of manoeuvres are usually controlled from ground and they end once an ‘initial aim point’ or a ‘trajectory gate’ are acquired);
- **far range rendezvous** (also called ‘homing’, the most important tasks of this phase are the acquisition of target orbit, the reduction of approach velocity, the synchronisation of mission time-line with external events, such as Sun illumination);
- **close range rendezvous** (divided in the closing phase and in the final approach subphase, where the tasks of the former are the reduction of range to the target and the acquisition of final approach corridor, while the scope of the latter is to achieve docking capture conditions from the point of view of velocity, position, relative attitude and angular rate. The GNC system must take count of the fact that actual docking axis will deviate from its nominal direction, due to disturbances such as bending of the target structure, attitude bias, so the chaser must acquire and follow the *instantaneous* docking axis. These conditions require strong GNC means, in particular the rendezvous sensor for the final approach must be able to measure axial and lateral position, but also the relative attitude between docking ports of target and chaser);
- **mating** (actually corresponds to the docking action. This phase starts once the GNC of the chaser has managed to bring the capture interfaces of both chaser and target into reception range. Mating has six main tasks: achievement of capture, attenuation of residual relative motion between the two vehicles, bringing interfaces of the structural latches into operational range, achievement of structural connection, achievement of gas-tight sealing of the connection of pressurised passage between vehicles, establishment of connection of data, power and, eventually, fluids). [1]

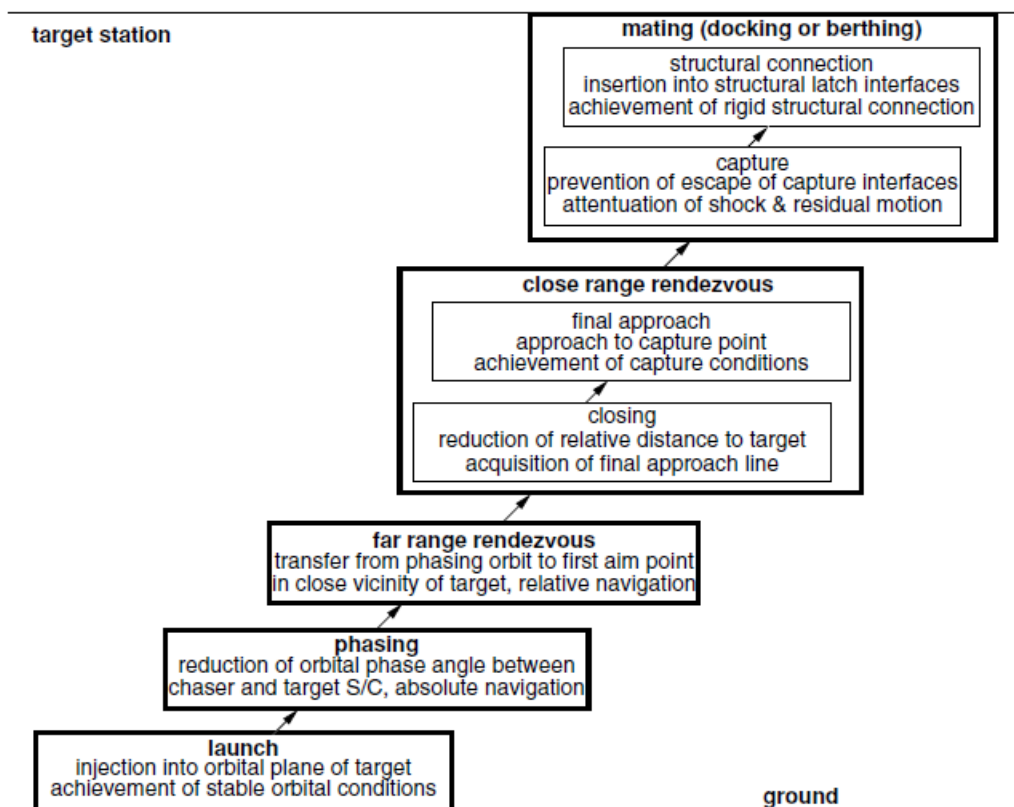


Figure 1: RVD overview [1]

This thesis will focus on the two final phases of the manoeuvre: close range rendezvous and mating, for which an automated control system is required.

## 1.2 Reference frame

Local Vertical Local Horizontal (LVLH) reference frame is depicted to describing the motion of a body with respect to the centre of Earth. In particular it is possible to identify:

- origin of the reference frame  $O_c$  corresponding to the center of mass of the vehicle;
- $a_1$  :  $a_1 = a_2 \times a_3$  along the same direction as the vector of orbital velocity, also called **V-bar**
- $a_3$  along the direction of the radius linking center of Earth and center of mass of the vehicle, also called **R-bar**
- $a_2$  completes the orthogonal triad and it is also called **H-bar** [1]

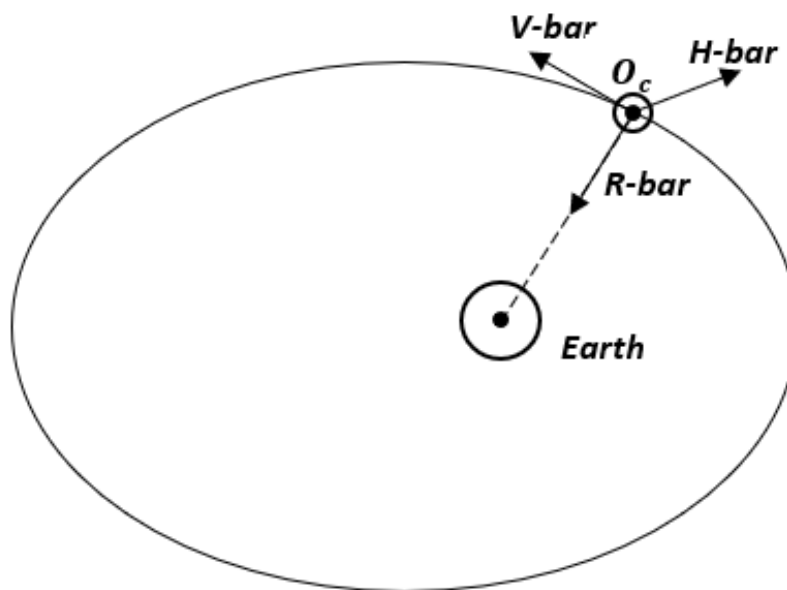


Figure 2: LVLH frame

## 1.3 SmallSats and CubeSat definition

Thanks to the late technological advancement in the fields of microelectronics, micro propulsion, long distance communications and the higher employment of commercial off the shelf (COTS) components, the development of small satellites, so called “SmallSats”, has been encouraged. The category of SmallSats includes, as the name suggests, satellites of small size and mass

(usually under 500 kg). Depending on mass, it is possible to identify several subcategories of small satellite as follows:

- Minisatellite: 150 – 500 kg
- Microsatellite: 10 – 150 kg
- Nanosatellite: 1 – 10 kg
- Picosatellite: 0.01 – 1 kg
- Femtosatellite: 0.001 – 0.01 kg

A CubeSat, in particular, is a cube-shaped satellite belonging to the category of SmallSats, with a modular structure, made up of one or more units. Each unit has dimensions of 10 cm × 10 cm × 10 cm and the current state of the art suggests availability of CubeSats ranging from 1U (one unit) to 24U (24 units).

The CubeSat concept was proposed by Prof. Jordi Puig-Suari (California Polytechnic State University) and Prof. Bob Twiggs (Stanford University) in 1999 for educational purposes, in the first place. Lately space agencies and companies operating in the field have shown great interest into this technology, by investing in the development of CubeSat-based platforms.

Many missions have taken place by means of CubeSats for in-orbit demonstration purposes. The European Space Agency (ESA), in particular, has been involved in missions such as: GOMX-3 and GOMX-4B led by Gomspace for telecommunication and propulsion demonstrative purposes, QARMAN, led by Von Karman Institute, a mission focused on a re-entry technology based on innovative heatshields, etc.

CubeSats have even been exploited for an interplanetary mission developed by NASA, Mars Cube One (MarCO), for telecommunications support in the framework of InSight mission.

As much as concerns the work described in this thesis, it was performed in collaboration with CubeSat Team Polito, a student team of Politecnico di Torino, involved in design and development of small platforms for scientific missions and in-orbit demonstration of novel technologies. The team was born in 2008 and has already launched two CubeSats into orbit: E-ST@R-I in 2012 and E-ST@R-II in 2016. Furthermore, the activity which this essay is willing to describe was performed in the framework of Space Rider Observer Cube (SROC), one of the four projects CubeSat team is currently working on. SROC is a CubeSat mission aimed at performing in-situ observations of Space Rider, a new transportation system developed by Thales-Alenia for ESA. In particular the focus of this thesis is centred on the RVD manoeuvre that will be performed by SROC (a 12U CubeSat inheriting the name of the mission), in order to ensure its retrieval inside the cargo bay of Space Rider.

## 1.4 Problem parameters

It is not possible to share detailed information on the specific components of SROC, due to the presence of a nondisclosure agreement between the parts involved in this project. It is anyway possible to describe some non neglectable features about the CubeSat, for the sake of a clear understanding of the control system design.

Mass properties:

<b>Parameter</b>	<b>Symbol</b>	<b>Value</b>
<i>mass</i>	$m_c$	$20 \text{ kg}$
<i>ballistic coefficient</i>	$C_b$	$0.001$
<i>base</i>	$b$	$0.226 \text{ m}$
<i>height</i>	$h$	$0.200 \text{ m}$
<i>width</i>	$w$	$0.366 \text{ m}$
<i>resistance coefficient</i>	$C_d$	$2$
<i>inertia moment wrt x-axis</i>	$I_x$	$0.152 \text{ kg} \cdot \text{m}^2$
<i>inertia moment wrt y-axis</i>	$I_y$	$0.290 \text{ kg} \cdot \text{m}^2$
<i>inertia moment wrt z-axis</i>	$I_z$	$0.308 \text{ kg} \cdot \text{m}^2$

Table 1: mass properties

Chaser orbital parameters:

<b>Parameter</b>	<b>Symbol</b>	<b>Value</b>
<i>right ascension of the ascending node</i>	$RAAN$	$0 \text{ rad}$
<i>latitude of the pericentre</i>	$\omega$	$0 \text{ rad}$
<i>orbit inclination</i>	$i_G$	$16 \text{ rad}$
<i>orbit eccentricity</i>	$e$	$0$
<i>mean anomaly</i>	$MG$	$0 \text{ rad}$
<i>orbit altitude</i>	$q$	$8.280 \cdot 10^5 \text{ m}$
<i>semi-major axis</i>	$a$	$7.206 \cdot 10^6 \text{ m}$
<i>perigee altitude</i>	$r_p$	$7.206 \cdot 10^6 \text{ m}$
<i>apogee altitude</i>	$r_a$	$7.206 \cdot 10^6 \text{ m}$
<i>semi-minor axis</i>	$b$	$7.206 \cdot 10^6 \text{ m}$
<i>orbital period</i>	$P$	$6.088 \cdot 10^3 \text{ s}$
<i>average satellite velocity</i>	$n$	$0.001 \text{ m/s}$
<i>number of daily orbits</i>	$N$	$14$

Table 2: chaser orbital parameters

Orbital parameters with respect to the target are the same as the ones related to the chaser so that the current setup is a cooperative-target scenario. Furthermore, the RVD procedure is intended to take place by means of the approach along V-bar.

## ***1.5 State of the art***

In the following section, a State of the Art analysis will take place in order to evaluate the most used control strategies employed for RVD procedure, both from orbit and attitude point of view.

For the ESA ORCSAT (On-line Reconfiguration Control System and Avionics Technologies) project, as outlined in Hartley, Trodden, Richards, Maciejowski, 2012 [3], a MPC control system was designed for being employed from target detection to capture. This project was developed as part of the Mars Sample Return mission, focused on the capturing of a Mars soil sample, enclosed into a passive container, performed by a chaser spacecraft. In the above mentioned paper it is highlighted how this control strategy is useful for fuel optimization which, in a space mission, represents a critical issue. Furthermore it is shown how MPC can be used both for trajectory and small-angle attitude control in order to ensure the target pointing.

The Rendezvous is partitioned in three different sequences: intermediate range, short range and very short range. For the intermediate range, more specifically addressed as Orbit Synchronisation Translational Guidance (OSTG), a prediction model based on Gauss' variational equalities is employed. The aim of this phase is to bring the chaser from a distance of about 300 km to an orbit characterised by the same Keplerian orbital elements as the target (apart from the true anomaly parameter which should still ensure an in-track separation between 10 and 30 km). The second phase, called Impulsive Nominal Translational Guidance (INTG), is aimed at performing passively safe impulsive manoeuvres between a sequence of hold points until reaching the distance of 100 meters from the target. The prediction model employed during this phase is based on the Yamanaka-Ankersen (2002) equations. There will be no further deepening about the two phases briefly described above as they are out of the scope of this thesis. The most important sequence for the sake of the thesis is the very short range, addressed as Forced Terminal Translational Guidance (FTTG) in the above mentioned paper. The internal model chosen for MPC optimization is once again based on Yamanaka-Ankersen equations for orbit control, while attitude control is performed by means of a quaternion-based model. The former model is a generalization of the Clohessy-Wiltshire-Hill (CWH) equations for an elliptical orbit and its biggest advantage is that it is numerically identical to CWH. Yamanaka-Andersen equations constitute a Linear Parameter Varying (LPV) model in terms of the true anomaly of the target but can be converted to a LTV model thanks to the assumption of passivity of the target. For attitude control also, a LTV model is used in order to take into account the rate of rotation between velocity orbital frame and inertial frame (Velocity orbital frame is a reference frame centred onto the target centre of mass, with x-axis aligned with  $\bar{V}$  direction, y-axis with the angular velocity direction of the orbit and z-axis completing the vector triad). This model derives from Euler's moment linearised equations. In order to estimate disturbance, the difference between predicted state and estimated state by means of navigation is integrated for estimating unmeasured disturbances.

As regards the MPC settings, a shorter sampling time is employed during this phase, with respect to the whole manoeuvre, since a higher accuracy is required. The selection of smaller sampling intervals is linked to the presence of a higher navigation noise, whose effect is actually minimised by setting a quadratic cost function, which includes states (weighed by means of a  $Q$  matrix) and input variations (weighed by means of a  $R$  matrix). The choice of including the variation of inputs into the cost function, instead of absolute input commands, is due to the higher priority given to accuracy than minimum propellant consumption, in this final phase. Although a terminal cost is usually added in order to ensure stability of the closed loop system, in this case it is not possible to add it because the prediction model is LTV, so stability is verified experimentally. Sampling time of the controller is synchronised with the one of the thruster subsystem and thus equal to 1 s, giving rise to computational availability constraints in terms of prediction horizon. On the other hand, with a too small horizon it resulted too difficult to avoid underdamping, thus a final selection of  $N = 15$  was done. Thanks to the MPC formulation also the planning of a collision avoidance manoeuvre (CAM) resulted possible. However a new cost function is implemented for the CAM, by employing a linear programming formulation, resulting in an open loop control logic. The reason for this choice is relied to the need for a computation that was as fast as possible. In order to evaluate the possibility to apply this control strategy to the real-life case, a rough scaling of computation time was performed from a desktop pc to two different microcontrollers, one running at 80 MHz and the other one at 798 MHz. The latter one resulted the better, by displaying a worst case execution time resulting to be by far within the allowed ranges.

From the point of view of simulation results, the main outcome is that MPC is much more advantageous with respect to carrying an extensively compiled library of optimal manoeuvres, in terms of time of convergence and propellant saving.

The work of Pirat, Ankersen, Walker, Gass, 2019 [4] is one of the most relevant in literature since it addresses the problem of RVD from a control perspective and, more interestingly, in a CubeSat-based framework. In particular, the aim of this work is to describe the control system designed for a RVD between two 6U CubeSat. The control strategy is based on H-infinity and  $\mu$ -synthesis, giving rise to a different perspective, based on Robust Stability and Robust Performance criteria fulfillment. A relative accuracy of 1 cm and  $2^\circ$  as requirements at docking, to be translated into frequency-dependent weights for the H-infinity controller design. A mixed sensitivity approach is used, in this case, in order to solve the optimization problem introduced by the H-infinity formulation, aiming to shape an output sensitivity function, a complementary sensitivity function and a gain sensitivity function. As much as concerns the plant model employed for simulations, it includes the relative rotational and translational dynamics of the chaser with respect to the target, coupled with a spring-mass-damper model, representing the sloshing phenomenon. The desired speed at docking, in the scenario proposed in this paper, is 1 cm/s. The expected performance of the controller is set by choosing three weighting matrices,

$W_1, W_2, W_3$ , all three shaped by first order transfer functions, whose parameters are tunable in order to map the performance requirements. They respectively weight sensitivity S, complementary sensitivity T and gain sensitivity KS. The controller solving the optimization problem results to be of the 42th order, respects the accuracy requirements during docking and prevents noise amplification. The performed  $\mu$ -analysis shows that the system is particularly sensitive to the uncertainties associated with damping coefficient involved in the sloshing model and with the fuel's sloshing natural frequency. Anyway, with two different setups (the first one including the H-infinity controller and the second one characterised by the  $\mu$ -synthesis based controller), both robust stability and robust performance conditions are verified. 600 Monte Carlo runs are performed, in both the setups below, by achieving an accuracy of 5-mm uncertainty on the final docking position.[4]

The paper by Luke Walker, 2012 [5] evaluates the possibility of employing a control strategy based on LQR for a RVD procedure involving a small spacecraft. The formulation of the problem is very similar to that one of a MPC strategy, with the substantial difference that LQR has a quasi-open loop nature: this condition sets the absolute necessity to decompose the trajectory into a wide series of orbital manoeuvres. To this aim, a solution is identified in employing a waypoint strategy, consisting of designing the LQR controller to guide the chaser spacecraft along small distances paths, marked by the so-called waypoints, until achieving the final position in correspondence of the target. Relative distance and frequency of waypoints comes as a result of a sensitivity analysis involving the estimation error caused by navigation. The control action provided by the LQR controller are fed directly to the actuation system, whose thrusters are activated by means of a PWM technique.

The paper by Farbod Fahimi, 2018 [6] describes a control strategy based on Sliding Mode Control. Conventional control laws in this framework provide an asymptotic convergence of the pose vector. But in case this latter vector is subject to rapid changes in time, an unwanted consequence could be a non-neglectable phase lag, resulting in a worse robust performance. In order to ensure the finite-time convergence, in this paper, a Higher Order Sliding Model is employed. This control strategy is employed for both attitude and formation dynamics. Two uncertain parameters are defined, in order to account for the mismatch between nominal and actual system. Each uncertain parameter is bounded by a finite quantity and a Lyapunov function is defined, in order to set the gain of the final controller. Actuation is ensured by means of reaction wheels, one for each axis. This approach results to be very effective, as the control performance has a very good behaviour, with every angular component getting to steady-state value after just 15 seconds, even with a penalising initial condition.

From the works described above, as some of the most relevant examples of projects concerning attitude and orbit control, a trade-off analysis is performed, in order to evaluate which strategy could be most suitable for the aim of this thesis. From the point of view of orbit control, the choice falls on Model Predictive Control, due to its significant computational power. The State

of the Art clearly outlines how the said control strategy can be flexible, thanks to a high amount of weighting factors and versatile constraints, and reliable for many different situations, due to its real-time logic. From the attitude point of view, Sliding Mode Control is selected, because of its tuning simplicity and widely proven effectiveness.

## 1.6 MPC theoretical foundations

Model Predictive Control and Rendezvous & Docking do not constitute a very usual binomial. Traditionally this orbital manoeuvre, as much as concerns the optimal control perspective, has been faced in the H-infinity framework. However, in the latest years, MPC is gaining interest even for such kind of applications in the space field.

MPC is a control method consisting of solving a Quadratic Programme optimization problem, subject to a-priori imposed constraints. This problem is faced according to the *Receding Horizon* principle: an optimizing sequence of inputs, able to minimize a cost functional, is found for every sampling instant of the so-called *Prediction Horizon*; from this sequence, only the first control action is selected and fed to the actual system, the following ones are discarded (*Figure 3*). This procedure is repeated for every sampling instant until the one corresponding to the value of the Prediction Horizon is reached. In order to accomplish this control strategy, a whole new optimization problem must be solved for every sampling interval, giving rise to a real time closed-loop controller.

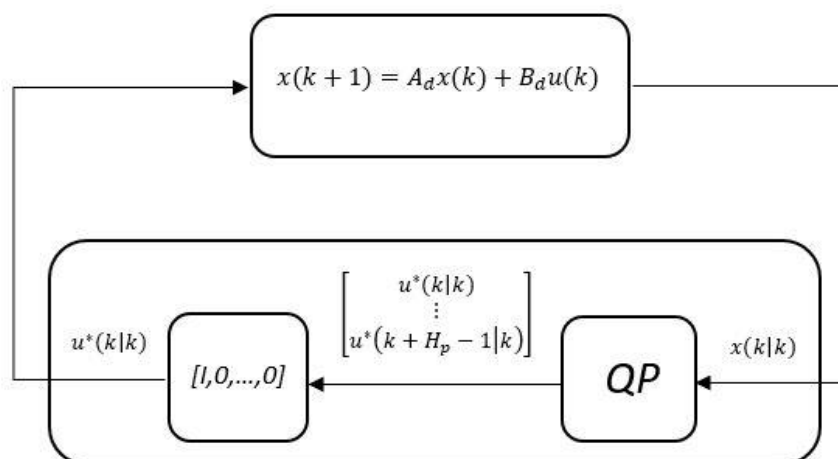


Figure 3: receding horizon in MPC

The optimization problem is formulated as follows:

$$\min_{U(k|k)} \sum_{i=0}^{H_p-1} x^T(k+i|k) Q x(k+i|k) + u^T(k+i|k) R u(k+i|k) \\ + x^T(k+H_p|k) P x(k+H_p|k)$$

s.t.  $G U(k|k) \leq h$

$$x \in \mathbb{X} \subset \mathbb{R}^n$$

$$u \in \mathbb{U} \subset \mathbb{R}^m$$

$k \in \mathbb{Z}^+$  time instants:  $k = 0, \dots, N$

The notation " $|k$ " outlines the dependence on an information up to the first time instant, i.e.  $k$ , as explained below.

$Q$ ,  $R$  and  $P$  are the weighting matrices, necessary to tune the MPC controller and to set the priority of the elements to be optimized. In particular,  $Q$  weights the states from the first discrete time instant to the one immediately prior to the prediction horizon  $H_p$ ,  $R$  weights the inputs and  $P$  is responsible of weighting the terminal state, i.e. the state corresponding to the last time instant of the prediction horizon.

It is also important to outline that

$$Q = Q' \geq 0$$

$$P = P' \geq 0$$

$$R = R' > 0$$

$$\text{rank}(Q) = n, \quad \text{rank}(R) = m$$

The expression  $G U(k|k) \leq h$  stands for the set of linear inequality constraints imposed on the variables of interest of the problem.

The objective function to minimize can be proven to be a Lyapunov function, by assuming convexity of initial and terminal set of states and by imposing the weighting matrix  $P$  as solution of the Algebraic Riccati Equation, in order to provide both feasibility of the optimization problem and stability of the controlled system [3]. In particular, from a multi-parametric programming point of view, it is possible to define as compact polyhedral sets both  $\mathbb{X}$  and  $\mathbb{U}$ . Furthermore, the  $N$ -step feasible set  $\mathbb{X}_f^N \subseteq \mathbb{R}^n$  can be defined as the set of initial states  $x(0)$  for which the constrained finite-time optimal control problem is feasible:

$$\mathbb{X}_f^N = \{x(0) \in \mathbb{R}^n \mid \exists(u_0, \dots, u_{N-1}) \in \mathbb{R}^{Nm}, x_k \in \mathbb{X}, u_{k-1} \in \mathbb{U}, \forall k \in \{1, \dots, N\}\}$$

where a more compact notation is employed to express the time dependence of variables, e.g.  $x_k$  stands for  $x(k)$ .

By denoting

$$X(k) = \begin{bmatrix} x(k) \\ x(k+1) \\ \vdots \\ x(k+H_p) \end{bmatrix}, \quad U(k) = \begin{bmatrix} u(k) \\ u(k+1) \\ \vdots \\ u(k+H_p-1) \end{bmatrix}$$

$$\mathcal{A} = \begin{bmatrix} I \\ A \\ \vdots \\ A^{H_p} \end{bmatrix}, \quad \mathcal{B} = \begin{bmatrix} 0 & 0 & \dots & 0 \\ B & 0 & \dots & 0 \\ AB & B & \dots & 0 \\ \vdots & \vdots & \vdots & \vdots \\ A^{H_p-2}B & A^{H_p-3}B & \dots & 0 \\ A^{H_p-1}B & A^{H_p-2}B & \dots & B \end{bmatrix}$$

It is possible to define thus

$$X(k) = \mathcal{A}x(k) + \mathcal{B}U(k)$$

Since

$$\mathcal{Q} = \begin{bmatrix} Q & 0 & \dots & 0 \\ 0 & \ddots & 0 & \vdots \\ \vdots & \ddots & Q & 0 \\ 0 & \dots & 0 & P \end{bmatrix} \in \mathbb{R}^{nH_p \times nH_p}, \quad \mathcal{R} = \begin{bmatrix} R & 0 & \dots & 0 \\ 0 & R & 0 & \vdots \\ \vdots & \ddots & \ddots & 0 \\ 0 & \dots & 0 & R \end{bmatrix} \in \mathbb{R}^{mH_p \times mH_p}$$

An alternative formulation of the cost function is provided:

$$J(x(k), U(k)) = x^T(k)\mathcal{A}'\mathcal{Q}\mathcal{A}x(k) + 2x^T(k)\mathcal{A}'\mathcal{Q}\mathcal{B}U(k) + U^T(k)(\mathcal{B}'\mathcal{Q}\mathcal{B} + \mathcal{R})U(k)$$

where

$$H = 2(\mathcal{B}'\mathcal{Z}\mathcal{B} + \mathcal{R})$$

$$F = 2\mathcal{A}'\mathcal{Z}\mathcal{B}$$

$$\bar{J} = x^T(k)\mathcal{A}'\mathcal{Z}\mathcal{A}x(k)$$

Note that  $H > 0$  is the Hessian matrix of the quadratic form and the solution to this optimization problem is  $U^*(k|k) = -H^{-1}F^T x(k|k)$ .

It is clear, from this formulation, that the problem depends only on the first state  $x(k)$ , so it can be solved as a multi-parametric program: by setting  $U^*(k)$  as the optimizing input sequence and considering  $x(k)$  as a parameter, a feedback solution is found such that  $\mathbb{X}_f^N$  is convex, the optimizer  $U^*: \mathbb{X}_f^N \rightarrow \mathbb{R}^{Nm}$  is continuous and piecewise affine and the optimal cost  $J^*: \mathbb{X}_f^N \rightarrow \mathbb{R}$  is continuous, convex and piecewise affine.

According to the multi-parametric programming framework,  $\mathbb{X}_f^N$  is partitioned into  $R$  polytopic regions. The more numerous the regions, the computationally heavier the problem; unfortunately, the number of regions increases exponentially with the prediction horizon, so it is necessary to find a trade-off between complexity and performance of the closed loop control system [4].

The working principle of this method is clear to be depending on a simplified model of the plant to control and on an optimizer: this is why MPC is able to provide both a guidance and a control function. In fact, the plant model inside MPC Controller is a simple description of the trajectory as it should be, in this case, while the optimizer is deputed to finding the best sequence of inputs able to minimize the cost functional (Figure 4). [7]

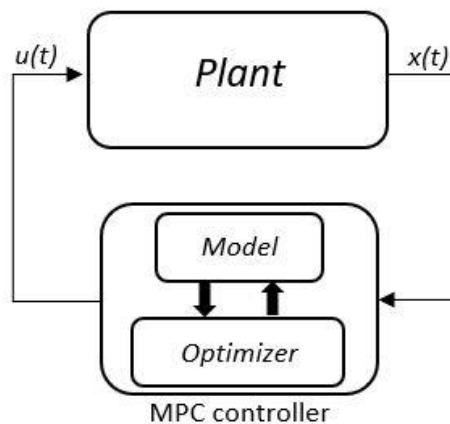


Figure 4: internal architecture of MPC

## 1.7 SMC theoretical foundations

Referring to every Control Engineering problem, in general, a non neglectable issue is the mismatch between the ideal model of the system to be controlled, employed for the controller design phase, and the actual plant. In order to ensure robustness even when the latter discrepancy is relevant, an excellent choice is Sliding Mode Control (SMC).

SMC belongs to the class of variable structure control systems (VSCS), which have their roots into the work of Emel'yanov and Barbashin in the 1960s. The strategies related to VSCS involve changing the control law along the control process, depending on the states of the system.

To summarize the purpose of SMC, first of all there is the definition of a *sliding surface*, i.e. a subset of the state-space on which the trajectory of the plant to be controlled is wanted to lie. Then a feedback control law is designed in order to ensure the latter condition is verified.

If a SISO nonlinear system is considered:

$$\begin{aligned}\dot{x} &= f(x) + g(x)u \\ y &= h(x)\end{aligned}$$

where

$x \in \mathbb{R}^n$  is the state

$u \in \mathbb{R}$  is the input

$y \in \mathbb{R}$  are is the output

$f, g, h$  are smooth functions on  $\mathbb{R}^{n_x}$ .

The normal form of the system is considered:

$$\begin{aligned}\dot{\mu} &= \begin{bmatrix} \mu_2 \\ \vdots \\ \mu_\gamma \\ a(x) + b(x)u \end{bmatrix} \\ a(x) &\equiv a(\mu, \psi) \doteq L_f^\gamma h(x) \\ b(x) &\equiv b(\mu, \psi) \doteq L_g L_f^{\gamma-1} h(x)\end{aligned}$$

where :

$\gamma$  is the relative degree

$(\mu, \psi)$  is the state

$\mu = (\mu_1, \dots, \mu_\gamma) \doteq (y, \dot{y}, \dots, y^{(\gamma-1)})$  is the external dynamics

$\psi \in \mathbb{R}^{n-\gamma}$  is the internal dynamics assumed locally asymptotically stable

$L_f^\gamma h(x)$  is the  $\gamma$ -th order Lie derivative of  $h(x)$  with respect to  $f$

Given a reference signal  $r(t)$  the desired behaviour of the system involves making the tracking error  $\tilde{y} = r - y$  converge to zero.

Given a *sliding surface*

$$S(t) \doteq \{x \in \mathbb{R}^n : \mathbf{s}(x, t) = 0\}$$

where  $\mathbf{s} : \mathbb{R}^{n+1} \rightarrow \mathbb{R}$  is defined as

$$s(x, t) = \tilde{y}^{(\gamma-1)} + k_\gamma \tilde{y}^{(\gamma-2)} + \dots + k_2 \tilde{y}$$

$k_i \in \mathbb{R}$  chosen in such way that all the roots of  $P(\lambda) = \lambda^{\gamma-1} + k_\gamma \lambda^{\gamma-2} + \dots + k_2$  have negative real part.

The design phase involves computing a control law able to ensure the sliding surface to be both attractive and an invariant set.

In case  $n = 2$  a phase portrait representing the system's motion on the surface, i.e. the *sliding mode* would be:

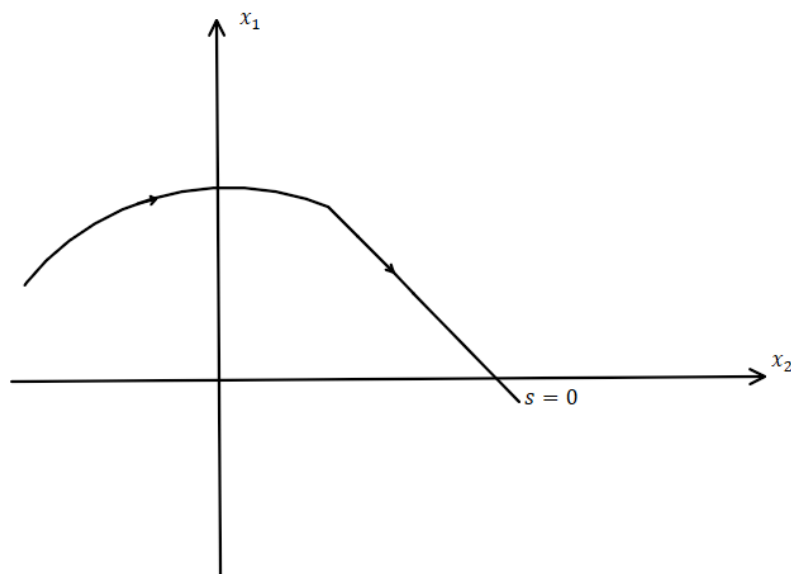


Figure 5: phase portrait of sliding mode

To ensure  $S$  to be an invariant set, it is necessary to set  $\dot{\mathbf{s}} = 0$ , meaning:

$$\tilde{y}^{(\gamma)} + k_\gamma \tilde{y}^{(\gamma-1)} + \dots + k_2 \dot{\tilde{y}} = 0$$

where  $\tilde{y}^{(\gamma)} = r^{(\gamma)} - y^{(\gamma)} = r^{(\gamma)} - a(x) - b(x)u$

and thus it is obtained that, in order to ensure  $S(t)$  to be invariant, the control law will be:

$$u_s = \frac{1}{b(x)} (r^{(\gamma)} - a(x) + k_\gamma \tilde{y}^{(\gamma-1)} + \dots + k_2 \dot{\tilde{y}})$$

In order to make  $S$  attractive, a discontinuous term is usually added to  $u_s$  multiplied by a constant term  $k_1 > 0$  (i.e.  $k_1 \text{sign}(\mathbf{s}(x, t))$ ) and, by setting  $\mathbf{s}(x, t) \dot{\mathbf{s}}(x, t) < 0 \forall x, t$  the attractiveness of  $S(t)$  is ensured.

In order to avoid eventual chattering problems, it is necessary to introduce into the control law also a sigmoid function, whose behaviour is similar to the term  $\text{sign}(\mathbf{s}(x, t))$  and depends on a third constant parameter  $\eta$ . A typical sigmoid function can be  $\tanh(\eta \mathbf{s})$ . [8]

In the MIMO setup, the following formulation holds:

$$\begin{bmatrix} y_1^{(\gamma_1)} \\ \vdots \\ y_{n_y}^{(\gamma_{n_y})} \end{bmatrix} = \begin{bmatrix} L_f^{\gamma_1} h_1(x) \\ \vdots \\ L_f^{\gamma_{n_y}} h_{n_y}(x) \end{bmatrix} + B(x)u, \quad B(x) \doteq \begin{bmatrix} L_g L_f^{\gamma_1 - 1} h_1(x) \\ \vdots \\ L_g L_f^{\gamma_{n_y} - 1} h_{n_y}(x) \end{bmatrix}$$

where:

$\gamma_i$  is the relative degree wrt  $y_i$ .

The sliding surface is defined as in the description above, apart from the following considerations:

$$\mathbf{s} : \mathbb{R}^{n+1} \rightarrow \mathbb{R}^{n_y}$$

$$k_i \in \mathbb{R}^{n_y \times n_y}$$

and thus the control law becomes ( $B(x)$  assumed invertible):

$$u = B(x)^{-1} (r^{(\gamma)} - a(x) + k_\gamma \tilde{\mu}_\gamma + \dots + k_2 \tilde{\mu}_2 + k_1 \sigma(\eta \mathbf{s}))$$

## ***2 Modelling and control design***

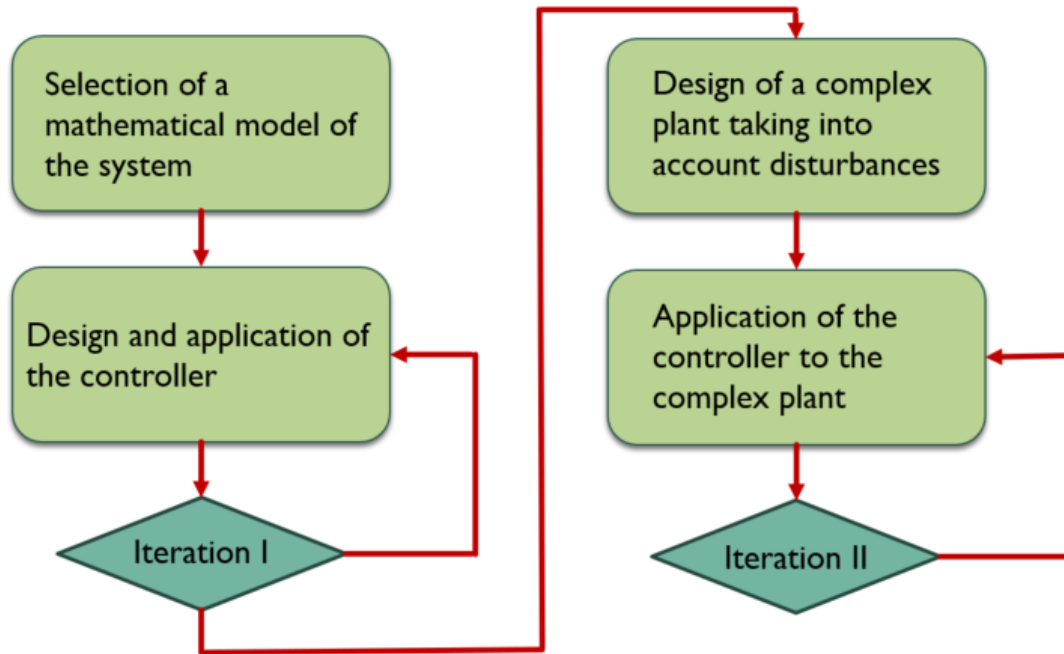
The final strategy chosen for controlling the motion of the CubeSat involved in the RVD manoeuvre is based on a Nonlinear Model Predictive Control, as regards trajectory, Sliding Mode Control, for attitude.

The following schematic illustrates the work logic of the orbit control strategy: after a selection of the mathematical model internal to the MPC, in order to perform prediction and optimization, a controller must be designed. The following step consists of performing some iterations, by means of a trial and error procedure, in order to obtain the best system behaviour with the chosen MPC tuning.

After this initial procedure, based on strongly ideal assumptions, there is a second macro-phase, starting with the design of a complex plant intended to represent a much more realistic scenario, including actuators and disturbances, both internal and external to the system. After the design of a more detailed system intended for realistic simulations, the same controller designed before must be applied to this setup and, by means of the same trial and error procedure described before, a second iteration takes place to obtain the best solution.

The design of the detailed system takes place in an increasing complexity fashion: once a first realistic model is designed, the controller is tuned; then, more realistic elements are gradually added to the system with a consequent tuning of the previous controller, in order to adapt its settings to the new scenario. This progressive addition of details is the key of this project, because the final system employed for simulations has a significant complexity and the controller must be gradually adapted to this setup, in order to avoid unexpected outcomes and waste of time.

Concerning the attitude control, the procedure is different since the control strategy is radically different, as it does not count on a predictive logic. Thus the adaptation of the controller to the detailed model of the RVD procedure is straightforward and the tuning of the Sliding Mode Control is directly performed in the more complex simulating scenario.



*Schematic 1: work logic of trajectory control design*

## ***2.1 Trajectory control – ideal conditions***

As it is possible to outline from *Schematic 1*, the first step consists of selecting a mathematical model able to ideally describe the translational motion involved in the RVD manoeuvre.

This choice falls on the Clohessy-Wiltshire-Hill equations [9]. According to this model, the position of the target vehicle is identified as the origin of the Hill's frame, whose x-axis is found along the orbital radius, y-axis is orthogonal to x-axis and lies on the orbital plane, z-axis is orthogonal to the orbital plane. In order to exploit this model, the target is assumed to be on a circular orbit.

The position of the chaser vehicle with respect to the centre of Earth is equal to

$$\vec{P} = \vec{P}_0 + \delta\vec{p}$$

where  $\vec{P}_0$  is the nominal orbital position of the target and  $\delta\vec{p}$  is the relative position vector of the chaser with respect to the target.

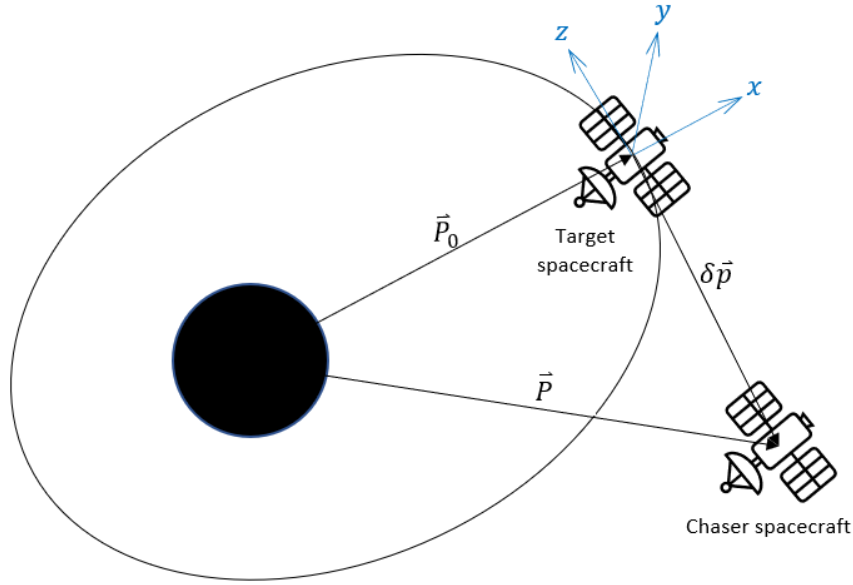


Figure 6: CWH schematic

If  $\delta\vec{p} \ll \vec{P}$  it is possible to approximate the model by means of the Clohessy-Wiltshire-Hill equations:

$$\begin{aligned} \ddot{x} - 3n^2x - 2n\dot{y} &= \frac{F_x}{m_c} \\ \ddot{y} + 2n\dot{x} &= \frac{F_y}{m_c} \\ \ddot{z} + n^2z &= \frac{F_z}{m_c} \end{aligned} \quad (1)$$

where  $F_x$ ,  $F_y$  and  $F_z$  are the three components of external force acting respectively on the  $x$ ,  $y$  and  $z$  direction,  $m_c$  is the mass of the chaser and  $n = \sqrt{\frac{\mu}{P_0^3}}$  ( $\mu$  is the gravitational constant).

In order to employ a Model Predictive Control strategy, a state-space form of the model must be provided.

The state vector  $x$  is defined as

$$x = \begin{bmatrix} \delta p \\ \delta v \end{bmatrix}$$

where  $\delta p = \begin{bmatrix} x \\ y \\ z \end{bmatrix}$  is the relative position of the chaser along the three axis and  $\delta v = \begin{bmatrix} \dot{x} \\ \dot{y} \\ \dot{z} \end{bmatrix}$  is the relative velocity of the chaser, as well as the first order time derivative of  $\delta p$ .

In state-space form, the characteristic matrices of the system are the following ones [2]:

$$A = \begin{bmatrix} 0 & 0 & 0 & 1 & 0 & 0 \\ 0 & 0 & 0 & 0 & 1 & 0 \\ 0 & 0 & 0 & 0 & 0 & 1 \\ 3n^2 & 0 & 0 & 0 & 2n & 0 \\ 0 & 0 & 0 & -2n & 0 & 0 \\ 0 & 0 & -n^2 & 0 & 0 & 0 \end{bmatrix} \quad B = \begin{bmatrix} 0 & 0 & 0 \\ 0 & 0 & 0 \\ 0 & 0 & 0 \\ 1 & 0 & 0 \\ 0 & 1 & 0 \\ 0 & 0 & 1 \end{bmatrix} \quad C = \begin{bmatrix} 1 & 0 & 0 & 0 & 0 & 0 \\ 0 & 1 & 0 & 0 & 0 & 0 \\ 0 & 0 & 1 & 0 & 0 & 0 \\ 0 & 0 & 0 & 1 & 0 & 0 \\ 0 & 0 & 0 & 0 & 1 & 0 \\ 0 & 0 & 0 & 0 & 0 & 1 \end{bmatrix} \quad D = 0$$

By means of the latter matrices, it is possible to compute state and output time responses

$$\dot{x}(t) = A x(t) + B u(t)$$

$$y(t) = C x(t) + D u(t)$$

$$x(t) \in \mathbb{R}^{6 \times 1}$$

$$y(t) \in \mathbb{R}^{6 \times 1}$$

$$u(t) \in \mathbb{R}^{3 \times 1}$$

In this model, outputs  $y(t)$  coincide with states  $x(t)$  ( $C$  is in fact an identity matrix), inputs  $u(t)$  represent the control actions fed to the system (i.e. force provided by actuators).

In order to adapt the model to the Model Predictive Control framework, it is necessary to consider its discretized version, whose state and output equations are:

$$x(k + 1) = A_d x(k) + B_d u(k)$$

$$y(k) = C_d x(k) + D_d u(k)$$

$$x \in \mathbb{X} \subset \mathbb{R}^n$$

$$y \in \mathbb{Y} \subset \mathbb{R}^n$$

$$u \in \mathbb{U} \subset \mathbb{R}^m$$

$k \in \mathbb{Z}^+$  time instants:  $k = 0, \dots, N$

CWH equations are selected for the internal model of the MPC, in order to predict the behaviour of the system.

After this initial step, a trade-off takes place between various software tools useful for designing the controller. In particular the evaluated options were:

- ACADO Toolbox
- Multi-Parametric Toolbox
- Custom Matab function

Simulations are performed by means of the first two toolboxes. As much as concerns the first one, its most appealing features are the possibility of solving optimal control problems, of course, but also multi-objective problems, C++ programming as well as an user-friendly MATLAB interface. Unfortunately the documentation about this toolbox is not exhaustive enough from the point of view of Simulink usage, which has a prior relevance in this project.

The second one among the listed options above is a very valid choice for designing explicit MPC controllers, it is in general very focused on reducing the computational load relied to predictive control-based calculations but it is not the optimal choice for this kind of problem, where a very high degree of accuracy is required.

Even though the first two software tools below are absolutely cutting edge choices for constrained optimal control systems, a custom MATLAB function, for the aim of this thesis, is the best choice, since it can be tailored specifically for the requirements imposed by this particular problem. The chosen solution is different with respect to the options previously listed, also because it offers the possibility of designing a Nonlinear MPC, which is basically an ordinary MPC including nonlinear constraints. This custom tool allows to set and tune the following parameters:

1.  $T_s$  sampling time;
2.  $T_p$  prediction horizon;
3.  $Q$  weighting matrix;
4.  $P$  weighting matrix;
5.  $R$  weighting matrix;
6. upper and lower bounds on control inputs;
7. nonlinear constraint.

In this first design phase, the simulation setup appears evident in *Figure 7*. It is an ideal scenario, where the plant to be controlled by NMPC is identical to the internal model employed by the controller for prediction and optimization problem solution. In the same figure it is possible to see that a column vector of zeros is provided to the controller as reference, as it corresponds to the condition of docking in terms of position and velocity.

An initial condition equal to  $x_0 = [0 \ 0 \ -30 \ 0 \ 0 \ 0]^T$  is set, thus imposing a distance along the z-axis (V-bar in LVLH frame) of 30 m.

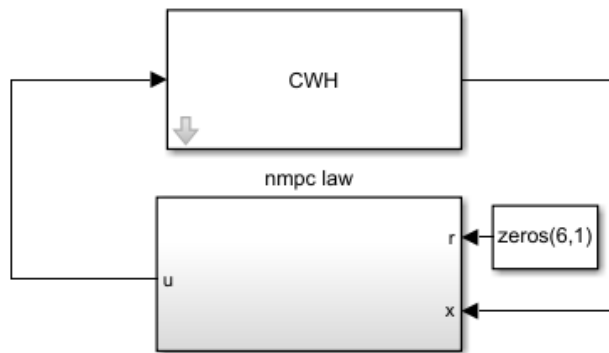


*Figure 7: block schematic of the ideal closed loop system*

In this scenario the tuning of MPC parameters is straightforward, since there is no model mismatch, so the settings are:

<b>Parameter</b>	<b>Chosen value</b>
$T_s$	0.5 s
$T_p$	0.5 s
$Q$	$\begin{bmatrix} 1 & 0 & 0 & 0 & 0 & 0 \\ 0 & 1 & 0 & 0 & 0 & 0 \\ 0 & 0 & 1 & 0 & 0 & 0 \\ 0 & 0 & 0 & 1 & 0 & 0 \\ 0 & 0 & 0 & 0 & 1 & 0 \\ 0 & 0 & 0 & 0 & 0 & 10^6 \end{bmatrix}$

$P$	$\begin{bmatrix} 1 & 0 & 0 & 0 & 0 & 0 \\ 0 & 1 & 0 & 0 & 0 & 0 \\ 0 & 0 & 1 & 0 & 0 & 0 \\ 0 & 0 & 0 & 1 & 0 & 0 \\ 0 & 0 & 0 & 0 & 1 & 0 \\ 0 & 0 & 0 & 0 & 0 & 1 \end{bmatrix}$
$R$	$\begin{bmatrix} 0.1 & 0 & 0 \\ 0 & 0.1 & 0 \\ 0 & 0 & 0.1 \end{bmatrix}$
$u_{min}$	$[-0.7 \quad -0.7 \quad -0.7]$
$u_{max}$	$[0.7 \quad 0.7 \quad 0.7]$

Table 3: MPC settings – ideal setup

As seen from the settings listed above, a prediction horizon equal to the sampling time is chosen for solving this optimization problem. By performing multiple simulations, with different values of prediction horizon, it appears more convenient to select such parameter to be as low as possible, in order to avoid waste of computational power and numerical conflicts. In fact, results obtained with this prediction horizon are significantly better than the ones arisen from a higher  $T_p$ .

Input constraints are due to the actuation limit of 35 mN. Considering the equations (1) of the prediction model, on the right-hand side there is the term  $\frac{F}{m}$ , so the control inputs to be fed to the system are equal to  $F \cdot m$ .

That is the reason why along all three coordinate axes:

$$u_{max} = F_{max} \cdot m = 0.035 \cdot 20 [N \cdot kg] = 0.700 [N \cdot kg]$$

$$u_{min} = F_{min} \cdot m = -0.035 \cdot 20 [N \cdot kg] = -0.700 [N \cdot kg]$$

The applied method for setting weighting matrices is to choose each one equal to identity matrices, at the beginning and then, whether any values are not able to satisfy the expected outcome, the tuning procedure takes place by means of a trial & error procedure. With the initial setup, the requirements imposed by the problems are not respected and docking cannot be achieved because of a too high approach velocity on the z-axis. Additionally, input control actions result too high, because of the high velocity, in particular concerning the term  $u_z$ . For this reason an intervention on weighting factors is required:  $Q$  matrix is chosen equal to an identity matrix apart from the last diagonal term, responsible of weighting the velocity along z-axis, which appears to be the most critical quantity in this problem. Furthermore elements of  $R$  matrix are decreased of one order of magnitude, to give higher importance to state minimization at the expense of actuation.

In this scenario it is not necessary to set a nonlinear constraint, since there are not particularly strict requirements due to the strongly ideal nature of the formulation.

In *Figure 8* the state time response is represented: it is possible to see that the states converge to zero after just 0.5 seconds. In *Figure 9* and *Figure 10* the relative position of the chaser with respect to the target is represented, on *zx*-axes in the former, on *zy*-axes in the latter. The scale on the ordinates' axis is of  $10^{-6}$  order of magnitude (could even be lower) just to show that the misalignment on *x* and *y* axes is null.

From *Figure 11* it is clear that velocity diverge from zero on all three axes but the order of magnitude is equal to  $10^{-4}$  so it can be considered neglectable. The same applies to input time response in *Figure 12*: while  $u_x$  and  $u_y$  converge to zero,  $u_z$  diverges concluding the sequence to a value of  $-1.7 \cdot 10^{-4}$ , which is neglectable. Additionally, input values are very much within upper and lower bounds, so requirements are very well satisfied.

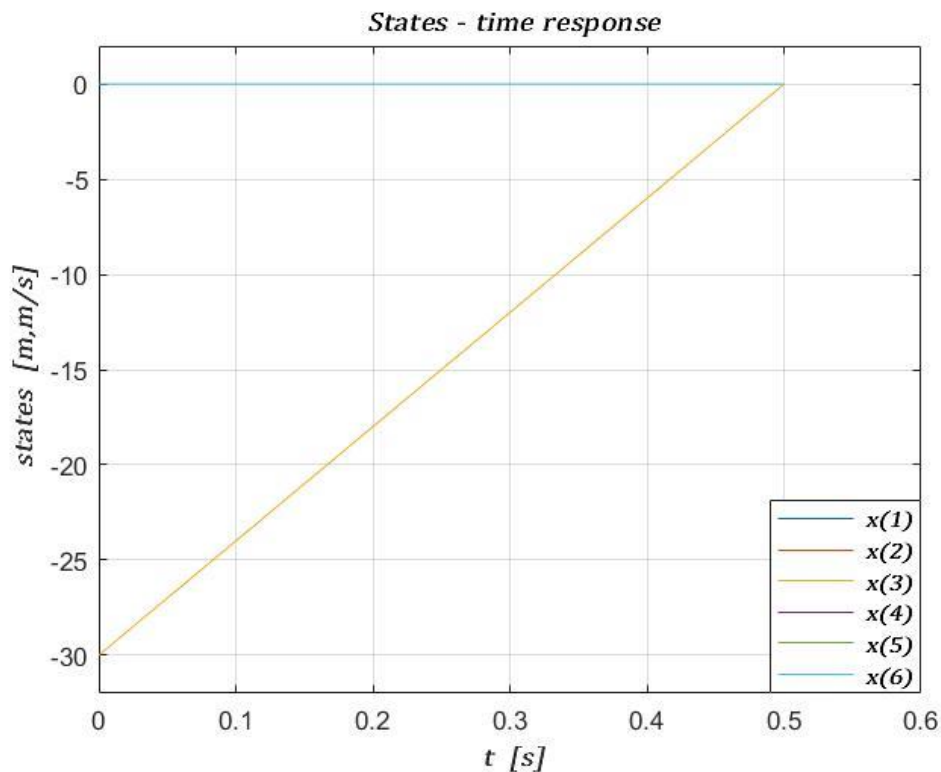


Figure 8: state time response – ideal setup

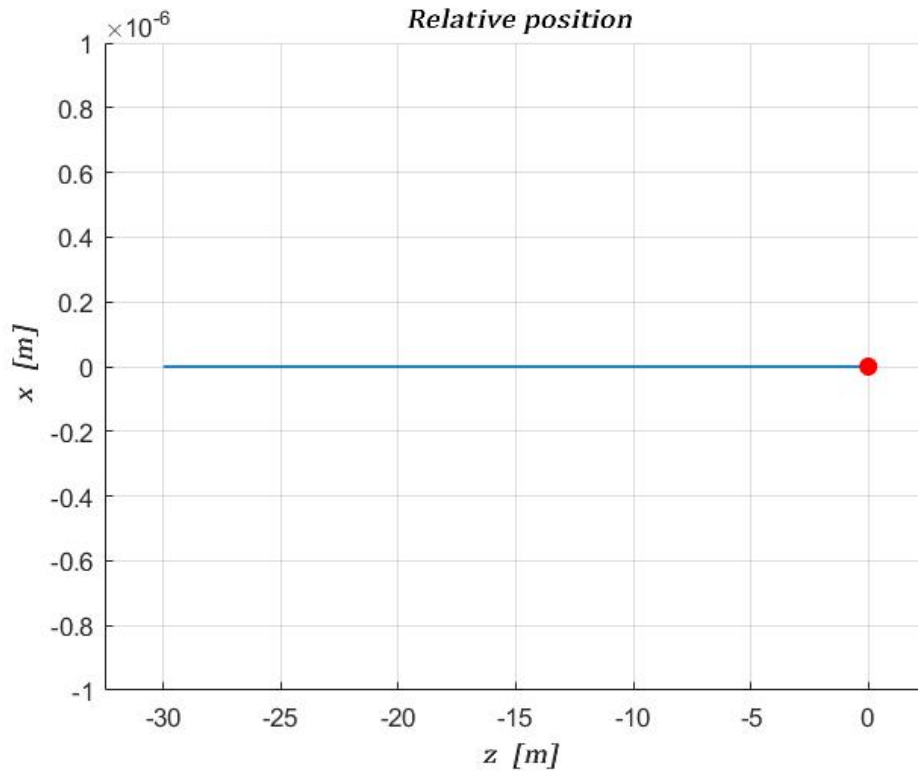


Figure 9: zx relative position – ideal setup

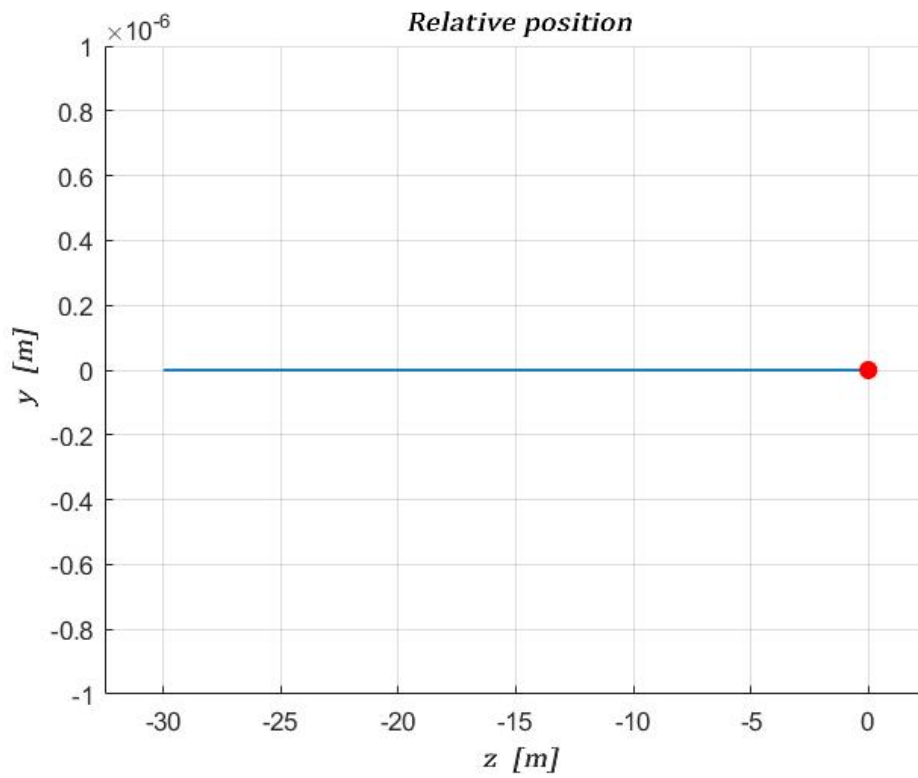


Figure 10: zy relative position – ideal setup

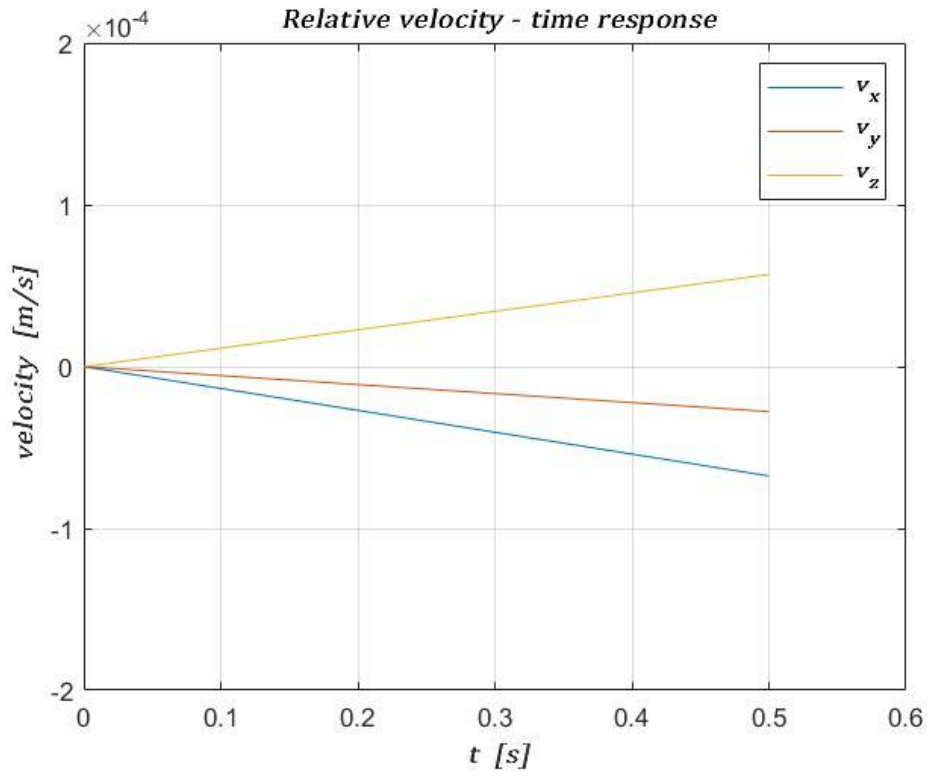


Figure 11: relative velocity – ideal setup

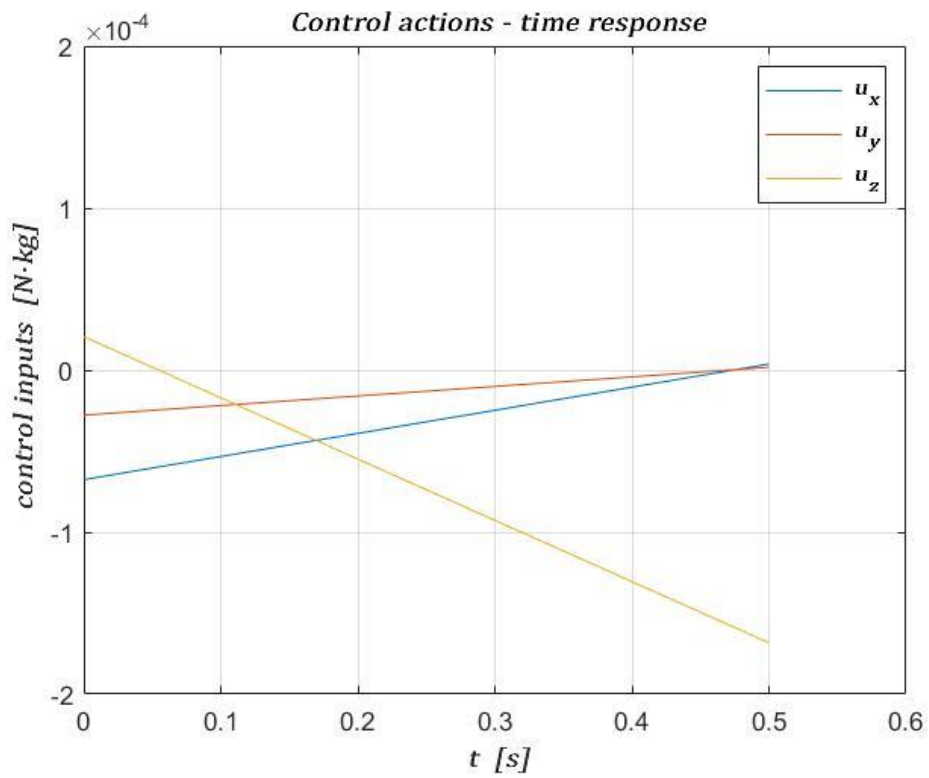


Figure 12: input time response – ideal setup

## 2.2 Realistic model design

The setting of a more realistic simulation scenario takes place, as explained at the beginning of this chapter, in a progressive fashion. In particular, this part is divided into three main phases:

- 1) design of translational and rotational dynamic models on Simulink which constitute the plant and inclusion of the external disturbances in the model, with a consequential application and tuning of attitude and orbit controllers;
- 2) design of actuator models in order to achieve a more realistic condition, thus controller tuning;
- 3) design of a model simulating sloshing phenomenon and disturbance associated to it.

As it is outlined in *Figure 13* the whole model is presented as a closed loop system where the light blue block called *Dynamics and Kinematics* includes the actual plant and the external disturbances acting on it, while the yellow block *GNC* is a subsystem containing only the controllers, in this phase.

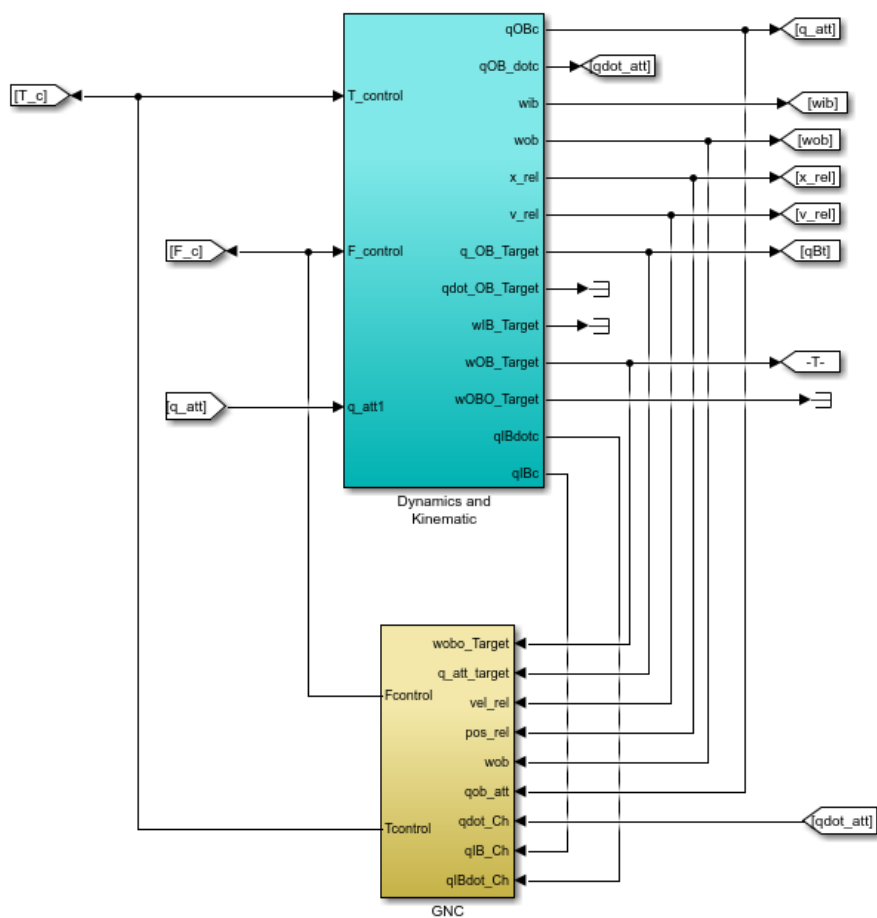


Figure 13: block schematic of the realistic closed loop system

## 2.2.1 Plant, external disturbances and controllers design

### 2.2.1.1 Dynamics and kinematics

The plant of the system can be divided in two main parts, which are translational and rotational dynamics/kinematics.

As much as concerns the part of the plant deputed to modelling translational dynamics and kinematics, Clohessy-Wiltshire equations are used, as in the prediction model of MPC.

As regards rotational motion, it is necessary to define a set of dynamic equations describing a system from the torque  $\mathbf{M}$  to the angular velocity  $\boldsymbol{\omega}$  and a set of kinematic equations related to a system from  $\boldsymbol{\omega}$  to  $\mathbf{q}$  (attitude expressed in quaternion). The overall system results into the one in *Figure 14* with  $\mathbf{M}$  as input torque applied to the body and  $\mathbf{q}$  as output to control [8].

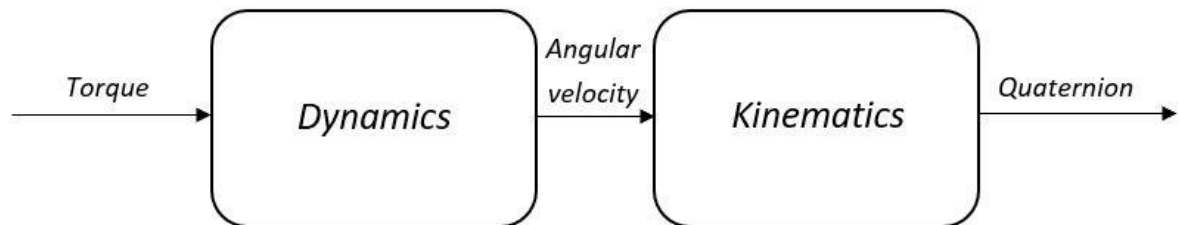


Figure 14: block schematic - rotational motion

Given a rigid body in rotating motion with respect to an inertial frame with angular velocity

$\boldsymbol{\omega} = \omega_1 \mathbf{b}_1 + \omega_2 \mathbf{b}_2 + \omega_3 \mathbf{b}_3$  it is possible thus to define the said inertial frame as a frame moving at constant velocity, with  $\mathbf{i}_1, \mathbf{i}_2, \mathbf{i}_3$  as unit vectors and axes  $X, Y, Z$ . Furthermore it is necessary to define a body frame whose origin is the centre of mass (CoM) of the body, with unit vectors  $\mathbf{b}_1, \mathbf{b}_2, \mathbf{b}_3$  and axes  $x, y, z$ .

Given the torque  $\mathbf{M}$  acting on the body and the inertia matrix of the body  $\mathbf{J}$ , the Euler moment equation is:

$$\mathbf{M} = \mathbf{J}\dot{\boldsymbol{\omega}} + \boldsymbol{\omega} \times \mathbf{J}\boldsymbol{\omega}$$

which can be implemented as the following block diagram:

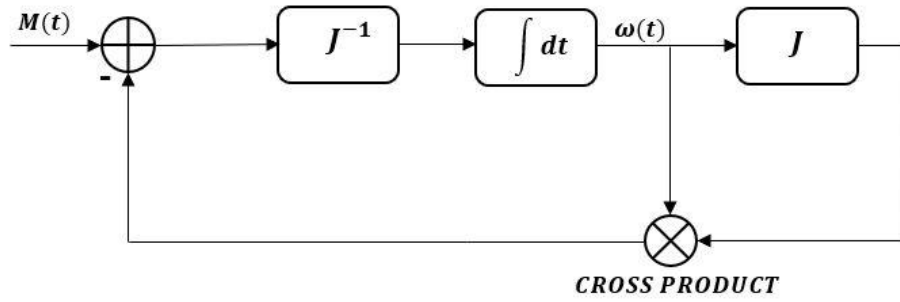


Figure 15: block schematic - Euler moment equations

The aim of rotational kinematics is to represent the time evolution of the quaternion in function of the angular velocity. At the time instant  $t + \Delta t$  attitude expression is obtained from the Hamilton product between the quaternion at time  $t$  and the quaternion variation occurred from time  $t$  and time  $t + \Delta t$ , i.e.:

$$\mathbf{q}(t + \Delta t) = \mathbf{q}(t) \otimes \Delta \mathbf{q}(t)$$

Given  $\omega$  the magnitude of the angular speed vector  $\boldsymbol{\omega}$ , for a small time variation  $\Delta t$  the rotation angle can be expressed as  $\omega \Delta t$ . Being  $\mathbf{u}$  the rotation axis, when  $|\mathbf{u}| = 1$ ,  $\boldsymbol{\omega} = \omega \mathbf{u}$ .

Thus for small  $\Delta t$ ,

$$\Delta \mathbf{q} \cong \begin{bmatrix} \cos \frac{\omega \Delta t}{2} \\ \mathbf{u} \sin \frac{\omega \Delta t}{2} \end{bmatrix} \cong \begin{bmatrix} 1 \\ \mathbf{u} \frac{\omega \Delta t}{2} \end{bmatrix} = \begin{bmatrix} 1 \\ \frac{\boldsymbol{\omega} \Delta t}{2} \end{bmatrix}$$

Which means that

$$\begin{aligned} \dot{\mathbf{q}} &= \lim_{\Delta t \rightarrow 0} \frac{\mathbf{q}(t + \Delta t) - \mathbf{q}(t)}{\Delta t} = \lim_{\Delta t \rightarrow 0} \frac{\mathbf{q} \otimes \Delta \mathbf{q} - \mathbf{q}}{\Delta t} \\ &= \lim_{\Delta t \rightarrow 0} \frac{\mathbf{q} \otimes (\Delta \mathbf{q} - (1,0,0,0))}{\Delta t} = \lim_{\Delta t \rightarrow 0} \frac{\mathbf{q} \otimes ((1, \frac{\boldsymbol{\omega} \Delta t}{2}) - (1,0,0,0))}{\Delta t} \end{aligned}$$

$$= \lim_{\Delta t \rightarrow 0} \frac{\mathbf{q} \otimes \left(0, \frac{\boldsymbol{\omega} \Delta t}{2}\right)}{\Delta t} = \frac{1}{2} \mathbf{q} \otimes (0, \boldsymbol{\omega}) = \frac{1}{2} \boldsymbol{\Omega} \mathbf{q}$$

Where  $\boldsymbol{\Omega}$  is the following skew-symmetric matrix:

$$\boldsymbol{\Omega} \doteq \begin{bmatrix} 0 & -\omega_1 & -\omega_2 & -\omega_3 \\ \omega_1 & 0 & \omega_3 & -\omega_2 \\ \omega_2 & -\omega_1 & 0 & -\omega_1 \\ \omega_3 & \omega_2 & -\omega_1 & 0 \end{bmatrix}$$

### 2.2.1.2 External disturbances

The main disturbances acting on the CubeSat are, in this design phase, coming from the external environment. The causes of these disturbing elements are the gravitational and magnetic field and atmospheric drag [10].

By making an a-priori assumption that the satellite is affected only by the Earth's gravitational field, the intensity of the latter on the chaser can be computed by means of the Newton's law of gravitation:

$$\bar{\mathbf{g}} = -\frac{GM}{r^2} \hat{\mathbf{r}}$$

$G$ : gravitational constant

$r$ : distance from the center of mass

$M$ : mass of the body

The parts of the vehicle, finding itself inside the gravitational field, which happen to be closer to the body generating the said field, are subject to a higher attraction force. This phenomenon generates an offset between the forces applied to different parts of the satellite, resulting in a disturbing torque trying to align the major axis of the spacecraft with the local vertical one. The expression of the disturbance torque is:

$$\bar{\mathbf{T}}_g = -3\omega^2 \hat{\mathbf{r}} \times \mathbf{J} \cdot \hat{\mathbf{r}}$$

The second source of external disturbance is the interaction between the residual magnetic field of the satellite and the Earth's magnetic field. Along its orbit, in fact, the CubeSat is included in

the Earth's magnetosphere whose greatest advantage is the protection of the spacecraft from the cosmic radiation. The satellite's residual magnetic field is due to electrical currents and hysteresis noise produced by on board electronics and ferromagnetic materials. The outcome of this phenomenon is a disturbing torque expressed as follows:

$$\bar{T}_{mr} = \bar{m}_r \times \bar{B}$$

$\bar{m}_r$ : residual magnetic dipole  
associated to the CubeSat

$\bar{B}$ : *Earth's magnetic field*

The phenomenon of atmospheric drag is due to the collision between atmospheric molecules and the CubeSat's surface, resulting into a slight perturbation in the attitude and in the height of the orbit too. The drag force is obtained as follows:

$$F_D = \frac{1}{2} C_D A \rho V^2$$

$C_D$ : ballistic coefficient

$A$ : reference area

$\rho$ : density of atmosphere

$V$ : velocity of the flow wrt the CubeSat

The resulting disturbance torque has a nonzero value only if the centre of mass and the centre of pressure of the spacecraft do not coincide; it can be expressed as:

$$\bar{T}_D = \bar{r}_{cp} \times \bar{F}_D$$

$\bar{r}_{cp}$ : distance vector between center of  
mass and centre of pressure

The product between the drag force  $\bar{F}_D$  and the rotation matrix resulting from the chaser's attitude is fed to the part of the plant modelling the translational motion: this makes the atmospheric drag a disturbance for both linear and rotational motion of the satellite.

### 2.2.1.3 Orbit controller

The first step consists of applying the controller described in chapter 2.1, employed for the ideal simulation setup, to the more realistic scenario previously presented, taking into account external disturbances.

By maintaining the same settings displayed in *Table 3*, the outcome is a poor control performance, due to the non-ideality of the scenario. A more refined control design is necessary, in this case, following two main steps:

1. Definition of an acceptance cone constraint
2. Refinement of MPC's weighting factors and settings

The acceptance cone constraint sets a varying upper and lower bound along the simulated sequence, in order to guarantee a more and more narrow approach corridor with the increase of simulating time. In *Figure 16* the region of space allowed by the constraint is outlined in red, while the angle between slant side and height of the cone is  $\alpha = 15^\circ$ .

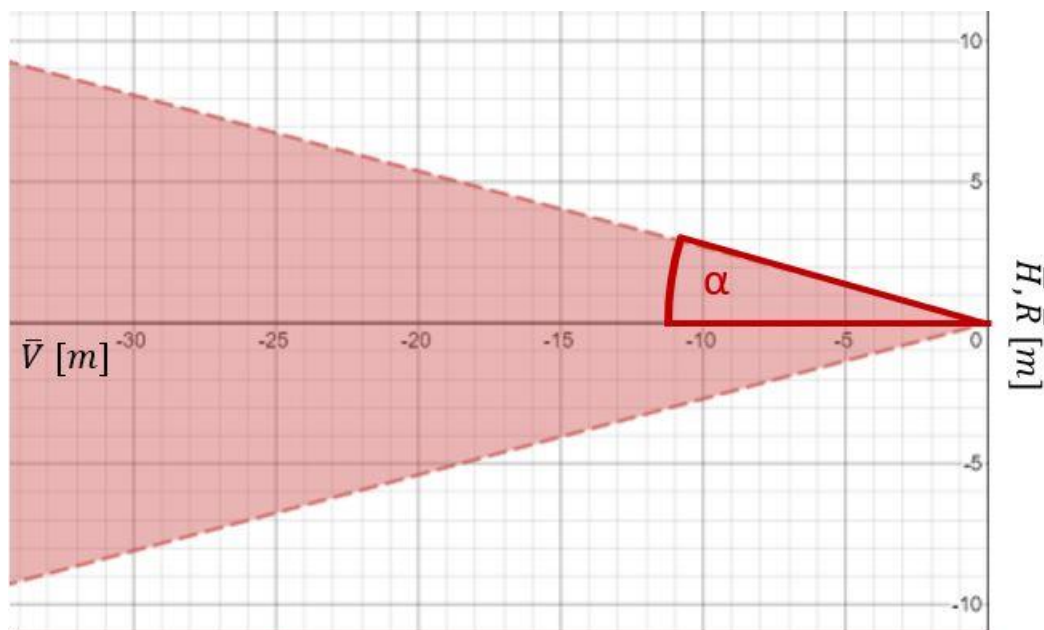


Figure 16: acceptance cone constraint

The chosen MPC parameters are listed in *Table 4*. The main changes with respect to the ideal scenario concern the prediction horizon, whose value is lower than before. Actually, by adopting the usual trial & error approach, the choice of a smaller prediction horizon resulted in a better overall performance, at the expense of a significantly slower response of the system. Although this latter consequence does not necessarily have to be considered a drawback: if a suitable trade off is found between speed of the system and satisfaction of constraints, a slower system

results to be easier to handle, in terms of overshoots and abrupt variation of parameters. This characteristic is particularly valuable for the purpose of a soft docking. Also from the point of view of the computational effort, a smaller prediction horizon means a smaller number of regions of the optimizing polytope, resulting in a shorter computing time. With a higher prediction horizon, larger values in terms of final relative position and velocity of the chaser spacecraft are obtained, because of numerical conflict due to the complexity of the optimization problem. To this end, also the sampling time of the whole model is decreased with respect to the previous case.

Parameters belonging to  $Q$  matrix are chosen in such a way that a higher weight is assigned to the first two states, the ones responsible for the largest overshoot. A lower weight wrt the other ones is given to the third state, i.e. relative position of the chaser along the approach axis, in order to slow down the response of the system, to avoid an undesired overshoot in terms of velocity along the approach axis. All three velocities along the different axes are weighted with a medium value among the used ones, i.e. 100, because it results to be a good trade-off between tracking performance and speed of convergence. Elements of  $P$  matrix are chosen with smaller values than the ones of  $Q$  matrix, since the latter is able to guarantee a satisfying performance and thus there is no need to waste computational power, in this case, by assigning higher weights also in this matrix.

The elements of  $R$  matrix are chosen extremely close to zero (they cannot be equal to zero because, for intrinsic requirements of the MPC formulation,  $R$  must be positive definite) in order to drive all the computational effort towards the optimization of states and to exploit all the available actuation, which is a key element in this phase of the manoeuvre.

Upper and lower bounds are absolutely identical to the ideal scenario, since the requirements imposed to the problem are the same, from the point of view of input constraints.

<b>Parameter</b>	<b>Chosen value</b>
$T_s$	0.1 s
$T_p$	0.2 s
$Q$	$\begin{bmatrix} 500 & 0 & 0 & 0 & 0 & 0 \\ 0 & 500 & 0 & 0 & 0 & 0 \\ 0 & 0 & 20 & 0 & 0 & 0 \\ 0 & 0 & 0 & 100 & 0 & 0 \\ 0 & 0 & 0 & 0 & 100 & 0 \\ 0 & 0 & 0 & 0 & 0 & 100 \end{bmatrix}$

$P$	$\begin{bmatrix} 0 & 0 & 0 & 0 & 0 & 0 \\ 0 & 0 & 0 & 0 & 0 & 0 \\ 0 & 0 & 10 & 0 & 0 & 0 \\ 0 & 0 & 0 & 10 & 0 & 0 \\ 0 & 0 & 0 & 0 & 10 & 0 \\ 0 & 0 & 0 & 0 & 0 & 100 \end{bmatrix}$
$R$	$\begin{bmatrix} 10^{-50} & 0 & 0 \\ 0 & 10^{-50} & 0 \\ 0 & 0 & 10^{-50} \end{bmatrix}$
$u_{min}$	$[-0.7 \quad -0.7 \quad -0.7]$
$u_{max}$	$[0.7 \quad 0.7 \quad 0.7]$

Table 4: MPC settings - realistic scenario 1

### 2.2.1.4 Attitude controller

A Sliding Mode controller is employed for attitude. The selected control law is:

$$u = k_1 \tilde{q} \cdot \text{sign}(\tilde{q}_0) - k_2 \omega (1 - \tilde{q})^T \cdot \tilde{q}$$

$\tilde{q}$ : vector part of the quaternion

tracking error  $\tilde{q} = q^{-1} \otimes q_r$

$q_r$ : reference quaternion

$\tilde{q}_0$ : real part of the quaternion

tracking error

$k_1, k_2$ : tuning parameters

$k_1$  is chosen equal to 15, while  $k_2$  is equal to 10 in this scenario. They are respectively deputed to weighting tracking performance and to minimize disturbance's action on attitude.

### 2.2.1.5 Results from simulations – realistic scenario 1

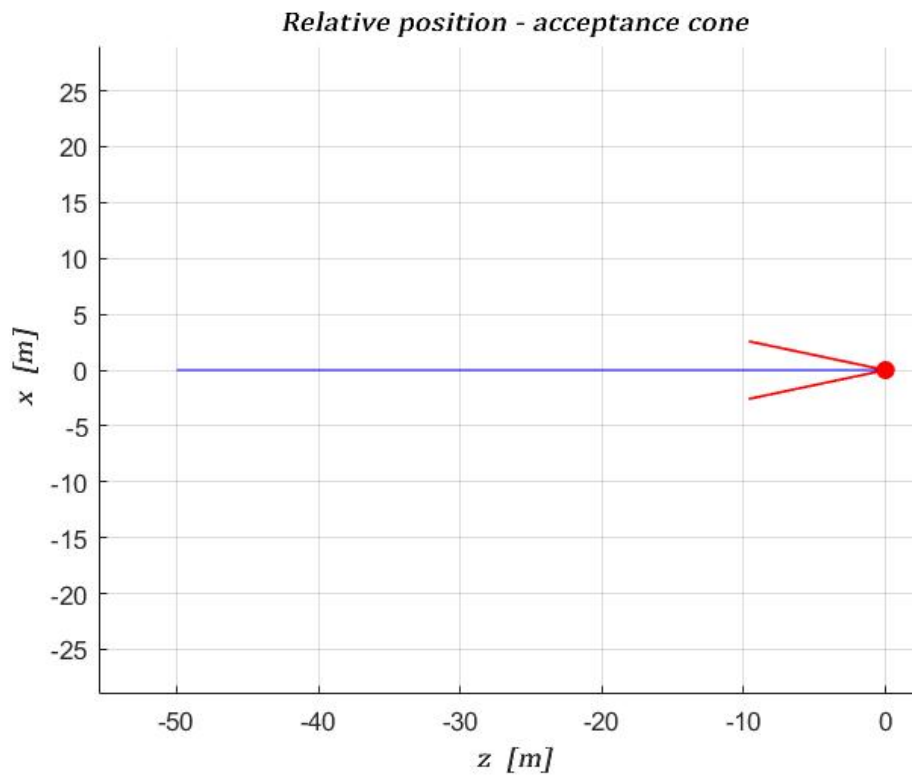


Figure 17:  $xz$  relative position - realistic scenario 1

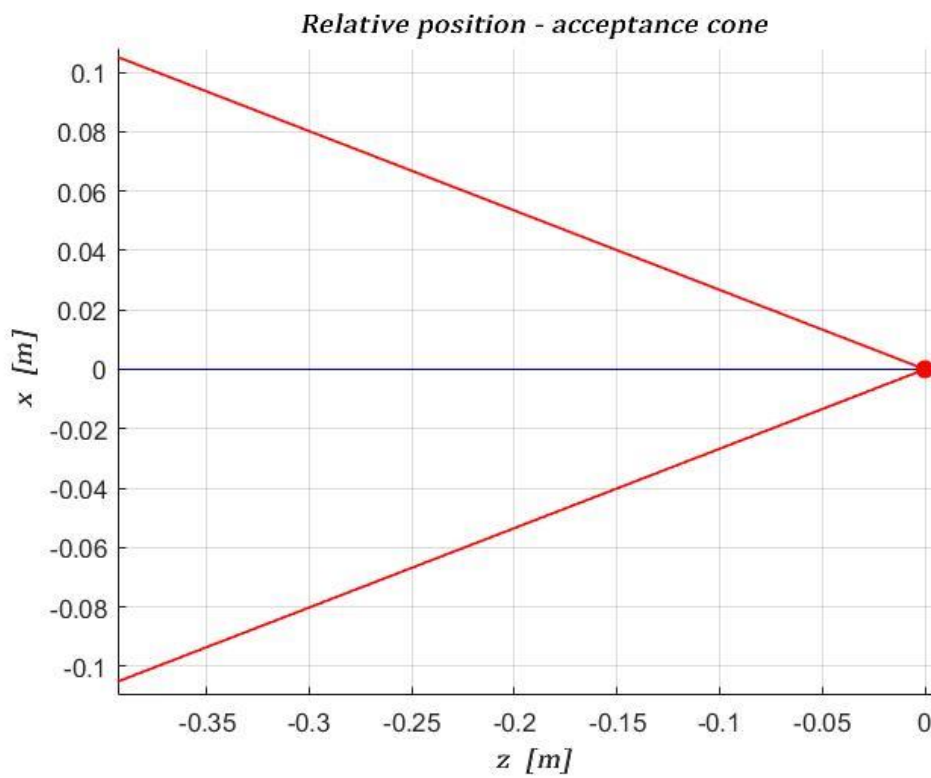


Figure 18:  $xz$  relative position (proximity detail) - realistic scenario 1

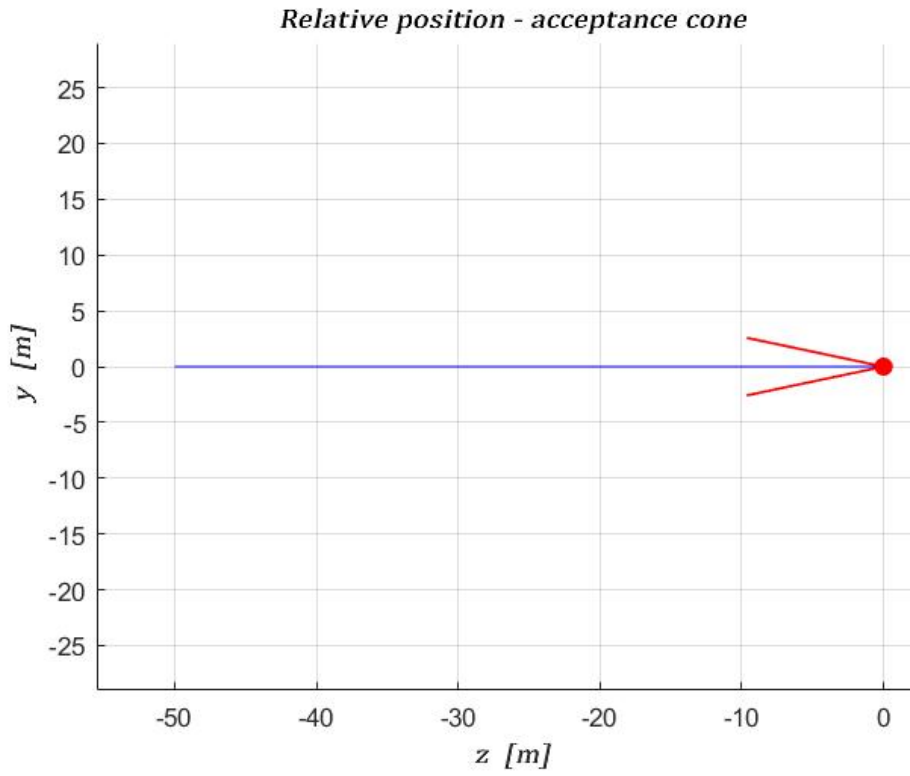


Figure 19: zy relative position - realistic scenario 1

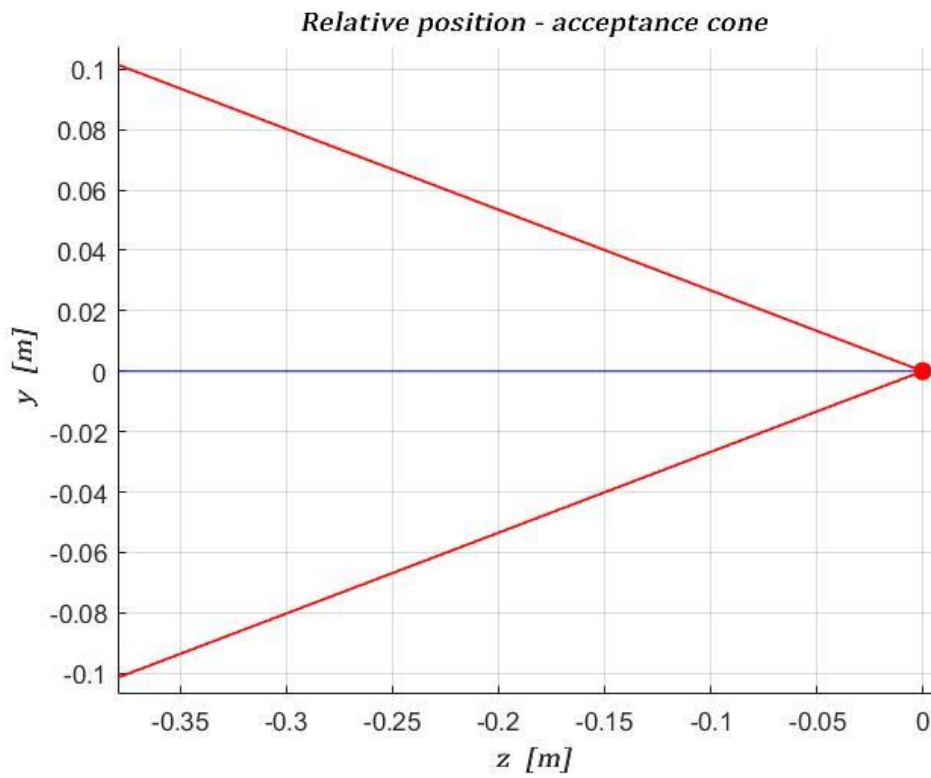


Figure 20: zy relative position (proximity detail) - realistic scenario 1

**Relative position 3d - acceptance cone**

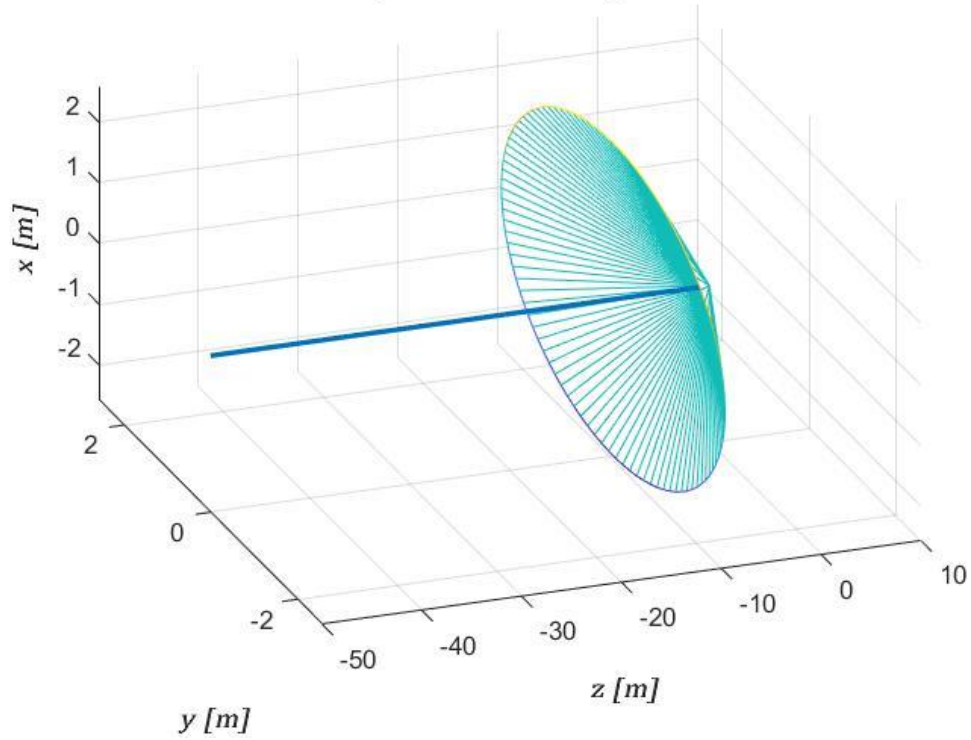


Figure 21: relative position 3d and acceptance cone – realistic scenario 1

**Input actions - time response**

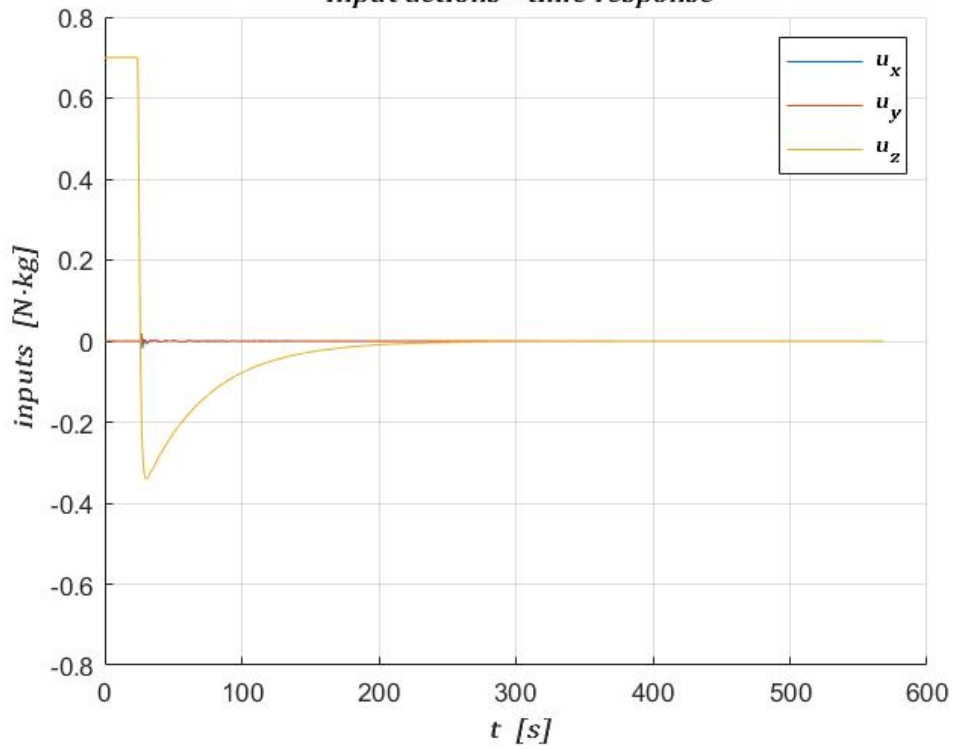


Figure 22: input time response - realistic scenario 1

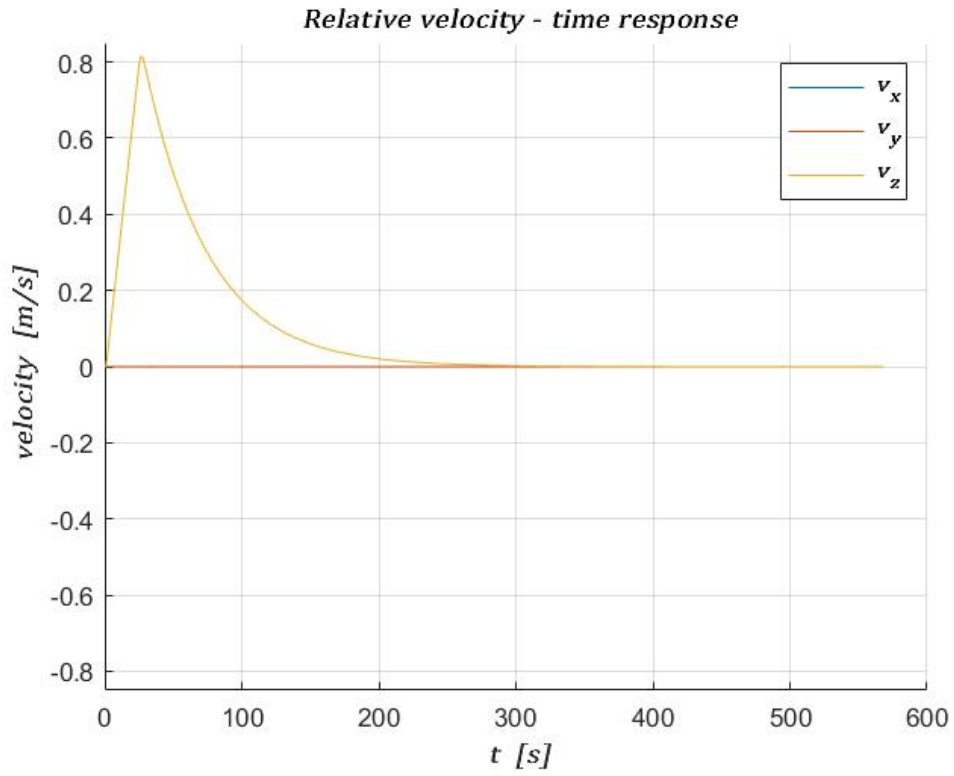


Figure 23: relative velocity time response - realistic scenario 1

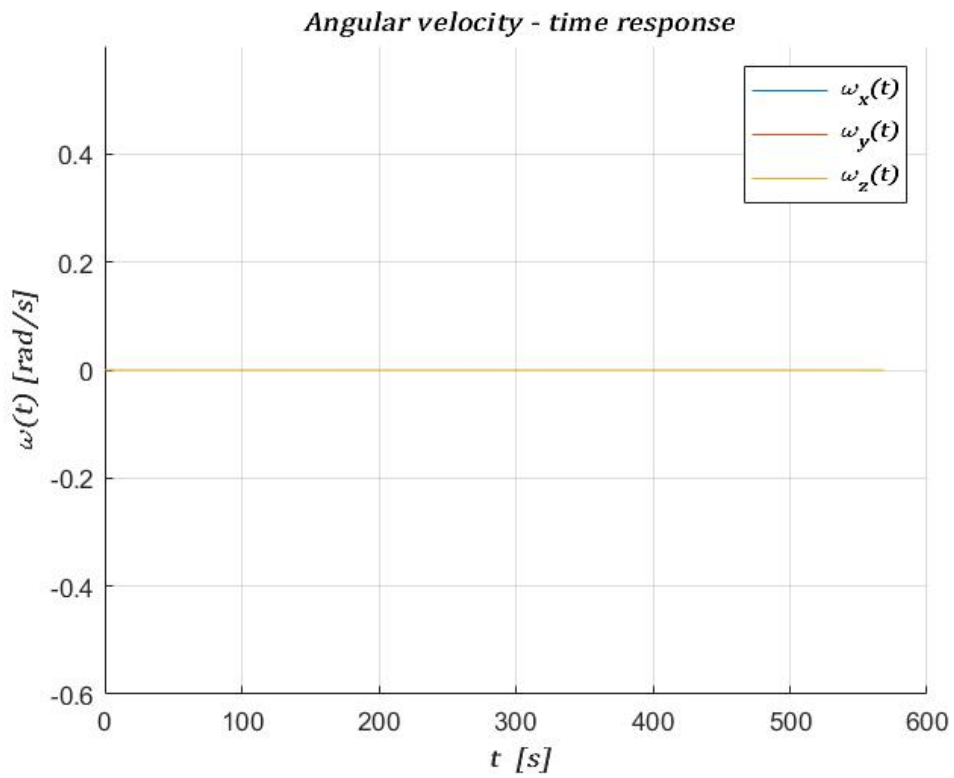


Figure 24: angular velocity time response - realistic scenario 1

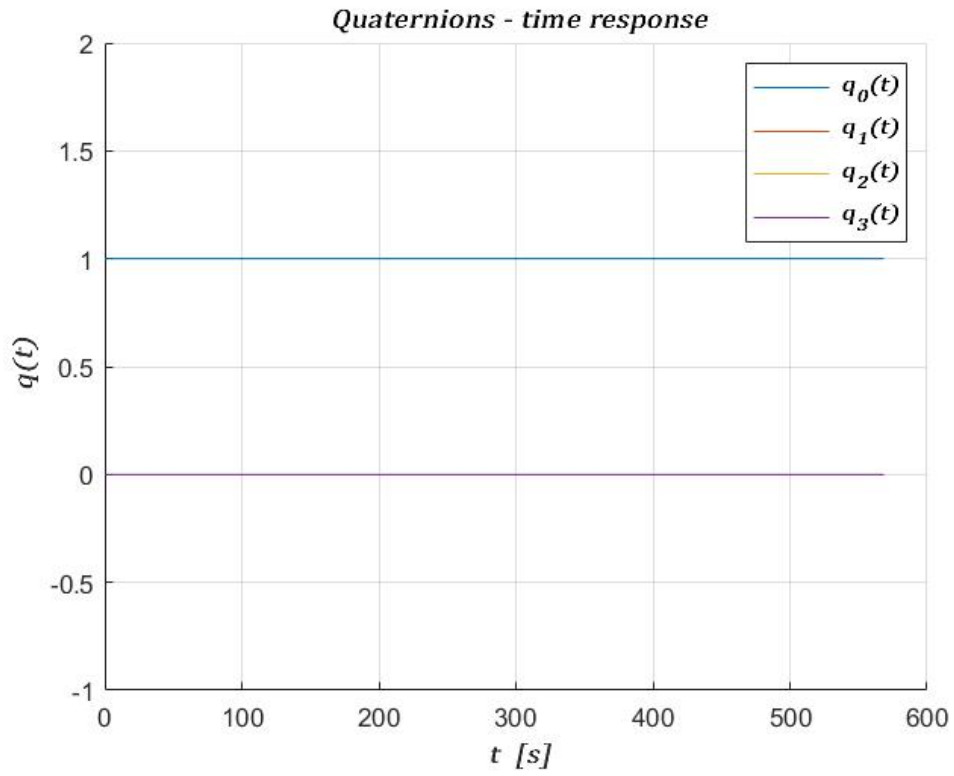


Figure 25: quaternions time response - realistic scenario 1

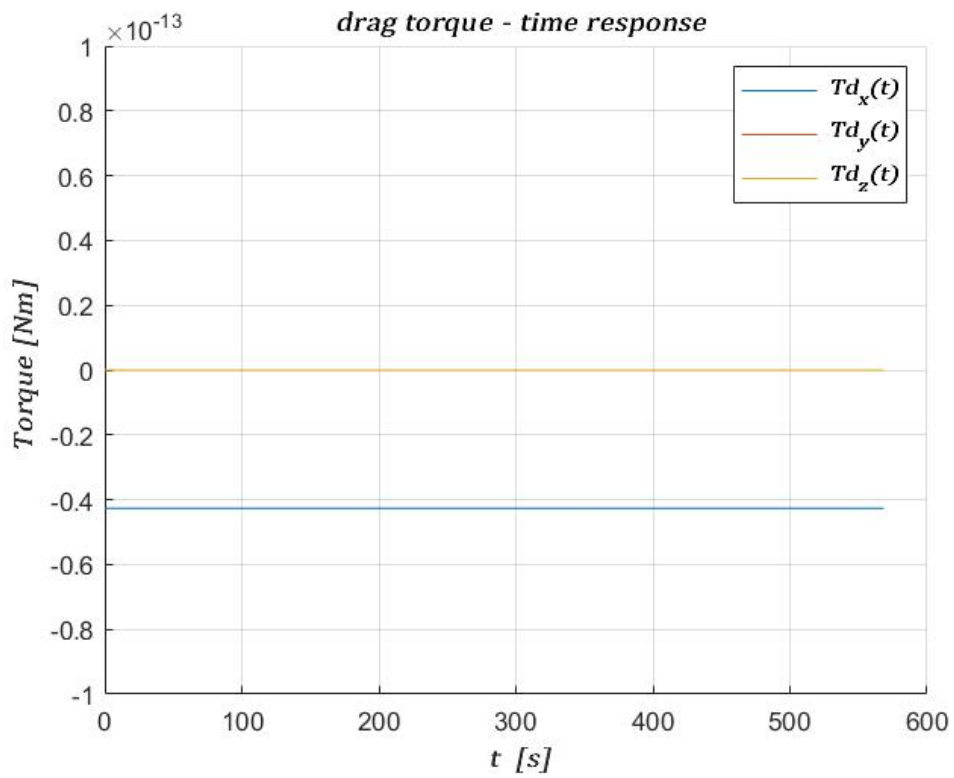


Figure 26: Drag torque time response - realistic scenario 1

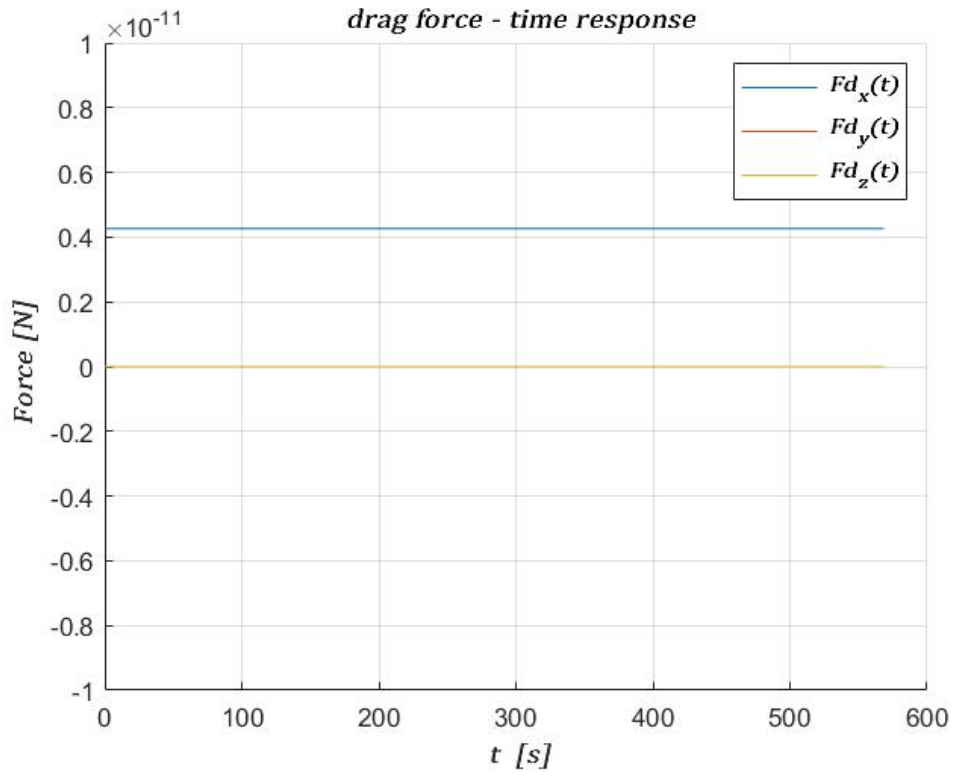


Figure 27: Drag force time response - realistic scenario 1

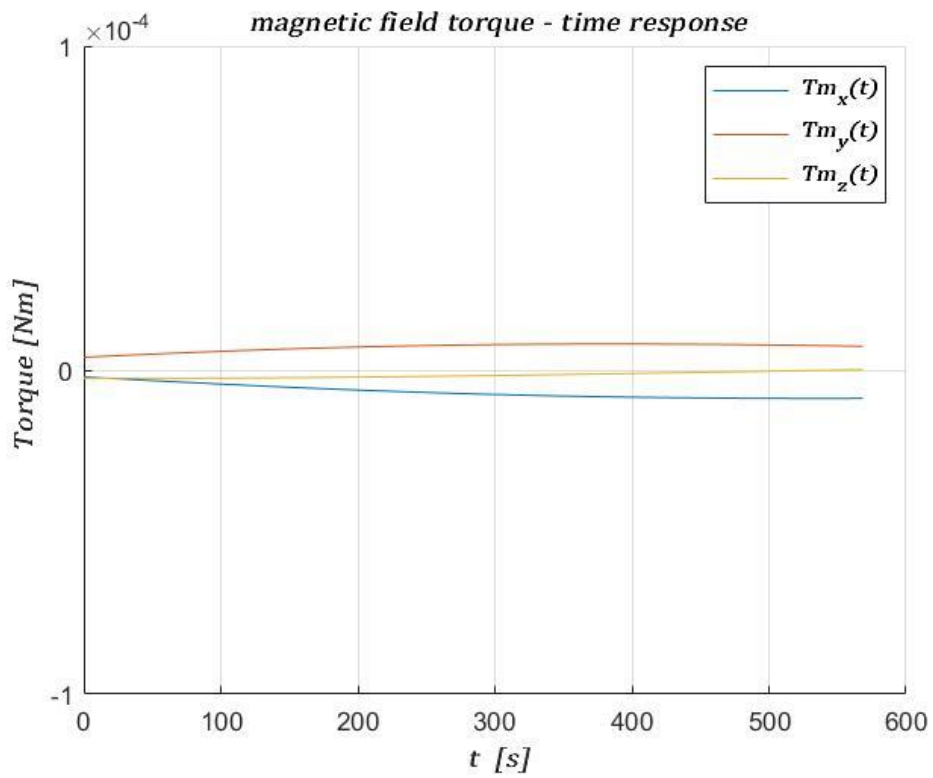


Figure 28: Magnetic field torque time response - realistic scenario 1

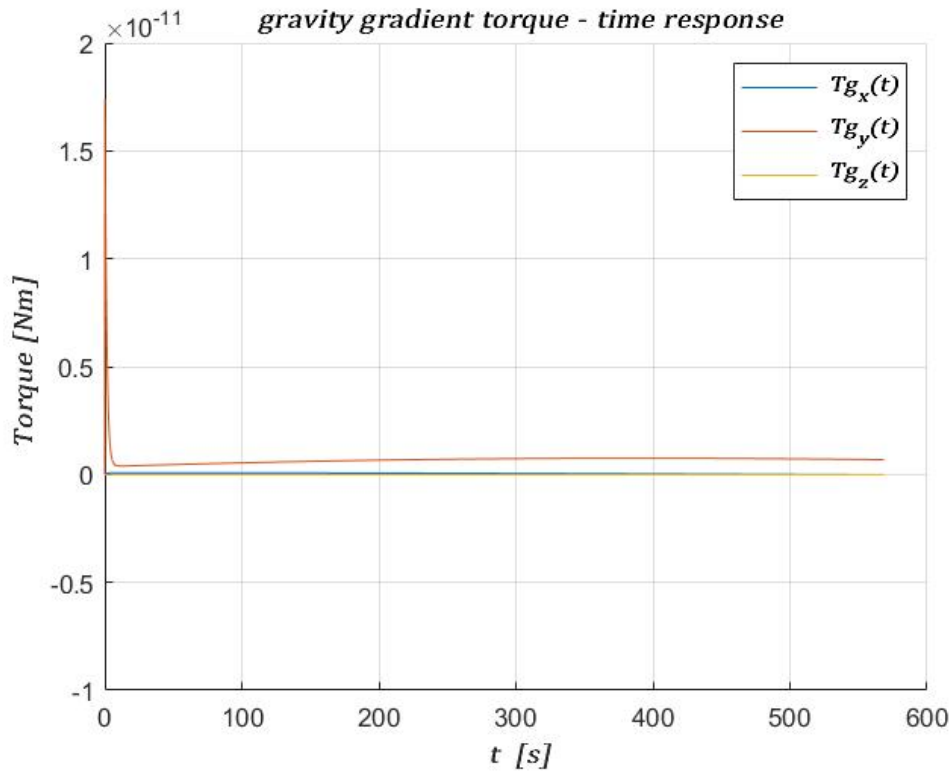


Figure 29: Gravity gradient torque time response - realistic scenario 1

The manoeuvre described in the plots above is slightly different with respect to the one related to the ideal scenario, since the offset distance on the z-axis ( $V\text{-bar}$ ) is increased up to -50 m. In fact, from mission analysis-related simulations, performed by other members of CubeSat team, it results most likely to have a hold point at 50 meters distance from the target. So, for the sake of a more realistic scenario, the initial condition along  $V\text{-bar}$  is modified.

As it is possible to see in the plots reported from *Figure 17* to *Figure 21*, acceptance cone constraint is fully respected (the final relative position on all three axes has an error with  $10^6$  order of magnitude).

Regarding *Figure 22* it is clear how, after an initial push bringing control inputs along the approach axis to saturation to the upper bound, the values rapidly decrease. MPC is able to automatically optimize the control input sequence and shows, especially in input time response, how suitable it is for this kind of applications.

In *Figure 23* velocity time response is presented, mirroring what is above written about input time response: after an initial increase of speed along the approach axis, the parameters' values rapidly decrease and then converge to zero.

From *Figure 24* and *25* it is clear how attitude is not affected by any perturbations: a straight line manoeuvre is described, in this particular scenario, so attitude control does not play a major role in this first case, it is only deputed to ensure tracking performance.

From *Figure 26* to *Figure 29* the time response of external disturbances is described. As it results clear from the orders of magnitude, they are quite neglectable with respect to the overall dynamics of the system, apart from the magnetic field torque.

In this simulating scenario all the problem requirements are satisfied, the system reacts well to disturbances, thus the chosen control strategy is able to guarantee a robust performance.

## 2.2.2 Actuator models

Actuators' design is articulated in two different phases, referring to the main employed actuation systems:

1. Thrusters;
2. Reaction wheels.

The first ones are intended to provide translational actuation, while the second ones are deputed to attitude actuation. While in the first scenario the two dynamics, translational and rotational, were independent one from the other, in the setup proposed below, this ideality is removed. In fact, even though the propulsion system is not responsible for attitude actuation, in this model, it is also true that thruster misalignment causes an unexpected disturbing torque which must be taken into account.

### 2.2.2.1 Thrusters

The CubeSat is equipped with eight thrusters [11], whose each one is made up of a valve couple with a nozzle. Each valve is represented in *Figure 30* as the vertices of the squares *abcd* and *efgh*.

Depending on the control actions  $[F_x, F_y, F_z]$  provided by the controller, the valves are activated according to the following table:

<i>Control action</i>	<i>Valve<sub>a</sub></i>	<i>Valve<sub>b</sub></i>	<i>Valve<sub>c</sub></i>	<i>Valve<sub>d</sub></i>	<i>Valve<sub>e</sub></i>	<i>Valve<sub>f</sub></i>	<i>Valve<sub>g</sub></i>	<i>Valve<sub>h</sub></i>
$F_x > 0$	OFF	ON	OFF	ON	OFF	ON	OFF	ON
$F_x < 0$	ON	OFF	ON	OFF	ON	OFF	ON	OFF
$F_y > 0$	OFF	OFF	ON	ON	OFF	OFF	ON	ON
$F_y < 0$	ON	ON	OFF	OFF	ON	ON	OFF	OFF
$F_z > 0$	OFF	OFF	OFF	OFF	ON	ON	ON	ON
$F_z < 0$	ON	ON	ON	ON	OFF	OFF	OFF	OFF

*Table 5: Valves activation criterion*

Every nozzle is inclined with respect to the body reference frame (outlined in *Figure 30* and whose origin is the CoM of the spacecraft) of the angles

- $\alpha = \frac{\pi}{4}$  with respect to x-axis;
- $\beta = \frac{\pi}{6}$  with respect to z-axis.

In the two following tables the position of each valve is expressed in the three cartesian coordinates, also referred to the body reference frame.

Parameter	Value	Parameter	Value	Parameter	Value	Parameter	Value
$a_x$	-0.0375	$b_x$	-0.0375	$c_x$	0.0375	$d_x$	0.0375
$a_y$	-0.0375	$b_y$	0.0375	$c_y$	0.0375	$d_y$	-0.0375
$a_z$	-0.1130	$b_z$	-0.1130	$c_z$	-0.1130	$d_z$	-0.1130

Table 6: thrusters position abcd

Parameter	Value	Parameter	Value	Parameter	Value	Parameter	Value
$e_x$	-0.0375	$f_x$	-0.0375	$g_x$	0.0375	$h_x$	0.0375
$e_y$	-0.0375	$f_y$	0.0375	$g_y$	0.0375	$h_y$	-0.0375
$e_z$	0.1130	$f_z$	0.1130	$g_z$	0.1130	$h_z$	0.1130

Table 7: thrusters position efgh

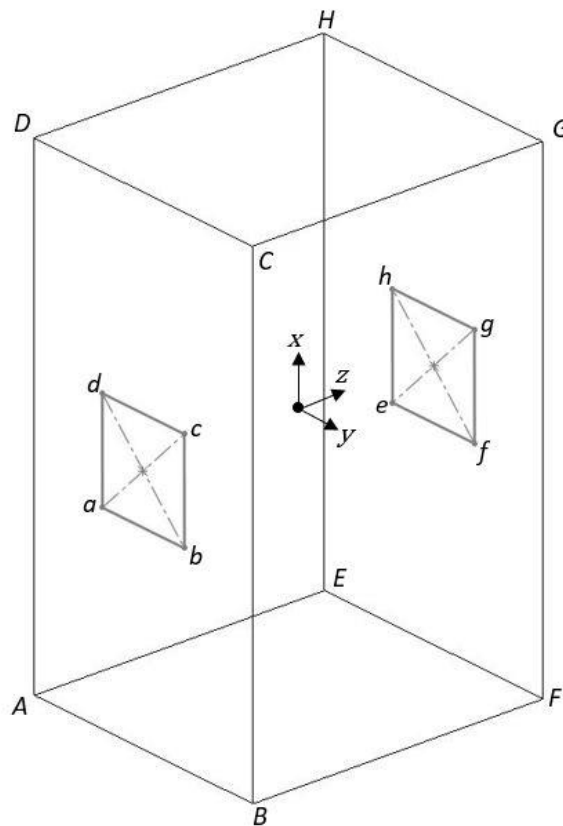


Figure 30: Thrusters position

From specifics of the propulsion system, it is known that the maximum thrust which the propulsion system is able to provide is equal to 35 mN, meaning that the maximum force provided by each thruster is 8.75 mN (vector norm).

For each thruster the following set of equations holds:

$$\begin{aligned} f_x &= f \cdot \sin(\beta) \\ f_y &= f \cdot \sin(\alpha) \cdot \cos(\beta) \\ f_z &= f \cdot \cos(\alpha) \cdot \cos(\beta) \end{aligned} \tag{2}$$

The propulsion system is designed in two different setups:

1. the first one, simpler, by employing PWM modulation;
2. the second one, more refined, by modelling the opening of each valve in a more realistic way.

Additionally, in order to obtain a higher degree of precision and to get closer to a more realistic setup, the effective thrust produced by the thrusters is multiplied by a rotation matrix expressing the relative attitude of the chaser with respect to the target. In this way it is possible to couple the two dynamics (translational and rotational) and to make them interdependent.

**First setup – PWM modulation**

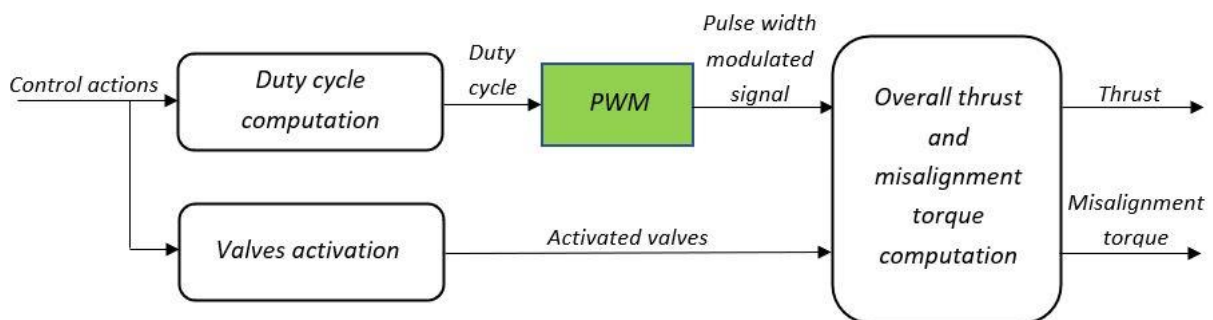


Figure 31: Thrusters setup 1 - block schematic

In order to better visualize the working principle of the first thrusters model, a block schematic is presented in Figure 31. The designed system has control actions provided by the Model Predictive Controller as inputs and the effective thrust produced by propulsion system as output, together with a disturbance torque obtained from the misalignment of the nozzles. Those

outputs are going to be fed to the actual plant of the overall system. This whole model cuts off another strong ideality, which is the straightforward link between controller and plant. Actually, in real life conditions, the physical limits of thrusters must be taken into account.

The block *Duty cycle computation*, as its name clearly suggests, is intended to compute the quantity  $\frac{F_{control}}{F_{max}}$  where  $F_{control}$  is the control action provided by MPC and  $F_{max} = 8.75 \text{ mN}$ .

The block *Valves activation* takes into account the instructions listed in *Table 5* and, (2) by setting  $f = F_{max}$ , computes the force components along the three axes for all the activated valves.

The green block *PWM* takes as input the duty cycle and produces as output a square wave signal whose amplitude is included in the interval  $[-1,1]$ , with period equal to 0.1 seconds and sample time of 0.05 seconds (in order to achieve a sufficiently high resolution).

The block *Overall thrust and torque misalignment computation* receives as inputs the pulse width modulated signal and the maximum force produced by each one of the activated valves. The aim of this block is to multiply the two inputs, in order to apply PWM modulation to the actually produced thrust, which is the first output of the whole model. Furthermore, this block is intended to compute the cross product between the thrust produced by each valve and the distance vector of each thruster from the CoM of the CubeSat. The result of this latter computation is the misalignment torque described above, seen as a disturbance from the plant.

In this particular setup, misalignment torque is null during the whole simulating sequence because of the ideality introduced by PWM: according to this technique, in fact, the opening of the valves is instantaneous so, even though there is an offset between each thruster, the force is simultaneously provided by every activated nozzle and then no undesired perturbation of attitude is obtained.

In order to obtain a more realistic scenario, also this ideality is removed in the following simulating setup, by introducing a delay in the valves' opening.

In the following figure (*Figure 32*) it is possible to see the Simulink scope of the effective thrust produced by the PWM-based setup multiplied times the mass of the spacecraft (1).

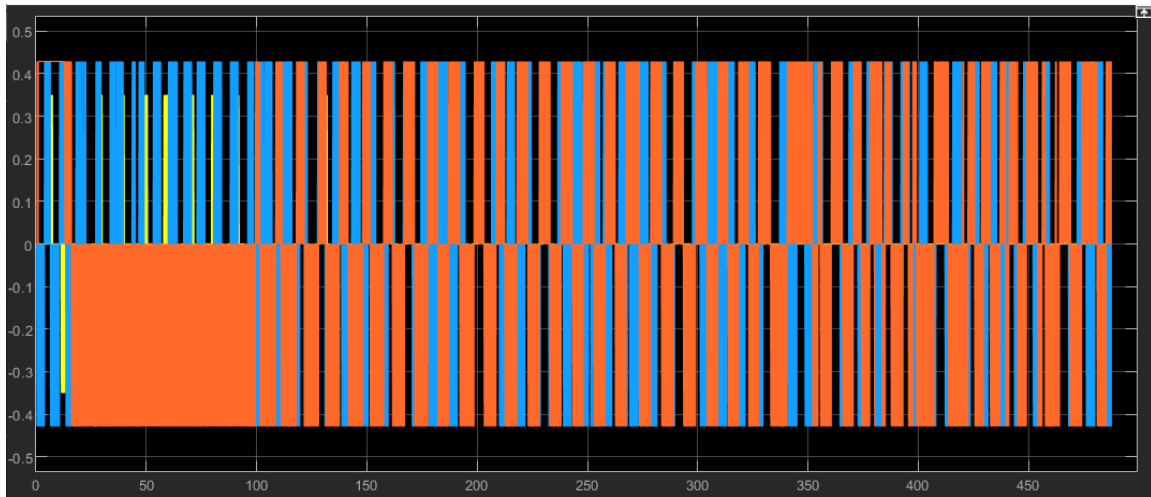


Figure 32: Simulink scope - thrust · mass [N·kg] in PWM-based setup

### Second setup – realistic valves opening

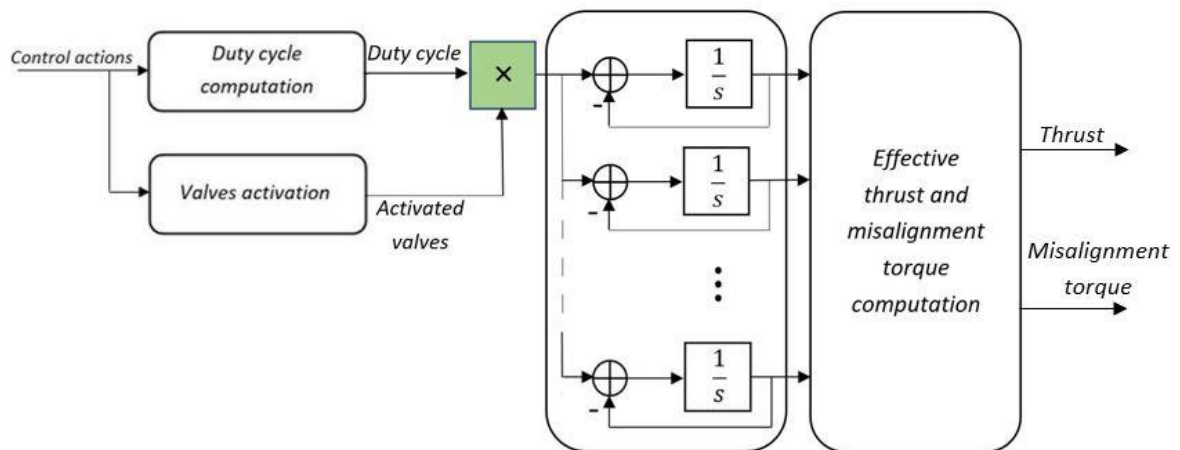


Figure 33: Thrusters setup 2 - block schematic

The first two blocks, *Duty cycle computation* and *Valves activation* are the same described above, in the previous paragraph. A multiplication takes place between those outputs, in order to compute the actual contribution provided by each activated valve. The resulting signals are fed to the next block, whose inputs are the forces produced by each thruster. Every input is fed to a negative feedback system, where the forward loop contains an integrator. This expedient is useful to simulate the behaviour of a quick-opening valve's characteristic (Figure 34).

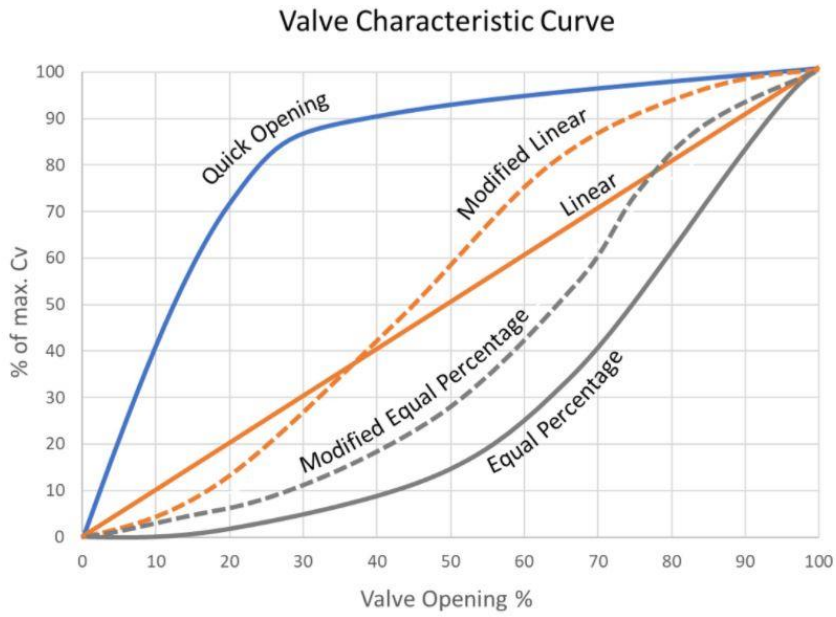


Figure 34: Valves characteristics

In the following Simulink scope extract, the thrust time response is shown with respect to z-axis. As it is possible to see, in particular from the blue curve at the beginning of the sequence, the starting behaviour is parabolic until saturation to the desired thrust value.

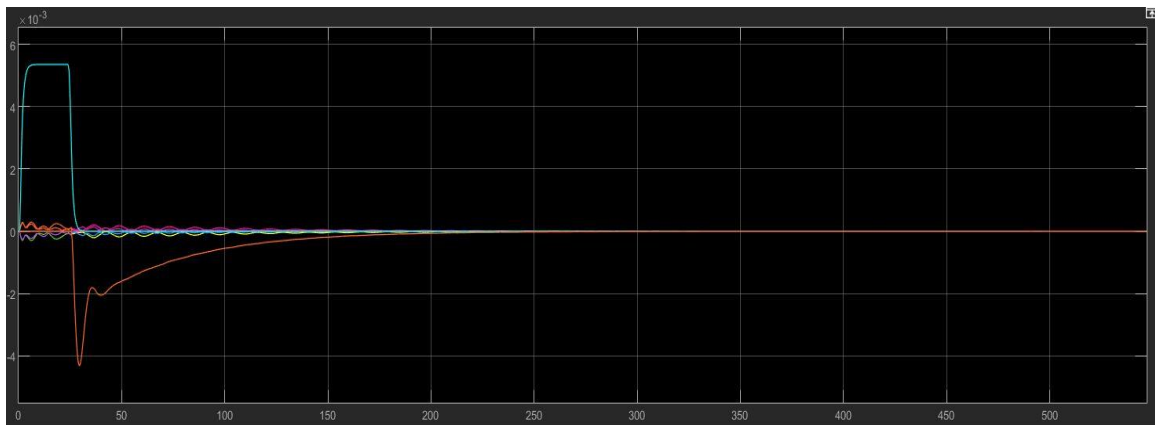


Figure 35: Simulink scope- realistic valve's behaviour (z-axis)

Figure 36 is a screenshot of the scope representing misalignment torque time response: the order of magnitude of this disturbance makes it neglectable with respect to the overall dynamics of the system.

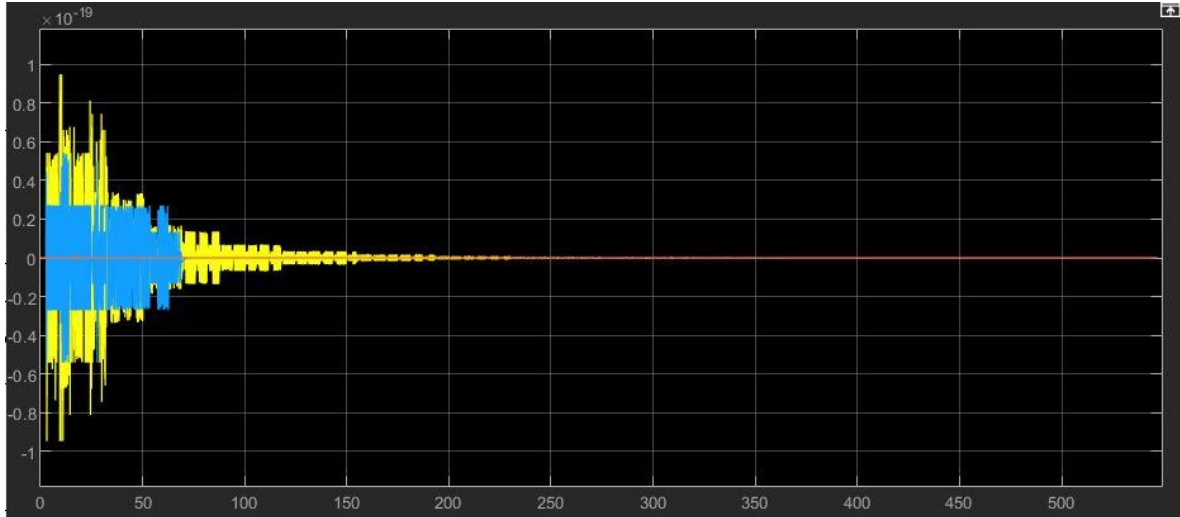


Figure 36: Simulink scope - misalignment torque [Nm]

### 2.2.2.2 Reaction wheels

In order to achieve a realistic condition, in terms of attitude actuation, a model of reaction wheels is designed.

The working principle of reaction wheels is based on a well defined architecture: an electric motor (usually a brushless one) attached to the CubeSat is intended to drive a wheel, free to rotate. According to the chosen model, three wheels are necessary because, the axis of rotation of each one must be aligned with the axes of the body reference frame of the spacecraft.

The control torque provided by the Sliding Mode Controller is fed to the electric motor which replicates it, in order to correct the error on attitude by means of the reaction wheel's rotation.

In this model [13], reaction wheels are in torque command mode. The main parameters of the system are listed in the following table and are employed for the design of the block schematic presented in *Figure 37*:

<i>Parameter</i>	<i>Name</i>	<i>Value</i>
$R_{term}$	Terminal resistance	$22 \Omega$
$K_t$	Torque constant	$3.64 \cdot 10^{-3} \frac{Nm}{A}$
$K_v$	Back EMF Constant	$0.36 \cdot 10^{-4} \frac{V}{rad/s}$
$RW_f$	Dynamic friction torque	$2.48 \cdot 10^{-8} \frac{Nm}{rad/s}$
$RW_J$	Flywheel inertia	$5.73 \cdot 10^{-6} kg \cdot m^2$
$[I_x \ I_y \ I_z]$	CubeSat inertia	$[0.152 \ 0.290 \ 0.308] kg \cdot m^2$

Table 8: Reaction wheel parameters

The parameters listed in the previous table are the same for all the reaction wheels' models, apart from the inertia moment vector, whose each element is applied to the related axis. The block schematic shown below is an example of the reaction wheel referred to y-axis.

The parameter  $K$ , included inside the green block in *Figure 37*, is the forward gain of the model. It must be chosen by means of a trial and error procedure, as it is an empirical parameter. In order to avoid an excessive mismatch between control torque and effective torque produced by actuation, the selected value for the said parameter is 1000.

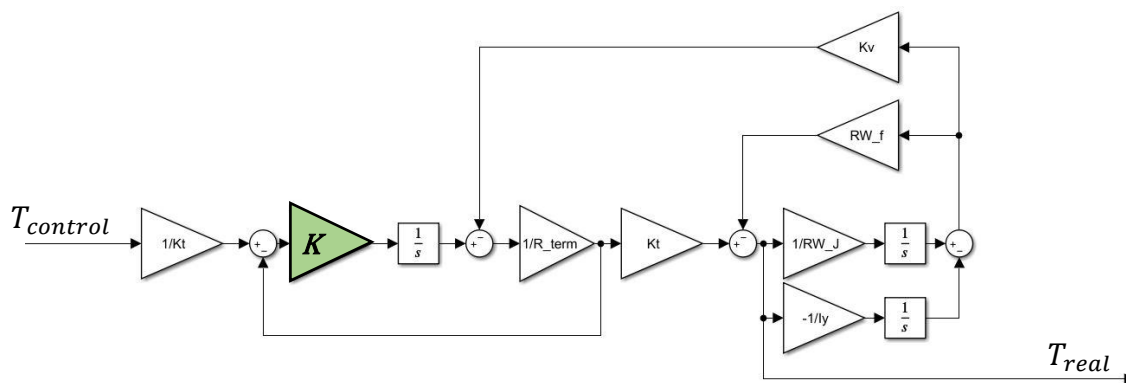


Figure 37: reaction wheel model – y-axis example

### 2.2.3 Sloshing model

In order to optimize the employment of the size of spacecrafts, especially in the small satellites framework, it is more and more common to use liquid propellant for CubeSat-based missions. A crucial aspect related to this choice is the predictability of the fluid's motion, the so-called *sloshing*.

Sloshing phenomenon has a very complex dynamics and, due to its significant nonlinearity, it is not easy to take into account such contribution to the overall system. From experimental evidences, slosh dynamics is mostly characterised by oscillating modes depending on the tank shape, fluid's properties and axial acceleration of the tank. Normally even the parameter of gravity acceleration is a key element but, in the case investigated for the sake of this thesis, as well as for all space applications, i.e. low-gravity conditions, it is not considered.

At this level of approximation, in a simulation environment as the one presented here, an actually very good degree of precision can be obtained by representing sloshing as an equivalent mechanical model [15]. In literature many variants of this kind of models are available but, in this case, a custom solution is employed, by worsening disturbance conditions in order to be

prepared for the worst-case scenario and to test the robustness guaranteed by the chosen control strategy.

The employed model is based on a torsional spring – mass – torsional damper architecture, constituting a second order dynamic autonomous system:

$$\frac{d^2\psi}{dt^2} + 2\gamma\omega_n \frac{d\psi}{dt} + \omega_n^2\psi = 0 \quad (3)$$

$$T_s = -c\dot{\psi} - k\psi$$

$$c = 2\gamma\omega_n ml^2$$

$$k = \omega_n^2 ml^2$$

The second order system described by the equations (3) above is represented in the form of a block schematic in *Figure 39*.  $\psi$  is a three-dimensional column vector whose elements are the angular deviations with respect to x, y and z axis of the slosh mass  $m_s$  (*Figure 38*). This latter parameter represents the mass of propellant in motion.  $T_s$  is the output of the system and corresponds to the slosh torque, the actual disturbance caused by sloshing.

Equations (3) represent a linear time varying system whose parameters change along the simulating sequence. In particular  $\gamma$  is the damping value and  $\omega_n$  is the natural frequency associated to the liquid propellant. These elements are computed by means of experimentally found relations [14] and on the basis of a priori assumptions. In detail, it is assumed that the shape of the tank is cylindrical and its centre of mass coincides with the one of the whole spacecraft (this assumption is important to justify condition \*).

In order to be able to compute the said parameters figuring in (3), it is necessary to compute the Bond number  $Bo$ , a dimensionless index typical of fluid dynamics systems, useful for determining the dominant regime regulating the flow of the liquid:

$$Bo = \frac{\rho a R_t^2}{\sigma}$$

$\rho$ : density of the fluid

$a$ : acceleration of the fluid in the body frame (i.e. acceleration

of the CubeSat\*)

$R_t$ : radius of the tank

$\sigma$ : surface tension of the fluid

The following table lists the main dimensions and parameters regarding tank and fluid:

<i>Parameter</i>	<i>Name</i>	<i>Value</i>
$R_t$	Tank radius	0.04 m
$H_t$	Tank height	0.14 m
$m_{s0}$	Initial fluid mass	1 kg
$m_{sf}$	Final fluid mass	0.964 kg
$h_{s0}$	Initial fluid height	0.046 m
$h_{sf}$	Final fluid height	0.045 m

Table 9: Tank and fluid parameters

As propellant, the choice falls on the refrigerant gas R134a. According to experimental evidence, given that  $h < 3R_t$ , it follows that

$$\omega_1 = 1.61 \left( \frac{\sigma}{\rho R_t^2} (1 + 0.798Bo) \right)^{\frac{1}{2}} \cdot \tanh \left( \frac{1.841h}{R_t} \right)$$

where  $h$  is the fluid height, varying along the simulating sequence between the interval  $[h_{s0}, h_{sf}]$ .

$\omega_1$  is the only natural frequency employed, in this setup, since it is relied to the oscillating mode including most of the mass of the fluid and the longest period of fluid motion. These considerations hold on the assumption of a  $0^\circ$  contact angle.

Given that, for the whole simulation,  $0 \leq Bo \leq 1$  it is possible to compute the damping as

$$\gamma = 4.47 \sqrt{\frac{\nu}{\omega_1 R_t^2}}$$

where  $\nu$  is the kinematic viscosity of the fluid.

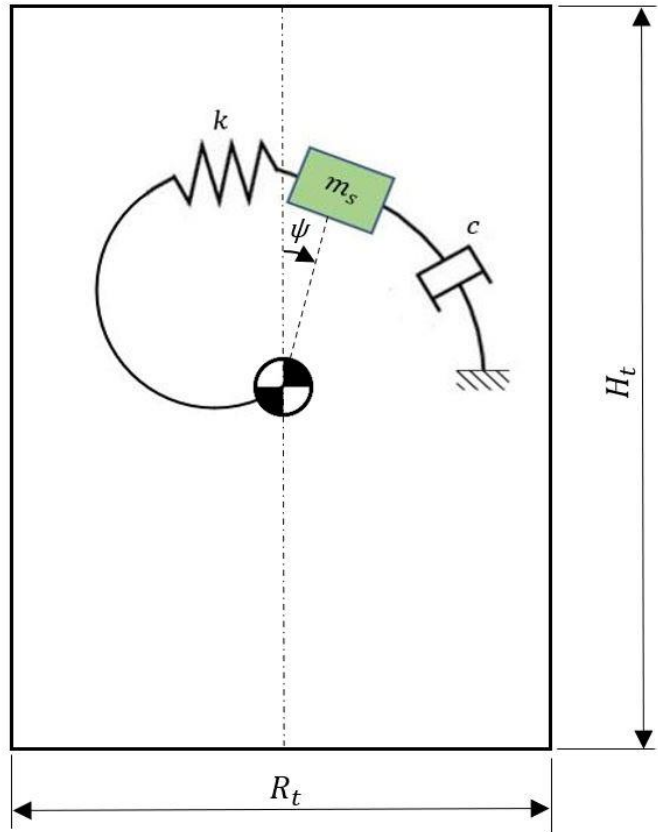


Figure 38: sloshing mechanical model

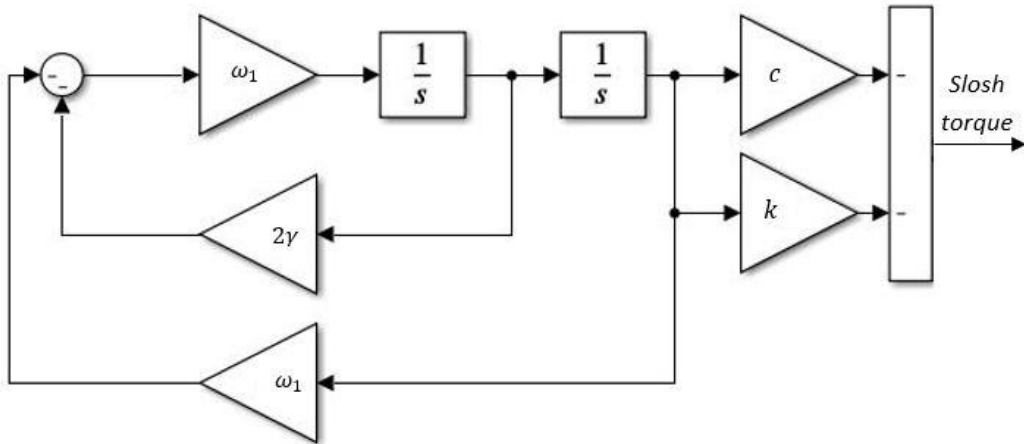


Figure 39: Sloshing model - block schematic

In the following scope extract (Figure 40) it is possible to outline the slosh disturbance torque time response, by setting an initial condition equal to 0.1 rad on the fluid mass angle wrt all three axis.

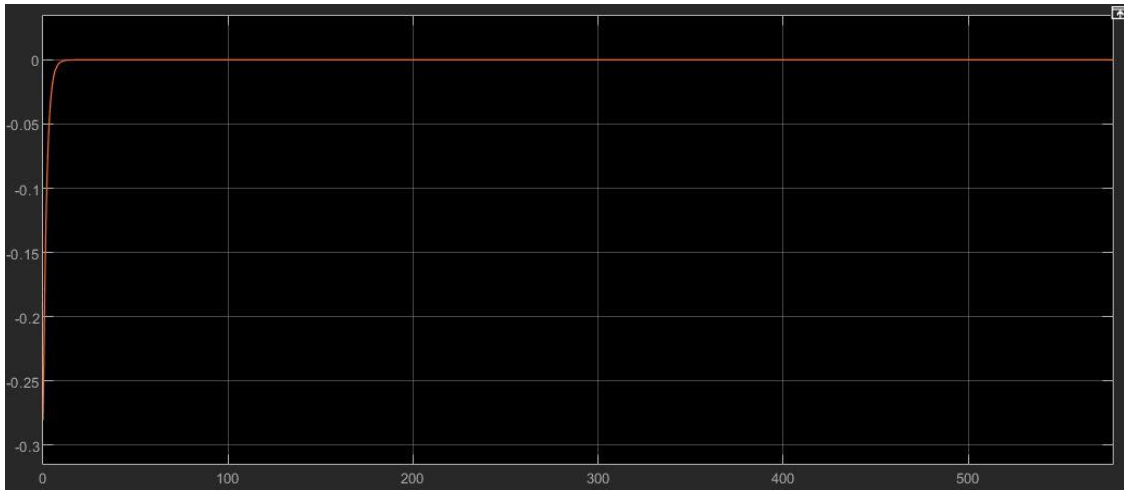


Figure 40: Slosh disturbance torque [Nm] - Simulink scope

### 2.2.4 Results from simulations – realistic scenario 2

The settings of both orbit and attitude controllers are identical to the setup previously discussed in the paragraphs 2.2.1.3 and 2.2.1.4, related to realistic scenario 1. It does not result necessary to perform any changes, which means that the control strategy is already well optimized and able to ensure a robust behaviour, as it is possible to see from the following plots.

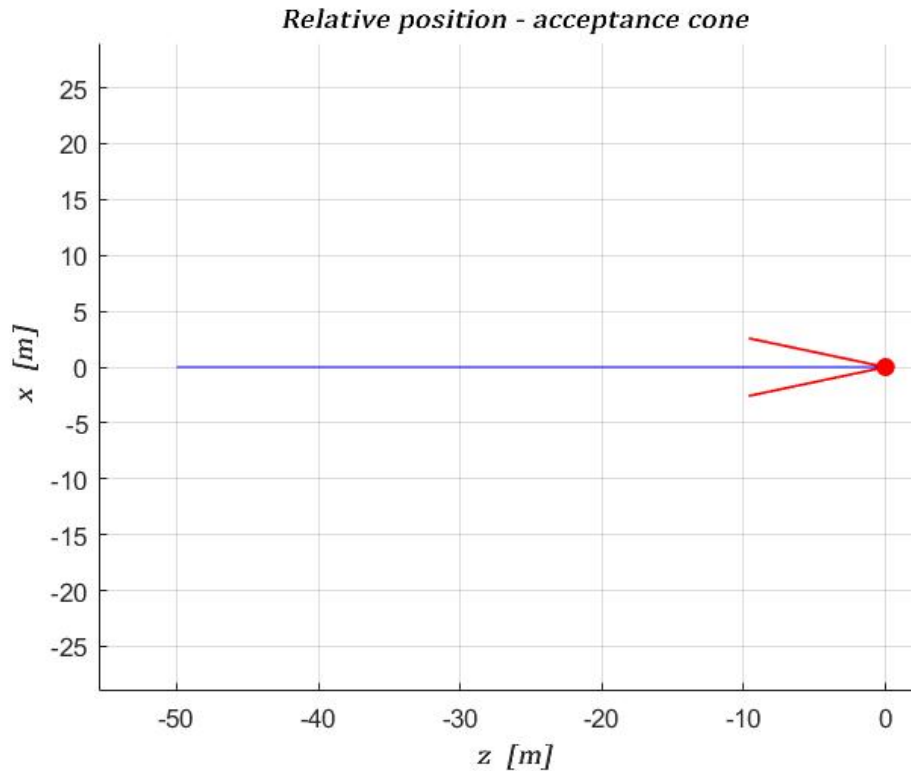


Figure 41: zx relative position - realistic scenario 2

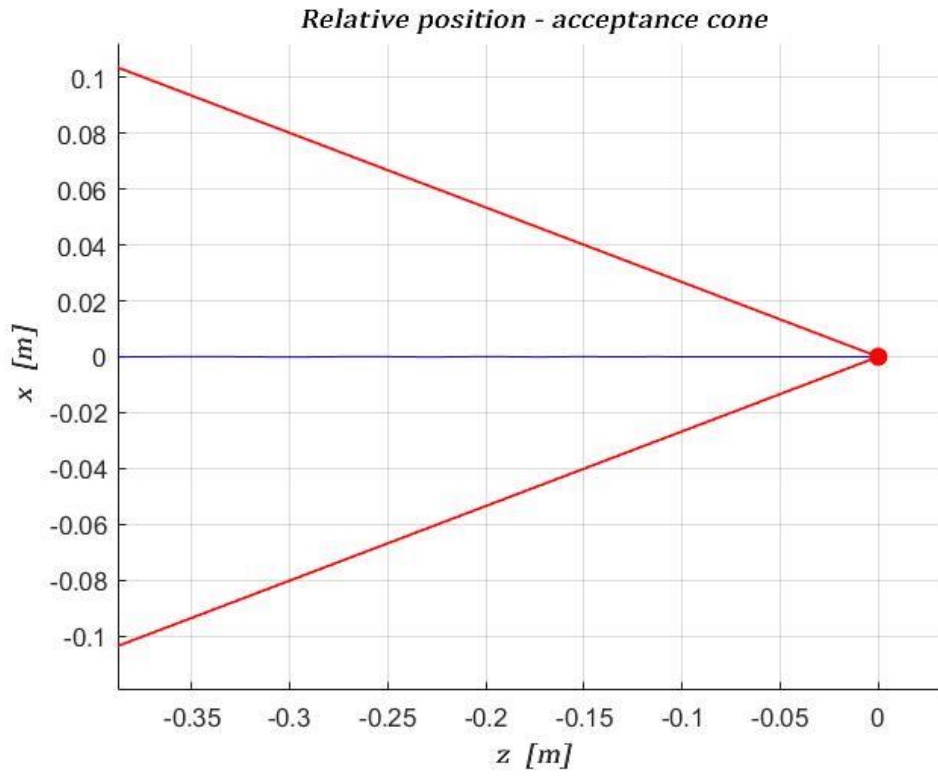


Figure 42: zx relative position (proximity detail) - realistic scenario 2

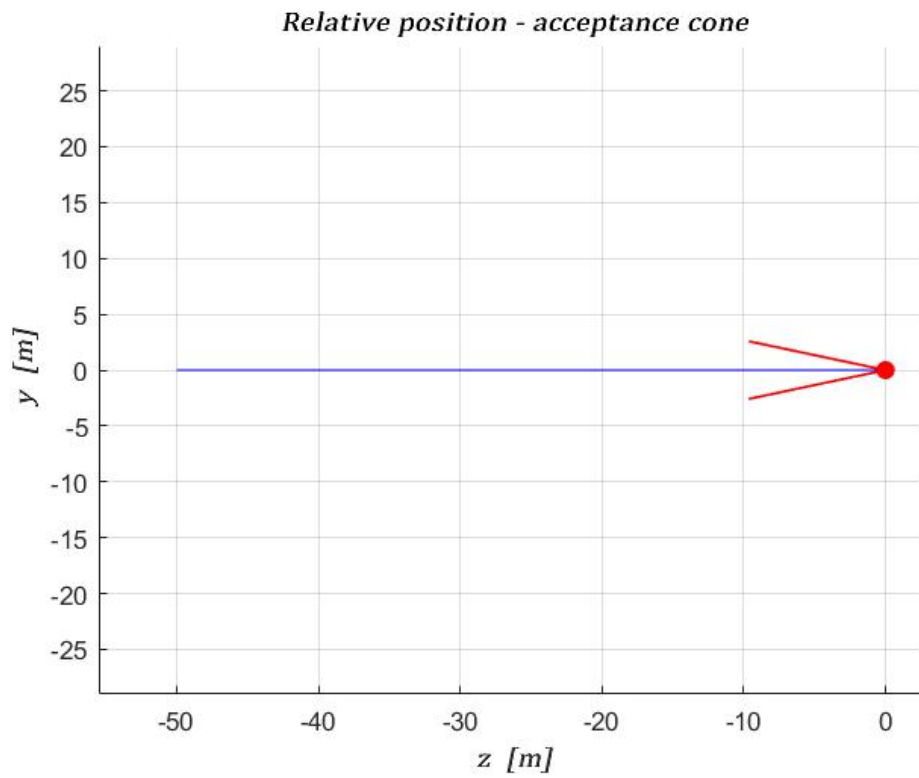


Figure 43: zy relative position - realistic scenario 2

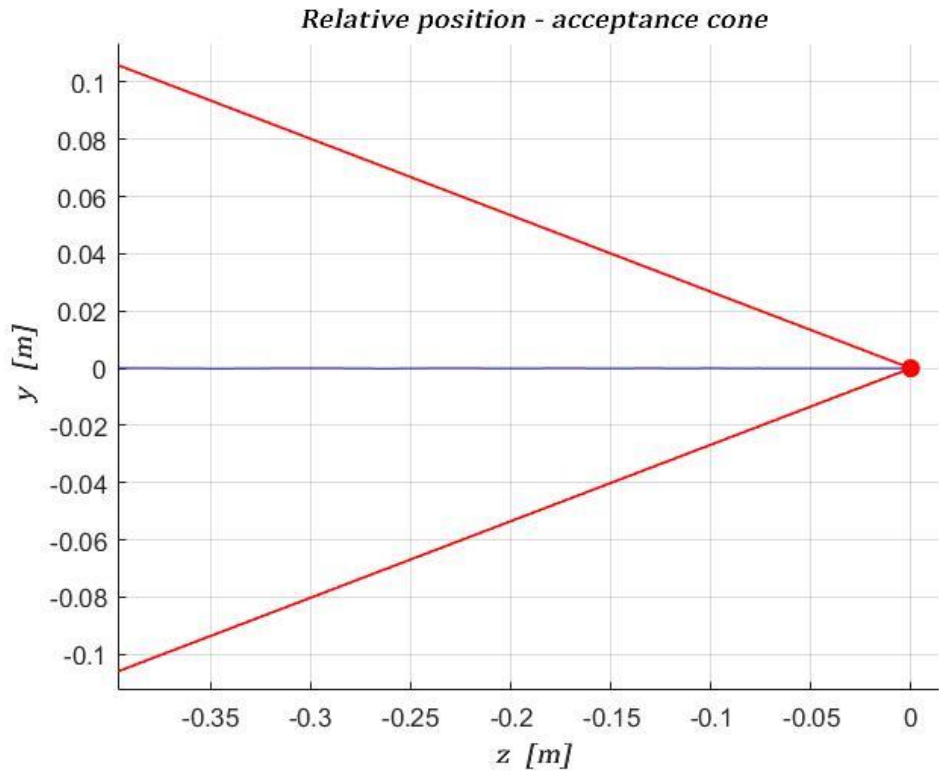


Figure 44: zy relative position (proximity detail) - realistic scenario 2

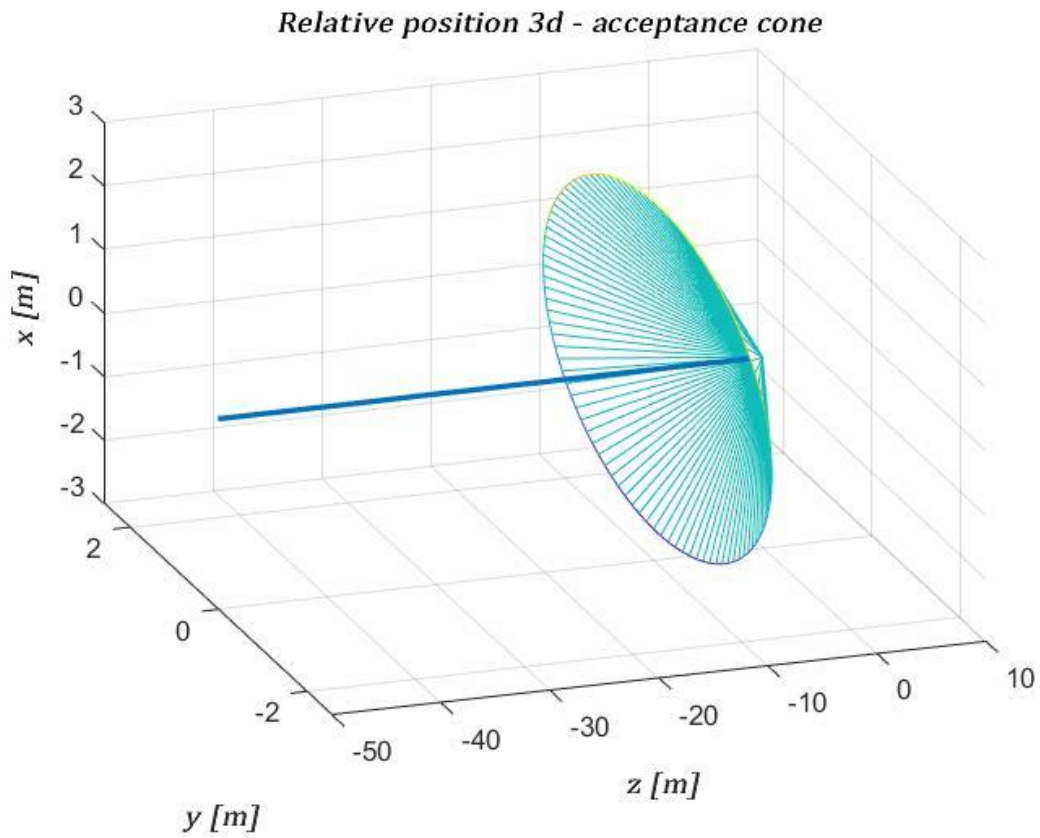


Figure 45: relative position 3d and acceptance cone – realistic scenario 2

In the plots presented from *Figure 41* to *Figure 45* it appears very clear how the acceptance cone constraint is respected even in this case. From the point of view of the translational motion, the described trajectory is a straight line, without any deviation or perturbation.

In terms of input actions, the same considerations expressed with respect to the first simulation scenario hold: in correspondence of the peak control action, there is the highest value of relative velocity of the chaser with an impulsive-like manoeuvre (*Figure 46* and *47*).

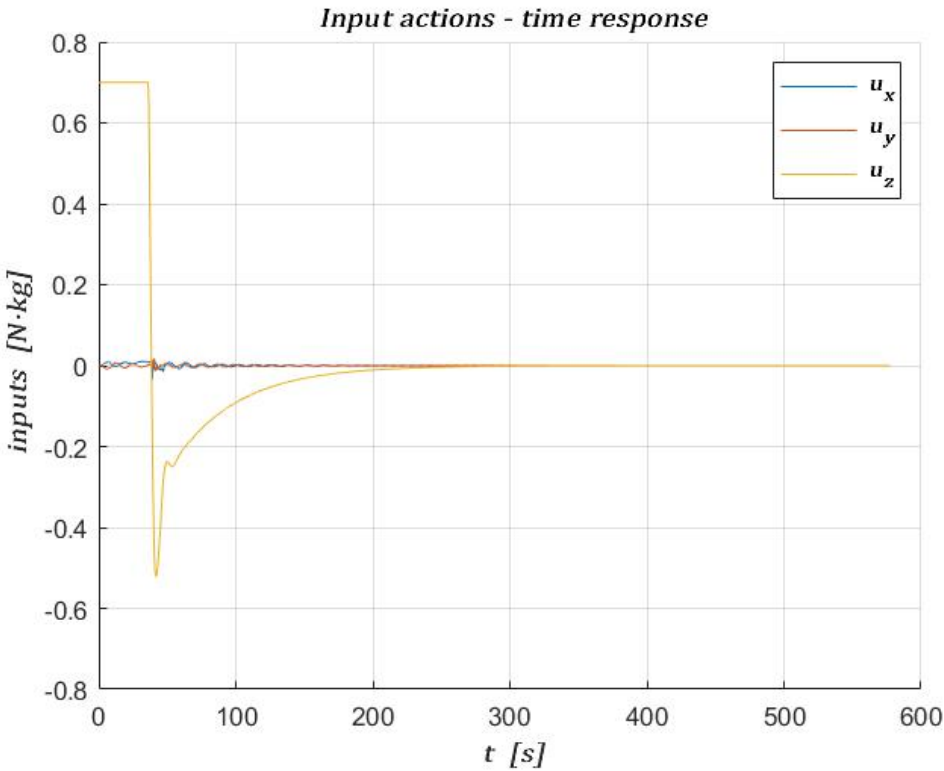


Figure 46: input time response - realistic scenario 2

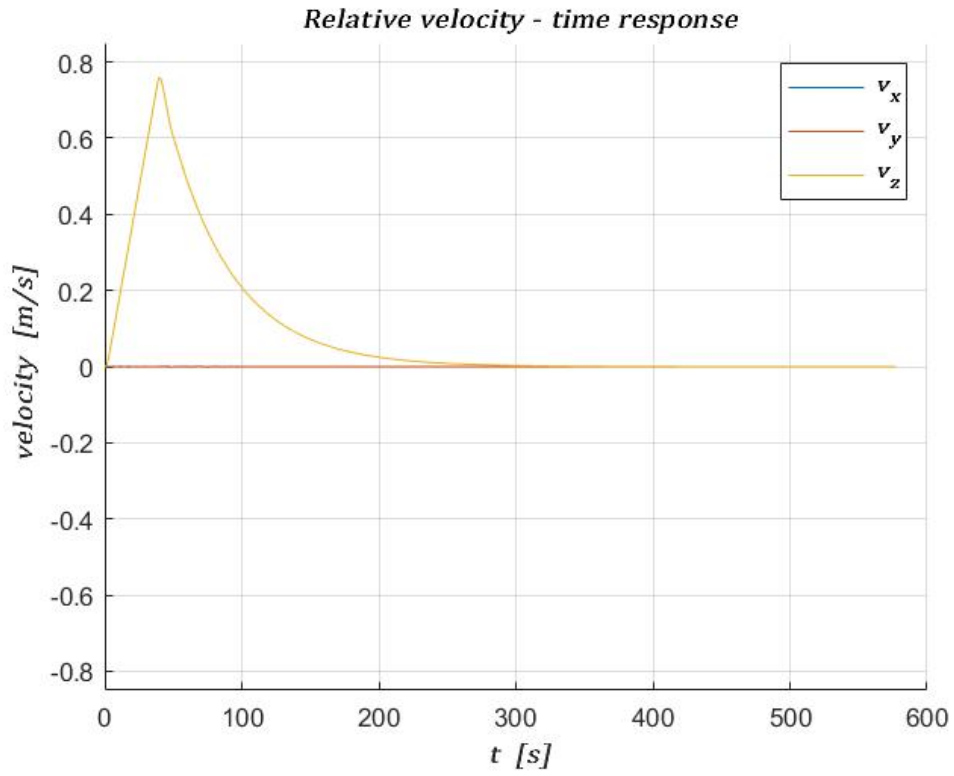


Figure 47: relative velocity time response - realistic scenario 2

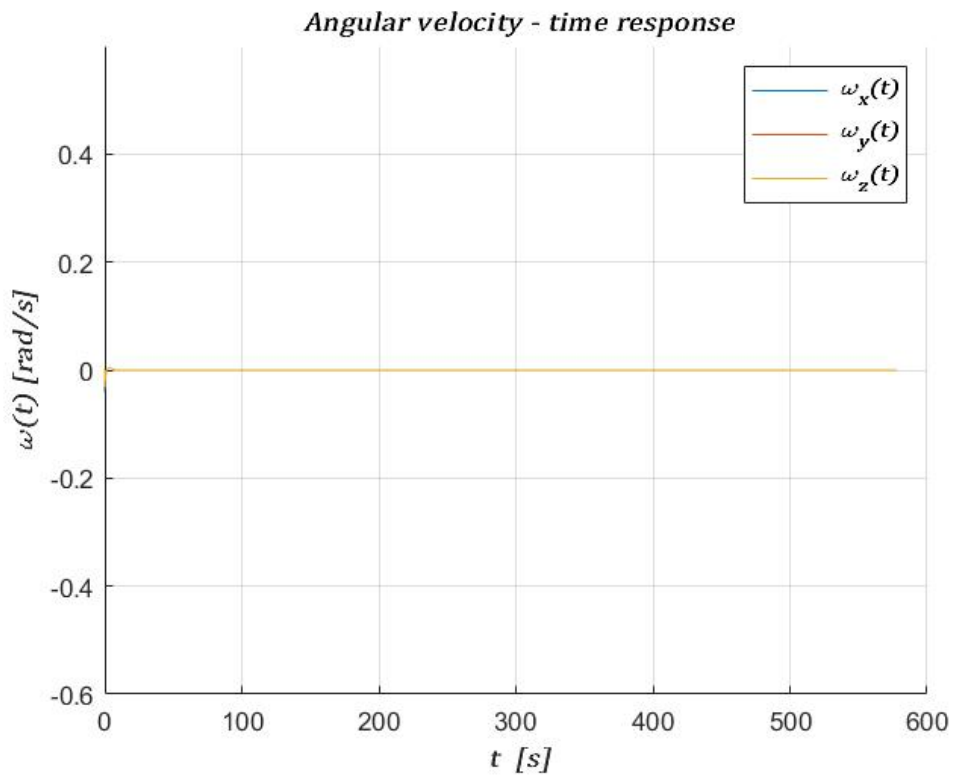


Figure 48: angular velocity time response - realistic scenario 2

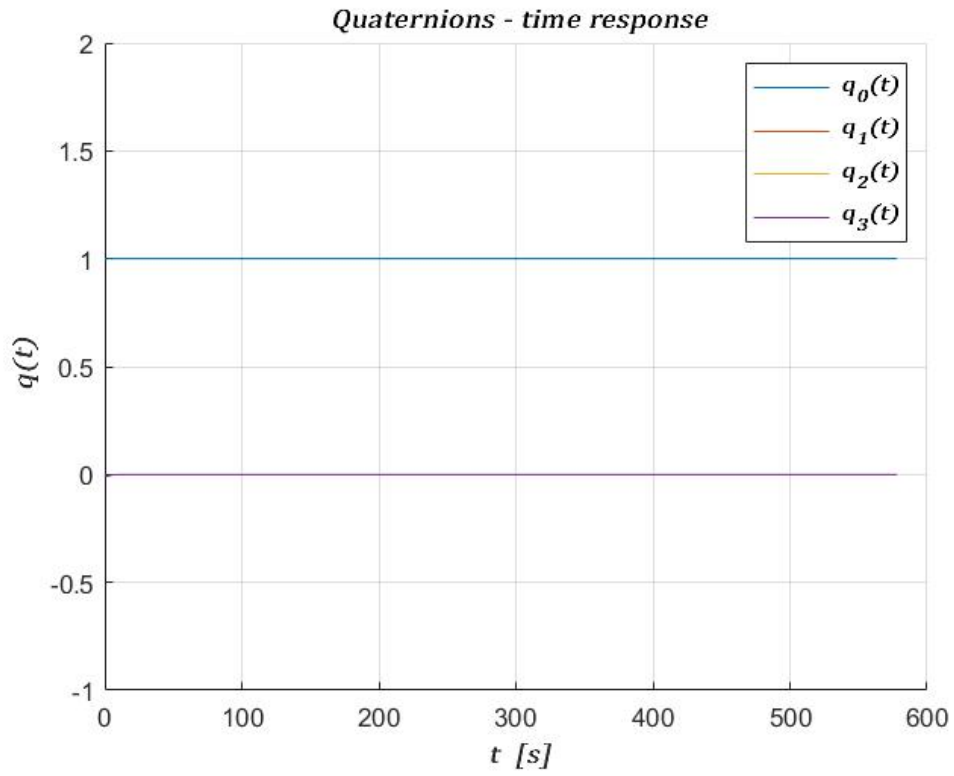


Figure 49: quaternions time response - realistic scenario 2

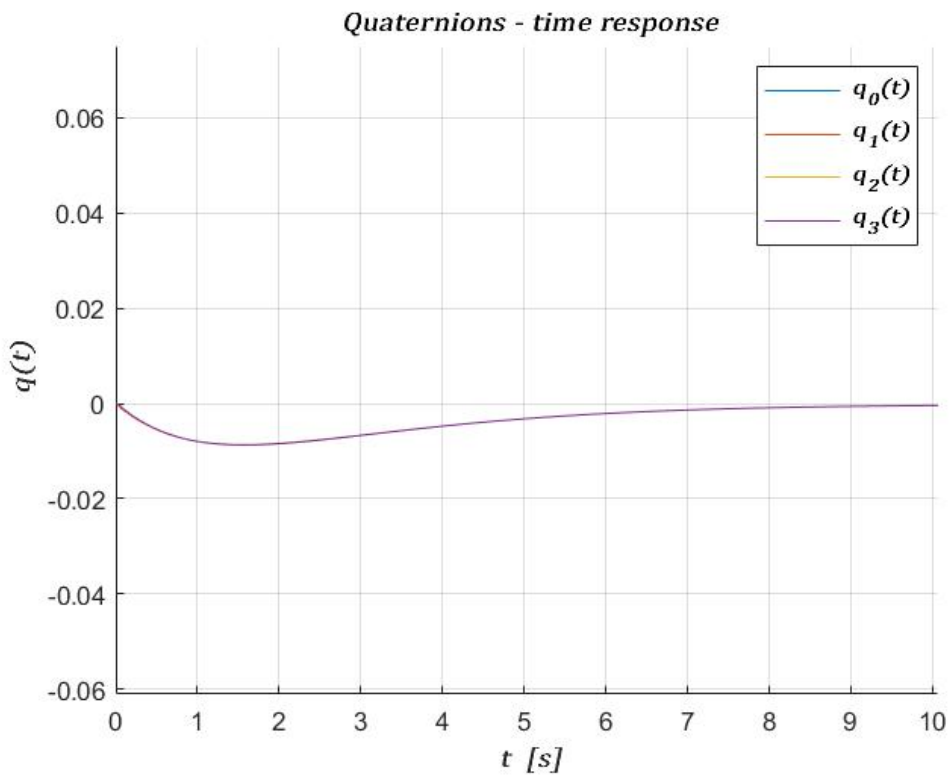


Figure 50: quaternions time response – overshoot

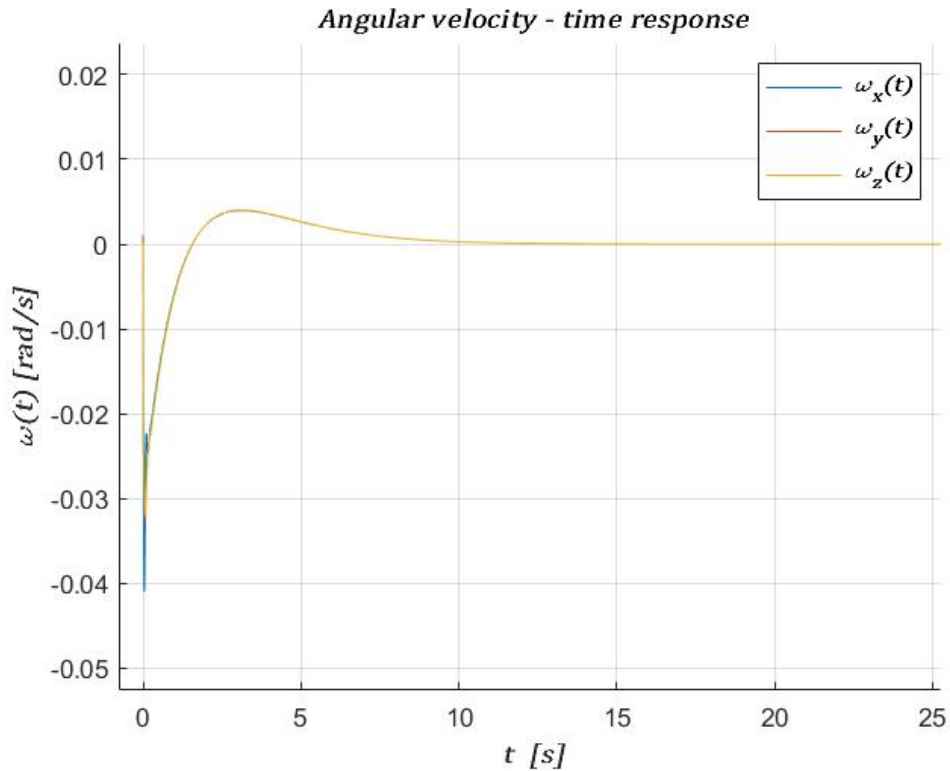


Figure 51: angular velocity time response – overshoot

The main difference with respect to the previous realistic setup, in terms of simulation results, is outlined on the attitude response of the system. In fact, as seen from the time response of the disturbances introduced in this phase of the design, the most invasive one is caused by sloshing phenomenon, creating an undesired torque interfering with attitude control actions. The result of this disturbance is evident from *Figure 48* to *51*, in particular in the last two it is possible to see an overshoot of both quaternions and angular velocity time response. It is not a significant perturbation (from the point of view of quaternions, the peak of the overshoot is -0.008, instead as regards angular velocity it is -0.04 rad/s) and it is immediately compensated by the action of SMC, thus proven to be effective, as both parameters are brought to steady state value after 10 seconds.

### ***3. Robustness analysis***

Apart from the external and internal disturbances discussed in the previous chapter, it is of primal importance to take into account the system's behaviour in presence of uncertainties on initial conditions of several fundamental parameters, corresponding to the CubeSat's mass (causing also a significant uncertainty on inertia matrix of the chaser), relative position, angular velocity and quaternions. In order to evaluate control performance in an uncertainty-based scenario, random disturbances are added in the simulation phase. This particular setup allows to perform a robustness analysis with respect to the above-mentioned parameters and to different kinds of manoeuvres, by gradually increasing the amplitude of uncertainties on the involved variables.

Since in nominal conditions the settings selected for both attitude and trajectory controllers result to be effective, as it is outlined by the obtained results described in the previous chapter, for the sake of a fair analysis those very same settings must be maintained without any change. Only in this way it is possible to demonstrate robustness of the closed loop control system; on the contrary, any adaptive change of the controllers' tuning in this phase may undermine the purpose of the considerations which are about to be made.

For the sake of this analysis, two main situations are investigated, complying with SROC mission options:

- V-bar approach
- R-bar approach

The first setup is the one analysed until now, the most used in RVD-based manoeuvre. However, according to mission analysis evaluations performed by the rest of CubeSat team, it may be necessary to switch, in the SROC framework, to a R-bar approach. For the sake of the mission also this condition must be studied. In case of a V-bar approach the starting point of the manoeuvre is  $[0, 0, -50]$  with respect to the target reference frame, meaning 50 meters behind Space Rider. In case of an R-bar approach, the relative distance of the chaser wrt. to the target at the beginning of the RVD procedure is  $[50, 0, 0]$ , i.e. 50 meters above the target.

### ***3.1 Montecarlo simulations***

In both above-mentioned scenarios, Montecarlo simulations are performed, in order to evaluate the reaction of the system to uncertainties in a large amount of manoeuvres, with randomly different initial conditions.

This approach involves performing a total of 300 simulations with a more and more increasing error on the uncertain parameters. In particular the simulations are divided in 10 steps of 30 simulations each. Each step is characterised by random uncertainties with a predefined magnitude on the initial conditions of the so-called uncertain parameters (mass, relative position, quaternions and angular velocity). As follows, the chosen setup on uncertainties is described for every step, from the first one to the tenth one:

1. 30 simulations with
  - a. random disturbance of amplitude  $2.5 \cdot 10^{-1} \text{ m}$  on relative position (all three axes);
  - b. random disturbance of amplitude  $2 \text{ kg}$  on the mass;
  - c. random disturbance of amplitude  $10^\circ$  on all three attitude angles;
  - d. random disturbance of amplitude  $0.2 \text{ rad/s}$  on angular velocity (all three axes).
  
2. 30 simulations with
  - a. random disturbance of amplitude  $2 \cdot 2.5 \cdot 10^{-1} \text{ m}$  on relative position (all three axes);
  - b. random disturbance of amplitude  $2 \text{ kg}$  on the mass;
  - c. random disturbance of amplitude  $10^\circ$  on all three attitude angles;
  - d. random disturbance of amplitude  $0.2 \text{ rad/s}$  on angular velocity (all three axes).
  
3. 30 simulations with
  - a. random disturbance of amplitude  $3 \cdot 2.5 \cdot 10^{-1} \text{ m}$  on relative position (all three axes);
  - b. random disturbance of amplitude  $2 \text{ kg}$  on the mass;
  - c. random disturbance of amplitude  $10^\circ$  on all three attitude angles;
  - d. random disturbance of amplitude  $0.2 \text{ rad/s}$  on angular velocity (all three axes).
  
4. 30 simulations with

- a. random disturbance of amplitude  $4 \cdot 2.5 \cdot 10^{-1} \text{ m}$  on relative position (all three axes);
  - b. random disturbance of amplitude  $2 \text{ kg}$  on the mass;
  - c. random disturbance of amplitude  $10^\circ$  on all three attitude angles;
  - d. random disturbance of amplitude  $0.2 \text{ rad/s}$  on angular velocity (all three axes).
5. 30 simulations with
- a. random disturbance of amplitude  $5 \cdot 2.5 \cdot 10^{-1} \text{ m}$  on relative position (all three axes);
  - b. random disturbance of amplitude  $2 \text{ kg}$  on the mass;
  - c. random disturbance of amplitude  $10^\circ$  on all three attitude angles;
  - d. random disturbance of amplitude  $0.2 \text{ rad/s}$  on angular velocity (all three axes).
6. 30 simulations with
- a. random disturbance of amplitude  $6 \cdot 2.5 \cdot 10^{-1} \text{ m}$  on relative position (all three axes);
  - b. random disturbance of amplitude  $2 \text{ kg}$  on the mass;
  - c. random disturbance of amplitude  $10^\circ$  on all three attitude angles;
  - d. random disturbance of amplitude  $0.2 \text{ rad/s}$  on angular velocity (all three axes).
7. 30 simulations with
- a. random disturbance of amplitude  $7 \cdot 2.5 \cdot 10^{-1} \text{ m}$  on relative position (all three axes);
  - b. random disturbance of amplitude  $2 \text{ kg}$  on the mass;
  - c. random disturbance of amplitude  $10^\circ$  on all three attitude angles;
  - d. random disturbance of amplitude  $0.2 \text{ rad/s}$  on angular velocity (all three axes).
8. 30 simulations with
- a. random disturbance of amplitude  $8 \cdot 2.5 \cdot 10^{-1} \text{ m}$  on relative position (all three axes);
  - b. random disturbance of amplitude  $2 \text{ kg}$  on the mass;
  - c. random disturbance of amplitude  $10^\circ$  on all three attitude angles;
  - d. random disturbance of amplitude  $0.2 \text{ rad/s}$  on angular velocity (all three axes).
9. 30 simulations with
- a. random disturbance of amplitude  $9 \cdot 2.5 \cdot 10^{-1} \text{ m}$  on relative position (all three axes);
  - b. random disturbance of amplitude  $2 \text{ kg}$  on the mass;
  - c. random disturbance of amplitude  $10^\circ$  on all three attitude angles;
  - d. random disturbance of amplitude  $0.2 \text{ rad/s}$  on angular velocity (all three axes).
10. 30 simulations with
- a. random disturbance of amplitude  $2.5 \text{ m}$  on relative position (all three axes);
  - b. random disturbance of amplitude  $2 \text{ kg}$  on the mass;
  - c. random disturbance of amplitude  $10^\circ$  on all three attitude angles;
  - d. random disturbance of amplitude  $0.2 \text{ rad/s}$  on angular velocity (all three axes).

A tolerance band is selected equal to  $[-2 \cdot 10^{-3}, 2 \cdot 10^{-3}]$  and it is referred to relative position. If the final relative position states are included in the said tolerance band for the last 20 sampling instants of simulation, the latter simulation is considered successful. This criterion is used to define a success rate of Montecarlo simulations for each one of the above listed steps.

### 3.1.1 Montecarlo simulations: V-bar approach

#### 3.1.1.1 Step 1

- random disturbance of amplitude  $2.5 \cdot 10^{-1} \text{ m}$  on relative position (all three axes);
- random disturbance of amplitude  $2 \text{ kg}$  on the mass;
- random disturbance of amplitude  $10^\circ$  on all three attitude angles;
- random disturbance of amplitude  $0.2 \text{ rad/s}$  on angular velocity (all three axes).

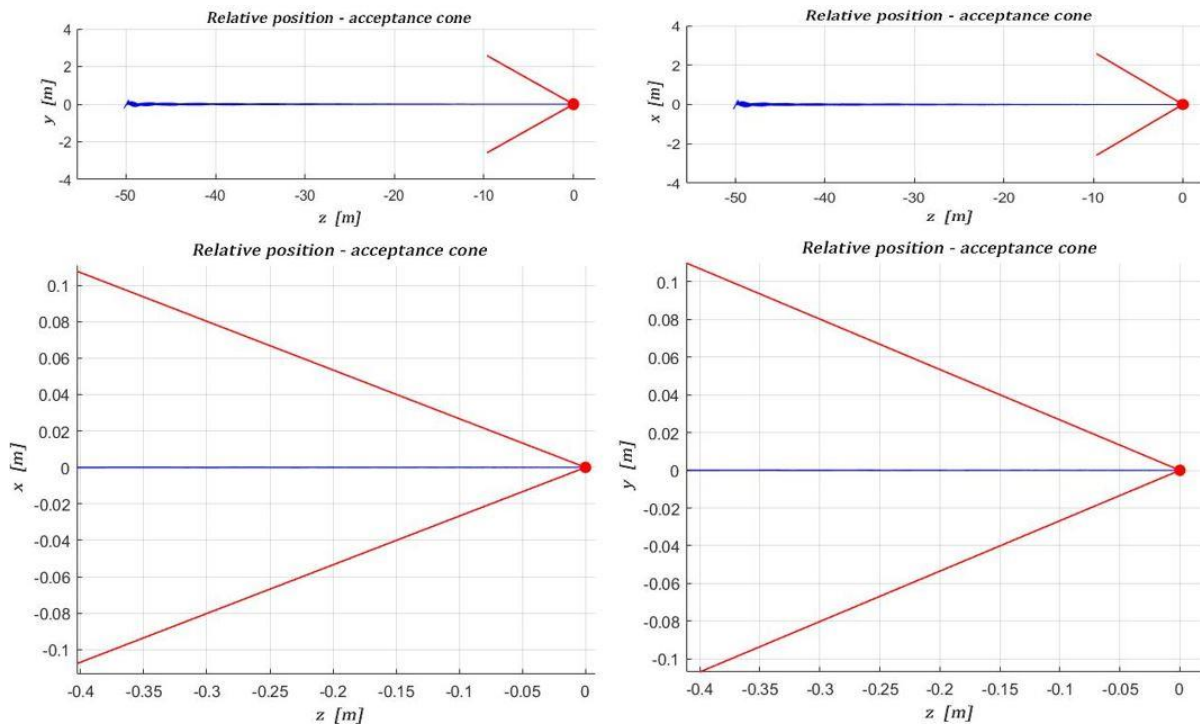


Figure 52: Relative position V-bar approach - Montecarlo 1

In these first 30 simulations the success rate results to be of 100% in fact, as it is possible to see from *Figure 52*, the acceptance cone constraint is always satisfied and the behaviour in terms of time responses (*Figure 53*) is absolutely comparable with the one obtained in the *realistic scenario 2* whose the second chapter talks about. The plots representing control efforts and effective thrust are absolutely identical apart from a scaling factor given by the mass of the chaser. The response is oscillating for the first 200 seconds of simulation, given the introduced uncertainties which must be compensated, but the values always are included into the

prescribed bounds. In terms of angular velocity and attitude, the results are comparable with the nominal case: there is a minimal overshoot at the beginning of the manoeuvre mainly due to sloshing disturbance which is immediately cancelled by the control system. The same considerations expressed on input actions hold for relative velocity time response: all the elements of the velocity vector have an oscillating behaviour for the first 200 seconds, getting to the peak value after 40 seconds of simulations and then rapidly decreasing to reference.

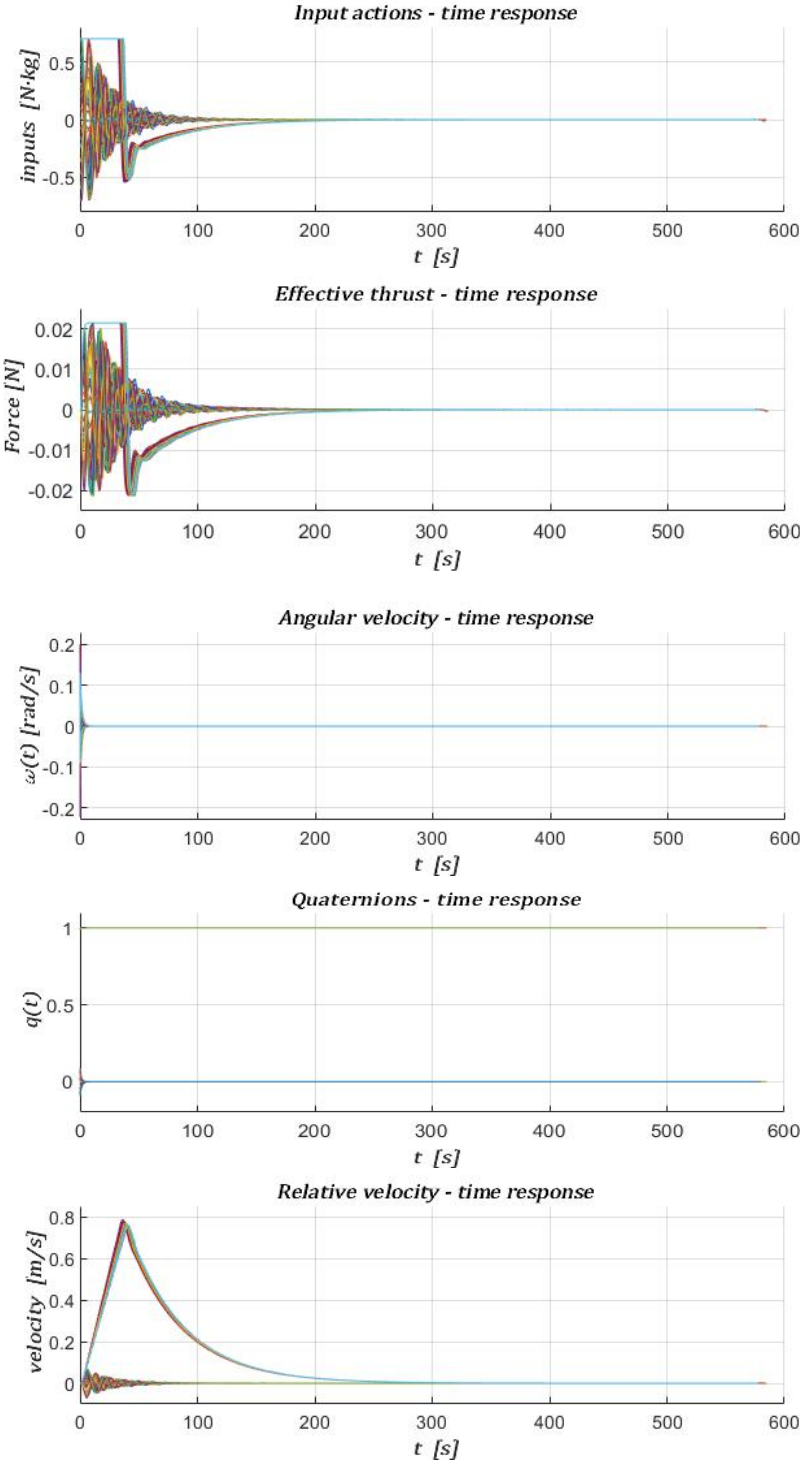


Figure 53: Time response plots in V-bar approach - Montecarlo 1

### 3.1.1.2 Step 2

- a) random disturbance of amplitude  $2 \cdot 2.5 \cdot 10^{-1} \text{ m}$  on relative position (all three axes);
- b) random disturbance of amplitude  $2 \text{ kg}$  on the mass;
- c) random disturbance of amplitude  $10^\circ$  on all three attitude angles;
- d) random disturbance of amplitude  $0.2 \text{ rad/s}$  on angular velocity (all three axes).

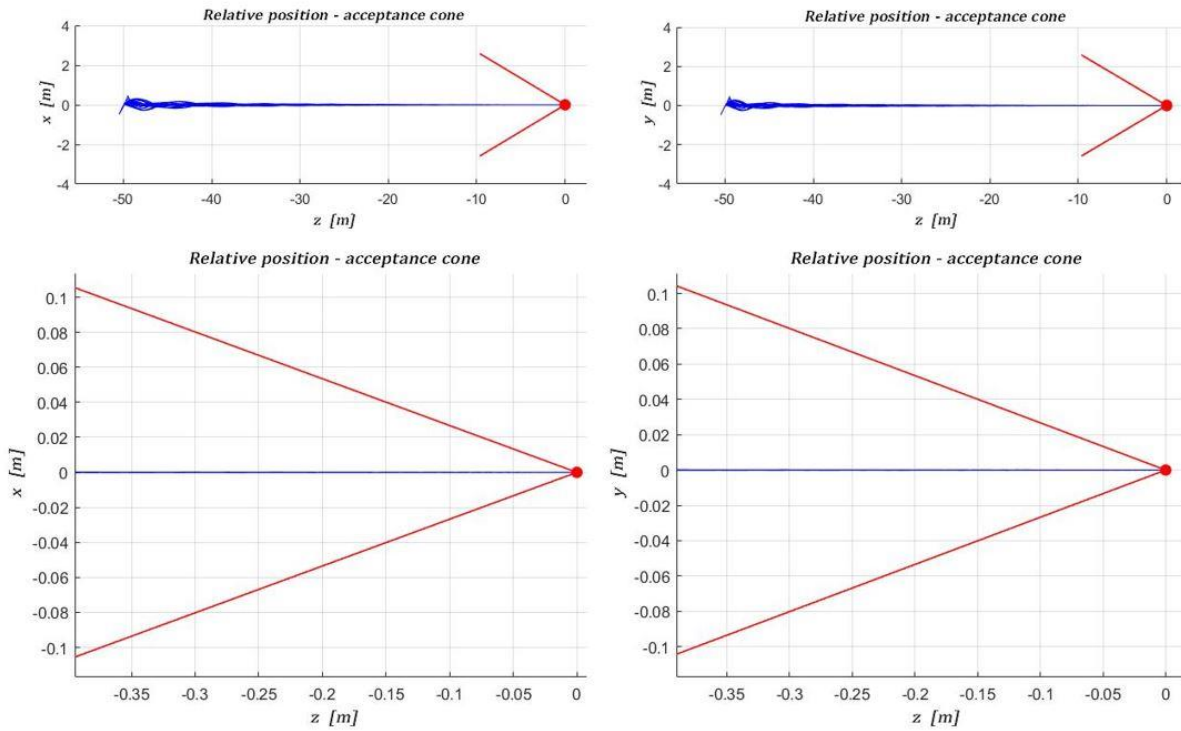


Figure 54: Relative position V-bar approach - Montecarlo 2

Also in this second step the success rate is 100% and there is no significant variation in terms of time responses. It is possible to see from *Figure 54* and *55* that there is a worsening in uncertainties on initial conditions and this phenomenon causes a slightly higher effort in terms of the required and provided thrust. Additionally there is a small general increase of velocity. In general it is clear how the system's behaviour is a bit more perturbed, with a slightly more oscillating time response in the starting phase of simulations. Anyway all the parameters are brought to steady state after few seconds.

In terms of attitude, no significant differences arise with respect to the previous case: the same overshoots are encountered at the beginning of the sequence but they are cancelled without any problems after few seconds. Control inputs and effective thrust time responses, instead, have a highly oscillating behaviour until 200 seconds of simulation, due to the higher amount of uncertainties introduced in this case. The same considerations hold as much as concerns velocity

time response, whose behaviour is oscillating for the first 200 seconds of simulation and whose peak value never exceeds 0.8 m/s, as in the previous simulations.

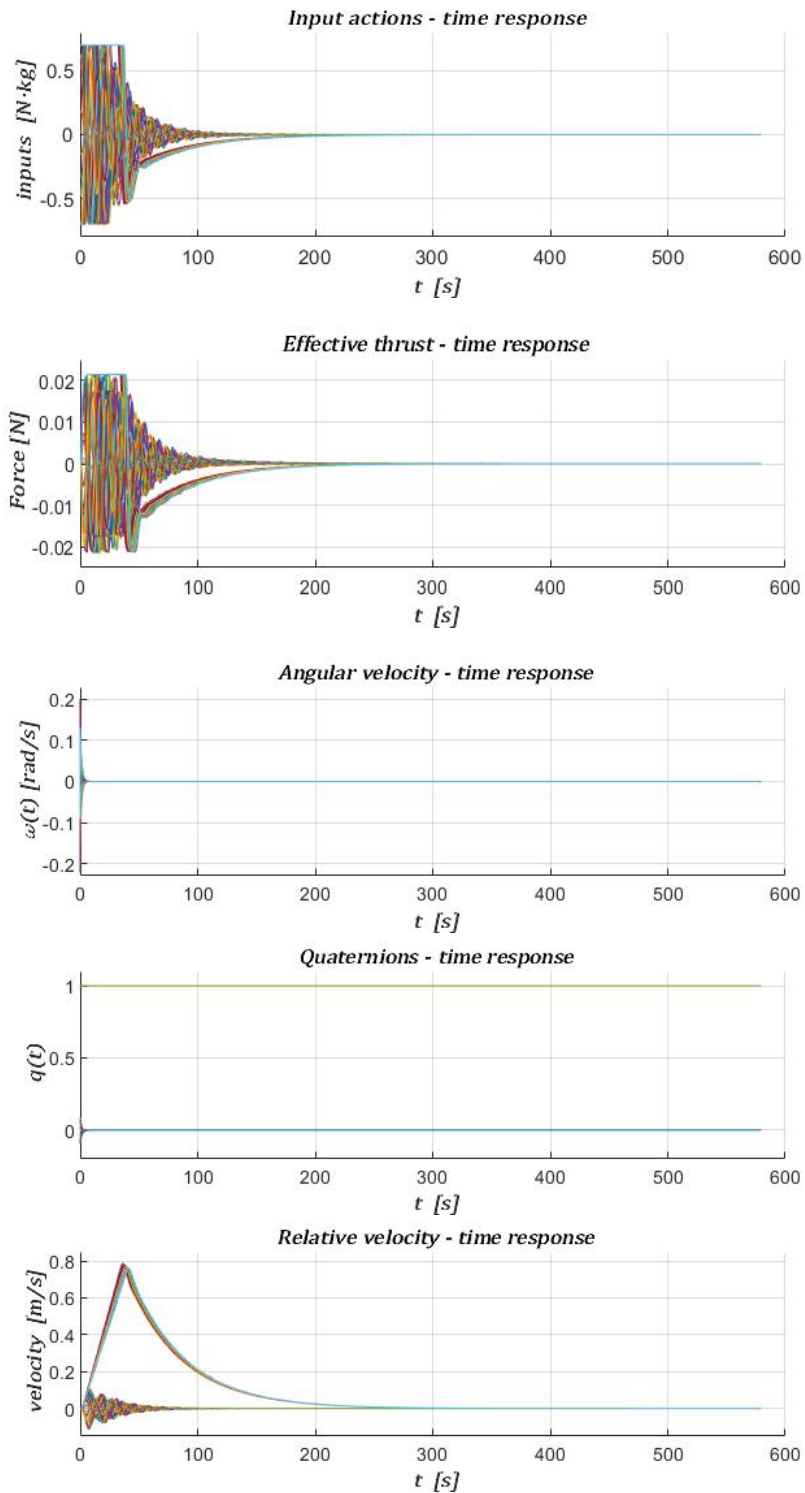


Figure 55: Time response plots in V-bar approach - Montecarlo 2

### 3.1.1.3 Step 3

- a) random disturbance of amplitude  $3 \cdot 2.5 \cdot 10^{-1} \text{ m}$  on relative position (all three axes);
- b) random disturbance of amplitude  $2 \text{ kg}$  on the mass;
- c) random disturbance of amplitude  $10^\circ$  on all three attitude angles;
- d) random disturbance of amplitude  $0.2 \text{ rad/s}$  on angular velocity (all three axes).

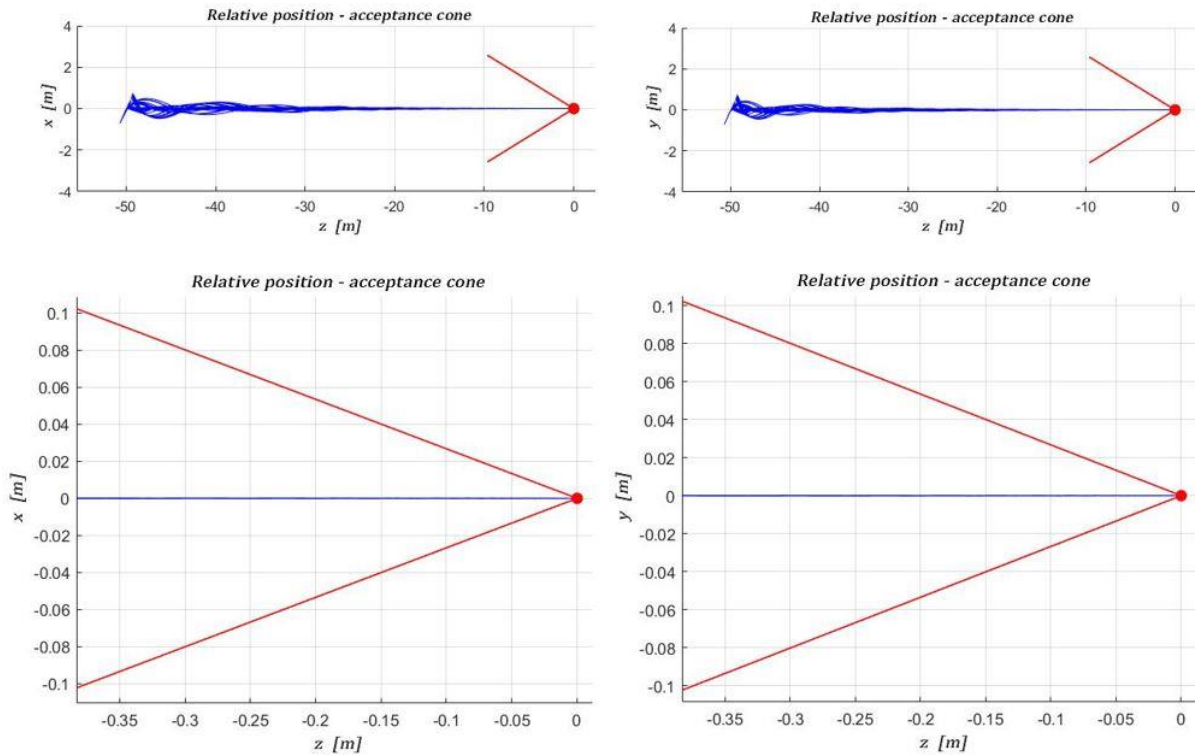


Figure 56: Relative position V-bar approach - Montecarlo 3

Also in this case the success rate is of 100% and the same considerations exerted in the previous step hold. The transient behaviours of time responses plotted in *Figure 57* are completely extinguished after 230 seconds.

From *Figure 56* it is clear how the acceptance cone constraint is satisfied in this case, given a smooth trajectory fixed onto reference values in the last meters of the approach to the target spacecraft. What appears different with respect to the previous cases is a more oscillating characteristic in the relative position at further distance from the arrival point, along x and y axes, due to the higher degree of uncertainty on initial conditions. It is thus possible to say that the first part of the manoeuvre appears to be the most sensitive to a variation of the nominal conditions, even though the deviations from reference values are always found within the bound of 0.7 meters, along both x and y axes.

This behaviour results in a more oscillating characteristic even in the time responses representing the variation of input parameters, effective thrust and relative velocity.

Once again control inputs and effective thrust are the same, apart from a scaling factor due to the mass of the CubeSat. However, the consequences of a more uncertain setup on initial conditions reflects on the more clustered area created by the oscillations in the above mentioned time response plots. All values are anyway within the prescribed bounds.

There is no significant variation in terms of attitude parameters, also in this case.

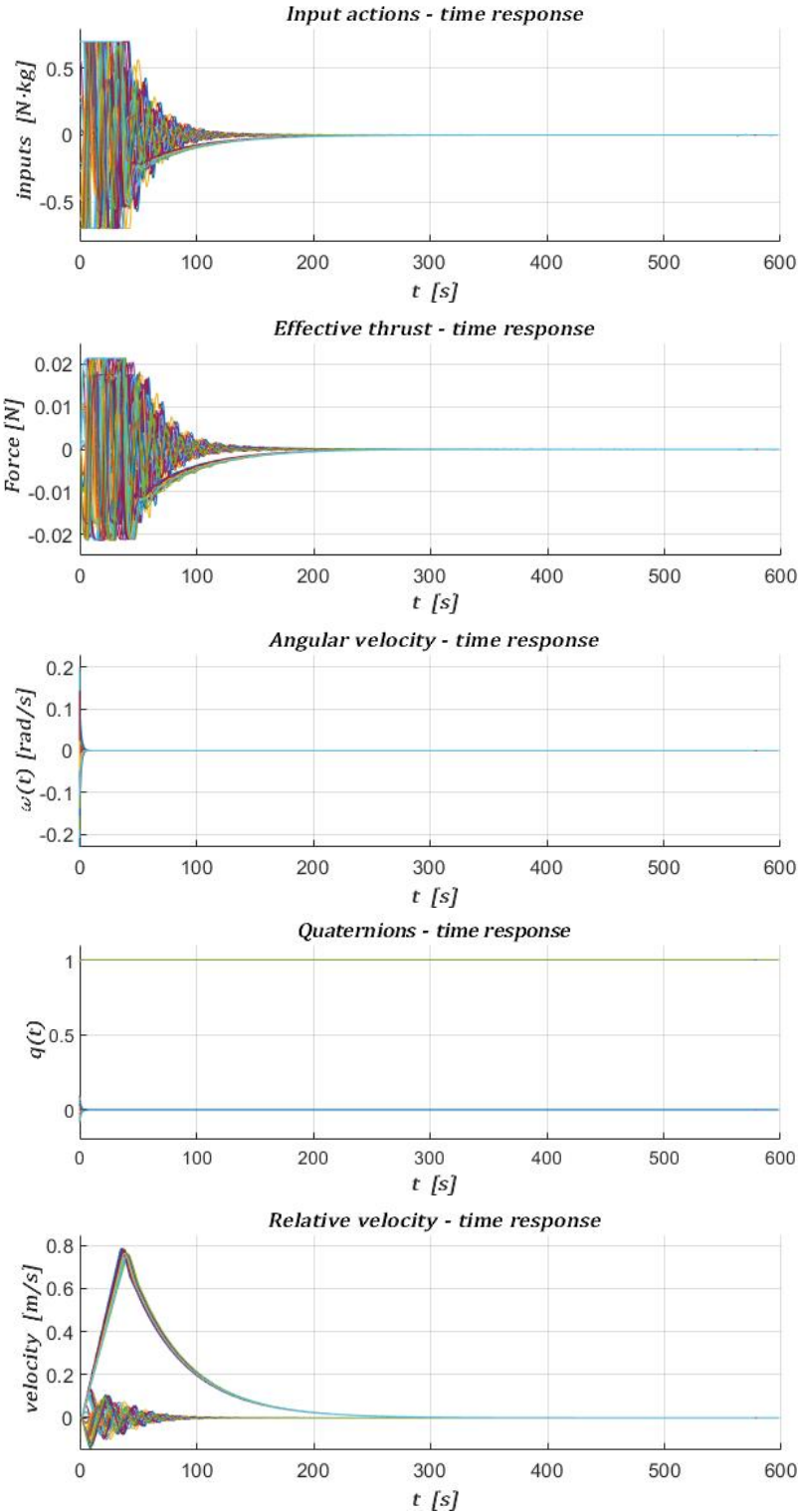


Figure 57: Time response plots in V-bar approach - Montecarlo 3

### 3.1.1.4 Step 4

- a) random disturbance of amplitude  $4 \cdot 2.5 \cdot 10^{-1} \text{ m}$  on relative position (all three axes);
- b) random disturbance of amplitude  $2 \text{ kg}$  on the mass;
- c) random disturbance of amplitude  $10^\circ$  on all three attitude angles;
- d) random disturbance of amplitude  $0.2 \text{ rad/s}$  on angular velocity (all three axes).

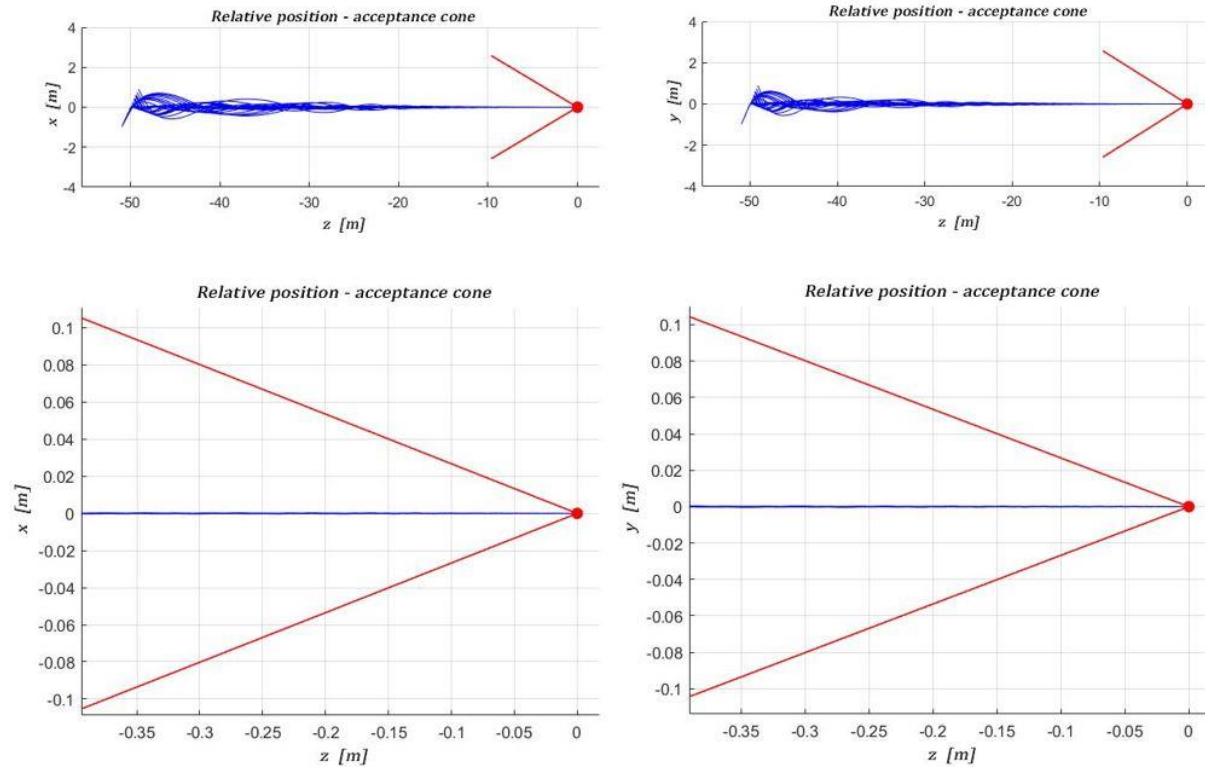


Figure 58: Relative position V-bar approach - Montecarlo 4

The success rate is 100% also in this step. The effects of a higher uncertainty are visible in this case, especially regarding input time response and effective thrust, brought to saturation values for a longer amount of time, with respect to the previous cases. Additionally the overshoot on angular velocity time response is slightly higher.

A neglectable perturbation arises at the end of the sequence in one simulation only, in terms of input and effective thrust time response. This is most likely due to numerical conflicts that may take place due to the computational effort of the control strategy but they are absolutely non significant and do not compromise the final outcome of the simulations, in fact the success rate of this step is 100%.

From Figure 58 it is possible to see that the situation is more critical than before, in terms of oscillations: their amplitude and frequency have a significant value until the chaser gets at 20

meters distance from the target, even though the overall bound never exceeds 0.8 meters along x and y axes.

The increasing trend of a more clustered input, effective thrust and velocity time responses is visible in *Figure 59*. In particular in this case, for the first time, relative velocity peak value gets to 0.8 m/s.

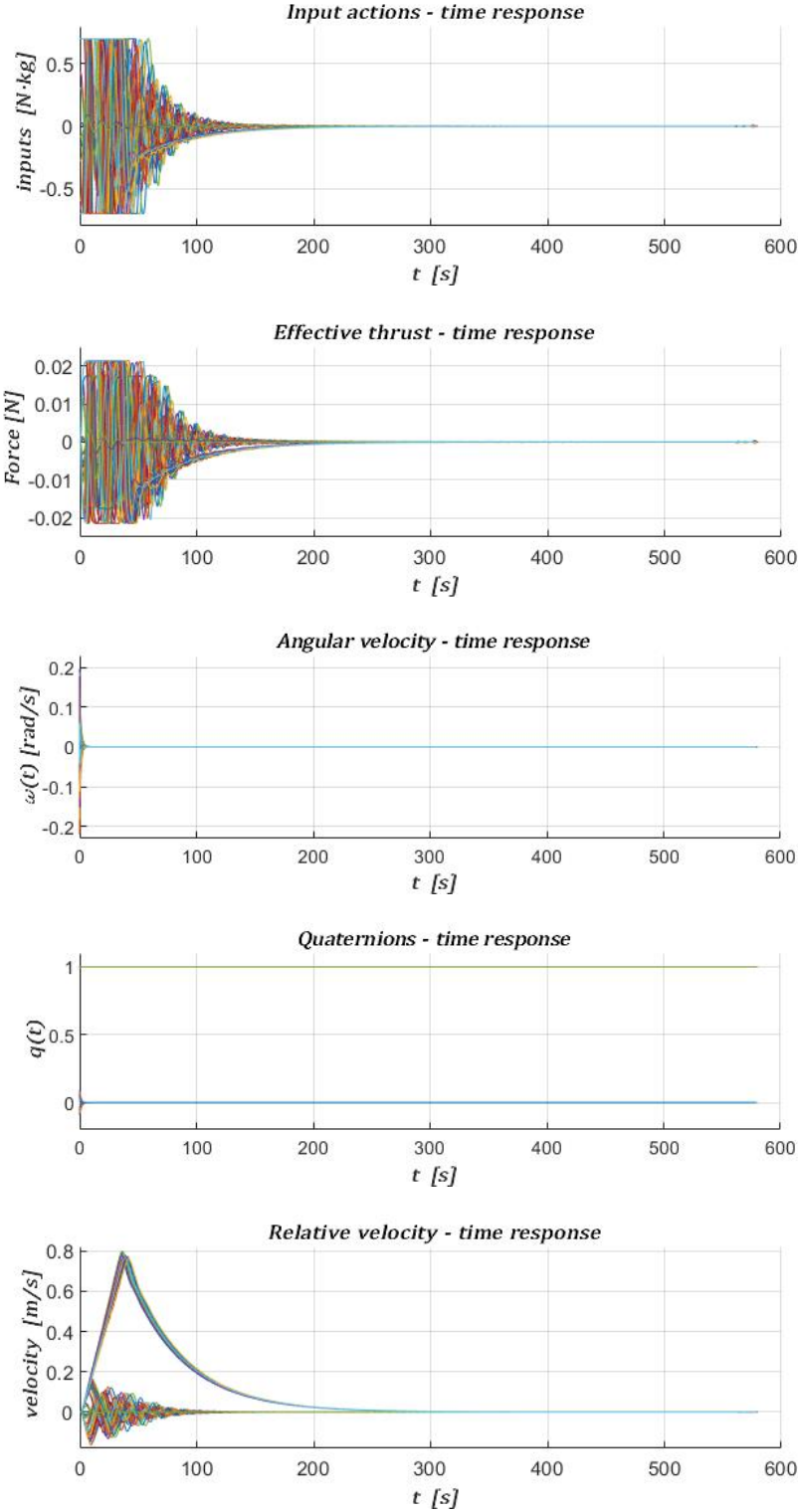


Figure 59: Time response plots in V-bar approach – Montecarlo 4

### 3.1.1.5 Step 5

- a) random disturbance of amplitude  $5 \cdot 2.5 \cdot 10^{-1} \text{ m}$  on relative position (all three axes);
- b) random disturbance of amplitude  $2 \text{ kg}$  on the mass;
- c) random disturbance of amplitude  $10^\circ$  on all three attitude angles;
- d) random disturbance of amplitude  $0.2 \text{ rad/s}$  on angular velocity (all three axes).

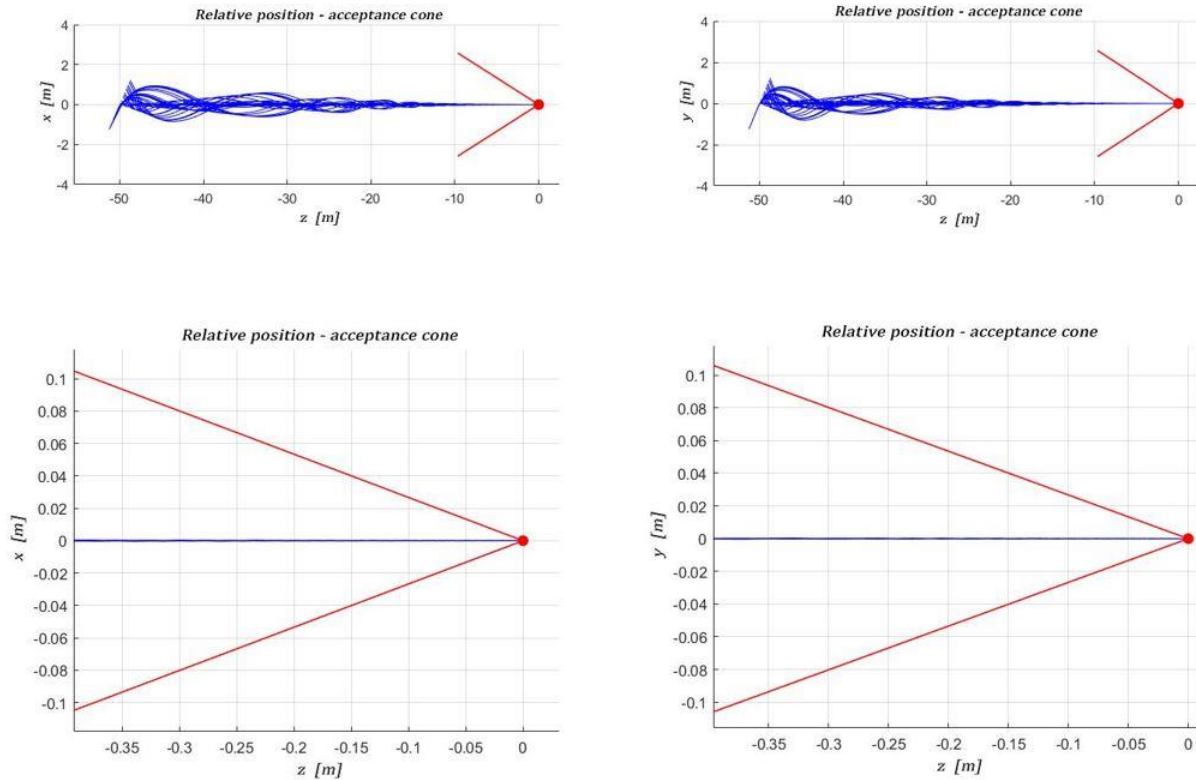


Figure 60: Relative position V-bar approach - Monte Carlo 5

Even in this case the success rate is 100% and the same considerations expressed on Step 4 are valid. Transient time, especially in terms of angular velocity, input and effective thrust time responses, is slightly longer but in every case is extinguished completely after 250 seconds.

In this scenario the upper and lower bounds of relative position along x and y axes never exceed 1 meter and oscillations remain significant until the chaser gets at 10 meters distance from the target. Despite this behaviour, in very close proximity of the arrival point, the chaser respects acceptance cone constraint and follows a straight line trajectory fixed onto reference values with no perturbations at all.

The perturbed characteristic on relative position is reflected directly on time responses in Figure 61, where it is clear how control inputs, effective thrust and relative velocity are very much affected by the higher amount of uncertainties a-priori imposed in this setup.

Even though the above-mentioned plots manifest a more clustered characteristic, brought to saturation in case of thrust-related parameters for the first 80 seconds straight of simulations, their values are always bounded by the physical limitations of the system. Relative velocity has a higher peak value as much as concerns both positive and negative overshoots. In terms of attitude there is no significant change with respect to the previous results.

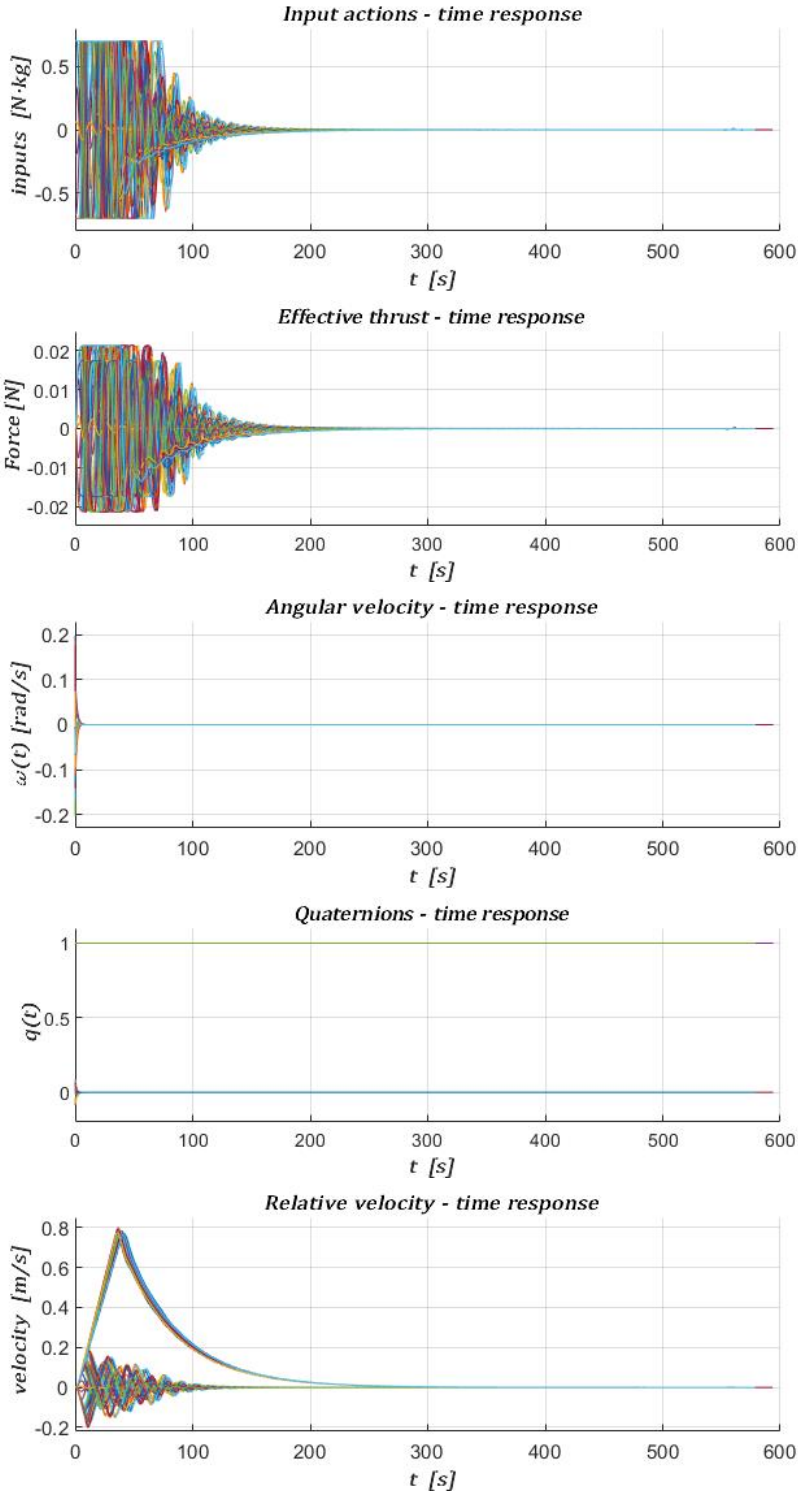


Figure 61: Time response plots in V-bar approach - Montecarlo 5

### 3.1.1.6 Step 6

- a) random disturbance of amplitude  $6 \cdot 2.5 \cdot 10^{-1} \text{ m}$  on relative position (all three axes);
- b) random disturbance of amplitude  $2 \text{ kg}$  on the mass;
- c) random disturbance of amplitude  $10^\circ$  on all three attitude angles;
- d) random disturbance of amplitude  $0.2 \text{ rad/s}$  on angular velocity (all three axes).

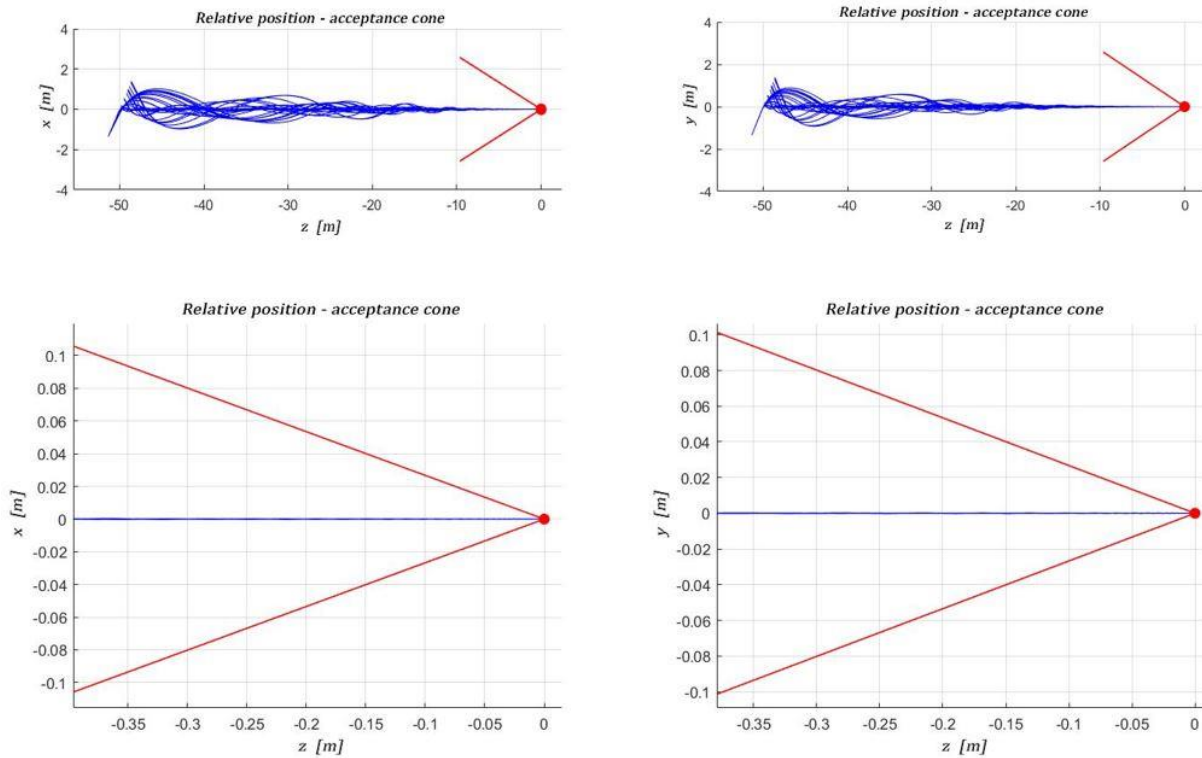


Figure 62: Relative position V-bar approach - Montecarlo 6

Success rate is equal to 100% also in this step, even though the uncertainties on initial position are much larger (Figure 62). Transient time and time responses' overshoots slightly increase because of the more invasive disturbances but steady state conditions are always ensured after 250 seconds.

It appears clear how, in this scenario, oscillation on relative position along x and y axes remain significant in terms of both frequency and amplitude until the chaser gets at 10 meters distance from the target. Perturbations on relative position are bounded by the quantity of 1.5 meters and the acceptance cone constraint satisfaction is always guaranteed even in this situation.

In terms of time responses (Figure 63) the trend analysed before is maintained: control inputs, effective thrust and relative velocity values are brought to saturation for a longer time span; additionally the time responses remain perturbed for a slightly longer time than before.

However there is no change in peak values, thus the upper and lower bounds remain the same as in the previous setup.

There is no significant variation in terms of attitude, overshoot are limited to the very beginning of the sequence and do not constitute a critical factor for the sake of the success of simulations.

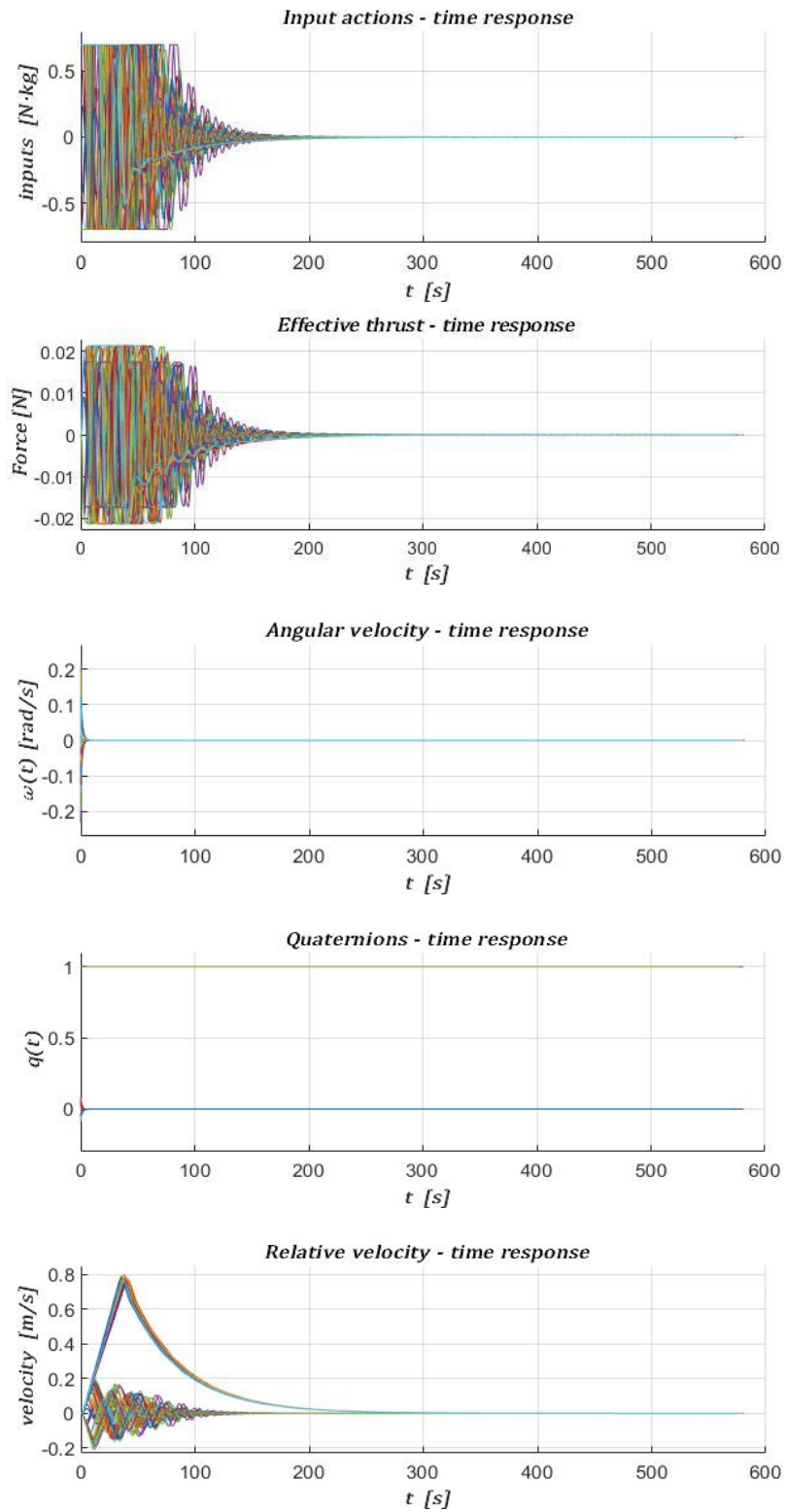


Figure 63: Time response plots in V-bar approach - Montecarlo 6

### 3.1.1.7 Step 7

- a) random disturbance of amplitude  $7 \cdot 2.5 \cdot 10^{-1} \text{ m}$  on relative position (all three axes);
- b) random disturbance of amplitude  $2 \text{ kg}$  on the mass;
- c) random disturbance of amplitude  $10^\circ$  on all three attitude angles;
- d) random disturbance of amplitude  $0.2 \text{ rad/s}$  on angular velocity (all three axes).

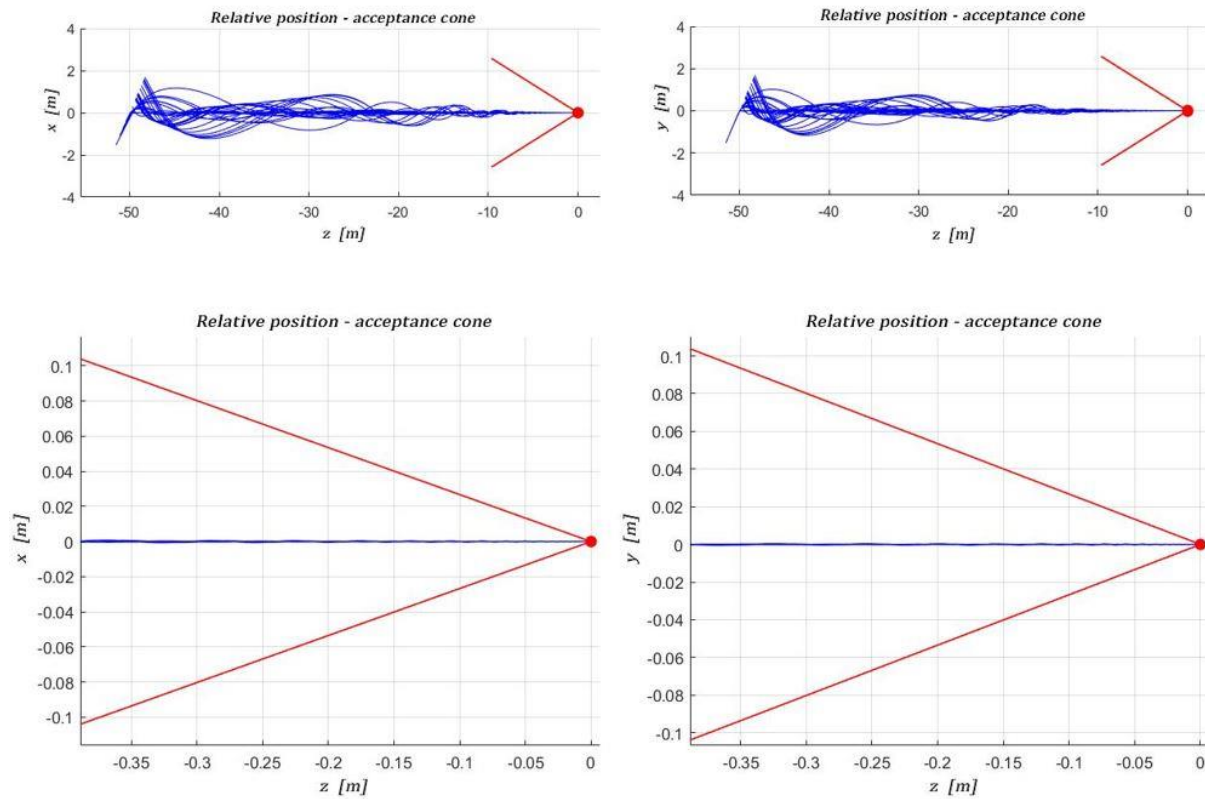


Figure 64: Relative position V-bar approach - Montecarlo 7

Success rate is equal to 100%, like in the previous chunks of simulation. Additionally, due to the higher uncertainties, it is possible to see that in only one case there is a small residual transient until 300 seconds of simulation in input and effective thrust time responses.

Also in this situation both amplitude and frequency of perturbations in terms of trajectory (Figure 64) slightly increase with respect to the previous set of simulations but never compromise the final outcome of the manoeuvre, which is brought to completion with success. The last meters in very close proximity to the target are described by a straight line fixed onto reference values, ensuring satisfaction of acceptance cone constraint. Even in this case there is no change in the attitude-related time responses, which are always subject to the same set of uncertainties. In terms of input, effective thrust and relative velocity time responses, the perturbations increase, as linear actuation and velocity need to compensate the higher amount of uncertainties on initial position. In this case the characteristic of the input time response, and

thus of effective thrust, remain fixed to saturation values almost until 100 seconds of simulation. Relative velocity exceeds the negative bound of  $-0.2$  m/s in the first meters of the manoeuvre. In general the time responses related to linear motion appear to be more disturbed but, in the long run, able to get to steady state values anyway, thus ensuring the success of the manoeuvre.

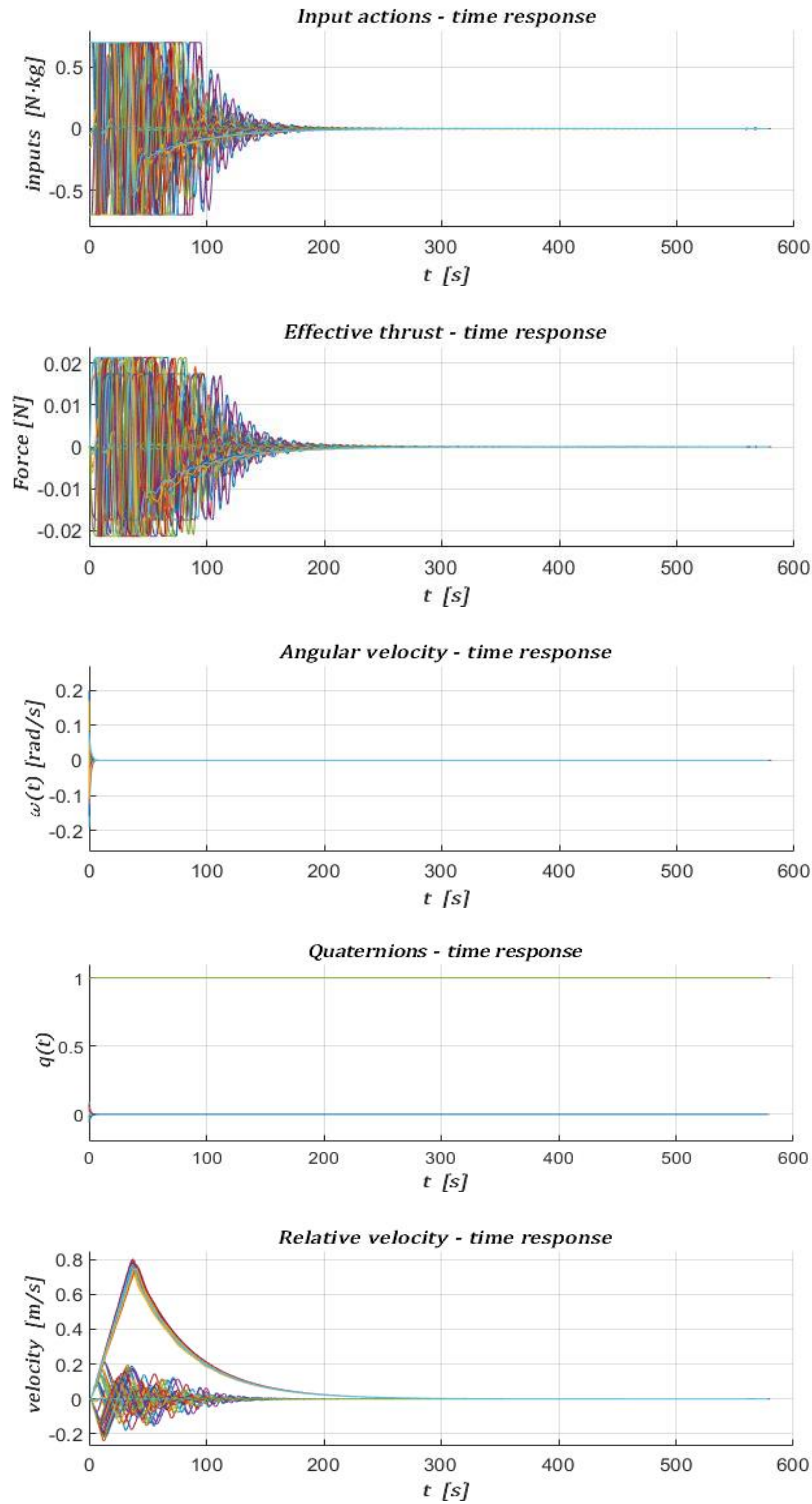


Figure 65: Time response plots in V-bar approach - Montecarlo 7

### 3.1.1.8 Step 8

- a) random disturbance of amplitude  $8 \cdot 2.5 \cdot 10^{-1} \text{ m}$  on relative position (all three axes);
- b) random disturbance of amplitude  $2 \text{ kg}$  on the mass;
- c) random disturbance of amplitude  $10^\circ$  on all three attitude angles;
- d) random disturbance of amplitude  $0.2 \text{ rad/s}$  on angular velocity (all three axes).

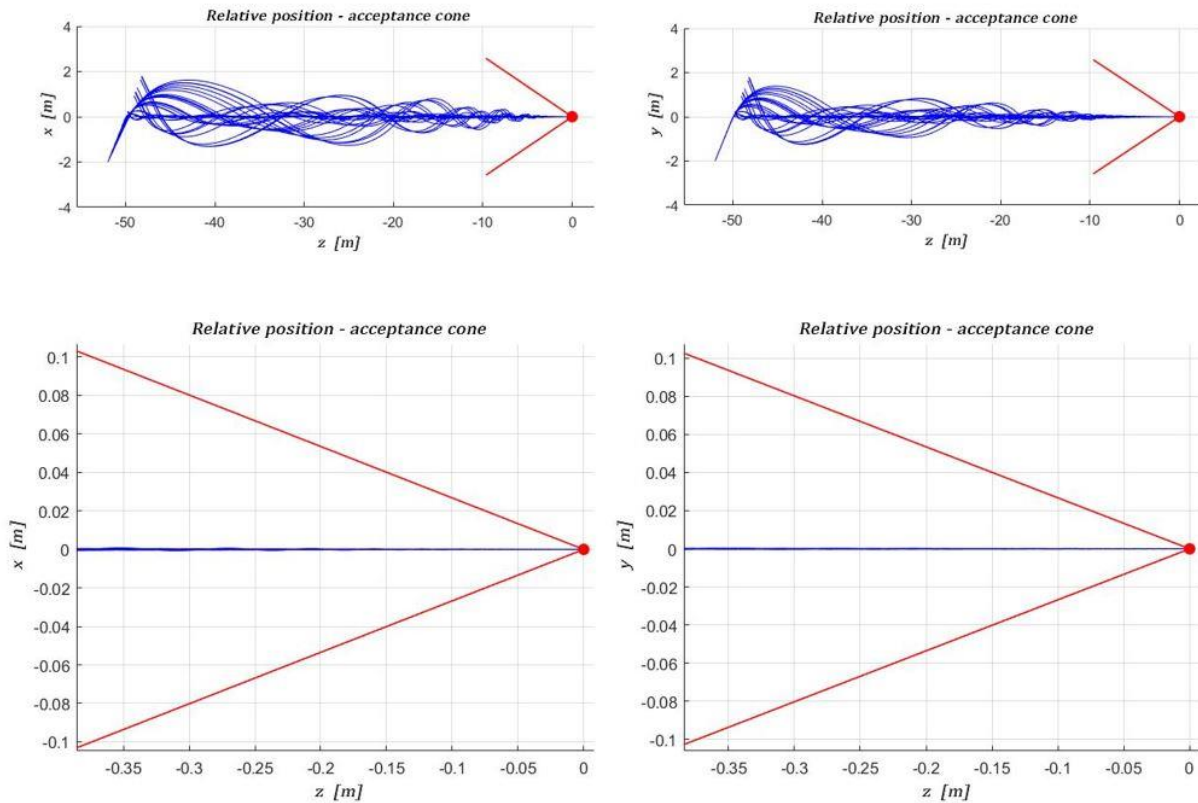


Figure 66: Relative position V-bar approach - Montecarlo 8

Success rate is equal to 100% and, as well as in the seventh step, residual transients extinguish after 300 seconds in this case, as much as concerns input and effective thrust time responses.

In this case, the perturbed situation becomes even more critical, since oscillations on x and y axes, as much as concerns relative position, are shown also inside the acceptance cone, i.e. until the chaser gets at 4 meters distance from the arrival point. Amplitude bounds of oscillation start to get closer to 2 meters in the peak values but the acceptance cone constraint is always respected, once again.

Saturation of values in input time response and, consequently, in effective thrust time response, overcomes the bound of 100 seconds, due to the higher control effort required to cancel the unexpected uncertainty.

The behaviour of attitude-related time responses does not change as neither uncertainties associated to quaternions and angular velocity change.

In terms of relative velocity time response, the behaviour does not differ much from the previous case, apart from a slightly more clustered characteristic at the beginning of the sequence.

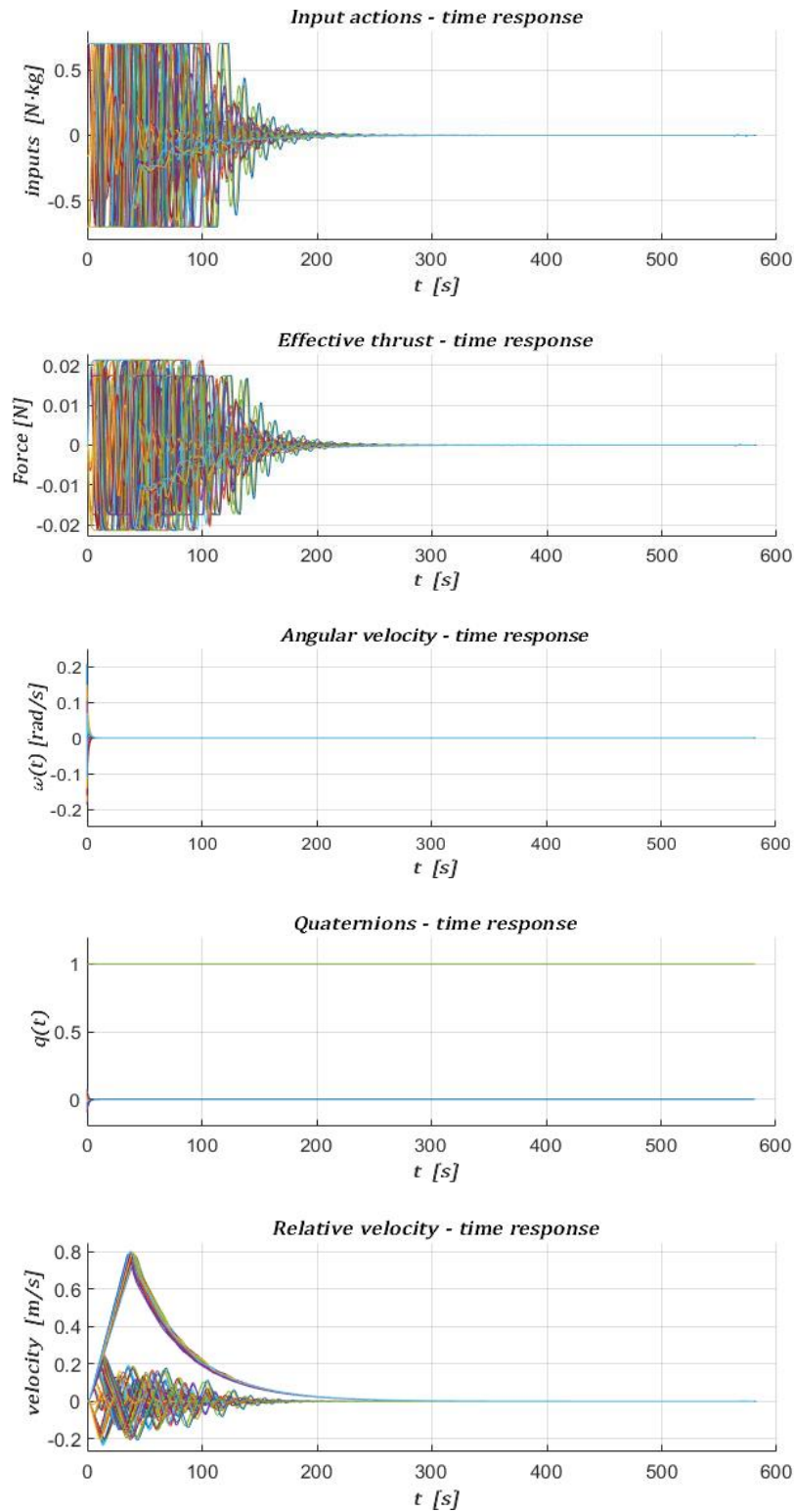


Figure 67: Time response plots in V-bar approach - Montecarlo 8

### 3.1.1.9 Step 9

- a) random disturbance of amplitude  $9 \cdot 2.5 \cdot 10^{-1} \text{ m}$  on relative position (all three axes);
- b) random disturbance of amplitude  $2 \text{ kg}$  on the mass;
- c) random disturbance of amplitude  $10^\circ$  on all three attitude angles;
- d) random disturbance of amplitude  $0.2 \text{ rad/s}$  on angular velocity (all three axes).

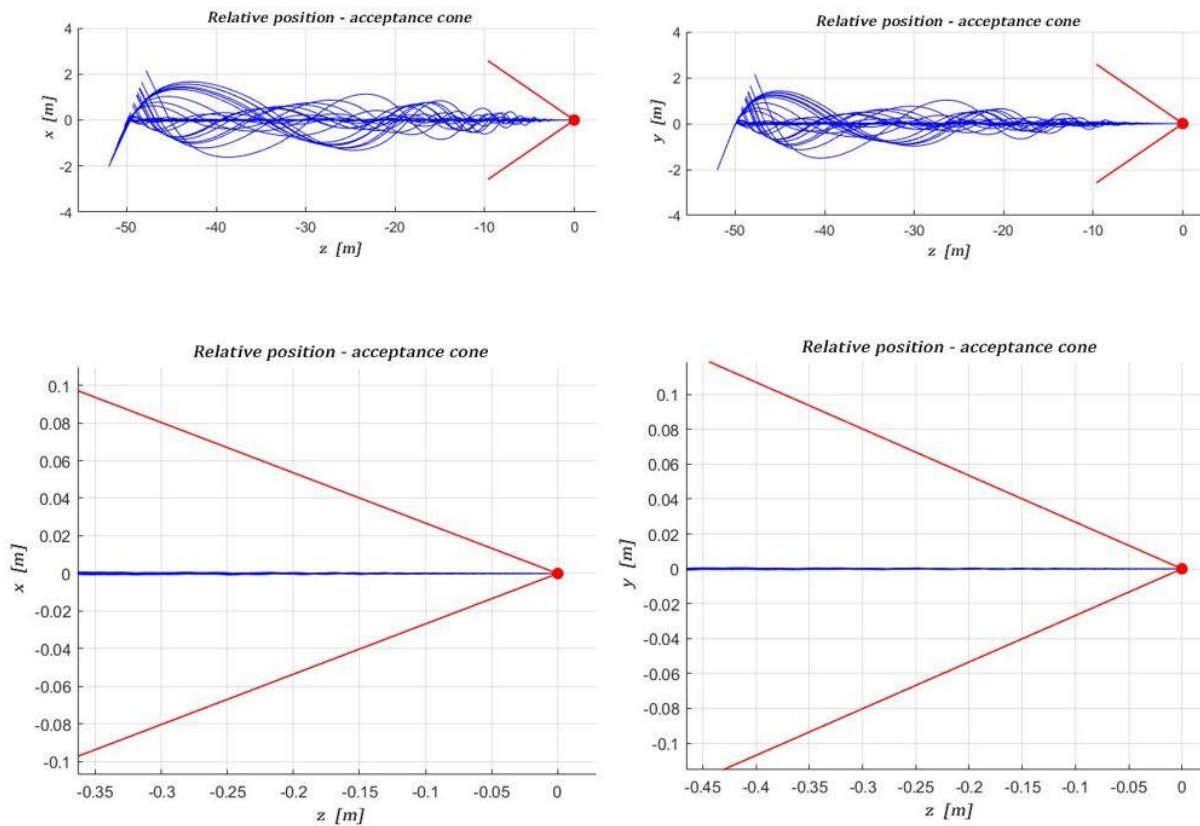


Figure 68: Relative position V-bar approach - Montecarlo 9

Even in this case the success rate is 100% and the same observations on residual transients made in the previous paragraph hold.

Upper and lower bounds of oscillations in relative positions slightly increase both on x and y axes but the parameters varying the most about these perturbations is frequency, which notably increases with respect to previous cases. Despite that, from the point of view of acceptance cone constraint, the manoeuvre is successful.

In terms of time responses, the increasing trend of a more and more clustered characteristic, in the starting phases of simulations, is confirmed even here. Saturated values of input actions and effective thrust are maintained until 120 seconds, showing a more severe condition to compensate, in terms of uncertainties.

The same considerations hold as much as concerns relative velocity time response, which becomes a bit more perturbed.

As before, no changes in the attitude behaviour can be identified, as there is no further uncertainty added to the dynamics in this case with respect to the previous ones.

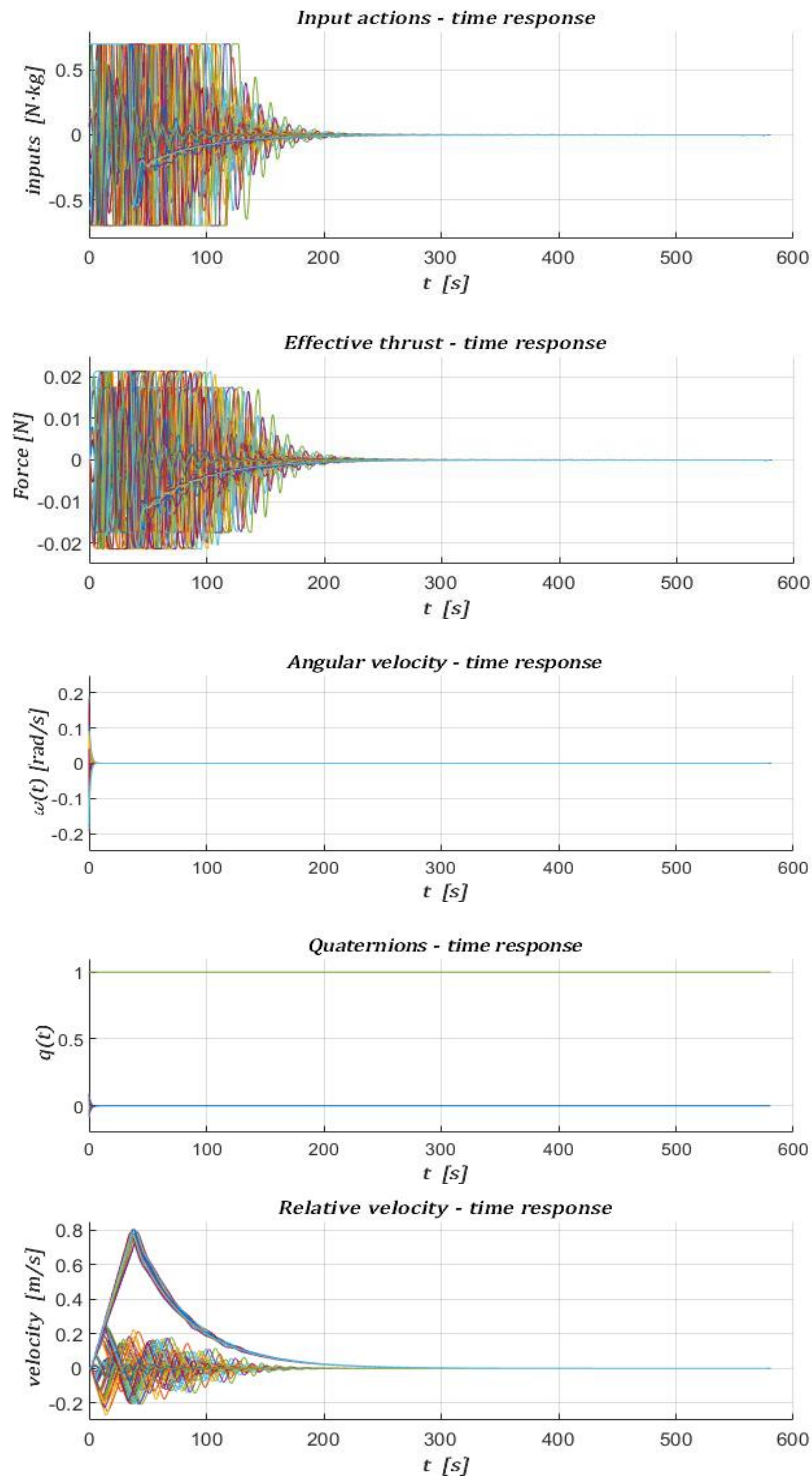


Figure 69: Time response plots in V-bar approach - Montecarlo 9

### 3.1.1.10 Step 10

- a) random disturbance of amplitude **2.5 m** on relative position (all three axes);
- b) random disturbance of amplitude **2 kg** on the mass;
- c) random disturbance of amplitude **10°** on all three attitude angles;
- d) random disturbance of amplitude **0.2 rad/s** on angular velocity (all three axes).

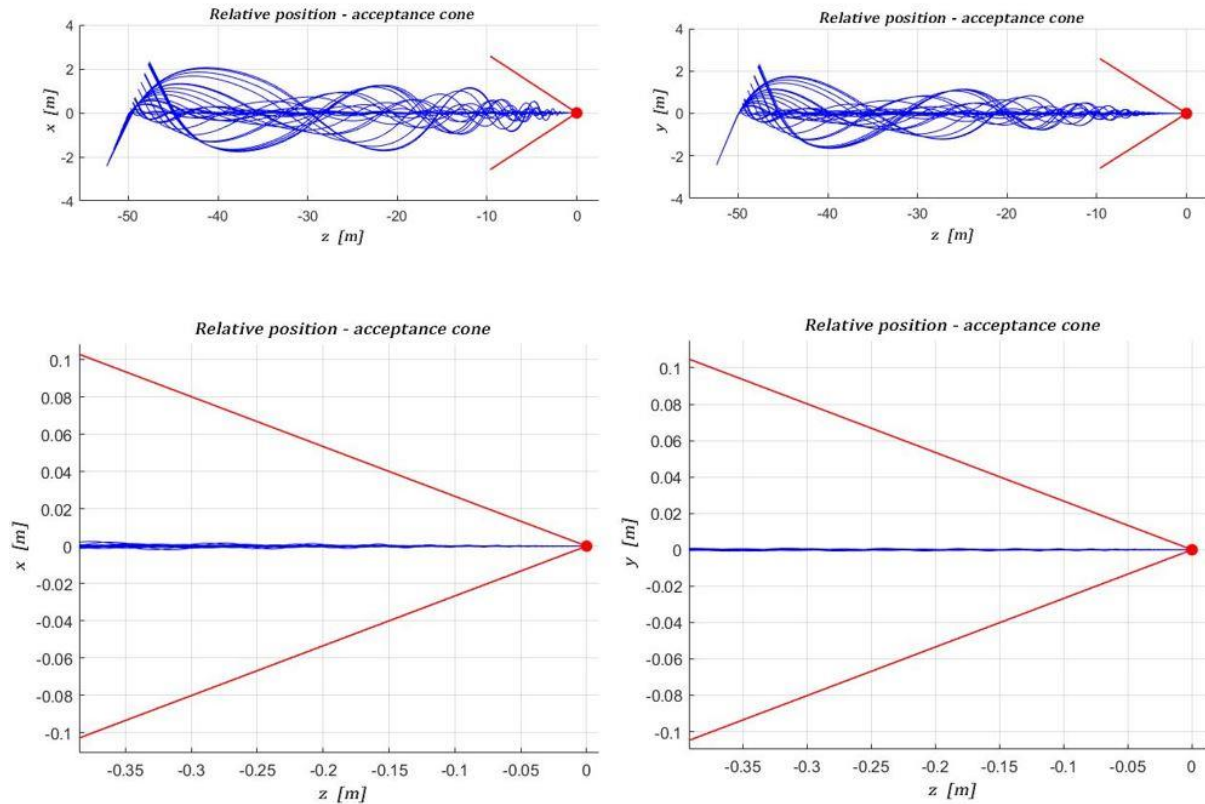


Figure 70: Relative position V-bar approach - Montecarlo 10

Even in the worst case scenario, step 10, the success rate results to be 100%. In this case residual transients overcome 300 seconds of simulation but from 400 seconds to the end of each sequence, steady state values are ensured for each time response, apart from a small perturbation in one only case due to numerical conflicts. Even in the latter case, however, the success of simulation is ensured by respecting the tolerance band of  $\pm 2$  mm on the last 20 states.

In this case it is possible to see that input values are stuck to saturation levels for 160 seconds straight, showing that linear actuation is particularly affected by the imposed uncertainties: the propulsion system’s availability must be fully exploited to correct the trajectory and reach reference values.

In terms of attitude, once again, there is no significant observation to add, as the behaviour is identical to the one observed in the previous cases.

Relative velocity time response appears more disturbed as much as concerns each element of the states vector, as a significant uncertainty must be compensated on relative position in this case, i.e. the worst case scenario.

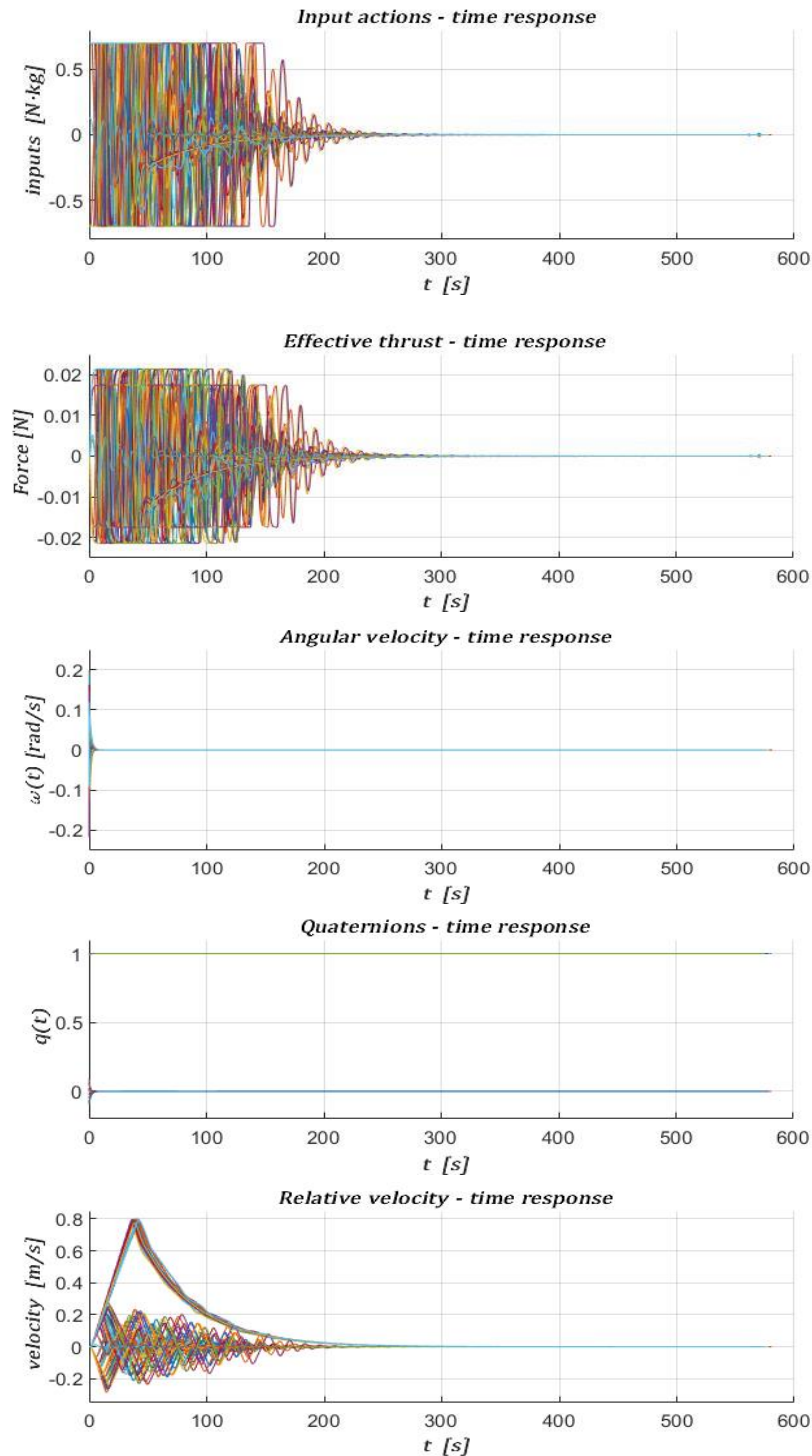


Figure 71: Time response plots in V-bar approach - Montecarlo 10

### 3.1.2 Montecarlo simulations: R-bar approach

In this scenario it is necessary to take into account a higher contribution of atmospheric drag. Since, in this case, the chaser finds itself 50 meters above the target and there is a significant difference between the so-called wet surface of the CubeSat and Space Rider, at the end of the manoeuvre there is going to be an offset along the z-axis. This phenomenon is modelled by increasing the drag force disturbance (2.2.1.2) of two orders of magnitude, once the chaser gets at 10 meters distance from the target.

#### 3.1.2.1 Step 1

- random disturbance of amplitude  $2.5 \cdot 10^{-1} \text{ m}$  on relative position (all three axes);
- random disturbance of amplitude  $2 \text{ kg}$  on the mass;
- random disturbance of amplitude  $10^\circ$  on all three attitude angles;
- random disturbance of amplitude  $0.2 \text{ rad/s}$  on angular velocity (all three axes).

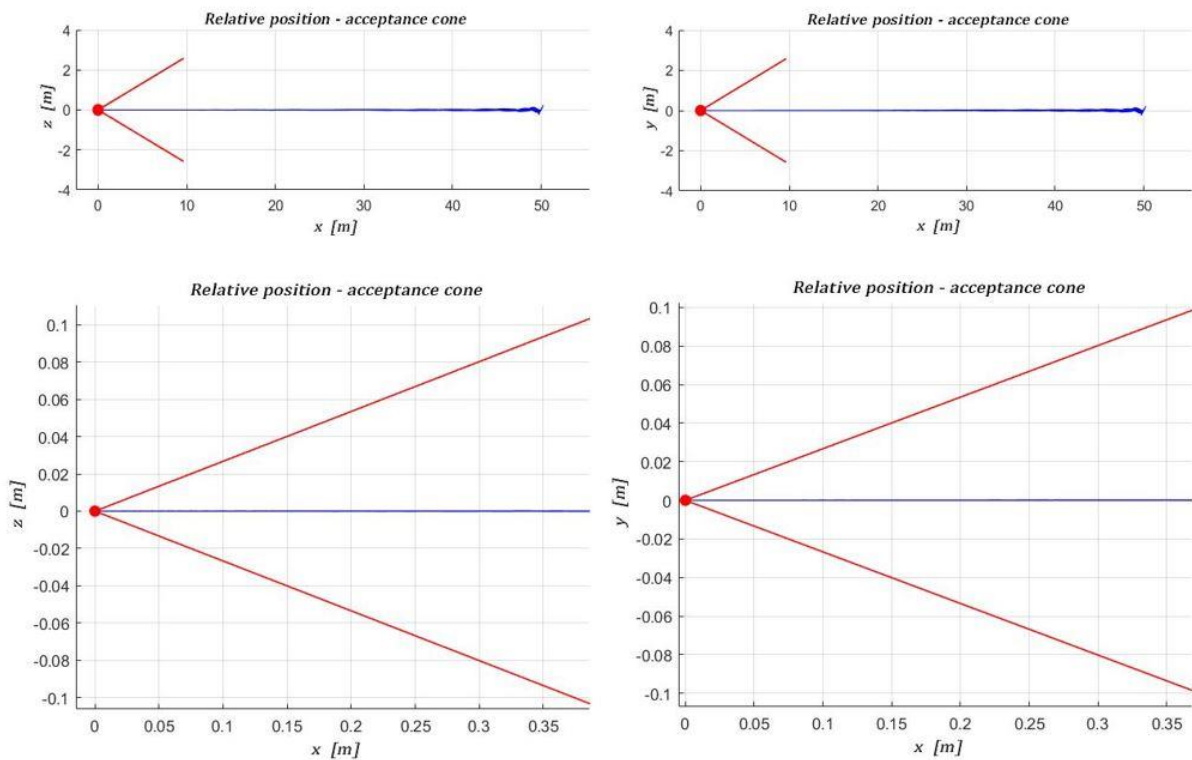


Figure 72: Relative position R-bar approach - Montecarlo 1

In these first 30 simulations the success rate results to be of 100% in fact, as it is possible to see from Figure 72, the acceptance cone constraint is always satisfied. Control effort and effective thrust time responses only differ of a scaling factor given by the mass of the chaser.

It is clear how time responses of input actions and effective thrust have an oscillating trend for the first 200 seconds of simulation, given the introduced uncertainties which must be compensated, but the values are always included into the prescribed bounds. In terms of angular velocity and attitude, the results are the same obtained in the nominal case: there is a minimal

overshoot at the beginning of the manoeuvre mainly due to sloshing disturbance which is immediately cancelled by the control system. The same considerations expressed on input actions hold for relative velocity time response: all the elements of the velocity vector have an oscillating behaviour for the first 200 seconds, getting to the peak value after 40 seconds of simulations and then rapidly decreasing to reference.

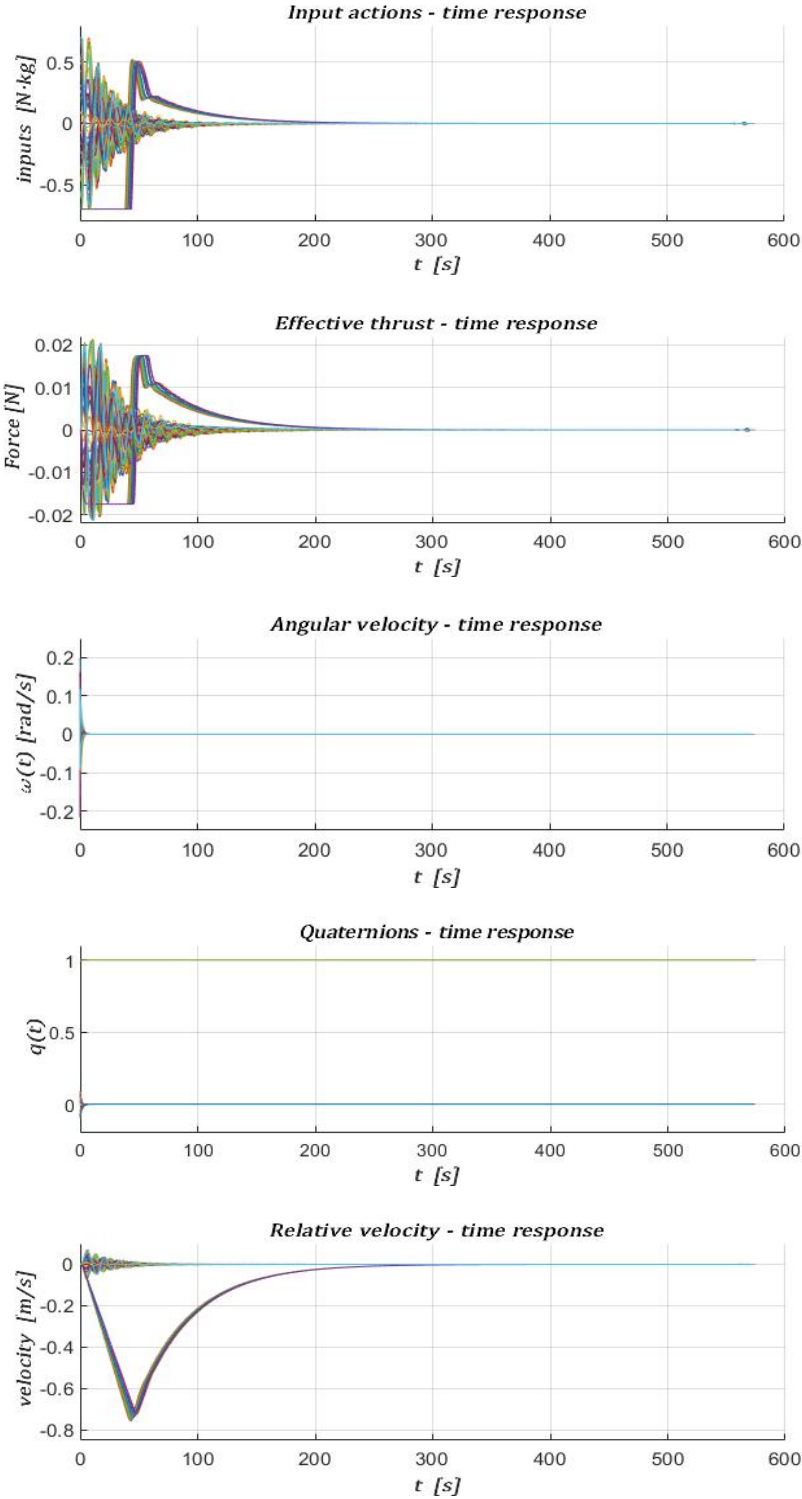


Figure 73: Time response plots in R-bar approach - Montecarlo 1

### 3.1.2.2 Step 2

- a) random disturbance of amplitude  $2 \cdot 2.5 \cdot 10^{-1} \text{ m}$  on relative position (all three axes);
- b) random disturbance of amplitude  $2 \text{ kg}$  on the mass;
- c) random disturbance of amplitude  $10^\circ$  on all three attitude angles;
- d) random disturbance of amplitude  $0.2 \text{ rad/s}$  on angular velocity (all three axes).

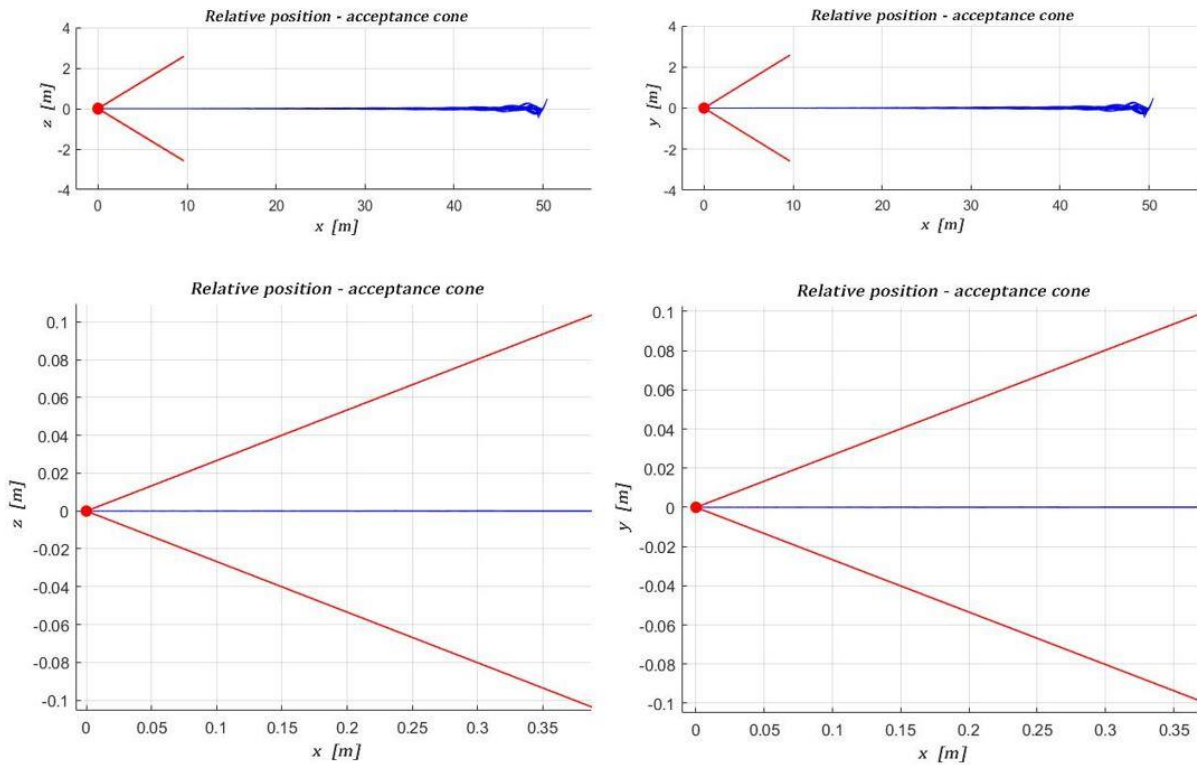


Figure 74: Relative position  $R\text{-bar}$  approach - Montecarlo 2

In this second step the success rate is 100%. It is possible to see from *Figure 74* and *75* that there is a worsening situation in uncertainties on initial conditions and this phenomenon causes a slightly higher effort in terms of the required and provided thrust.

In general it is clear how the system's behaviour is more perturbed, with a slightly more oscillating time response in the starting phase of simulations even though all the parameters are brought to steady state after few seconds.

In terms of attitude, no significant differences arise with respect to the previous case: the same overshoots are encountered at the beginning of the sequence but they are cancelled without any problems after few seconds. Control inputs and effective thrust time responses, instead, have a highly oscillating behaviour until 200 seconds of simulation, due to the higher amount of uncertainties introduced in this case.

The same considerations hold as much as concerns velocity time response, whose behaviour is oscillating for the first 200 seconds of simulation and whose peak value never exceeds -0.8 m/s, as in the previous simulations.

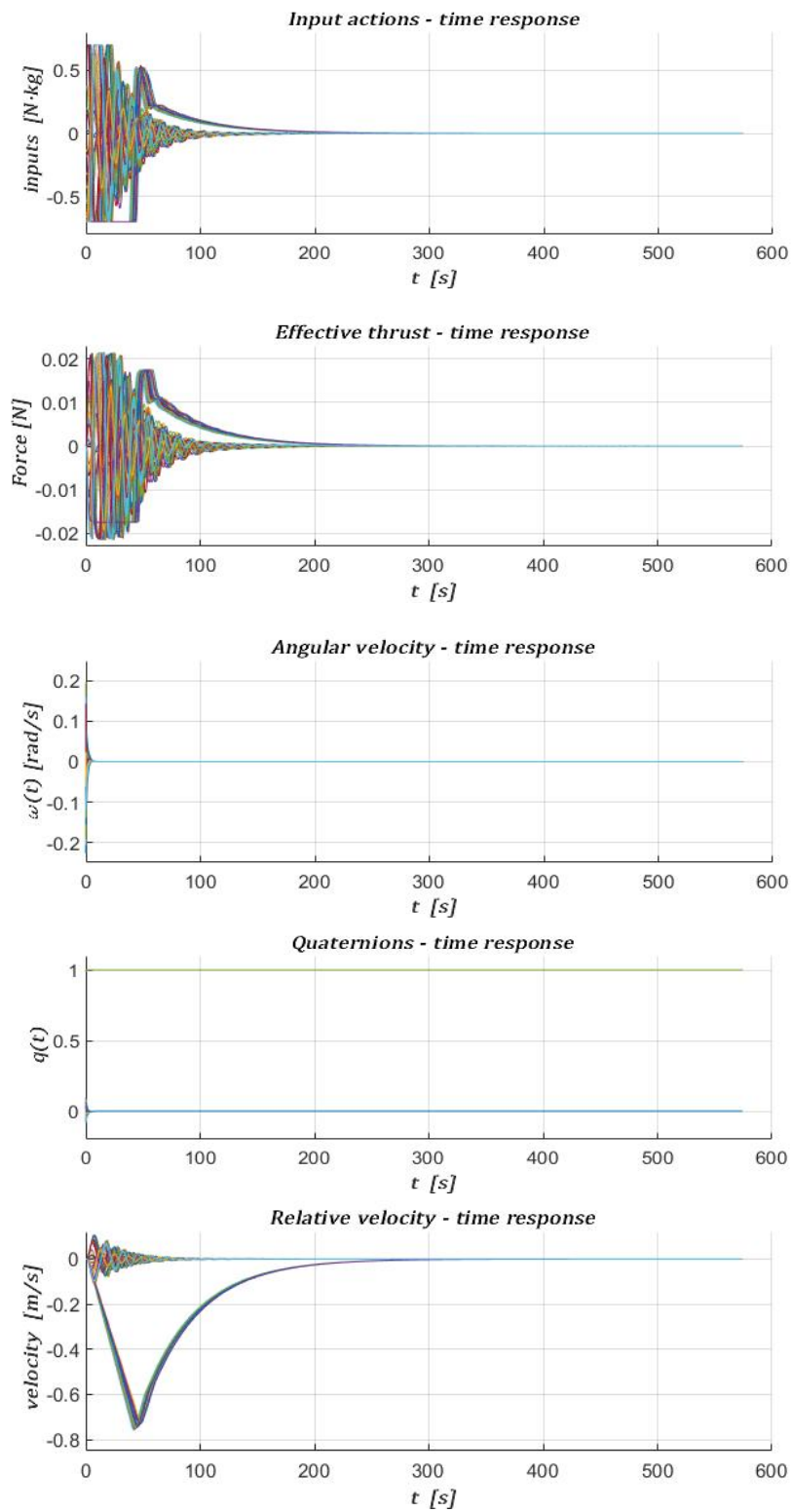


Figure 75: Time response plots in R-bar approach - Montecarlo 2

### 3.1.2.3 Step 3

- e) random disturbance of amplitude  $3 \cdot 2.5 \cdot 10^{-1} \text{ m}$  on relative position (all three axes);
- f) random disturbance of amplitude  $2 \text{ kg}$  on the mass;
- g) random disturbance of amplitude  $10^\circ$  on all three attitude angles;
- h) random disturbance of amplitude  $0.2 \text{ rad/s}$  on angular velocity (all three axes).

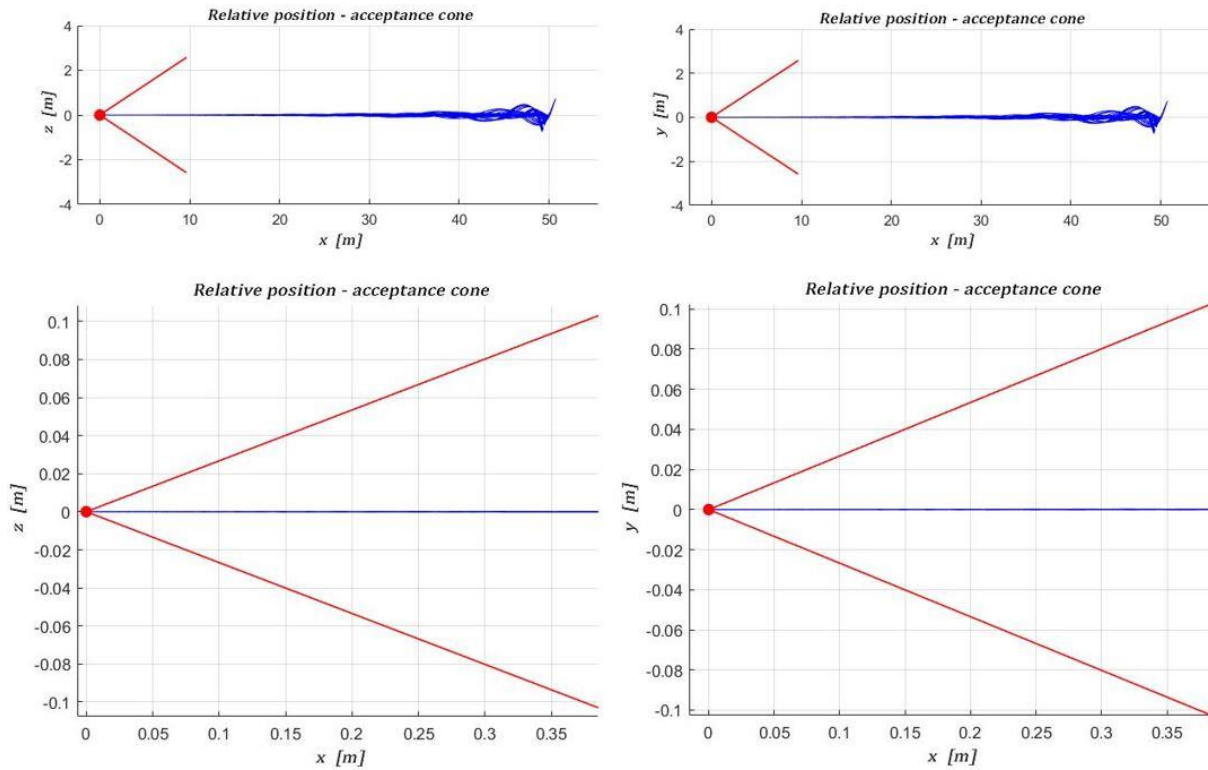


Figure 76: Relative position  $R\text{-bar}$  approach - Monte Carlo 3

Success rate is equal to 100 % also in this step: from *Figure 76* it is clear how the acceptance cone constraint is satisfied, given a smooth trajectory fixed onto reference values in the last meters of the approach to the target spacecraft. However there is a more oscillating characteristic in the relative position at further distance from the arrival point, along  $z$  and  $y$  axes, due to the higher degree of uncertainty on initial conditions. Also in this scenario, as in the  $V\text{-bar}$  approach, it is clear that the first part of the manoeuvre appears to be the most sensitive to a variation of the nominal conditions, even though the deviations from reference values are always found within the bound of 0.7 meters, along both  $z$  and  $y$  axes.

Due to the higher uncertainty, there is a more oscillating characteristic even in the time responses representing the variation of input parameters, effective thrust and relative velocity.

Control inputs and effective thrust are the same, apart from a scaling factor due to the mass of the CubeSat. However the consequences of a more uncertain setup on initial conditions reflects

on the more clustered area created by the oscillations in the above mentioned time response plots. All values are anyway within the prescribed bounds.

There is no significant variation in terms of attitude parameters, also in this case.

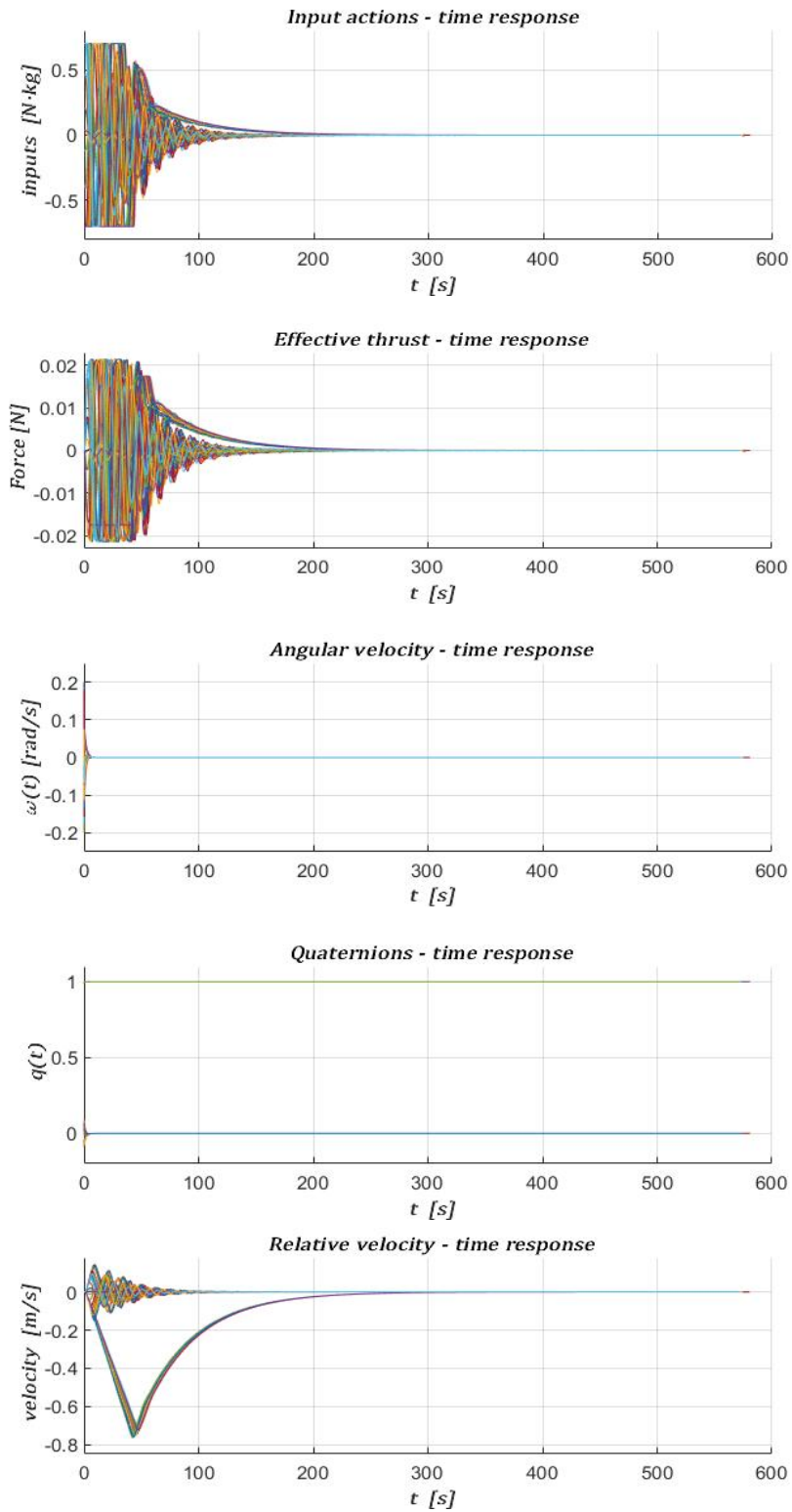


Figure 77: Time response plots in R-bar approach - Montecarlo 3

### 3.1.2.4 Step 4

- a) random disturbance of amplitude  $4 \cdot 2.5 \cdot 10^{-1} \text{ m}$  on relative position (all three axes);
- b) random disturbance of amplitude  $2 \text{ kg}$  on the mass;
- c) random disturbance of amplitude  $10^\circ$  on all three attitude angles;
- d) random disturbance of amplitude  $0.2 \text{ rad/s}$  on angular velocity (all three axes).

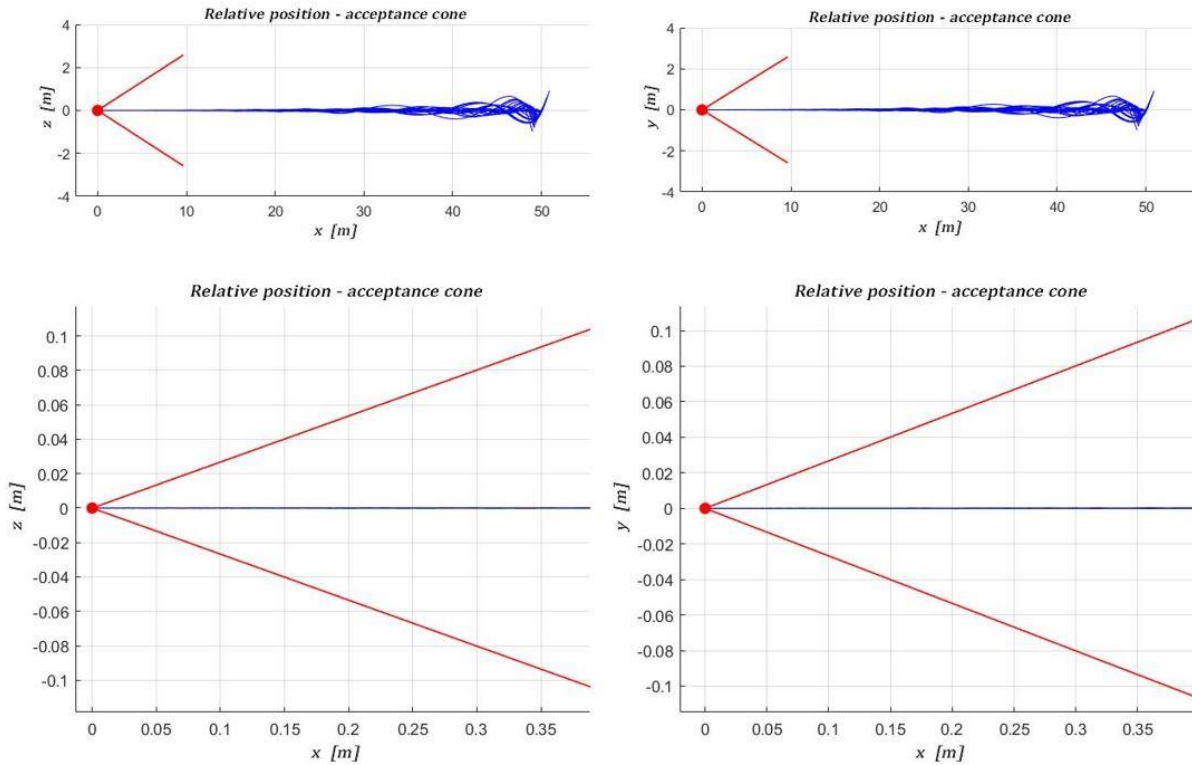


Figure 78: Relative position  $R\text{-bar}$  approach - Montecarlo 4

The success rate is 100% also in this step. It is clear how a more uncertain setup causes input time response and effective thrust to be brought to saturation values for a longer amount of time, with respect to the previous cases. Additionally the overshoot on angular velocity time response is slightly higher.

A small deviation takes place from reference at the end of the sequence in one simulation only, in terms of input and effective thrust time response, because of numerical conflicts happening due to the computational effort of the control strategy but they are absolutely non significant and do not compromise the final outcome of the simulations, in fact the success rate of this step is 100%.

From *Figure 78* it is possible to see that the situation is slightly worse than before, in terms of oscillations in the trajectory: amplitude and frequency of perturbations have a significant value until the chaser gets at 20 meters distance from the target, even though the overall bound never exceeds -0.8 meters along z and y axes.

Control inputs, effective thrust and velocity time responses have a more clustered behaviour (Figure 79). As much as concerns linear actuation, time responses are brought to saturation values until 65 seconds.

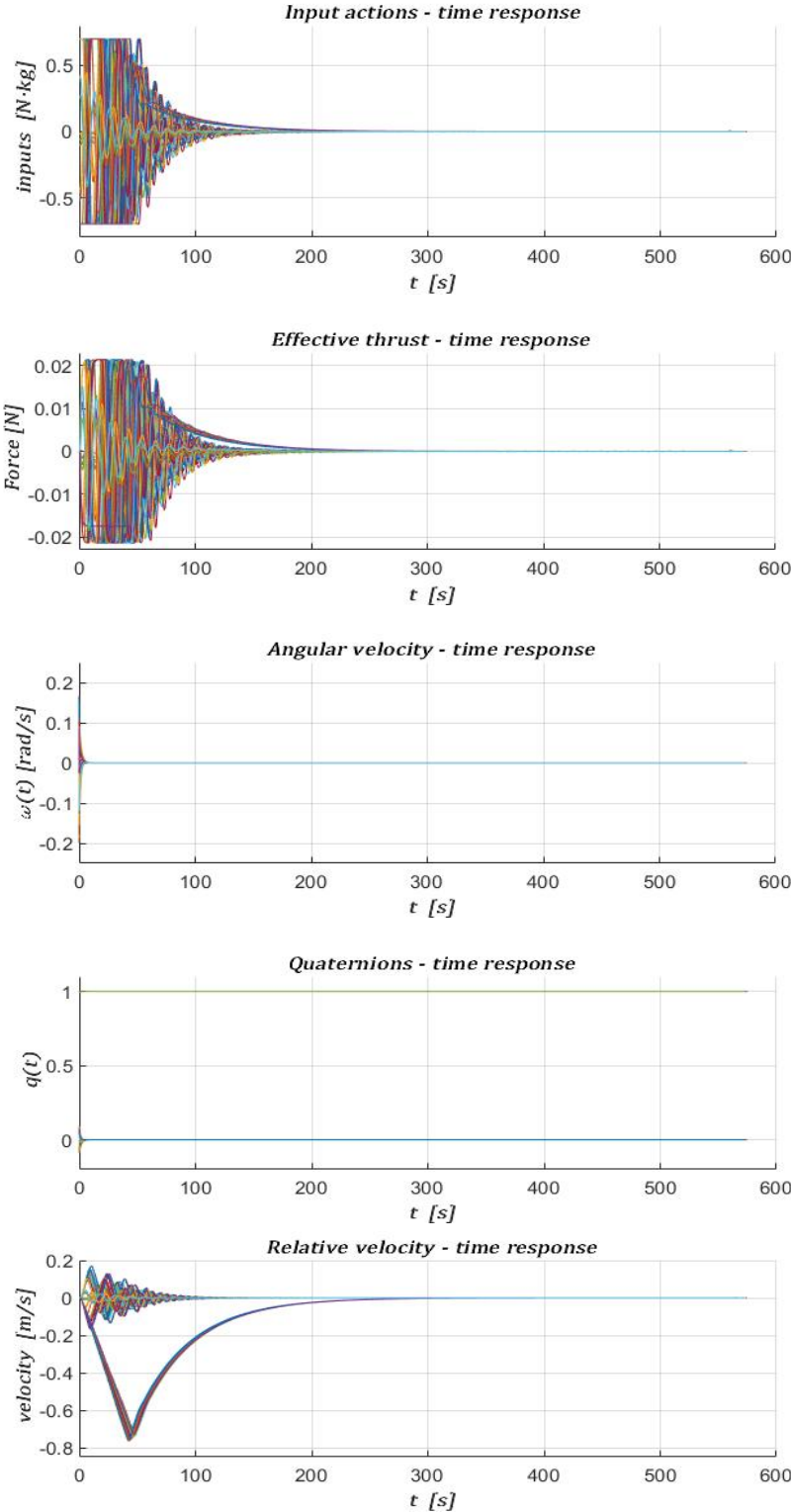


Figure 79: Time response plots in R-bar approach - Montecarlo 4

### 3.1.2.5 Step 5

- a) random disturbance of amplitude  $5 \cdot 2.5 \cdot 10^{-1} \text{ m}$  on relative position (all three axes);
- b) random disturbance of amplitude  $2 \text{ kg}$  on the mass;
- c) random disturbance of amplitude  $10^\circ$  on all three attitude angles;
- d) random disturbance of amplitude  $0.2 \text{ rad/s}$  on angular velocity (all three axes).

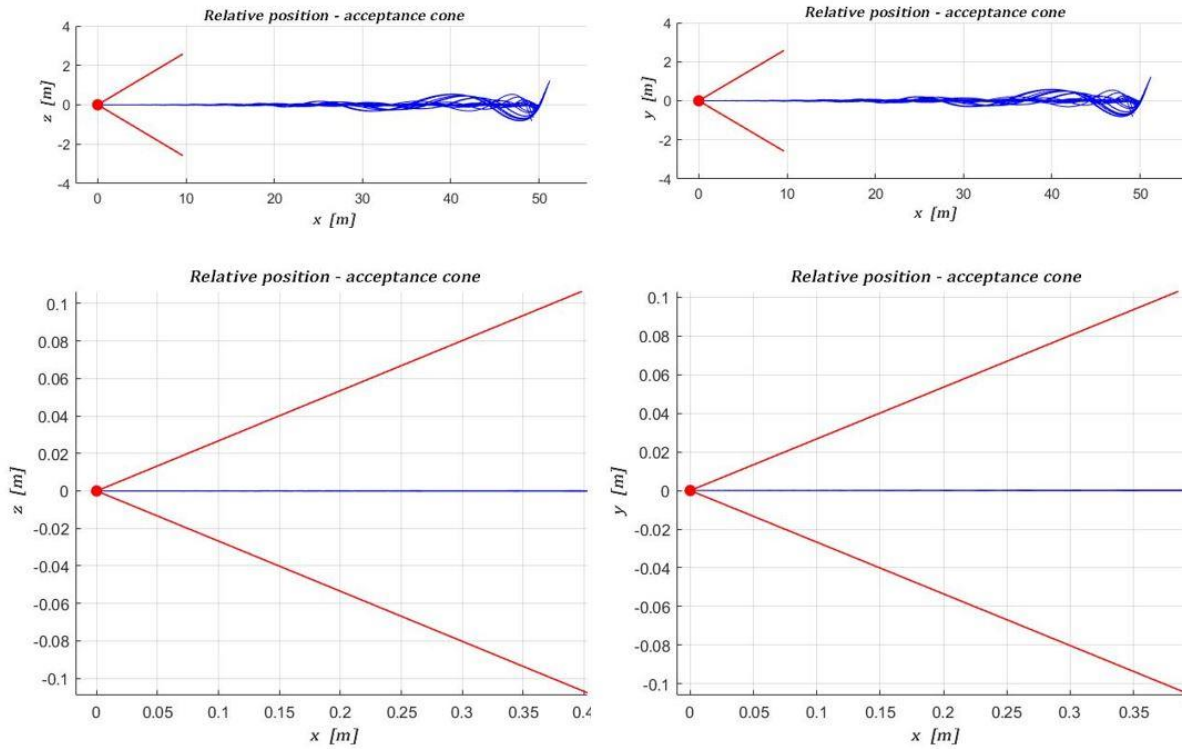


Figure 80: Relative position  $\bar{R}$ -bar approach - Montecarlo 5

In this chunk of simulations the success rate is 100%. Transient time, especially in terms of angular velocity, input and effective thrust time responses, is slightly longer but in every case is extinguished completely after 250 seconds.

Upper and lower bounds of relative position along z and y axes never exceed 1 meter and oscillations remain significant until the chaser gets at 10 meters distance from the target. The chaser respects acceptance cone constraint and follows a straight line trajectory fixed onto reference values (Figure 80).

It is clear from Figure 81 how control inputs, effective thrust and relative velocity time responses are influenced by the newly introduced uncertainties, with a more perturbed behaviour.

Thrust-related parameters saturate to upper and lower bounds for the first 80 seconds straight of simulations. Relative velocity has a higher peak value as much as concerns both positive and negative overshoots.

In terms of attitude there is no significant change with respect to the previous results.

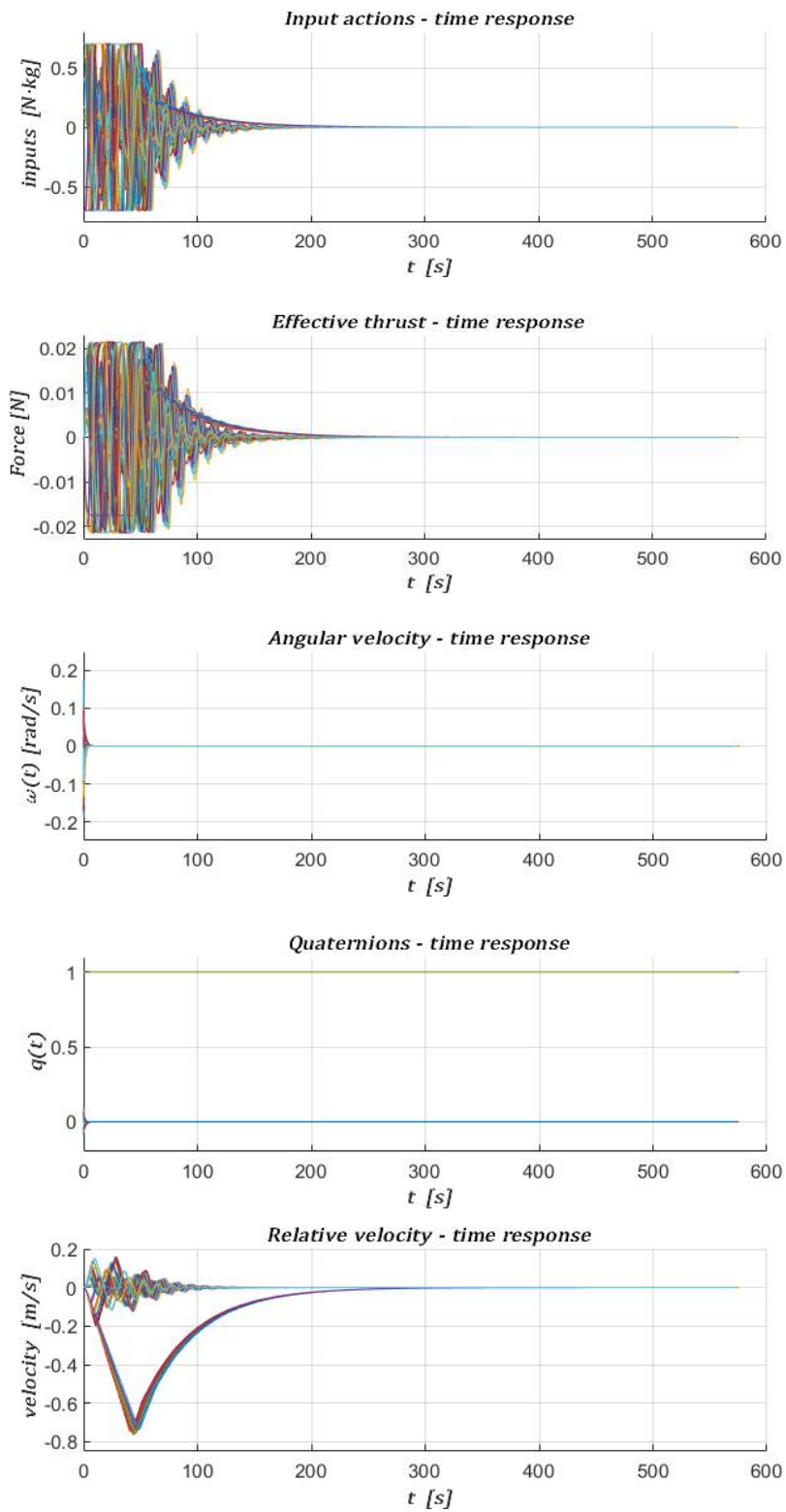


Figure 81: Time response plots in R-bar approach - Montecarlo 5

### 3.1.2.6 Step 6

- a) random disturbance of amplitude  $6 \cdot 2.5 \cdot 10^{-1} \text{ m}$  on relative position (all three axes);
- b) random disturbance of amplitude  $2 \text{ kg}$  on the mass;
- c) random disturbance of amplitude  $10^\circ$  on all three attitude angles;
- d) random disturbance of amplitude  $0.2 \text{ rad/s}$  on angular velocity (all three axes).

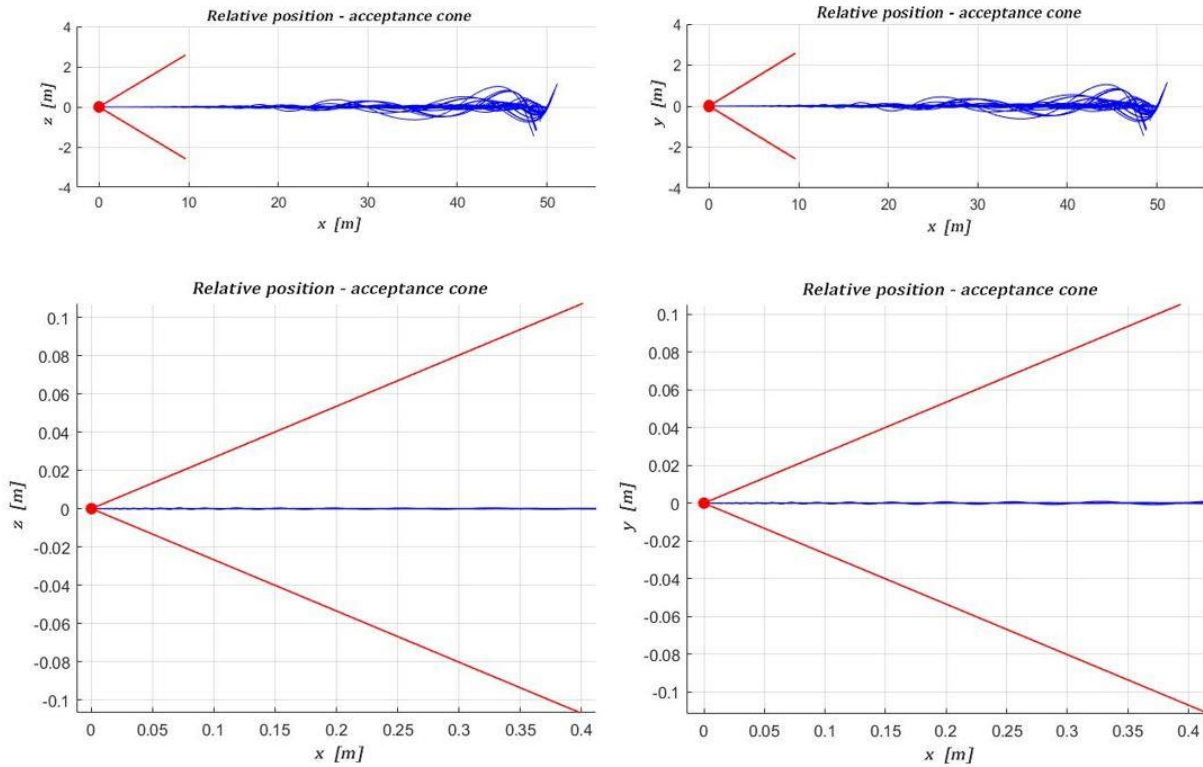


Figure 82: Relative position  $R\text{-bar}$  approach - Montecarlo 6

Success rate is equal to 100% also in this step, even though the uncertainties on initial position are much larger (Figure 82). Overshoots on relative position increase because of the more invasive disturbances but steady state conditions are always ensured after 250 seconds.

Oscillations on relative position along z and y axes have a higher values in frequency and amplitude until the chaser gets at 10 meters distance from the target. Perturbations on relative position are bounded by the quantity of 1.5 meters and the acceptance cone constraint satisfaction is always guaranteed even in this situation.

Figure 83 shows that the trend of increasingly clustered time responses is confirmed, as regards control inputs, effective thrust and relative velocity. Their values are brought to saturation for a longer time, in this step; additionally they remain perturbed for a slightly longer time than before. However there is no change in peak values, thus the upper and lower bounds remain the

same as in the previous setup, apart from relative velocity, whose upper bound slightly exceeds 0.2 m/s.

Nothing changes in terms of attitude, overshoot are related only to the very beginning of the sequence and do not constitute a critical factor for the sake of the success of simulations.

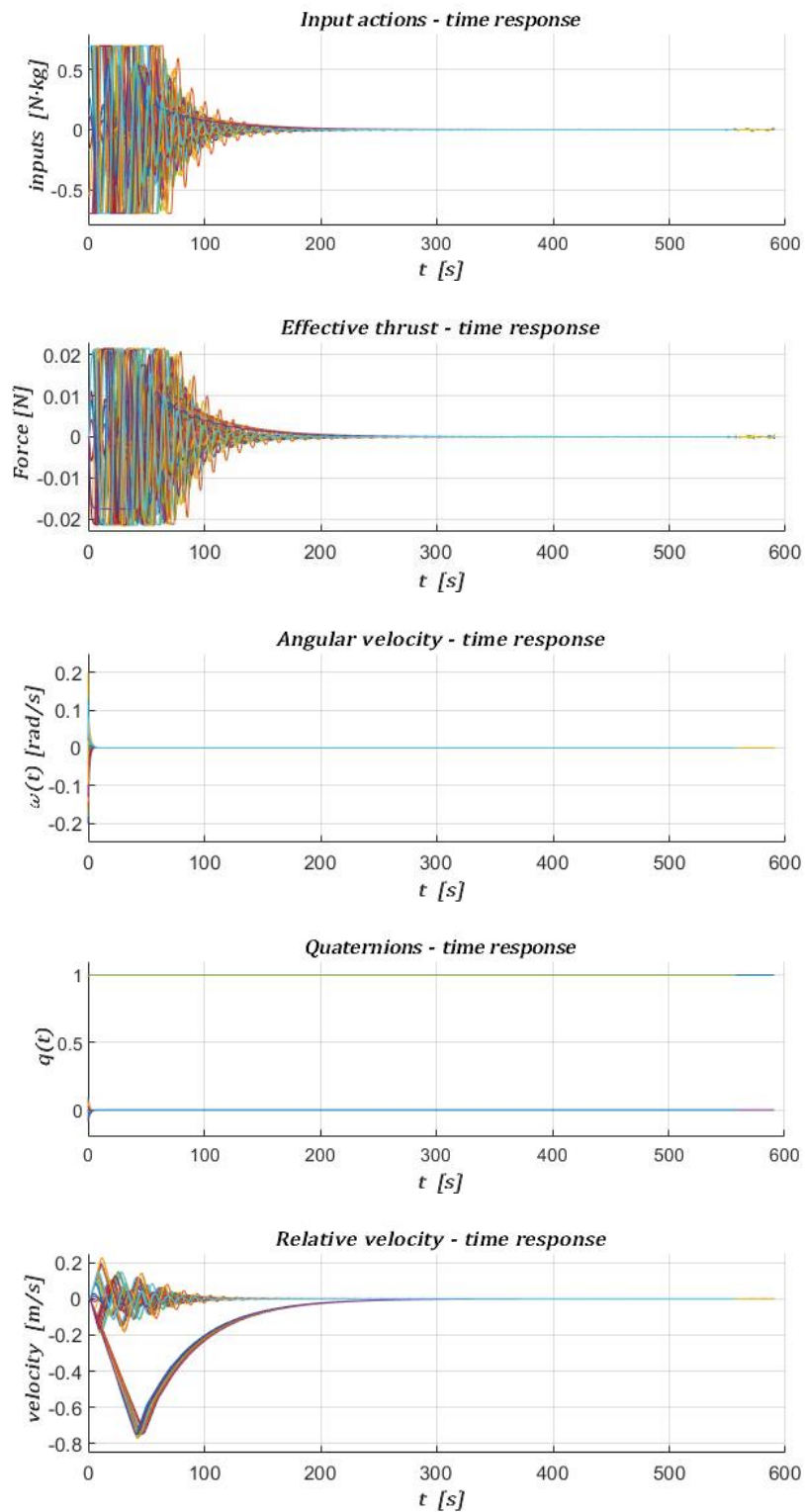


Figure 83: Time response plots in R-bar approach - Montecarlo 6

### 3.1.2.7 Step 7

- a) random disturbance of amplitude  $7 \cdot 2.5 \cdot 10^{-1} \text{ m}$  on relative position (all three axes);
- b) random disturbance of amplitude  $2 \text{ kg}$  on the mass;
- c) random disturbance of amplitude  $10^\circ$  on all three attitude angles;
- d) random disturbance of amplitude  $0.2 \text{ rad/s}$  on angular velocity (all three axes).

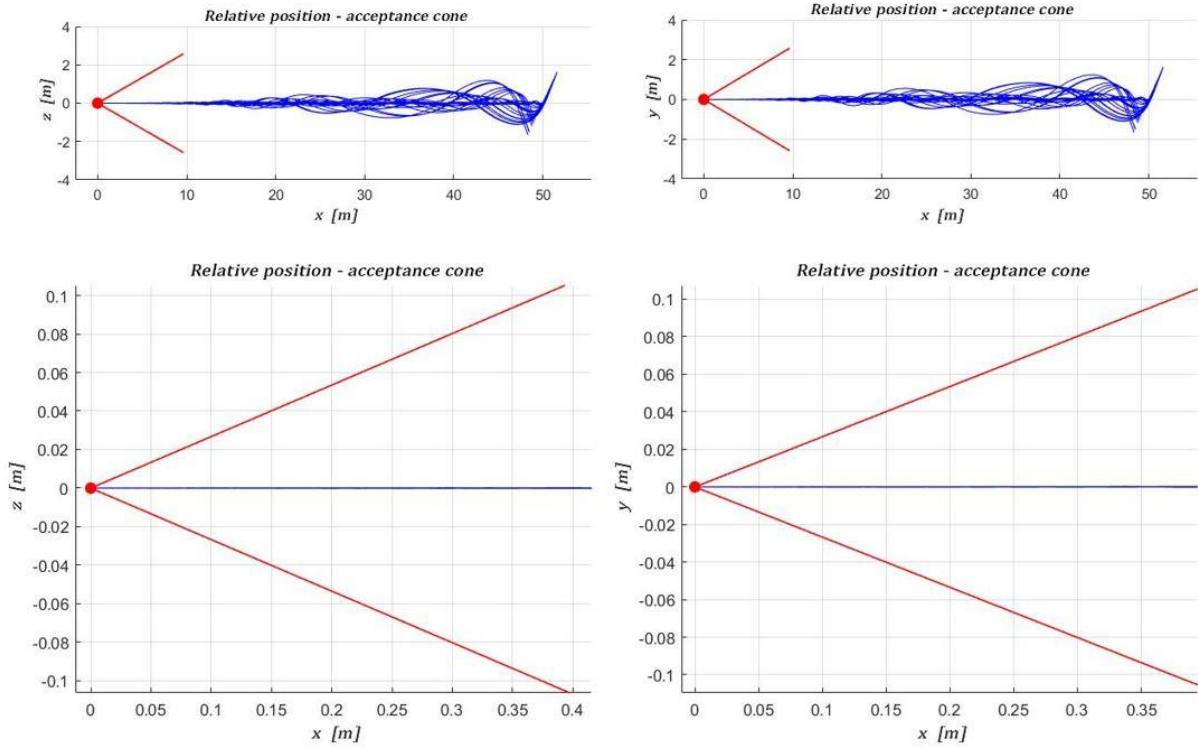


Figure 84: Relative position  $R\text{-bar}$  approach - Montecarlo 7

Success rate is equal to 100%. In this step, due to the higher uncertainties, it is possible to see that in only one case there is a small residual transient until 250 seconds of simulation in input and effective thrust time responses.

Amplitude and frequency of perturbations in terms of trajectory (*Figure 84*) slightly increase but never affect the success of the manoeuvre, which is completed without difficulties. In fact, once inside the acceptance cone, the trajectory is a straight line remaining onto reference values.

Furthermore, no variation is found in attitude with respect to previous steps, as both quaternions and angular velocity are always subject to the same set of uncertainties. Oscillations increase in linear actuation and velocity, as they need to compensate the higher amount of uncertainties on initial position. In this case the characteristic of the input time response, and thus of effective thrust, remain fixed to saturation values almost until 80 seconds of simulation. Relative velocity slightly exceeds the upper bound of  $0.2 \text{ m/s}$  in the first meters of the manoeuvre, but remains within the lower bound of  $-0.8 \text{ m/s}$ .

As in the steps analysed in the previous sections, time responses related to linear motion appear to be more disturbed but, in the long run, able to get to steady state values anyway, thus ensuring the success of the manoeuvre.

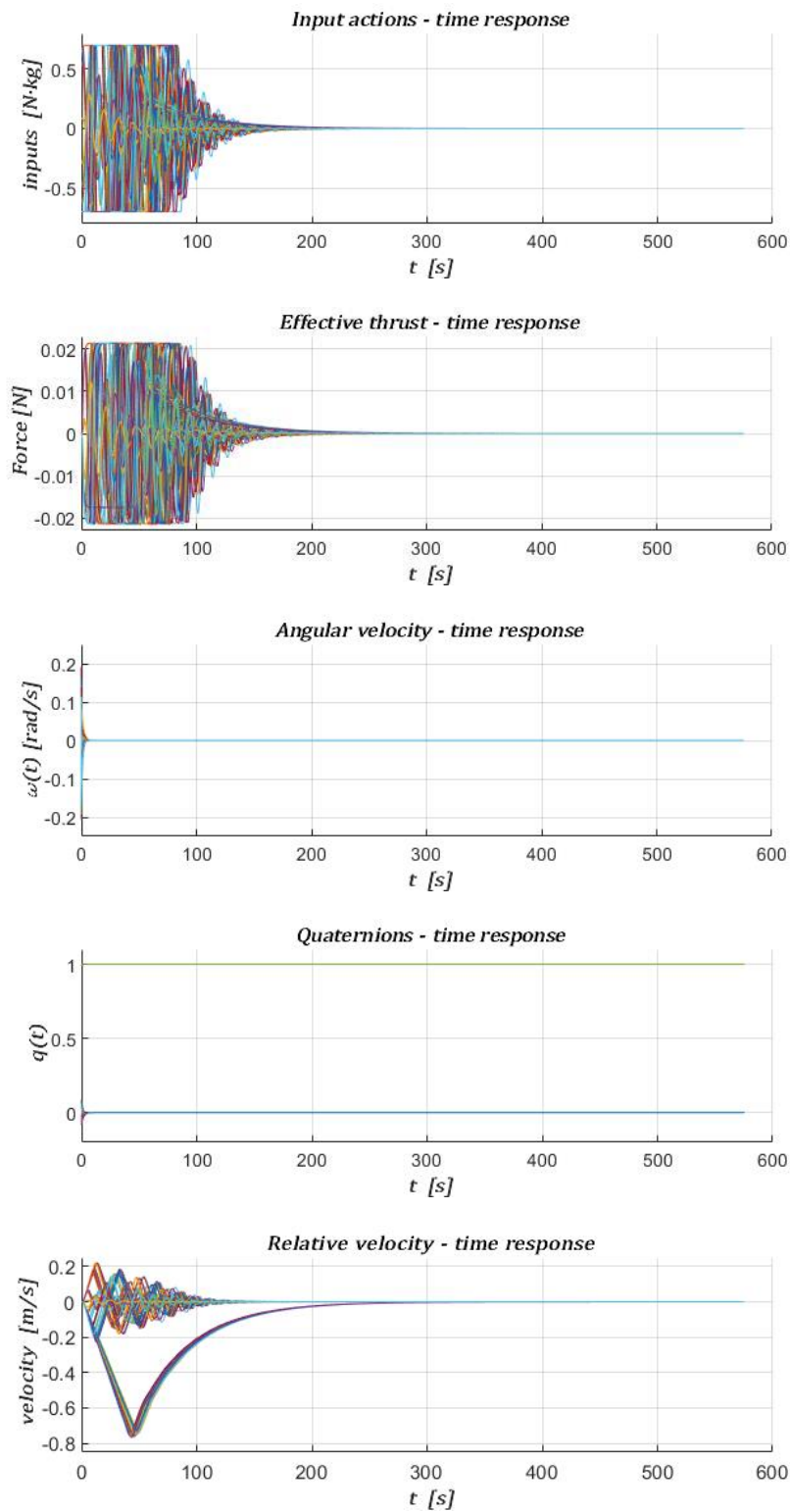


Figure 85: Time response plots in R-bar approach - Montecarlo 7

### 3.1.2.8 Step 8

- a) random disturbance of amplitude  $8 \cdot 2.5 \cdot 10^{-1} \text{ m}$  on relative position (all three axes);
- b) random disturbance of amplitude  $2 \text{ kg}$  on the mass;
- c) random disturbance of amplitude  $10^\circ$  on all three attitude angles;
- d) random disturbance of amplitude  $0.2 \text{ rad/s}$  on angular velocity (all three axes).

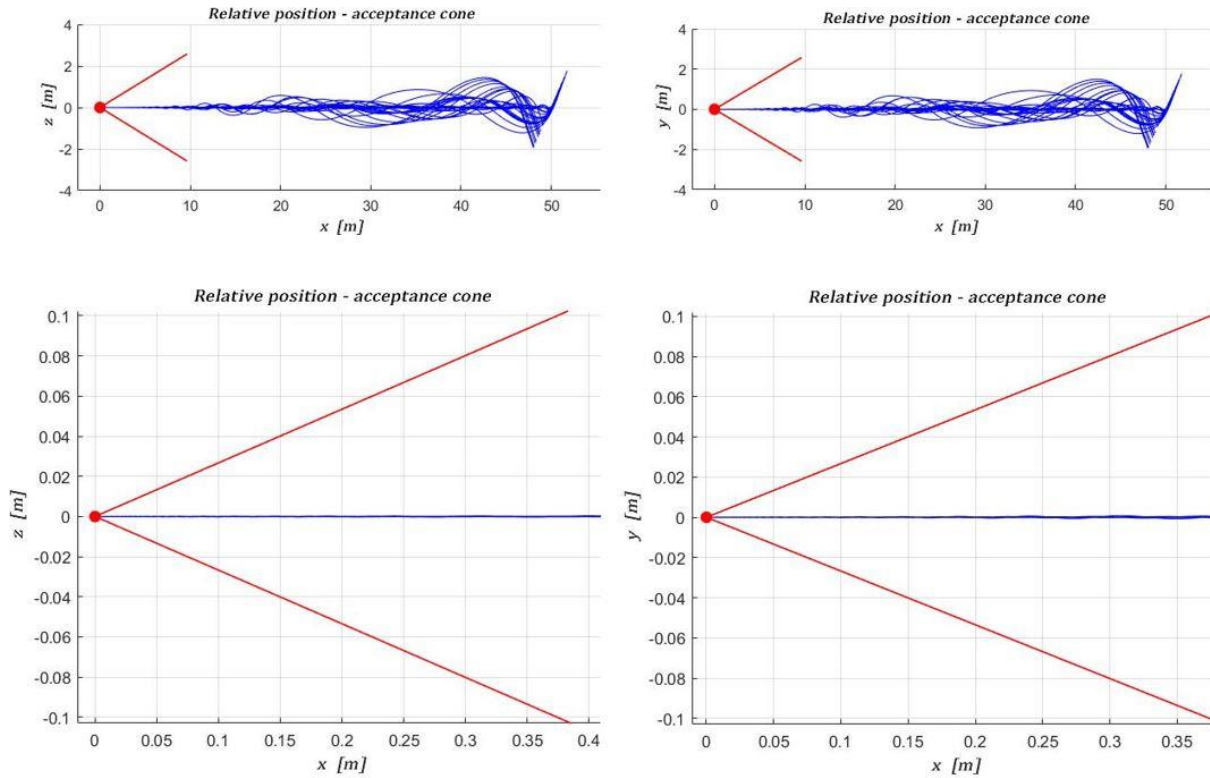


Figure 86: Relative position  $\bar{R}$  approach - Montecarlo 8

Success rate is equal to 100% and, as well as in the seventh step, residual transients extinguish after 300 seconds in this case, as much as concerns input, effective thrust and relative velocity time responses. Oscillations become even more critical, both on  $z$  and  $y$  axes, as much as concerns relative position, as they are visible, especially on  $y$  axis, also inside the acceptance cone, i.e. until the chaser gets at 5 meters distance from the arrival point. Upper and lower bounds of oscillation never get to reach the value of 2 meters and the acceptance cone constraint is always respected, once again, despite perturbations.

Saturation of values in input time response and, consequently, in effective thrust time response, is found even after 100 seconds of simulation, due to the higher control effort required to cancel the unexpected uncertainty.

Overshoots in attitude remain identical to the other steps, as neither uncertainties associated to quaternions and angular velocity change.

In terms of relative velocity time response, the upper bound of 0.2 m/s is abundantly overcome, this time and, in general the behaviour is more disturbed, concerning the second and the third elements of the velocity states vector (velocity along y and z axes). The negative peak gets closer to -0.8 m/s and it is related to velocity along x-axis.

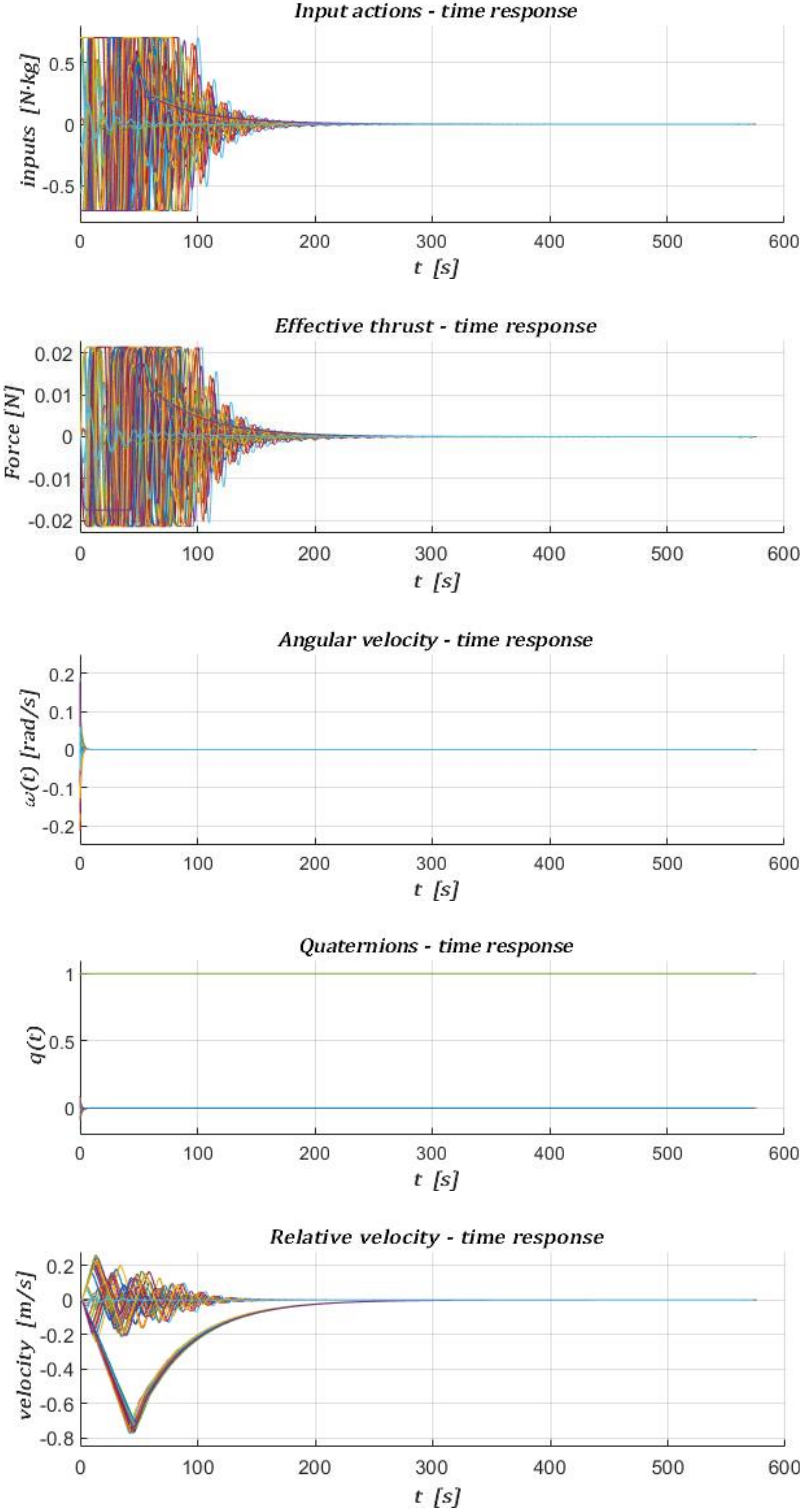


Figure 87: Time response plots in R-bar approach - Montecarlo 8

### 3.1.2.9 Step 9

- a) random disturbance of amplitude  $9 \cdot 2.5 \cdot 10^{-1} \text{ m}$  on relative position (all three axes);
- b) random disturbance of amplitude  $2 \text{ kg}$  on the mass;
- c) random disturbance of amplitude  $10^\circ$  on all three attitude angles;
- d) random disturbance of amplitude  $0.2 \text{ rad/s}$  on angular velocity (all three axes).

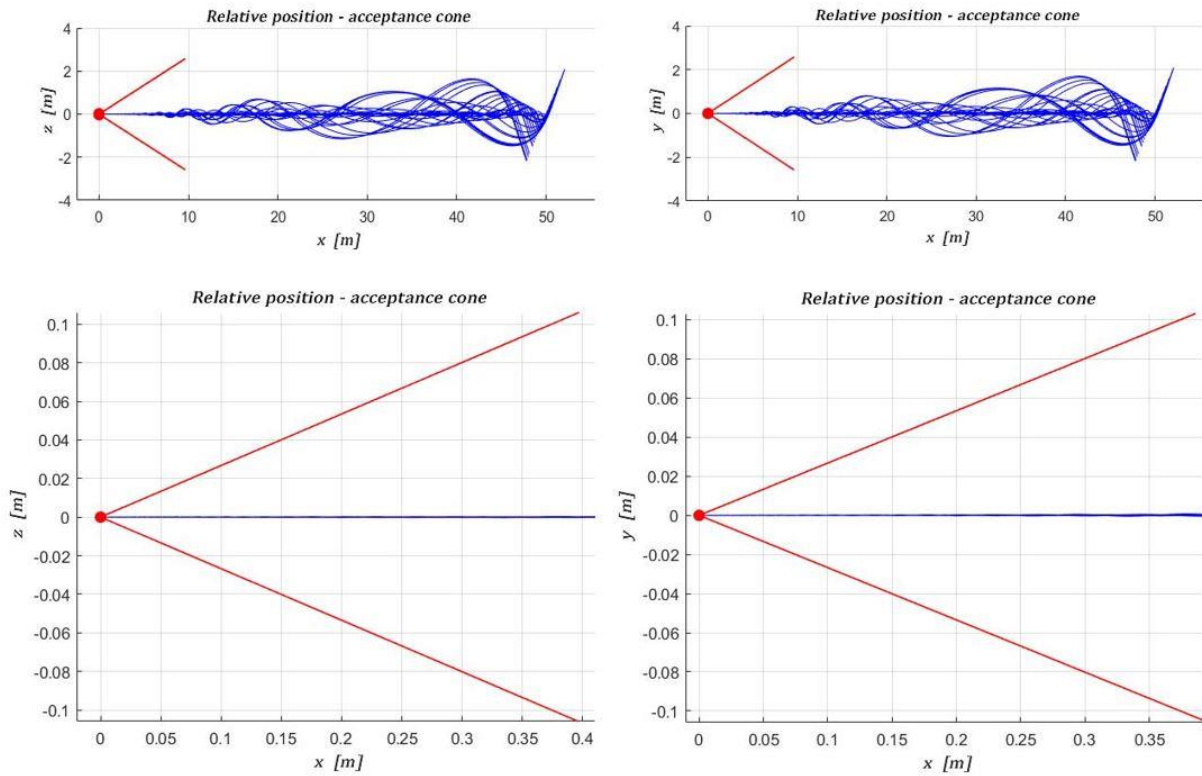


Figure 88: Relative position  $R\text{-bar}$  approach - Montecarlo 9

Even in this case the success rate is 100% and the same observations on residual transients made in the previous paragraph hold. Amplitude and frequency of oscillations in relative positions increase both on z and y axes. The perturbations are visible also inside the acceptance cone, until 4 meters distance from the arrival point (*Figure 88*). Despite that, from the point of view of acceptance cone constraint, the manoeuvre is successful.

Increasingly more clustered characteristics of time responses, in the starting phases of simulations, is confirmed even here. Saturated values of input actions and effective thrust are maintained until 120 seconds, showing a more severe condition to compensate, in terms of uncertainties.

Relative velocity time response does not differ much with respect to the one observed in the previous step, it only becomes a bit more perturbed.

As before, no changes in the attitude behaviour can be identified, as there is no further uncertainty added to the dynamics in this case with respect to the previous ones.

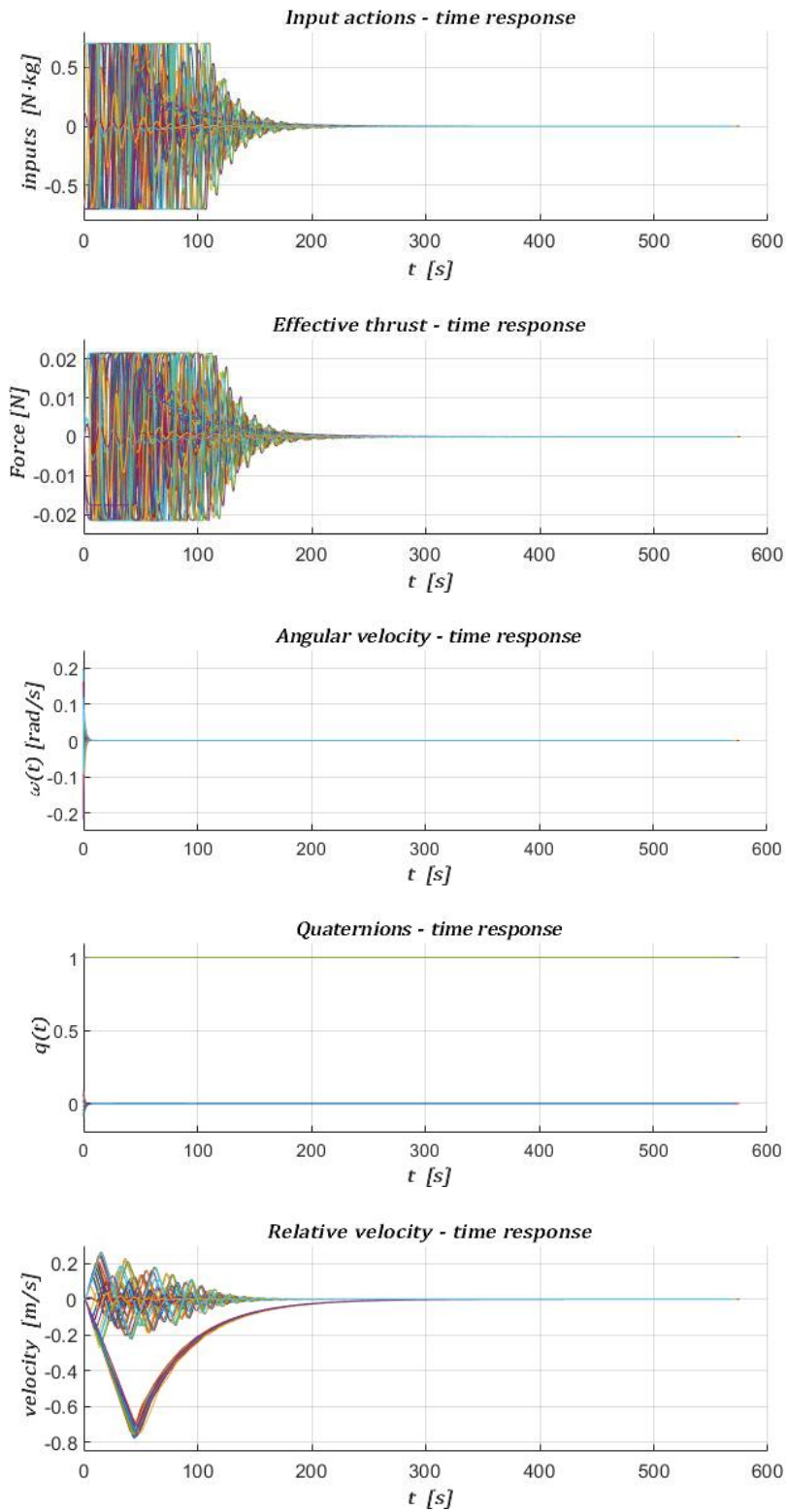


Figure 89: Time response plots in R-bar approach - Montecarlo 9

### 3.1.2.10 Step 10

- a) random disturbance of amplitude **2.5 m** on relative position (all three axes);
- b) random disturbance of amplitude **2 kg** on the mass;
- c) random disturbance of amplitude **10°** on all three attitude angles;
- d) random disturbance of amplitude **0.2 rad/s** on angular velocity (all three axes).

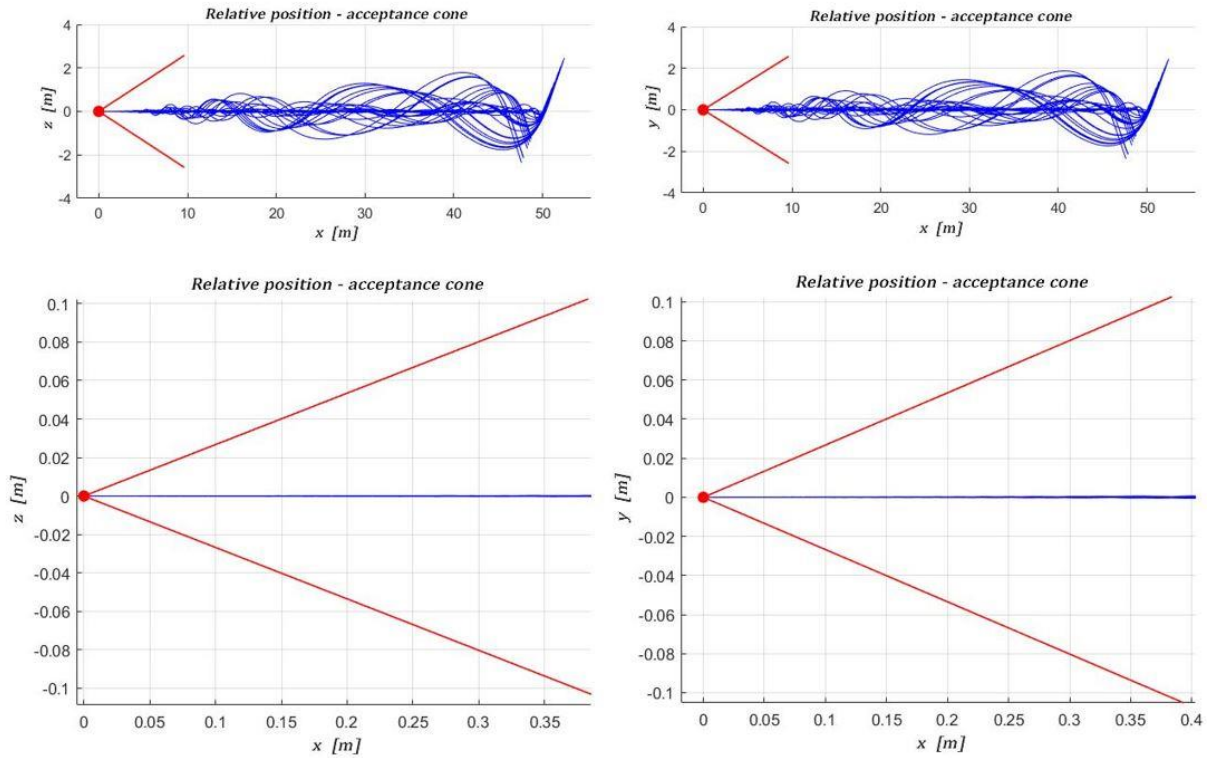


Figure 90: Relative position  $\bar{R}$  approach - Montecarlo 10

The success rate results to be 100%. In this case residual transients do not overcome 260 seconds of simulation and from that instant to the end of each sequence, steady state values are ensured for each time response.

In this case it is possible to see that input values are stuck to saturation levels for 160 seconds straight, showing that linear actuation is particularly affected by the imposed uncertainties: the propulsion system's availability must be fully exploited to correct the trajectory and reach reference values.

There is no significant change in quaternion and angular velocity time response, as the behaviour is identical to the one observed in the previous cases.

Relative velocity time response appears more disturbed as much as concerns each element of the states vector. Additionally, the upper bound of 0.2 m/s is exceeded by relative velocity in the first part of the simulation, while the lower bound of -0.8 m/s is not overcome.

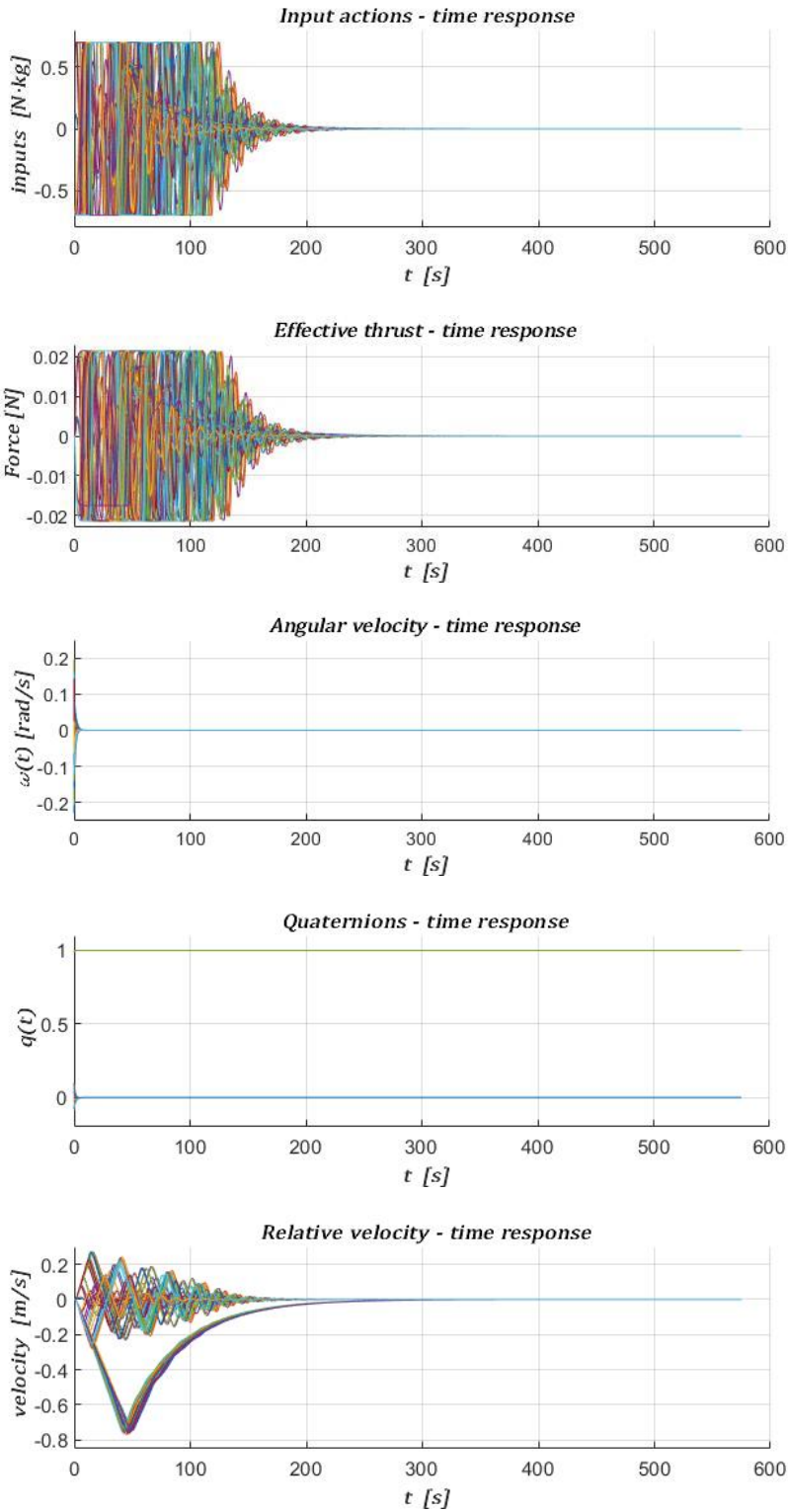


Figure 91: Time response plots in R-bar approach - Montecarlo 10

### 3.2 Controller refinement

From the above-discussed Montecarlo simulations, it is clear how the system can be considered robust to even invasive uncertainties. Although there is still room for improvement, from the control performance point of view. The aim of this section is to describe the employed strategy to avoid excessive oscillations and overshoots outlined in the worst case scenario's simulations, concerning relative position (*Figure 70* and *Figure 90*). Even though the only constraint imposed on MPC settings, in the previous setup, is the one on the acceptance cone, always respected, a higher attention must be paid to the starting phases of the manoeuvre. In the worst case scenarios (from the point of view of uncertainties) the upper and lower bounds of relative position even exceed 2 meters. At a distance from the target spanning from 50 to 10 meters, both frequency and amplitude of oscillations is not negligible. From a pure control system perspective, the behaviour of the system is optimal but, if considering the manoeuvre with a real-life problem approach, this behaviour can be source of many problems. These many oscillations can cause a huge number of errors from the point of view of navigation: this is why, ideally, a straight line trajectory is always preferred.

Due to this inconvenience, a refinement of the trajectory control strategy is necessary, at this point. This very same refinement consists of choosing to employ two different MPC controllers, one acting from 50 to 15 meters distance from the target (MPC 1), while the other one is used for the final phases of the manoeuvre, from 15 meters to docking (MPC 2).

Parameter	Chosen value
$T_s$	0.1 s
$T_p$	0.1 s
$Q$	$\begin{bmatrix} 500 & 0 & 0 & 0 & 0 & 0 \\ 0 & 500 & 0 & 0 & 0 & 0 \\ 0 & 0 & 20 & 0 & 0 & 0 \\ 0 & 0 & 0 & 100 & 0 & 0 \\ 0 & 0 & 0 & 0 & 100 & 0 \\ 0 & 0 & 0 & 0 & 0 & 20 \end{bmatrix}$
$P$	$\begin{bmatrix} 0 & 0 & 0 & 0 & 0 & 0 \\ 0 & 0 & 0 & 0 & 0 & 0 \\ 0 & 0 & 10 & 0 & 0 & 0 \\ 0 & 0 & 0 & 10 & 0 & 0 \\ 0 & 0 & 0 & 0 & 10 & 0 \\ 0 & 0 & 0 & 0 & 0 & 100 \end{bmatrix}$

$R$	$\begin{bmatrix} 10^{-50} & 0 & 0 \\ 0 & 10^{-50} & 0 \\ 0 & 0 & 10^{-50} \end{bmatrix}$
$u_{min}$	$[-0.7 \quad -0.7 \quad -0.7]$
$u_{max}$	$[0.7 \quad 0.7 \quad 0.7]$

Table 10: MPC 1 settings

Parameter	Chosen value
$T_s$	0.1 s
$T_p$	0.2 s
$Q$	$\begin{bmatrix} 500 & 0 & 0 & 0 & 0 & 0 \\ 0 & 500 & 0 & 0 & 0 & 0 \\ 0 & 0 & 20 & 0 & 0 & 0 \\ 0 & 0 & 0 & 100 & 0 & 0 \\ 0 & 0 & 0 & 0 & 100 & 0 \\ 0 & 0 & 0 & 0 & 0 & 100 \end{bmatrix}$
$P$	$\begin{bmatrix} 0 & 0 & 0 & 0 & 0 & 0 \\ 0 & 0 & 0 & 0 & 0 & 0 \\ 0 & 0 & 10 & 0 & 0 & 0 \\ 0 & 0 & 0 & 10 & 0 & 0 \\ 0 & 0 & 0 & 0 & 10 & 0 \\ 0 & 0 & 0 & 0 & 0 & 100 \end{bmatrix}$
$R$	$\begin{bmatrix} 10^{-50} & 0 & 0 \\ 0 & 10^{-50} & 0 \\ 0 & 0 & 10^{-50} \end{bmatrix}$
$u_{min}$	$[-0.7 \quad -0.7 \quad -0.7]$
$u_{max}$	$[0.7 \quad 0.7 \quad 0.7]$

Table 11: MPC 2 settings

The main differences between the two controllers is related only to two elements, how it is possible to see from *Table 10* and *11*: prediction horizon and sixth diagonal parameters of the  $Q$  matrix. MPC 2 is identical to the one employed in the previous simulations, as it always resulted more than effective in the final phase of the manoeuvre. However, for MPC 1, the choice of a smaller prediction horizon and a sensitively smaller weight on the velocity with respect to the approach axis results optimal. The main consequence of a smaller prediction horizon is a slower

response of the system, but also the absence of overshoots and undesired behaviours. In this case, in particular, the prediction horizon is equal to the sampling time, thus the predictive capability of the MPC is reduced to minimum. In spite of this, the results are absolutely satisfying. The weight on velocity is lowered to 20 in order to force the relative positions to get faster to reference values, and to avoid a too long transient and too invasive oscillations.

After applying these changes to the control strategy, the simulation setup is chosen: the worst case scenario is imposed in terms of uncertainties on initial conditions, by applying

- a)** +2.5 m on relative position (all three axes);
- b)** +2 kg on the mass;
- c)** +10° on all three attitude angles;
- d)** +0.2 rad/s on angular velocity (all three axes).

Simulations are performed both for V-bar and R-bar approach, outlining the very same results in both cases. In *Figures* from 92 to 96 and from 99 to 103 it is clear how the system behaves in the expected way as much as concerns relative position: there are no overshoots in the initial phase of the manoeuvre, the parameters converge to reference values after less than 5 meters along the approach axis. Acceptance cone constraint is respected in both cases and, additionally, there is no need to introduce a further hold point in the manoeuvre, in correspondence of the change between MPC 1 and MPC 2 which results smooth and homogeneous. In *Figures* 97, 98, 104, 105 input and velocity time responses are described in order to outline that there are no significant changes in terms of control efforts and speed of the chaser with respect to the previous simulations.

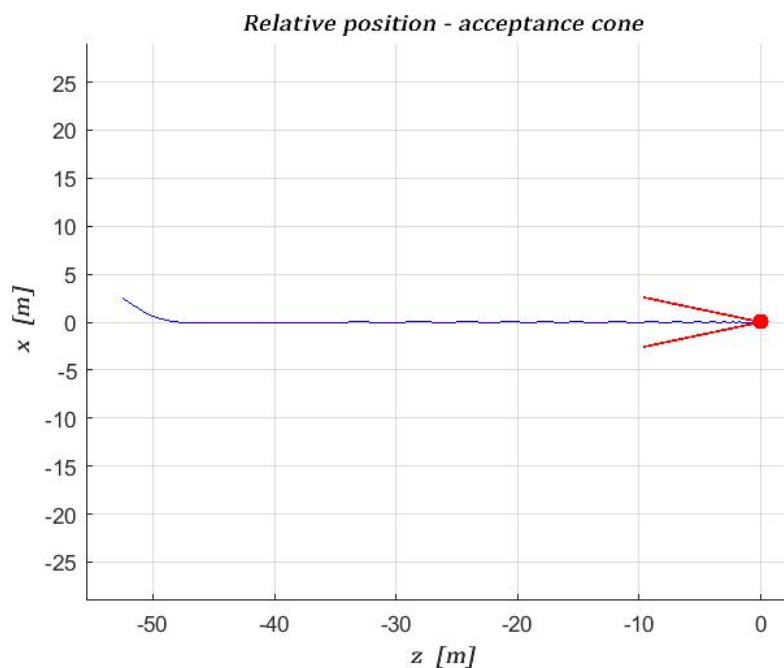


Figure 92: zx relative position - worst case scenario

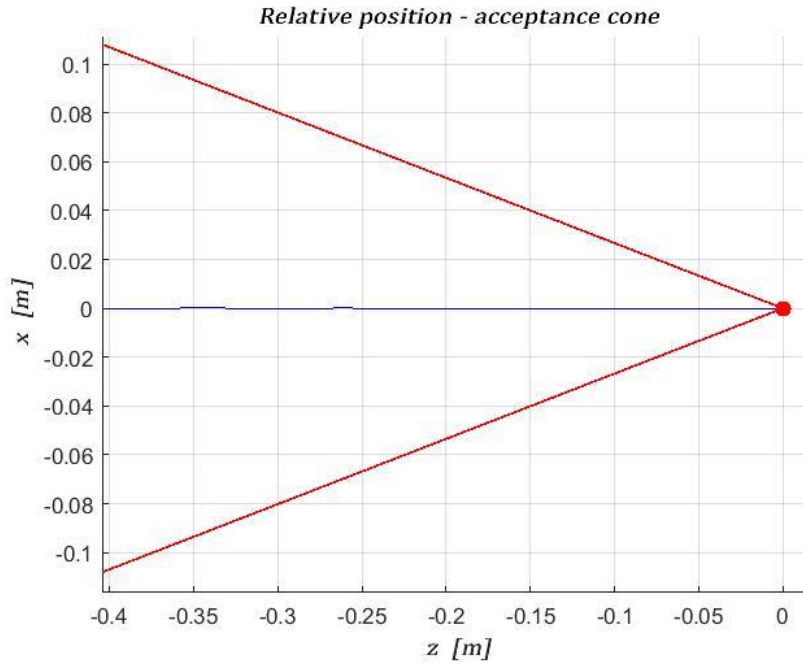


Figure 93: zx relative position (detail) - worst case scenario

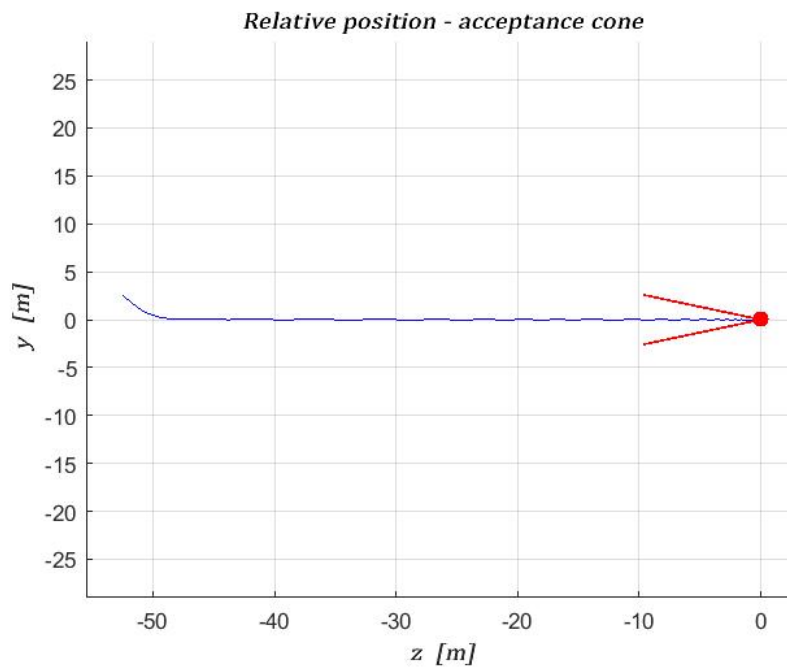


Figure 94: zy relative position - worst case scenario

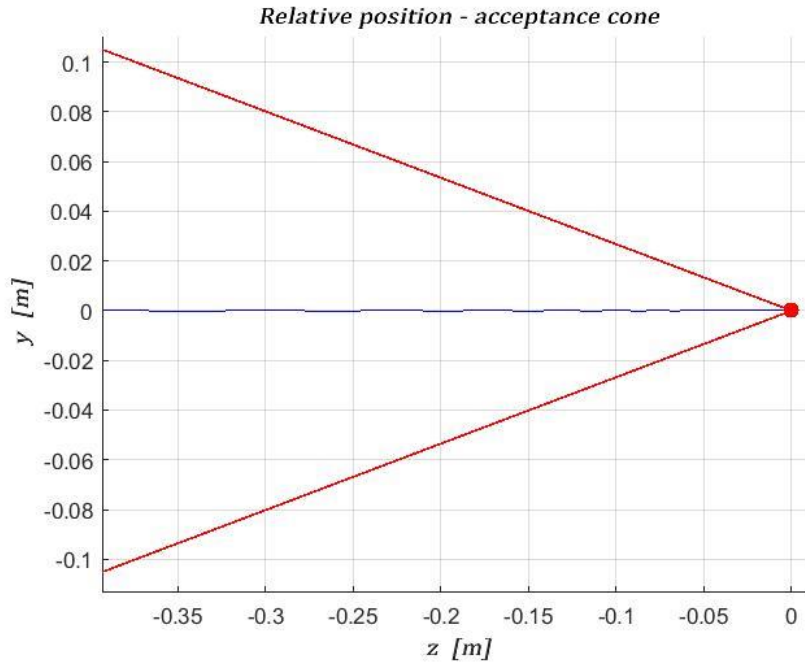


Figure 95: zy relative position (detail) - worst case scenario

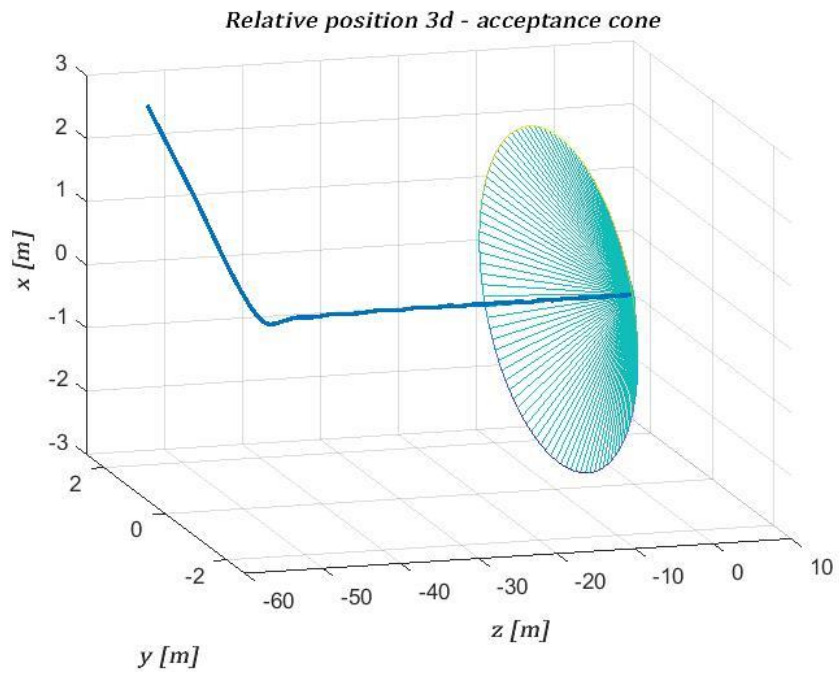


Figure 96: relative position 3d and acceptance cone on  $V_{\bar{}}$  - worst case scenario

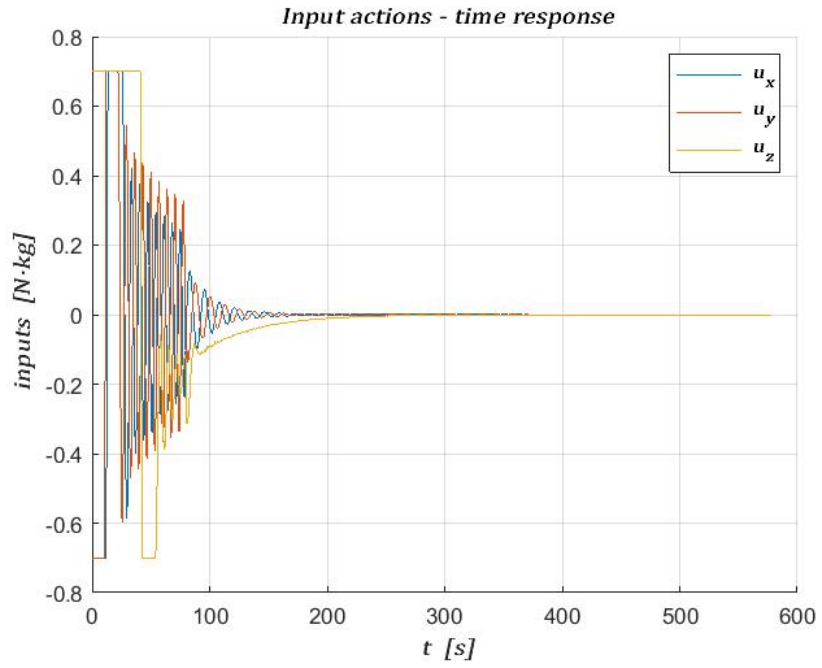


Figure 97: input time response on  $V_{bar}$  - worst case scenario

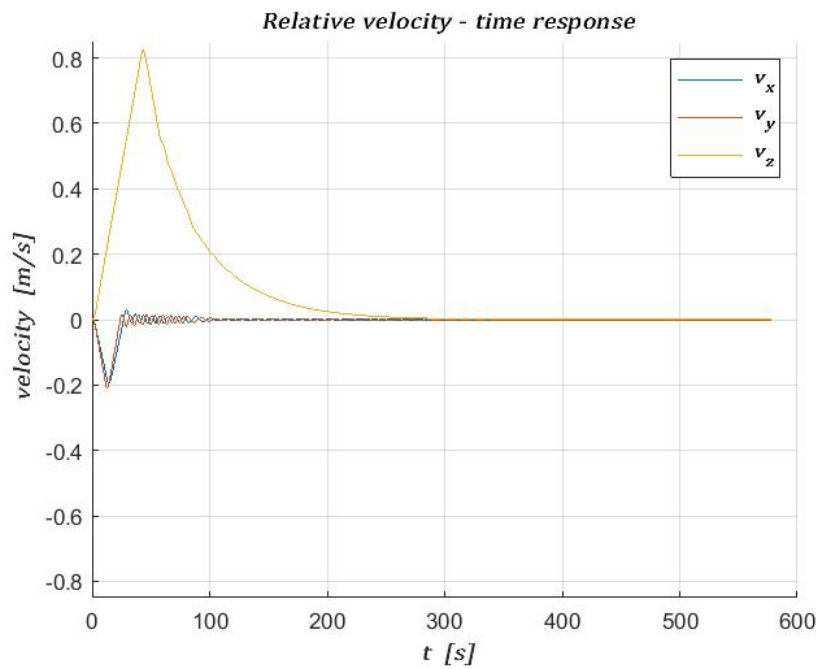


Figure 98: relative velocity time response on  $V_{bar}$  - worst case scenario

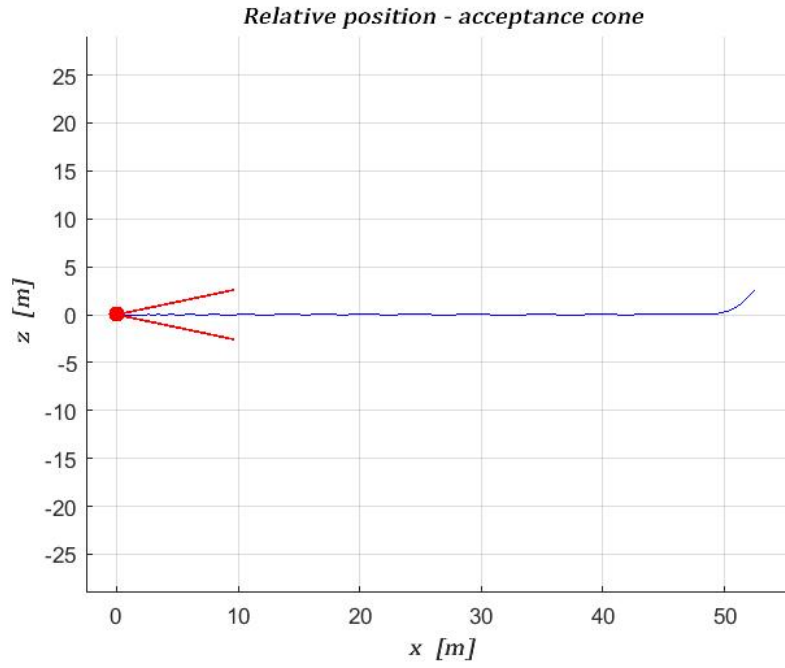


Figure 99: xz relative position - worst case scenario

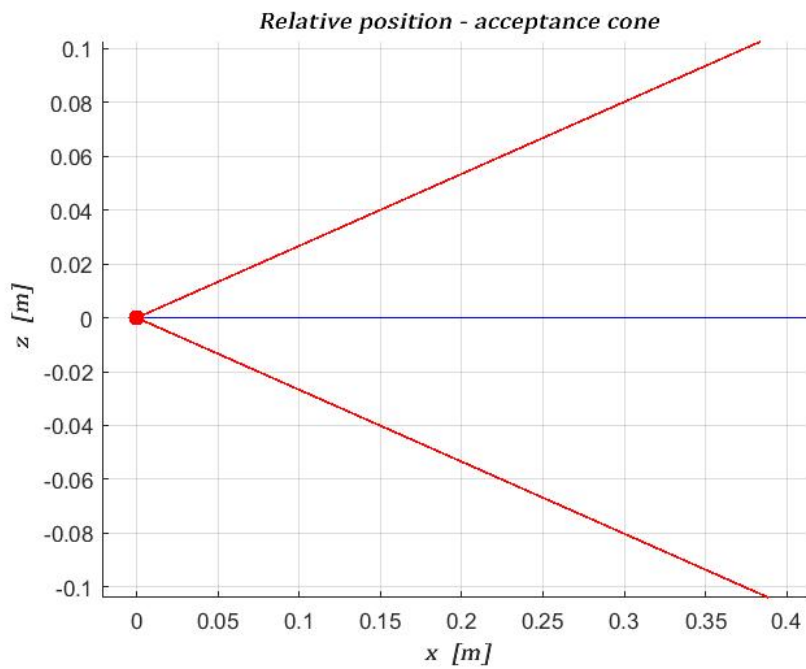


Figure 100: xz relative position (detail) - worst case scenario

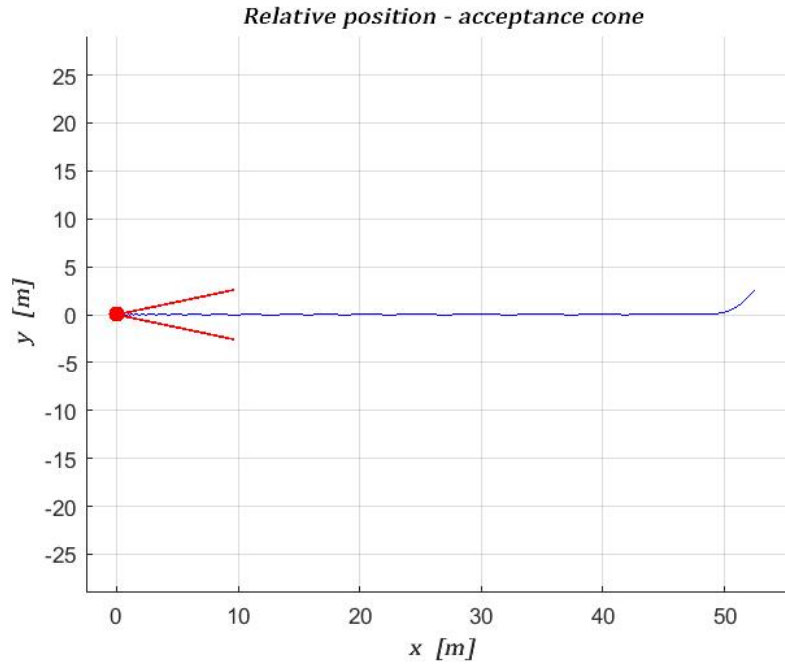


Figure 101: xy relative position - worst case scenario

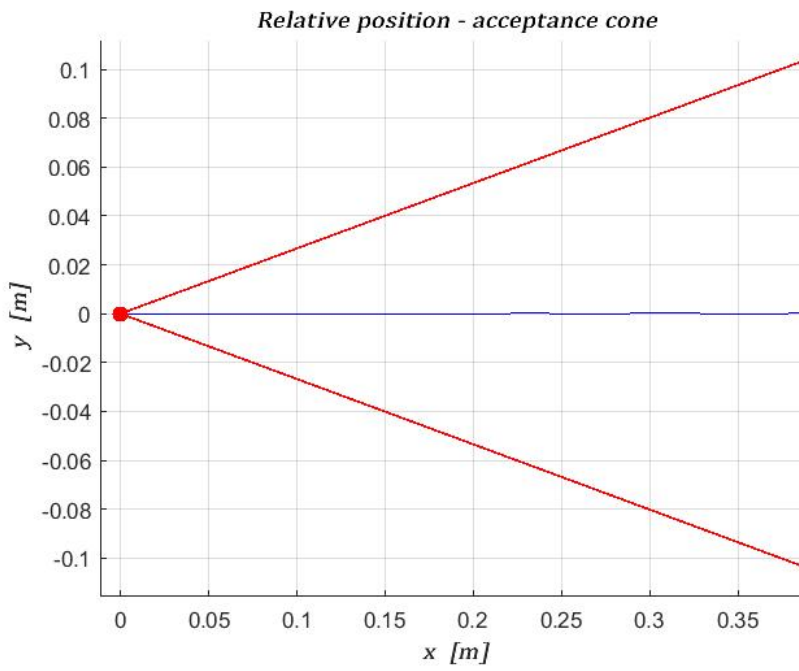


Figure 102: xy relative position (detail) - worst case scenario

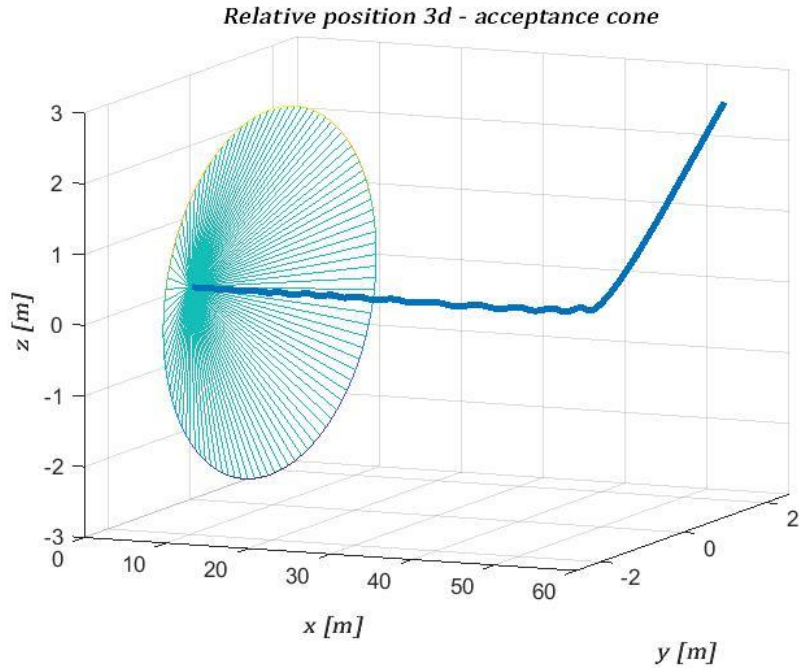


Figure 103: relative position 3d and acceptance cone on  $R_{bar}$  - worst case scenario

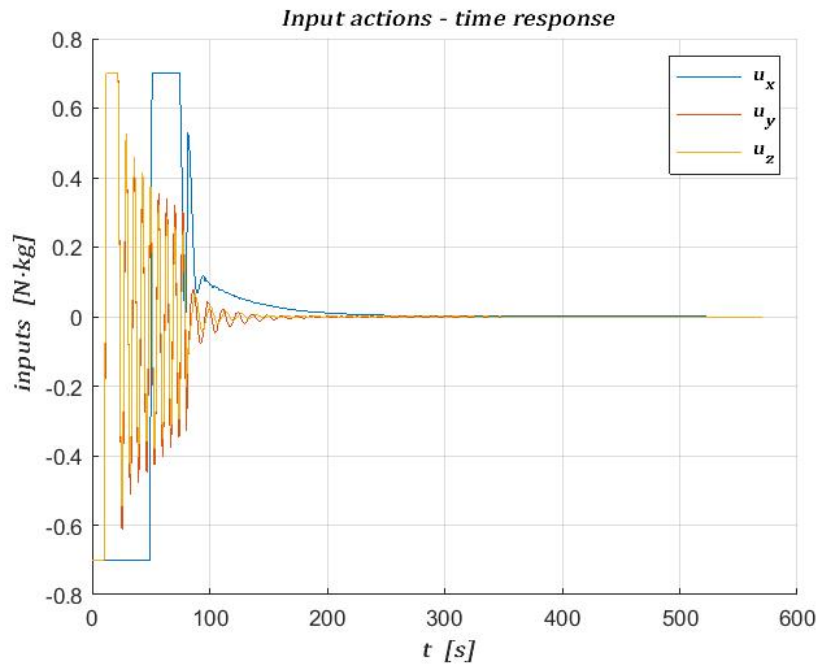


Figure 104: input time response on  $R_{bar}$  - worst case scenario

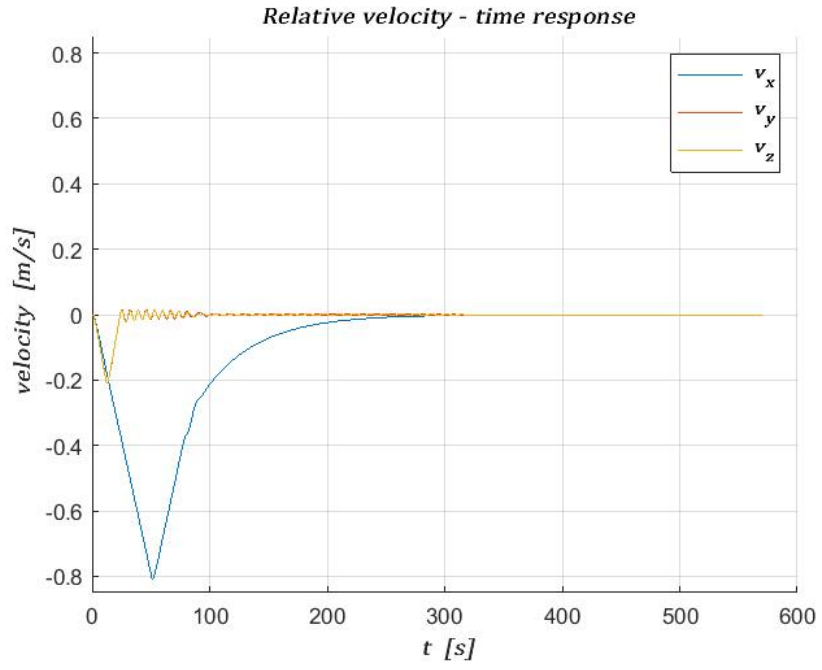


Figure 105: relative velocity time response on  $R_{bar}$  - worst case scenario

## 4. *Off nominal conditions*

In order to deepen the topic of safety, which is a crucial condition in such applications as space missions, a scenario of fault tolerance is investigated, as much as concerns the thrusters. In particular, random uncertainty with  $0.1^\circ$  amplitude is introduced in the inclination of each one of the eight nozzles involved in the propulsion system ( $\alpha$  and  $\beta$  angles introduced in 2.2.2.1). This is, in fact, a reasonable disturbance due to construction errors which can actually occur in a real-life scenario.

However, the most critical condition studied for the sake of this thesis is the breakdown of a thruster valve, in a single failure framework. The most common scenario consists of the total opening or total closing of a valve, along the whole studied manoeuvre. In the former case hence, one of the eight thrusters produces the maximum amount of thrust which is available per each nozzle. In the latter case, one of the eight nozzles is practically shut down and does not produce any force. Due to the peculiar disposition of the nozzles on the spacecraft (*Figure 30*), the failure on every different thruster causes different reactions on the whole manoeuvre, thus resulting in a not at all trivial problem. In this part, the above discussed scenario is described, by means of the results obtained from simulations performed in both V-bar and R-bar approach conditions. Each simulation is developed with one valve closed/open at a time, outlining a total of 16 different cases (referring to *Figure 30* for thrusters' identification, valve *a* closed, valve *a* open, valve *b* closed, valve *b* open, ..., valve *h* open). Only the plots which result effective for the sake of the discussion are reported in the following paragraphs: that is why angular velocity and quaternion time responses are not present. Even though these parameters are fundamental for the purpose of the manoeuvre and have always been outlined in the previous analysis, in this

part of the work no significant variations are encountered in them with respect to the nominal case, so they are excluded from further considerations.

## 4.1 Valve a closed

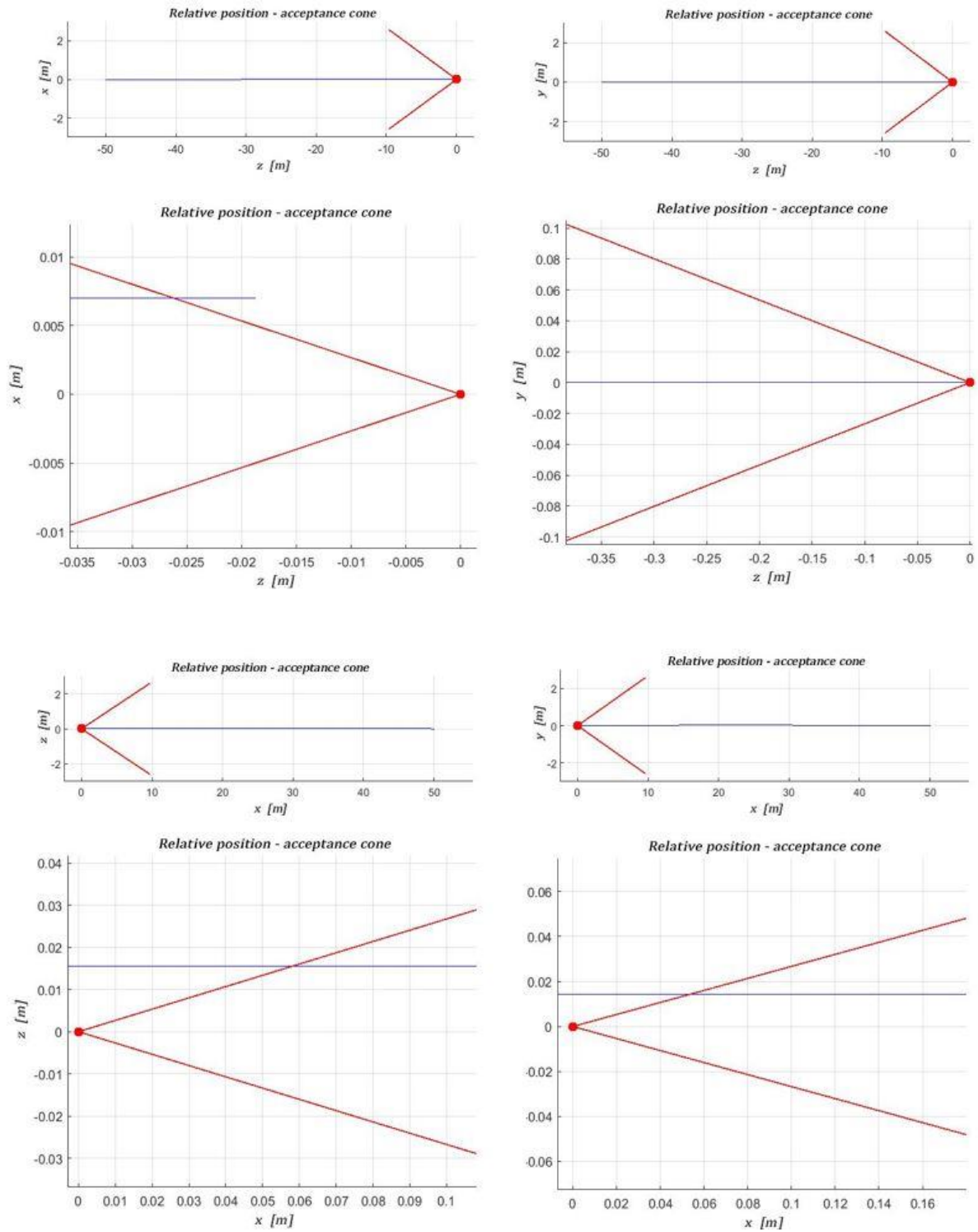


Figure 106: relative position - valve a closed

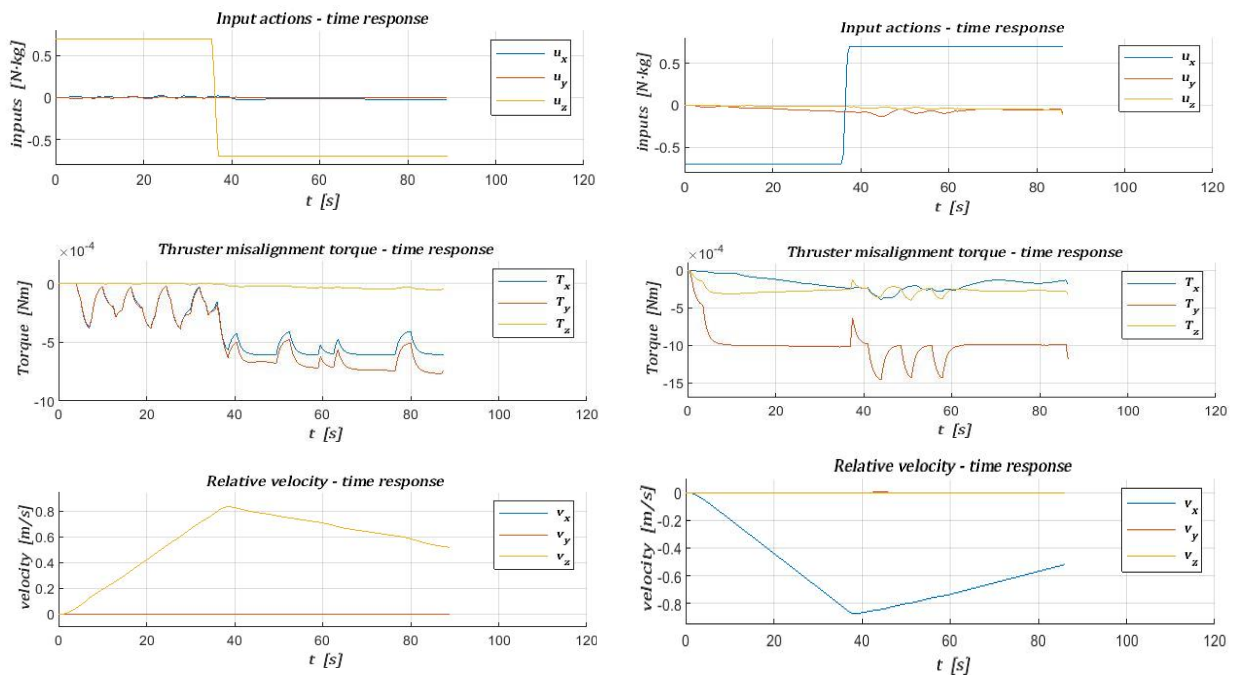


Figure 107: time responses - valve a closed

It is clear from Figure 106 (four upper plots related to V-bar approach, the four lower ones referred to R-bar) how, in this case, acceptance cone constraint is not satisfied, apart from the  $z_y$  relative position case. The manoeuvre, in this case, lasts less than 90 seconds, since the lack of actuation causes the inability to well balance the thrust, bringing thus the chaser to mating too soon. This results in a too high final velocity.

In Figure 107, representing time responses, it is possible to outline how, both in V-bar and R-bar (respectively on the left and on the right) approaches, input actions are included in the prescribed bound, although for the whole sequence they are brought to saturation values. Disturbance torque caused by thruster misalignment has a significant value, with respect to the nominal case (2.2.2.1), in both kinds of approach. Velocities along V-bar and R-bar have a comparable time response, similar to the nominal case but truncated right after the peak value of the overshoot.

## 4.2 Valve a open

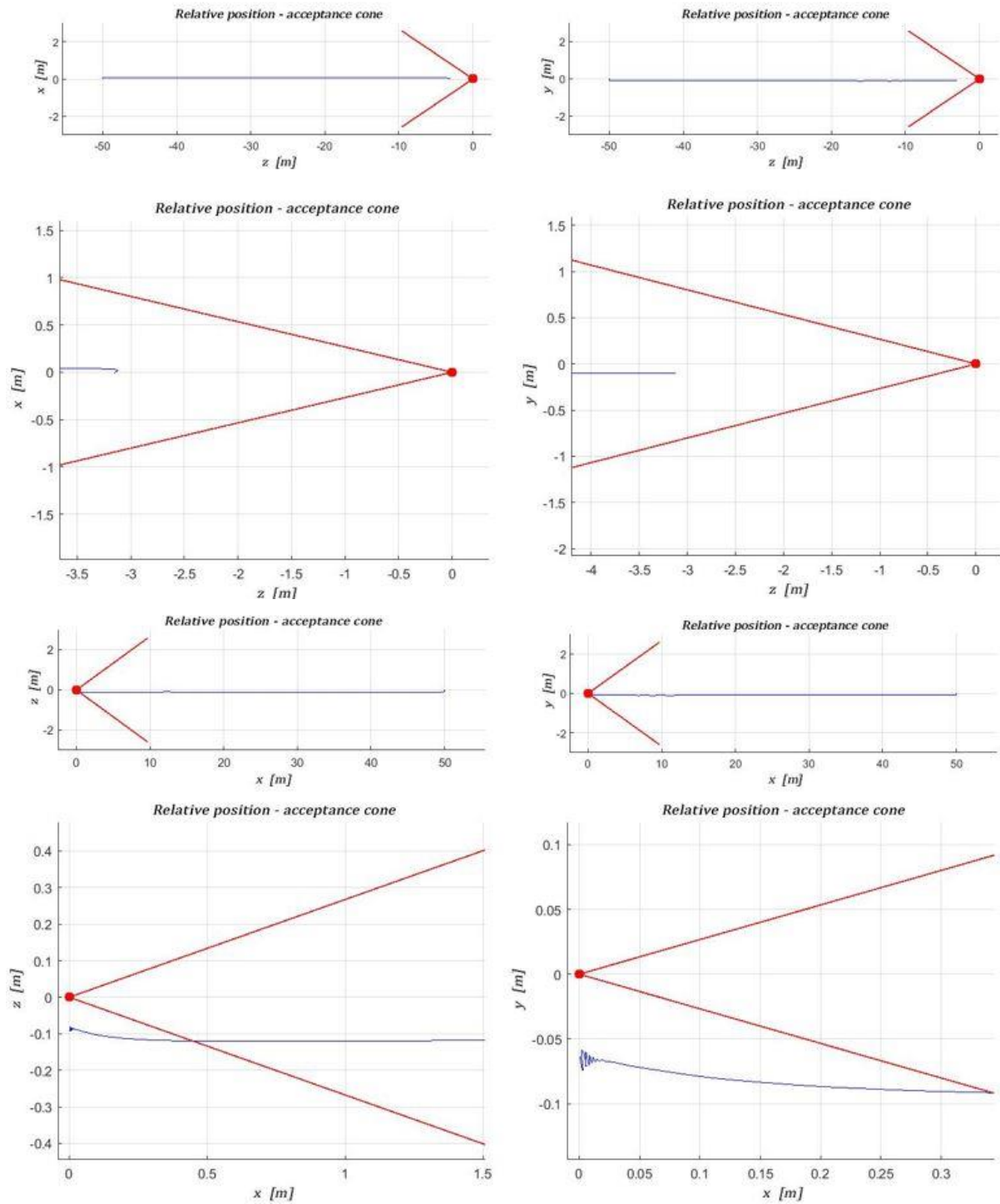


Figure 108: relative position - valve a open

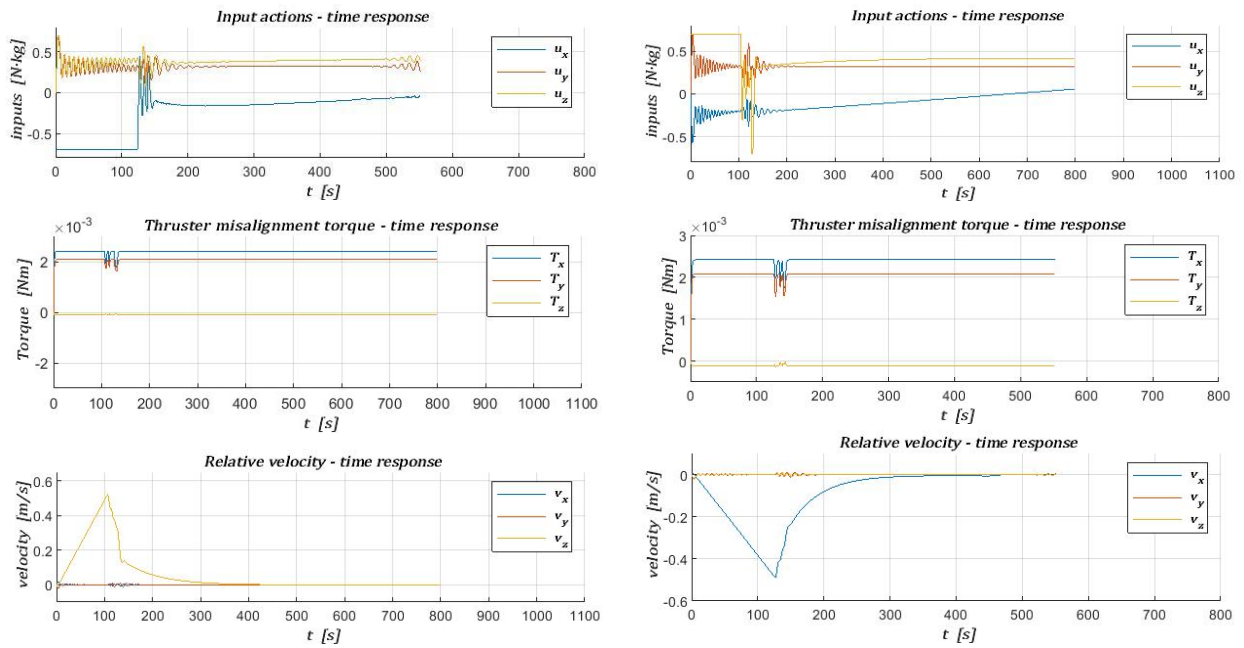


Figure 109: time responses - valve a open

In this case, as much as concerns V-bar approach, the chaser is not even able to complete the manoeuvre and never reaches the target (four upper plots in *Figure 108*), basically remaining fixed at the same point (approximately at 3 meters from the docking point) for most of the simulating sequence, because of the invasive disturbance introduced by the above-said failure.

As regards R-bar, it is clear from the four lower plots in *Figure 108* how the acceptance cone constraint is not satisfied even in this case.

Concerning time responses (*Figure 109*, left V-bar, right R-bar), input actions never exceed the prescribed bound values. The main difference in terms of input actions with respect to the nominal case is that the behaviour is not impulsive (i.e. peak value at the beginning of the sequence, then decreasing and converging to zero) but remains close to saturation values (at least for two elements of the input vector) for the whole simulation. This phenomenon is due to the attempt of the system to compensate the undesired action of the thruster caused by the failure and happens in both V-bar and R-bar cases.

Torque due to thruster misalignment is even higher than before, gaining an order of magnitude with respect to the “valve a closed” case. The overall velocity of the chaser decreases because of the conflict in the actuation system due to the said failure. This lower velocity causes the impossibility to conclude the manoeuvre, along V-bar, and the deviation from the docking point with violation of acceptance cone constraint, along R-bar.

### 4.3 Valve b closed

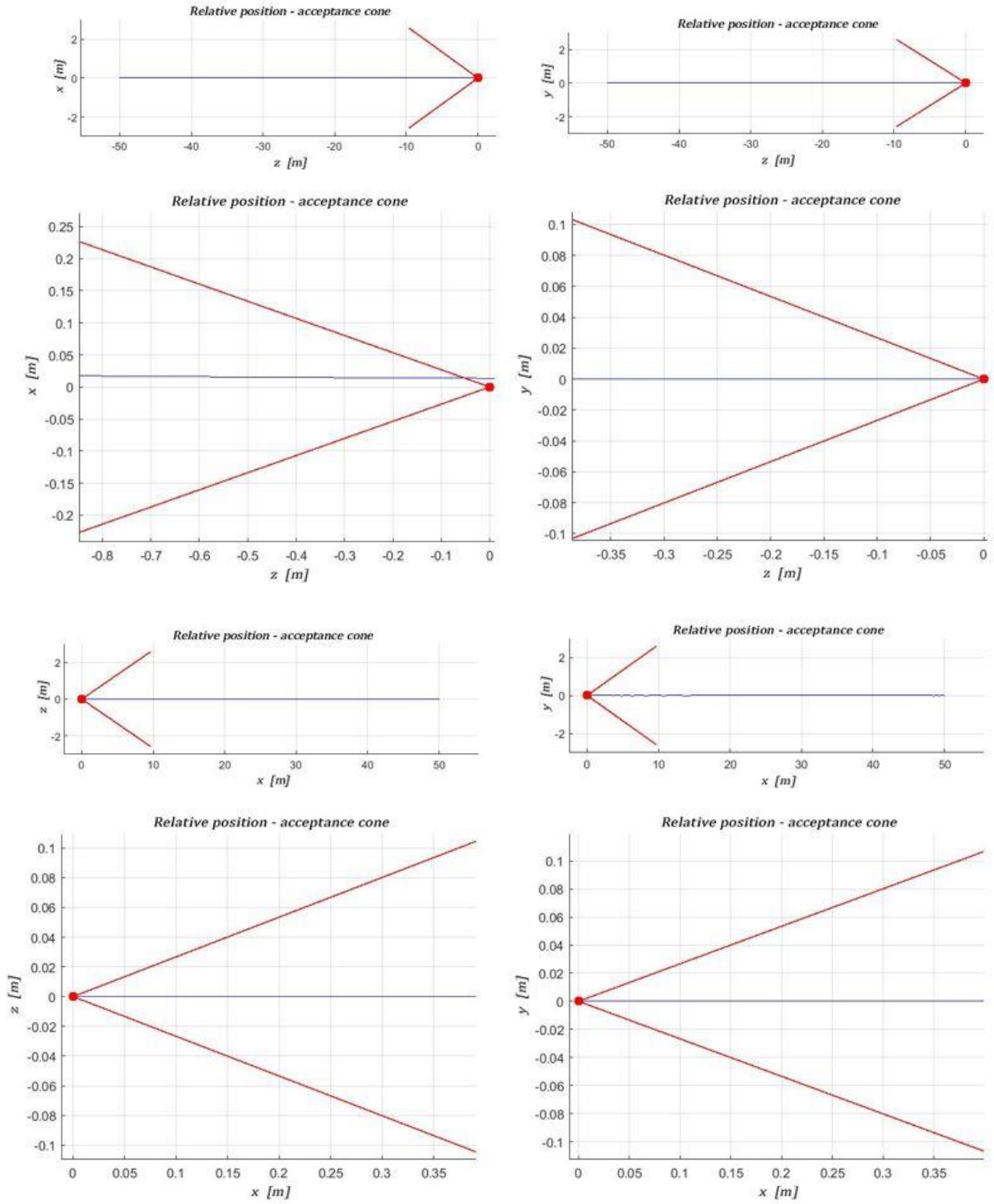


Figure 110: relative position - valve b closed

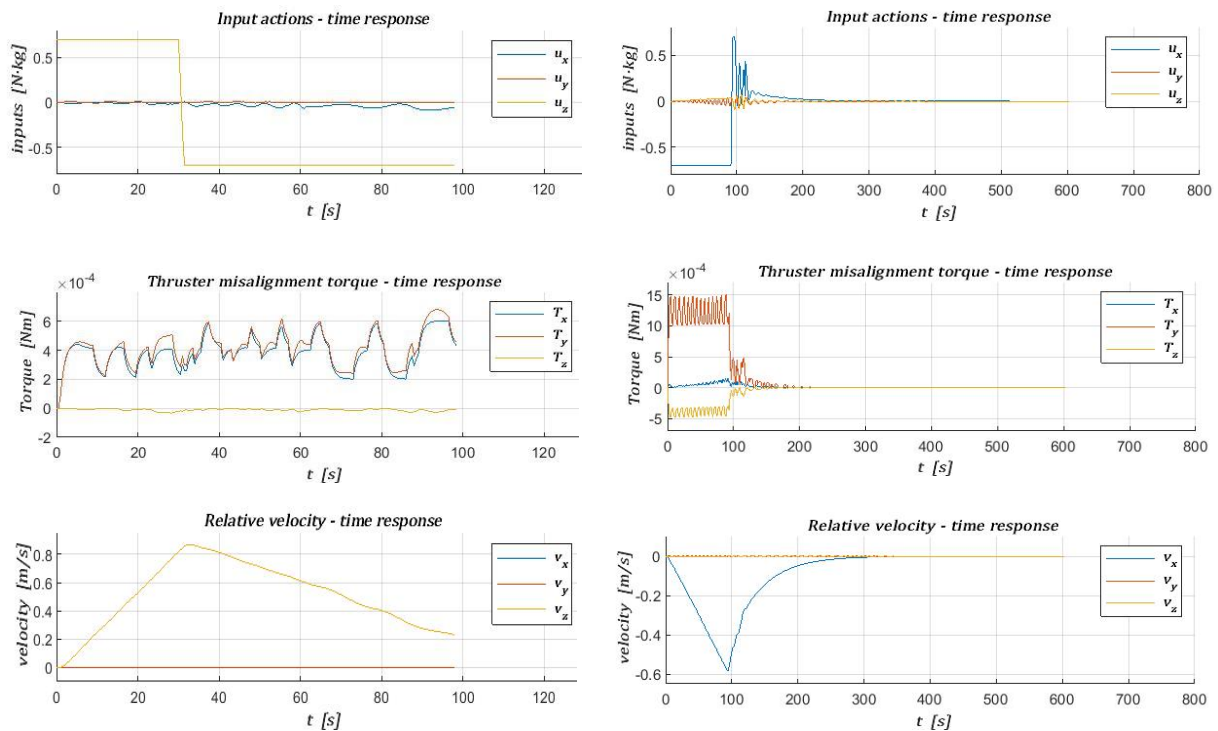


Figure 111: time responses - valve b closed

In Figure 110 it is possible to outline that the R-bar approach, in this case, is successful: acceptance cone constraint is satisfied and no particular anomalies emerge from the behaviour of the system. As regards V-bar approach, along the x-axis there is an error on the final position of the chaser equal to 2 cm at approximately 5 cm distance from the arrival point, thus the acceptance cone constraint is not satisfied.

It is possible to see, from time response plots in Figure 111, that in the V-bar approach scenario the simulation lasts less than 100 seconds, resulting in a too high approach velocity, just like in the case of a valve's failure (fully closed). This happens, once again, because the propulsion system is not able to well balance the necessary thrust and the spacecraft cannot slow down properly. In this case, in fact, control efforts are saturated for the whole sequence since the system is attempting to correct the failure without success. As regards the R-bar approach, instead, there are no significant differences with respect to the nominal case, so it is fair to say that this kind of failure does not affect the success of the R-bar RVD manoeuvre at all.

## 4.4 Valve b open

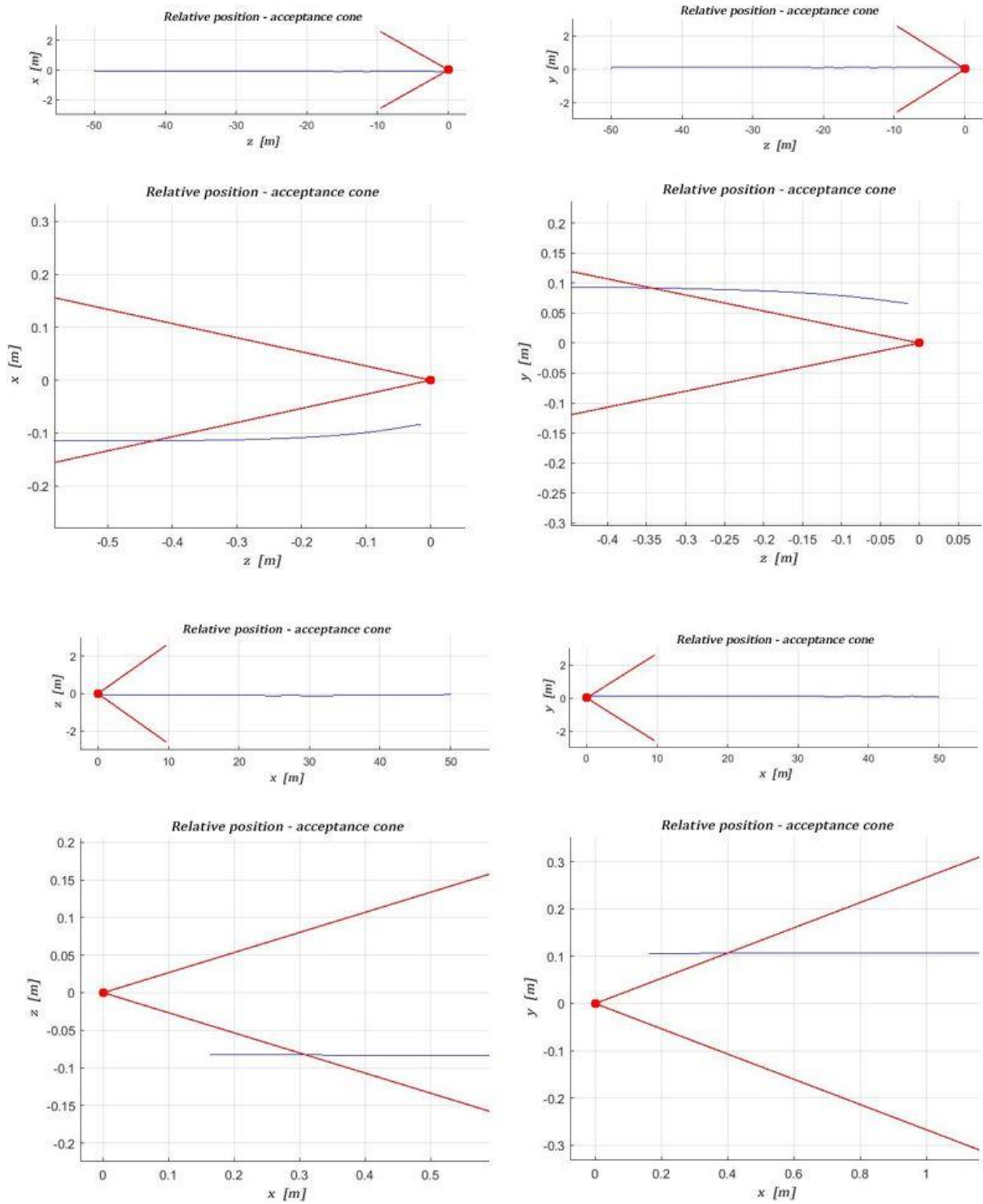


Figure 112: relative position - valve b open

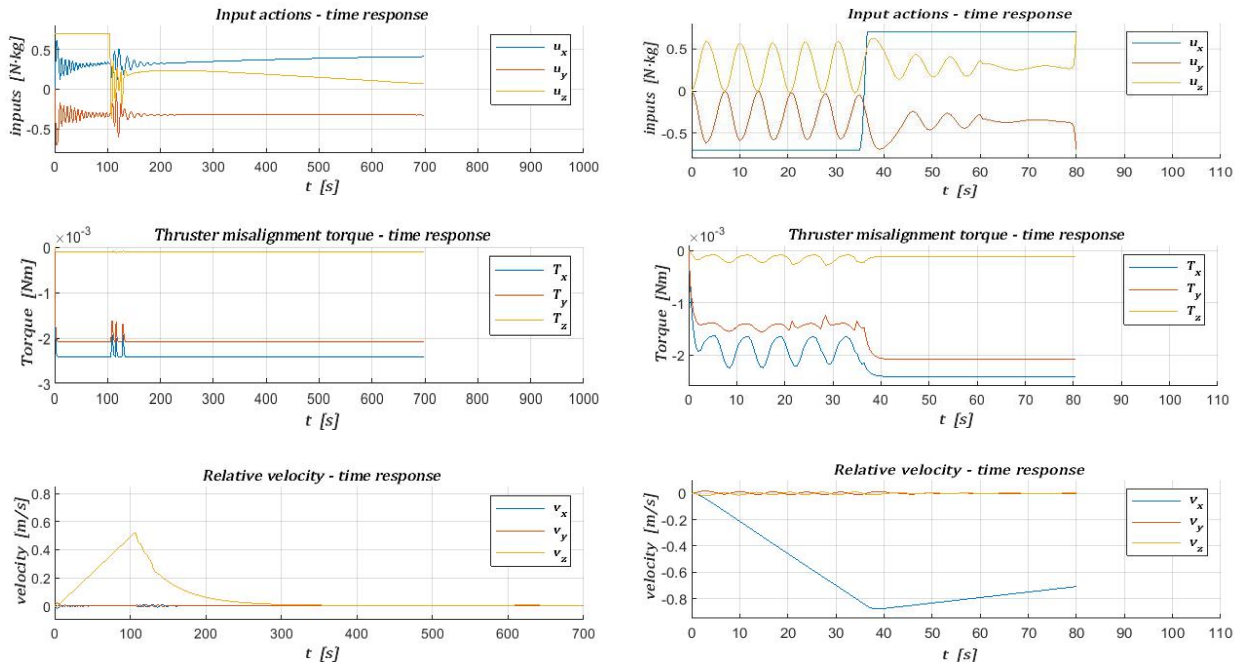


Figure 113: time responses - valve b open

Both in V-bar and R-bar approaches the acceptance cone constraint is not satisfied (Figure 112). From time responses (Figure 113) it is clear how the torque due to thruster misalignment has a relevant value, in this case. In the V-bar approach the manoeuvre lasts more than the usual, with an overall velocity lower than nominal case and input values trying to compensate the unwanted thrust caused by the failure. In the R-bar case what happens is very similar to the previous failure related to V-bar approach: the chaser gets to the target too soon, because of the excess of actuation due to the opening of the valve, resulting in a too high approach velocity, whose time response is truncated right after the peak of its overshoot. In this case, in fact, control inputs are brought to saturation for the whole sequence.

## 4.5 Valve *c* closed

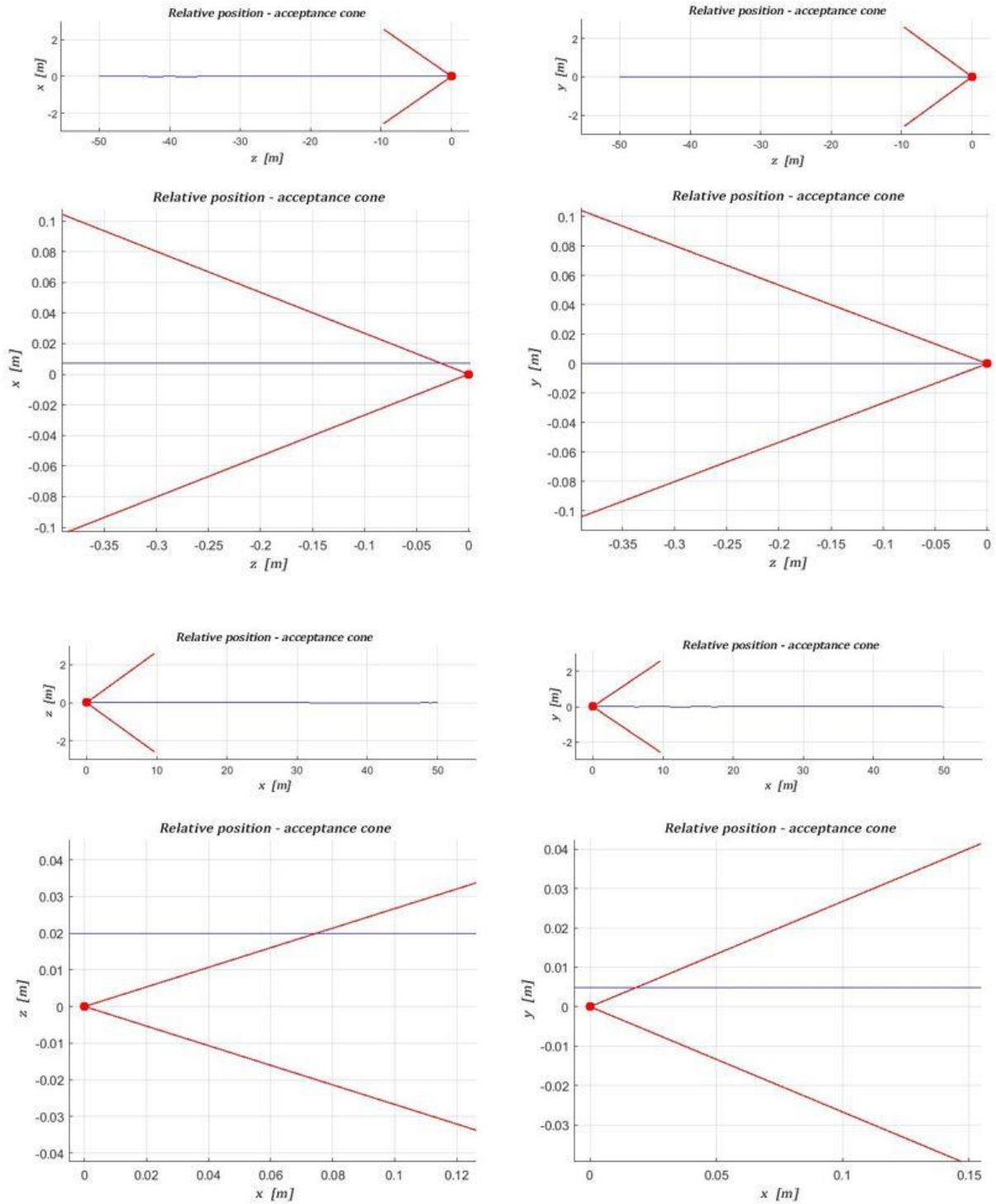


Figure 114: relative position - valve *c* closed

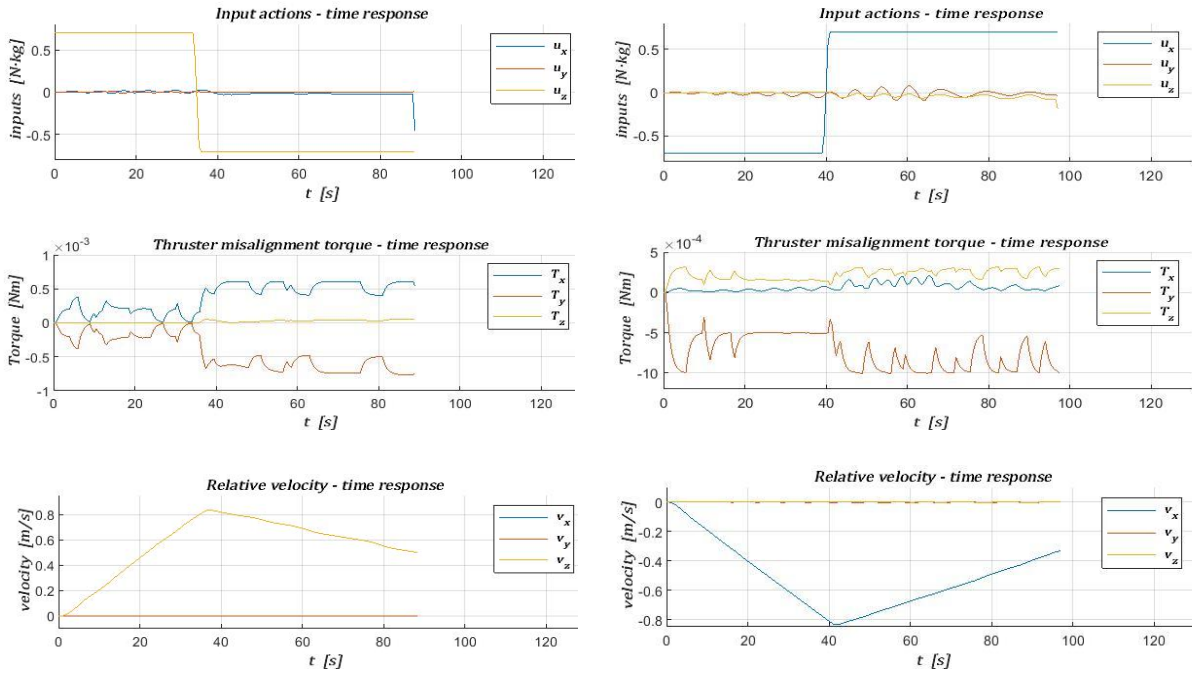


Figure 115: time responses - valve c closed

In this case the behaviour of the system is the same as the one described in 4.1 (valve a closed): in both V-bar and R-bar approaches the manoeuvre ends too soon because of the inability to slow down caused by the lack of actuation. All the plots described in Figure 114 and 115 are almost identical to the ones in 4.1, so the same considerations hold.

## 4.6 Valve c open

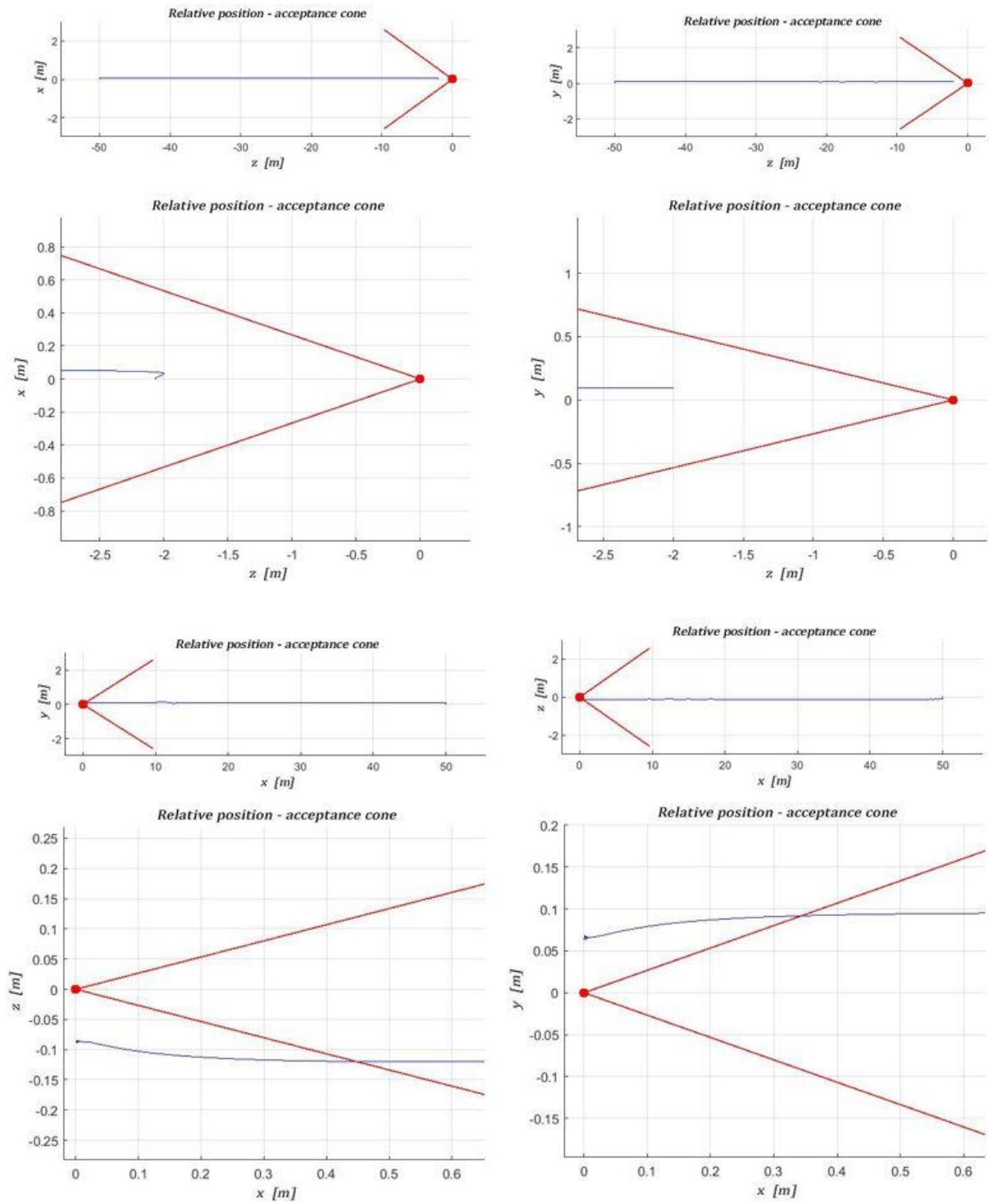


Figure 116: relative position - valve c open

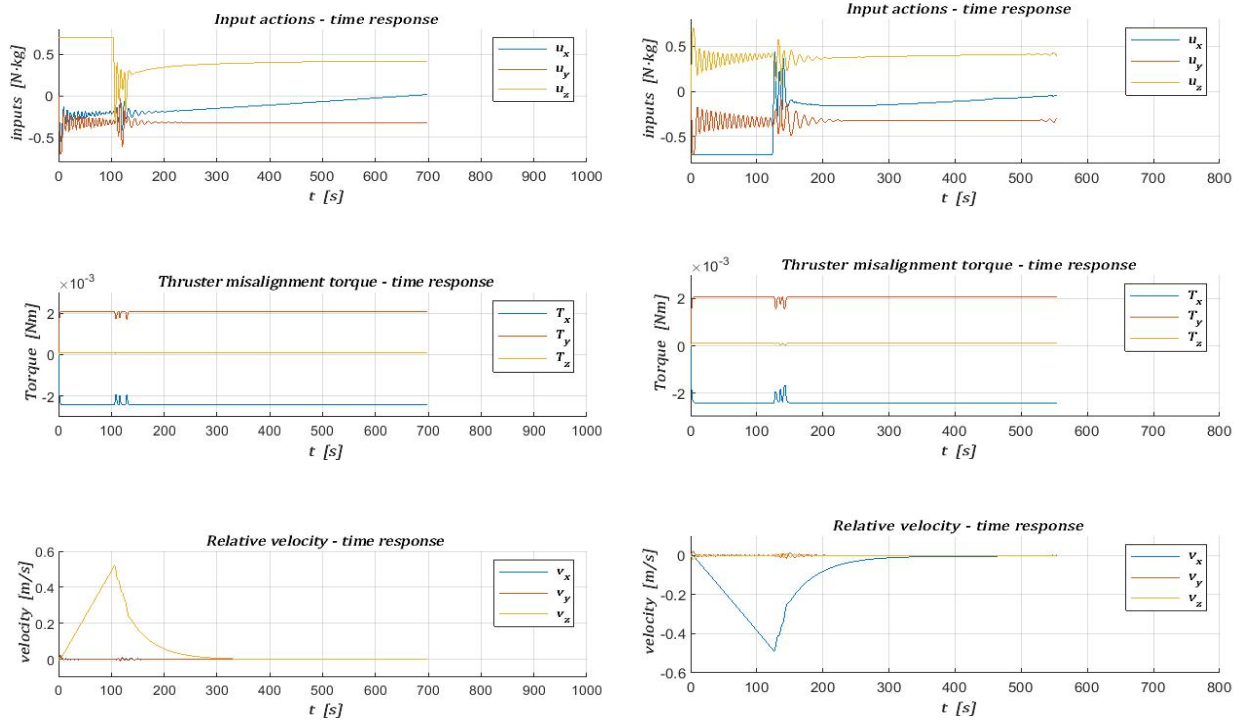


Figure 117: time responses - valve c open

In this case the behaviour of the system is the same as the one described in 4.2 (valve a open): while in V-bar approach the manoeuvre cannot be brought to completion, in the R-bar case the chaser deviates from the docking point, exiting acceptance cone boundaries. All the plots described in Figure 116 and 117 are almost identical to the ones in 4.2, so the same considerations hold.

## 4.7 Valve *d* closed

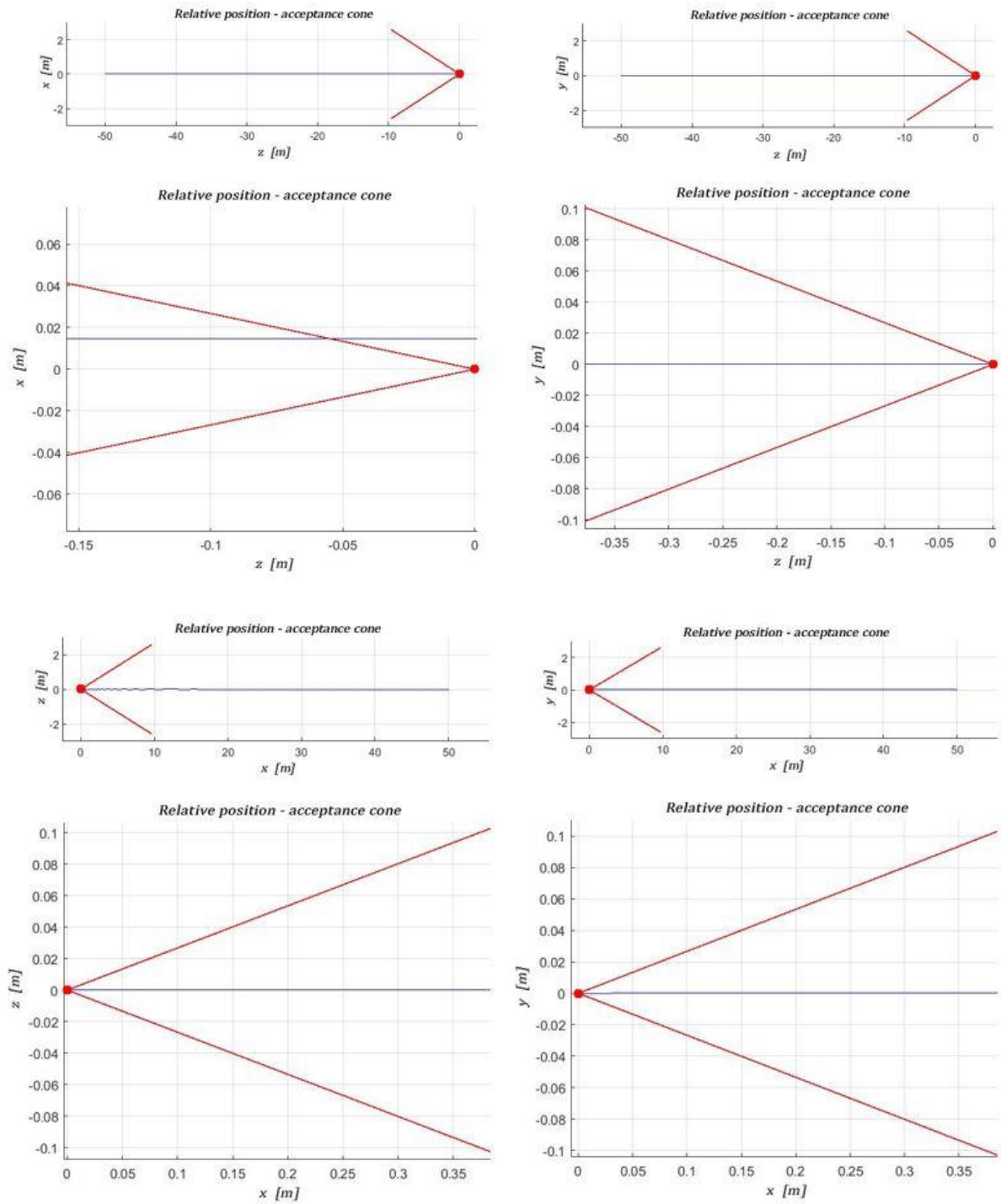


Figure 118: relative position - valve *d* closed

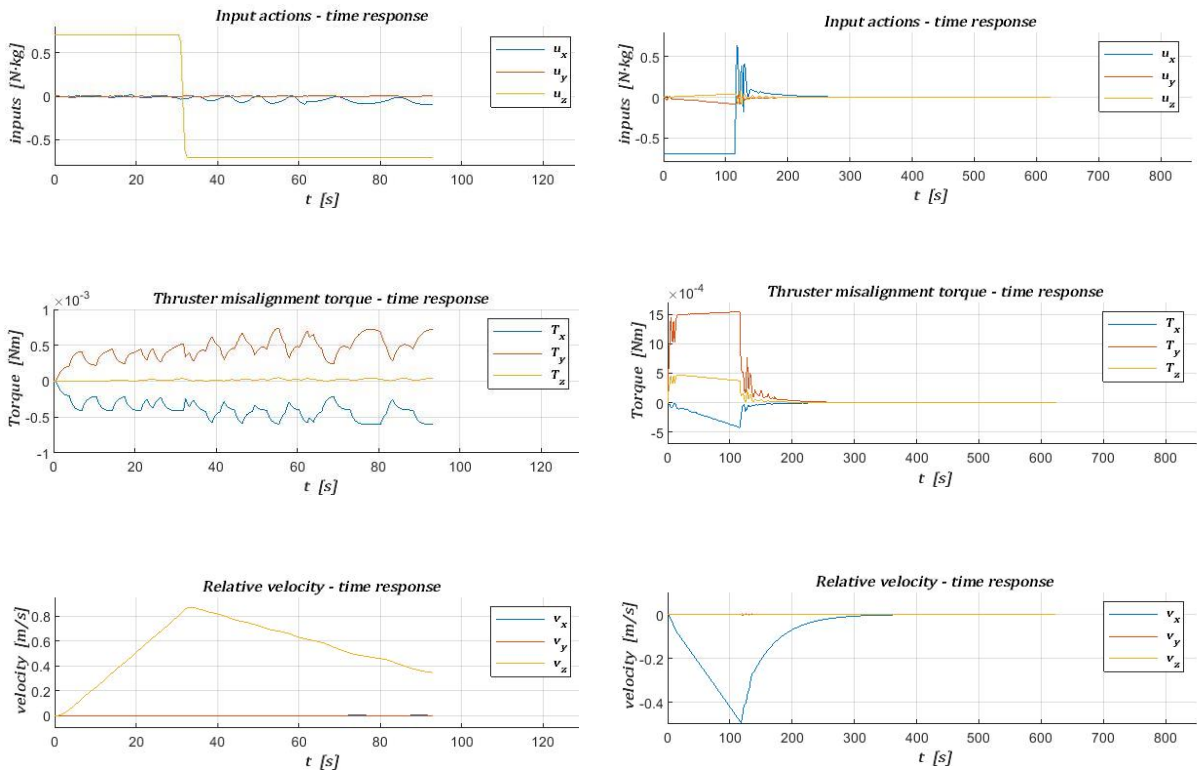


Figure 119: time responses - valve *d* closed

In this case the behaviour of the system is the same as the one described in 4.3 (valve *b* closed): while in V-bar approach acceptance cone boundaries are not respected, R-bar manoeuvre proceeds smoothly with acceptance cone satisfaction. All the plots described in Figure 118 and 119 are almost identical to the ones in 4.2, so the same considerations hold.

## 4.8 Valve *d* open

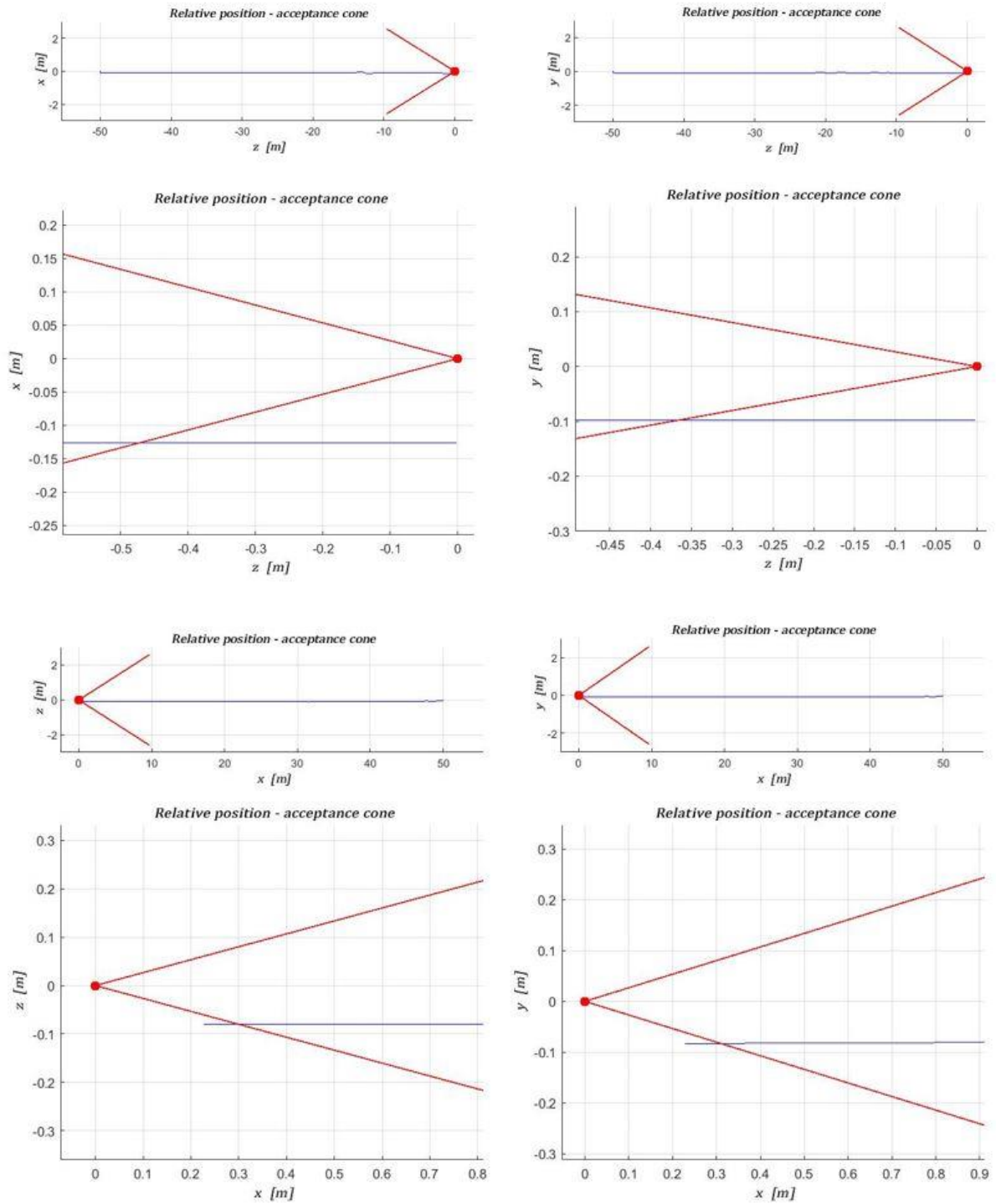


Figure 120: relative position - valve *d* open

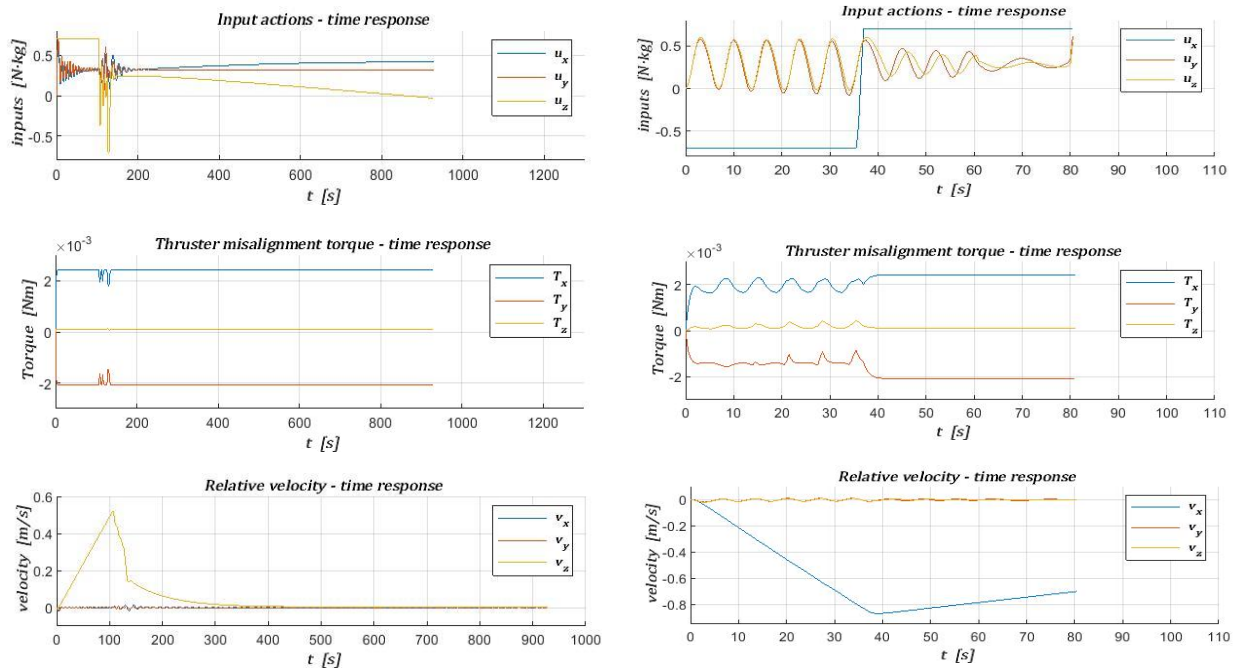


Figure 121: time responses - valve d open

From Figure 120 it is clear how the acceptance cone constraint is not satisfied in both kinds of approach, so the manoeuvre does not result successful in both scenarios.

In terms of time responses (Figure 121) the control actions are always included within the prescribed bounds: in the V-bar case it is evident how the controller tries to compensate the undesired thrust caused by the failure, while in the R-bar approach input values are brought to saturation for the whole sequence. In the V-bar case, the manoeuvre lasts much longer than the nominal case, the overall velocity is lower than the nominal scenario; in the R-bar approach, although, the simulation ends after just 80 seconds, resulting in the situation largely described in the previous paragraphs: too high approach velocity, whose time response is truncated after the peak value. Torque induced by thruster misalignment is comparable in both cases, with the same order of magnitude.

## 4.9 Valve e closed

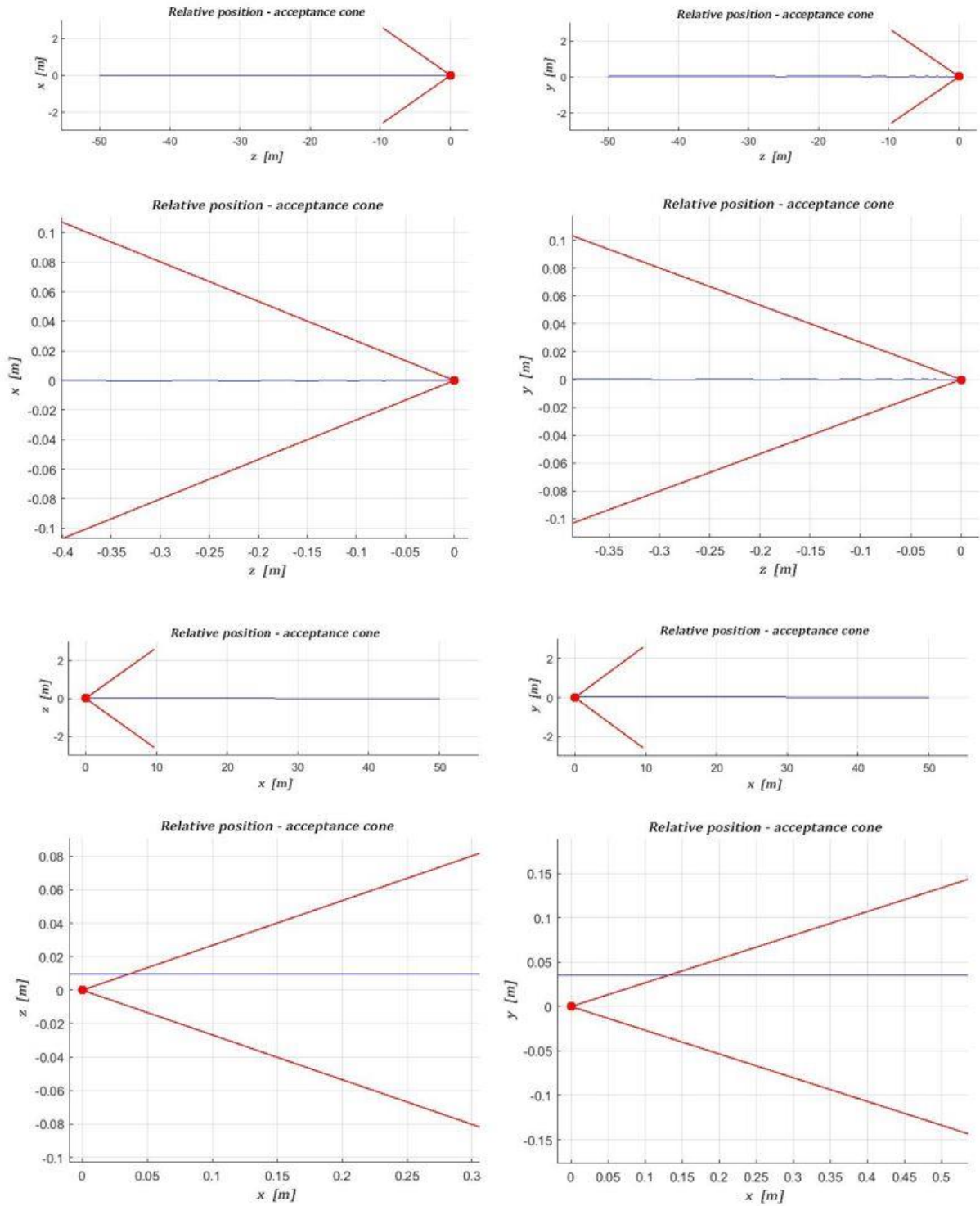


Figure 122: relative position - valve e closed

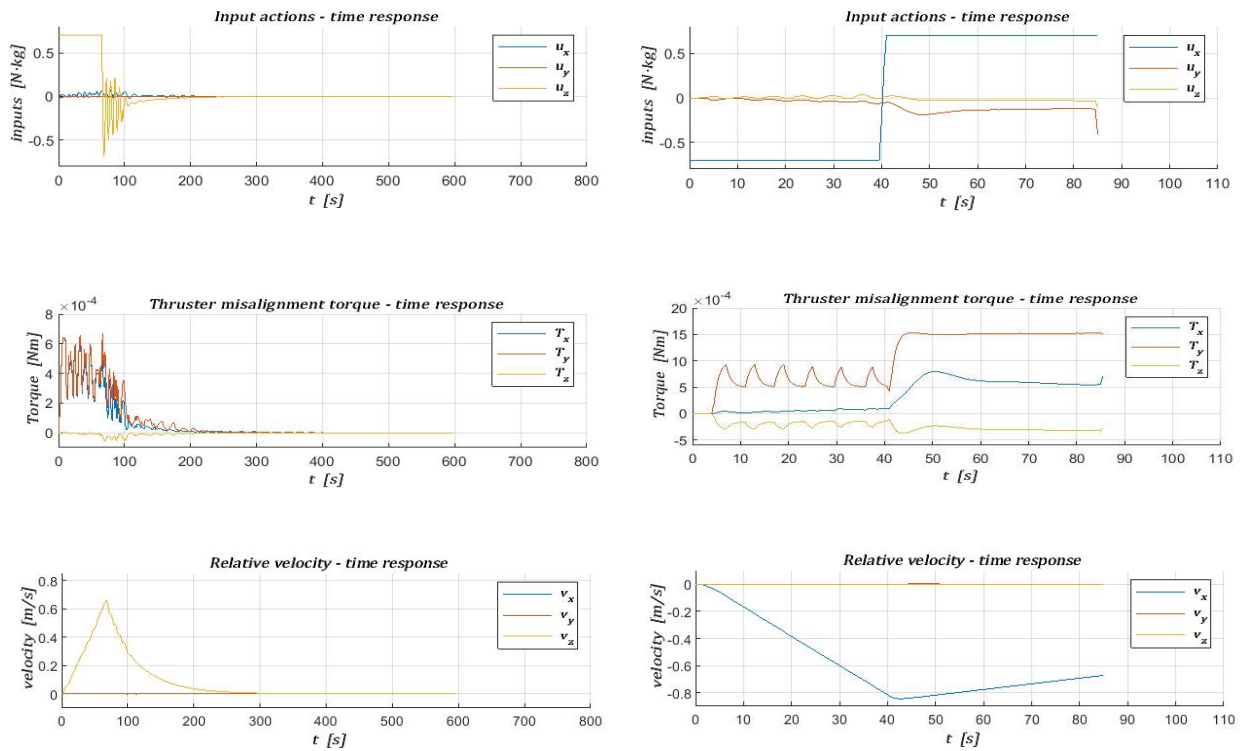


Figure 123: time responses - valve e closed

In the manoeuvre along V-bar, the acceptance cone constraint is satisfied, while in the R-bar case it is not (Figure 122). The procedure along R-bar ends after 85 seconds, with the same features discussed before in case of a too brief simulation (high approach velocity, saturated input actions). V-bar parameters are the same as the one obtained in nominal conditions, apart from the torque resulting from thruster misalignment, so the manoeuvre along V-bar is successful.

## 4.10 Valve e open

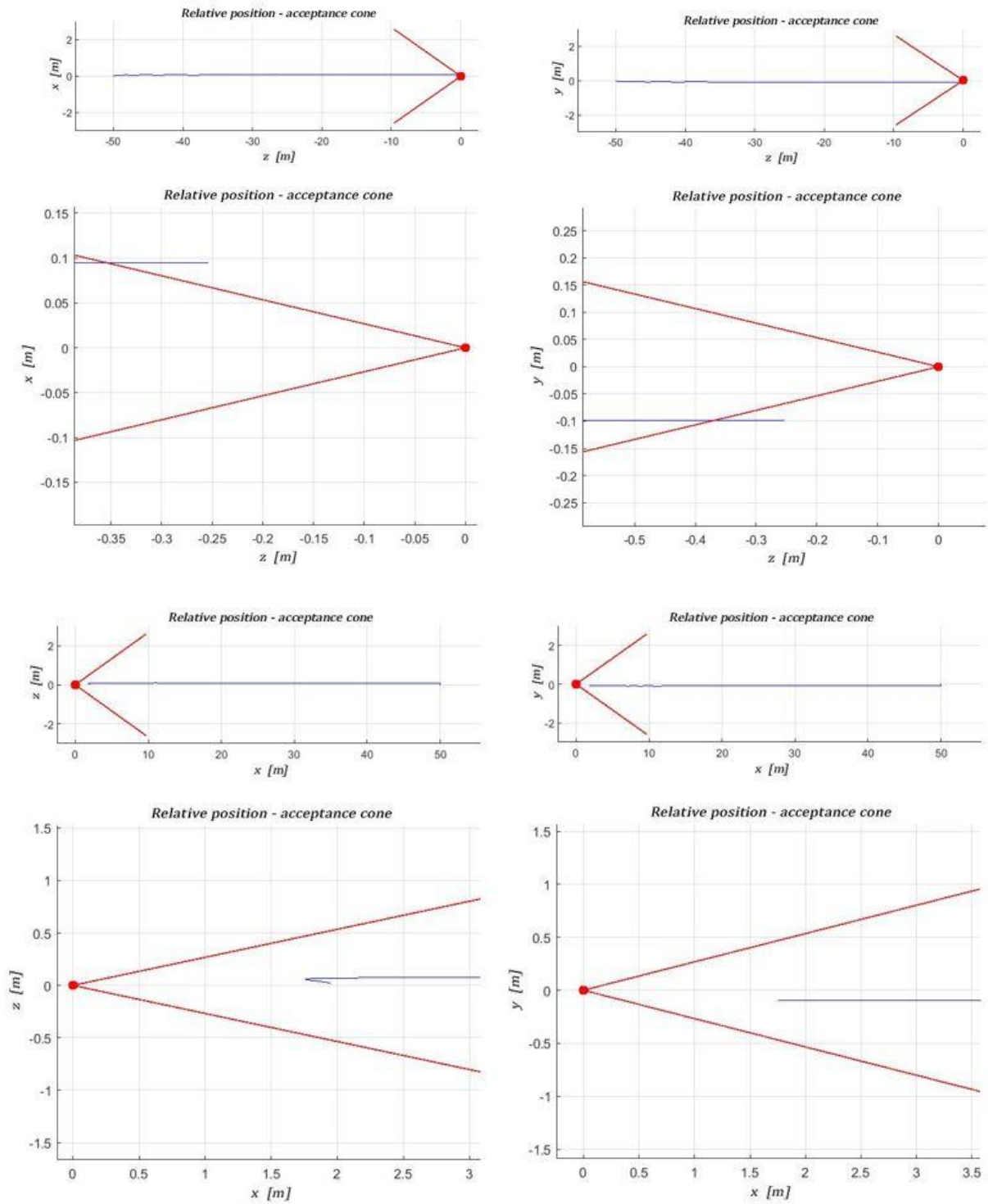


Figure 124: relative position - valve e open

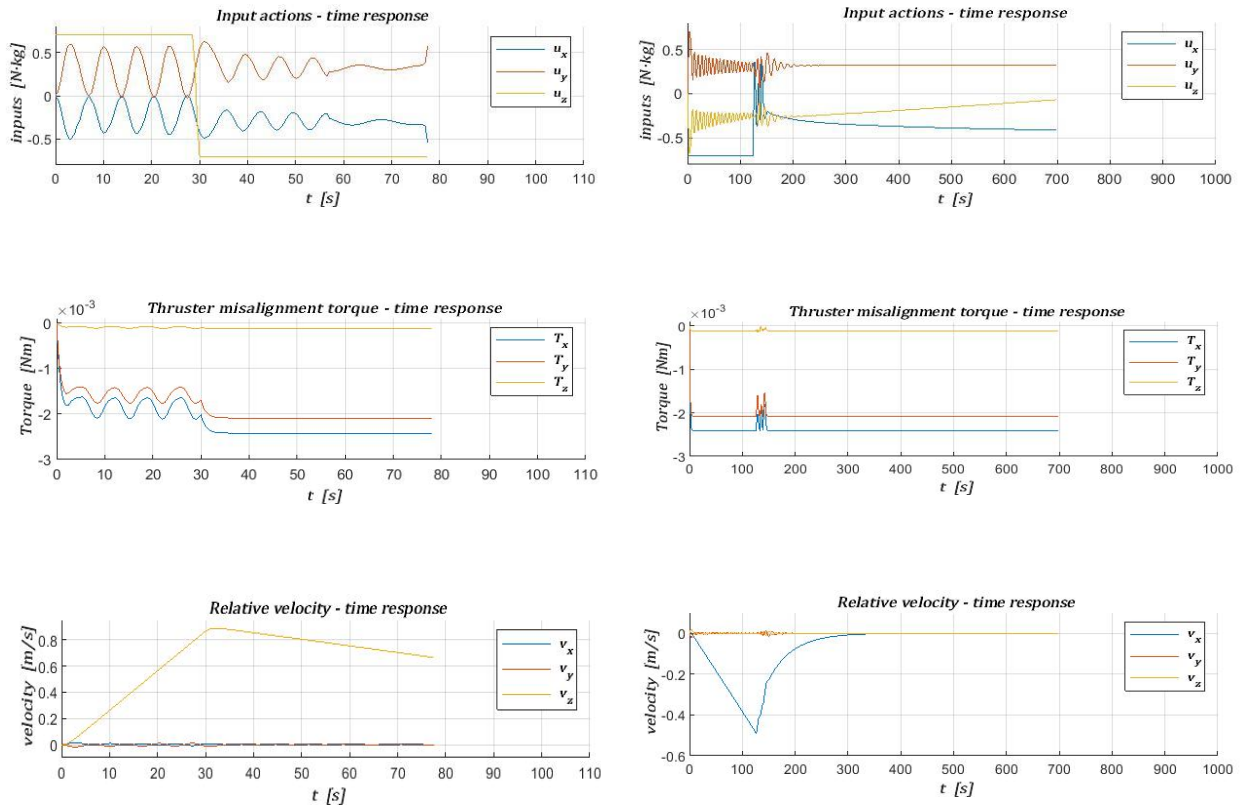


Figure 125: time responses - valve e open

In this case, *Figure 124* shows how acceptance cone constraint is not satisfied in anyone of the two studied cases. From *Figure 125* it is possible to see that simulation along V-bar lasts less than 80 seconds, showing all the same features observed, in the previous cases, in such a short-timed simulation: saturated input values, too high approach velocity. In the R-bar case, the peak velocity of the chaser is much lower with respect to the nominal case. Additionally, input commands do not have the behaviour which is typical of nominal conditions, since they are trying to compensate the unwanted action of the faulty thruster. This phenomenon causes the inability to get to docking point because of the impossibility to well balance the overall thrust. In both scenarios, misalignment torque has a significant value.

# 4.11 Valve f closed

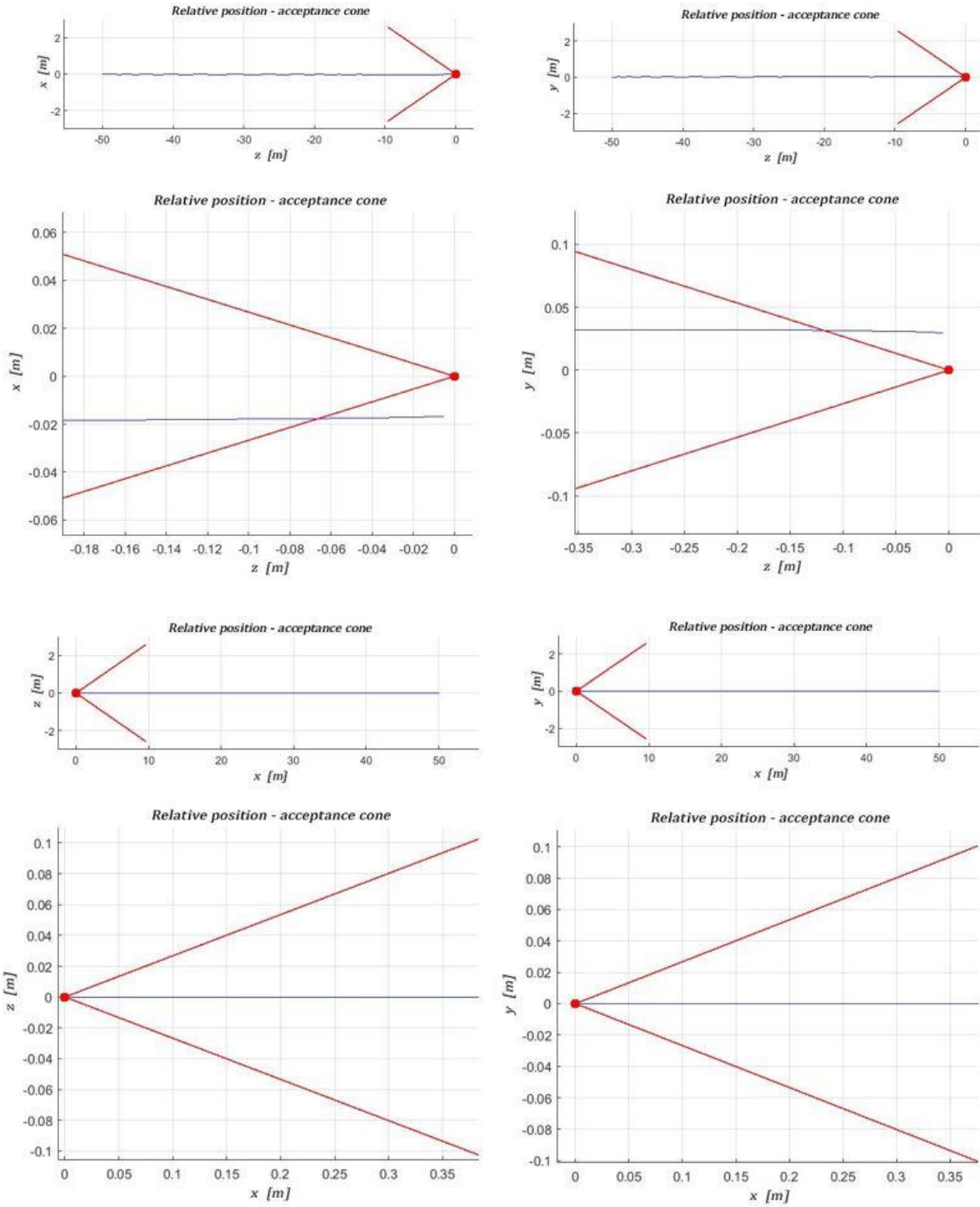


Figure 126: relative position - valve f closed

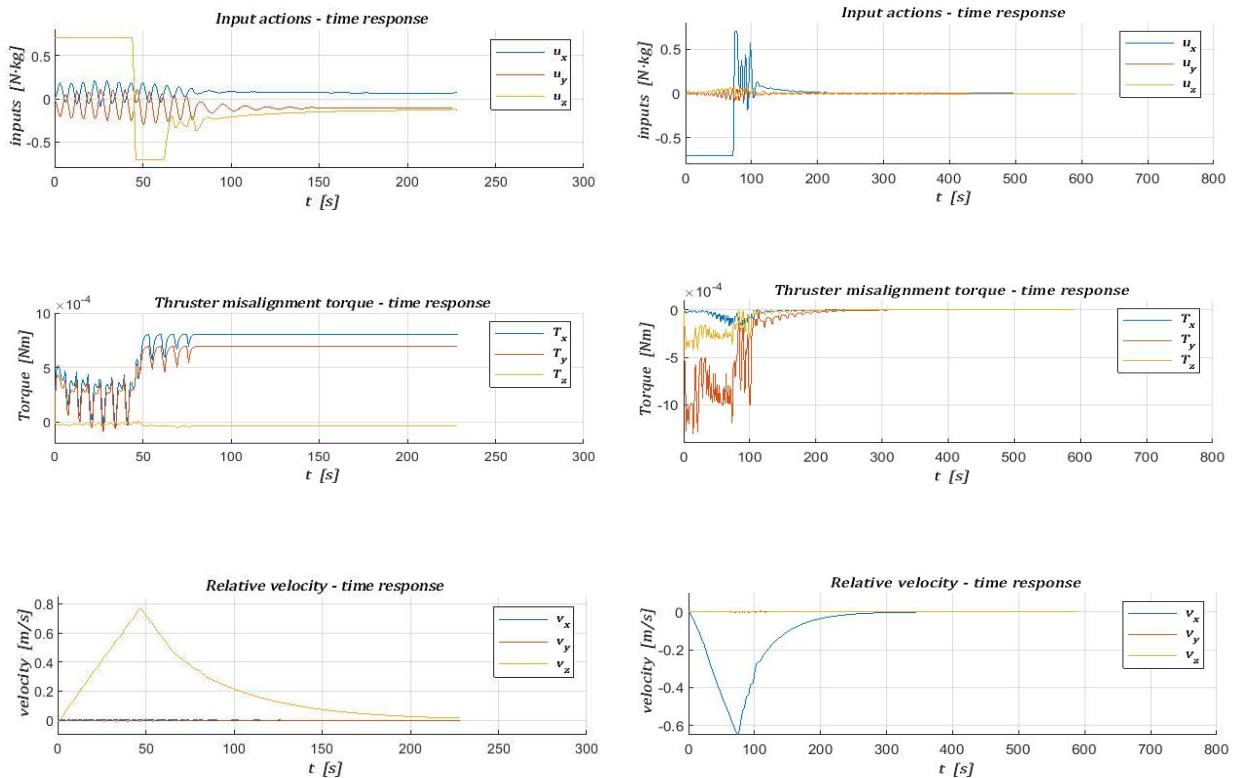


Figure 127: time responses - valve f closed

While in the R-bar approach *Figure 126* shows that the acceptance cone constraint is respected, in the case of the simulation along V-bar, this requirement is not satisfied.

Time responses described by the plots in *Figure 127* outline a close to nominal behaviour concerning R-bar approach, apart from misalignment torque which has a non negligible value, as usual. In the case of V-bar approach, the simulations lasts less than 250 seconds and, thus, is not able to guarantee an optimal performance.

## 4.12 Valve *f* open

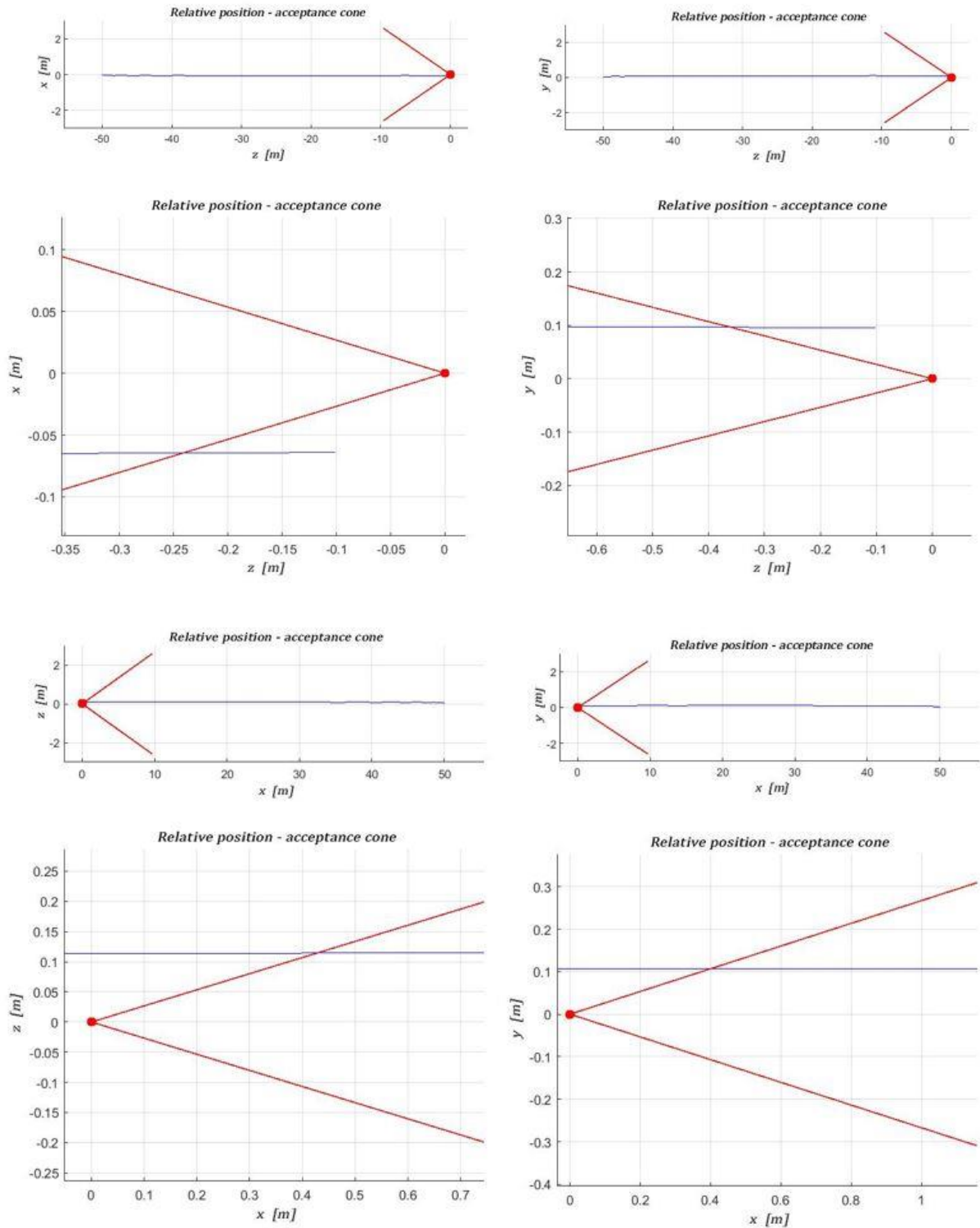


Figure 128: relative position - valve *f* open

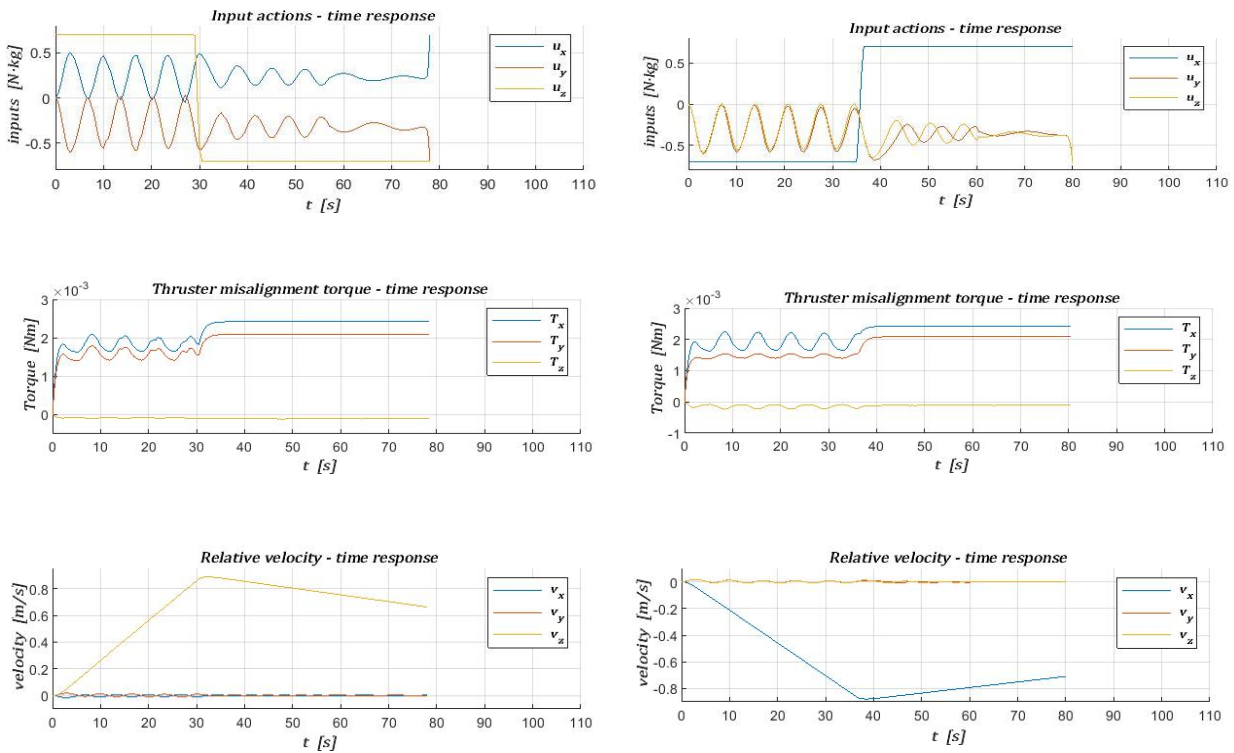


Figure 129: time responses - valve f open

Figure 128 shows how no simulation results successful in this case, for both the approaches. From Figure 129 it results clear how the simulations are completed in a too short time, causing the main problems already outlined above in similar cases, resulting in an unsuccessful manoeuvres with this kind of failure.

## 4.13 Valve g closed

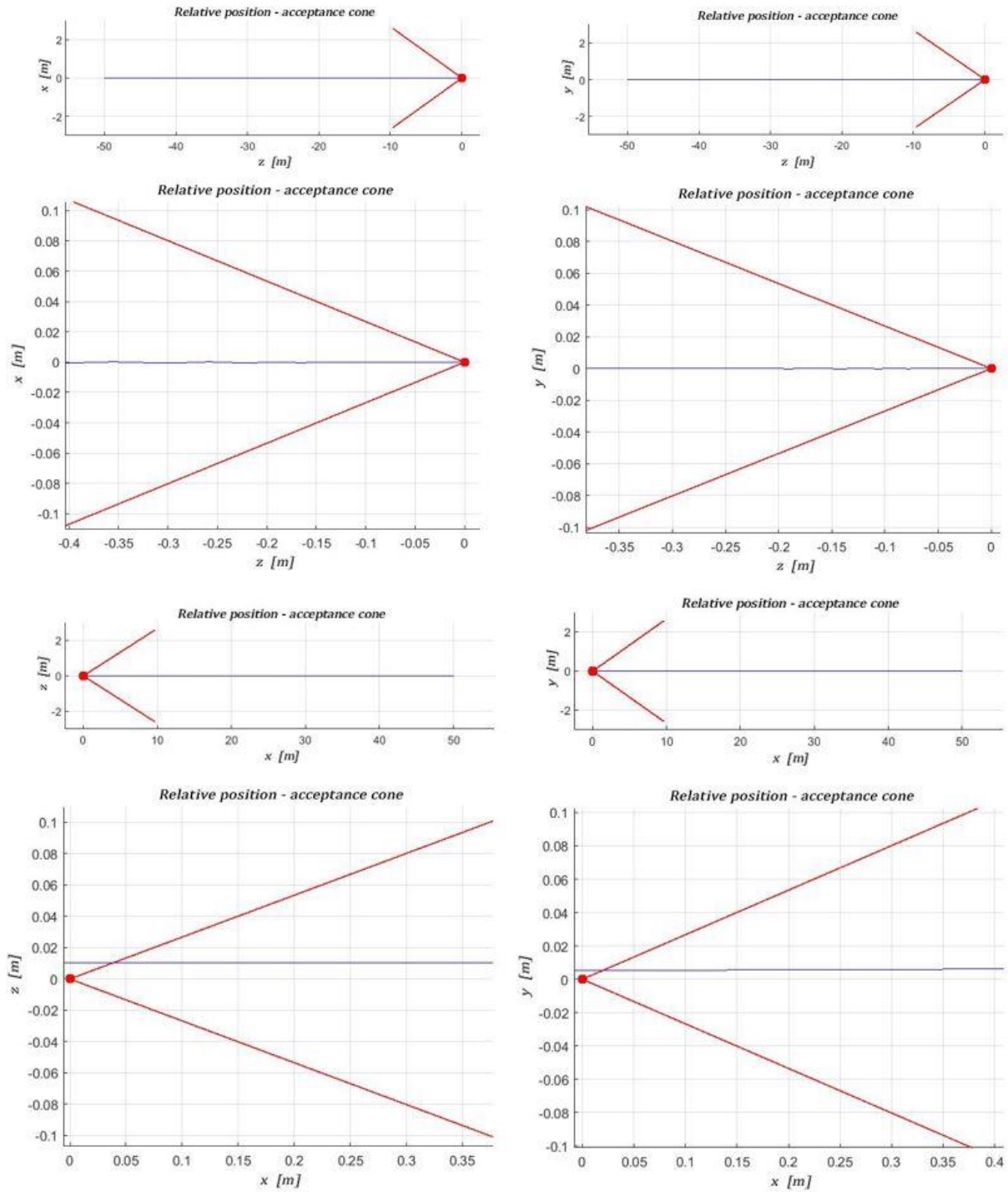


Figure 130: relative position - valve g closed

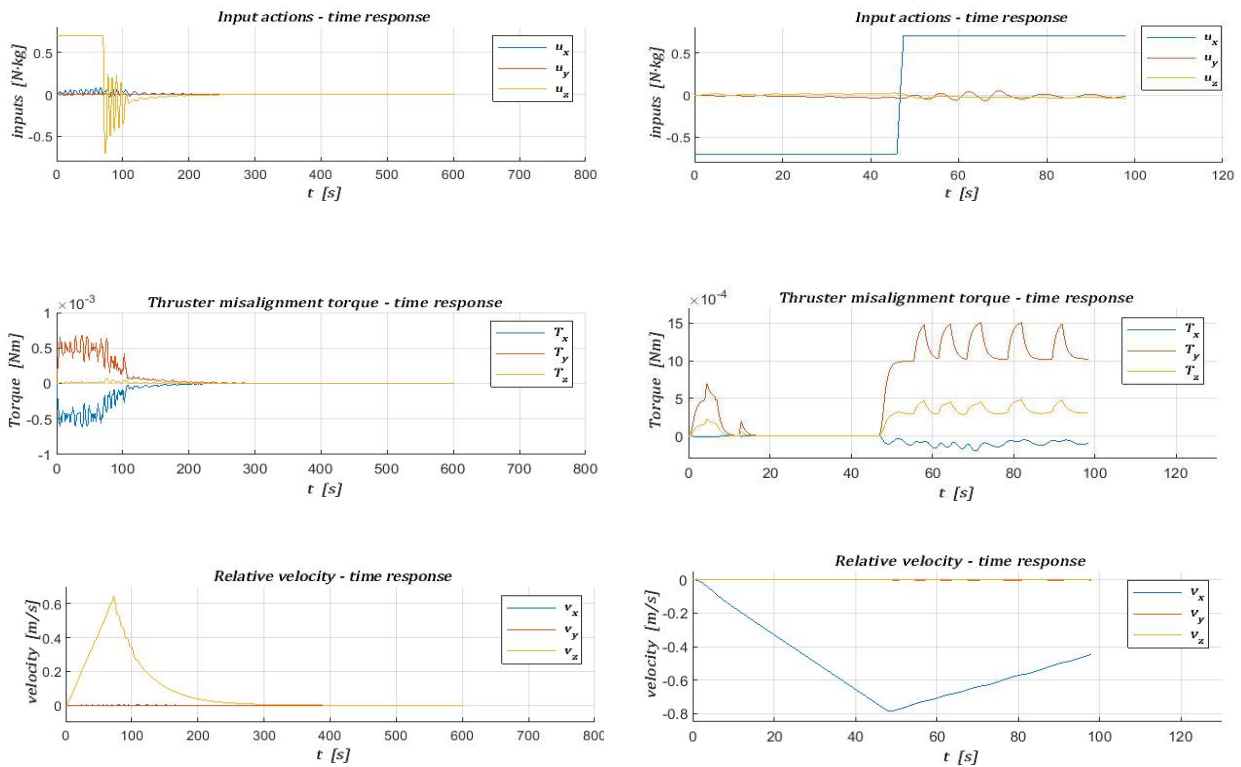


Figure 131: time responses - valve g closed

In this case, plots described in Figures 130 and 131 show that this scenario is absolutely analogous to the one discussed in 4.9 (valve e closed). Manoeuvre along V-bar results effective, thanks to the satisfaction of cone constraint and, furthermore, time response plots do not show any anomaly. However the manoeuvre along R-bar is completed after less than 100 seconds, resulting in an undesired condition already analysed before.

## 4.14 Valve g open

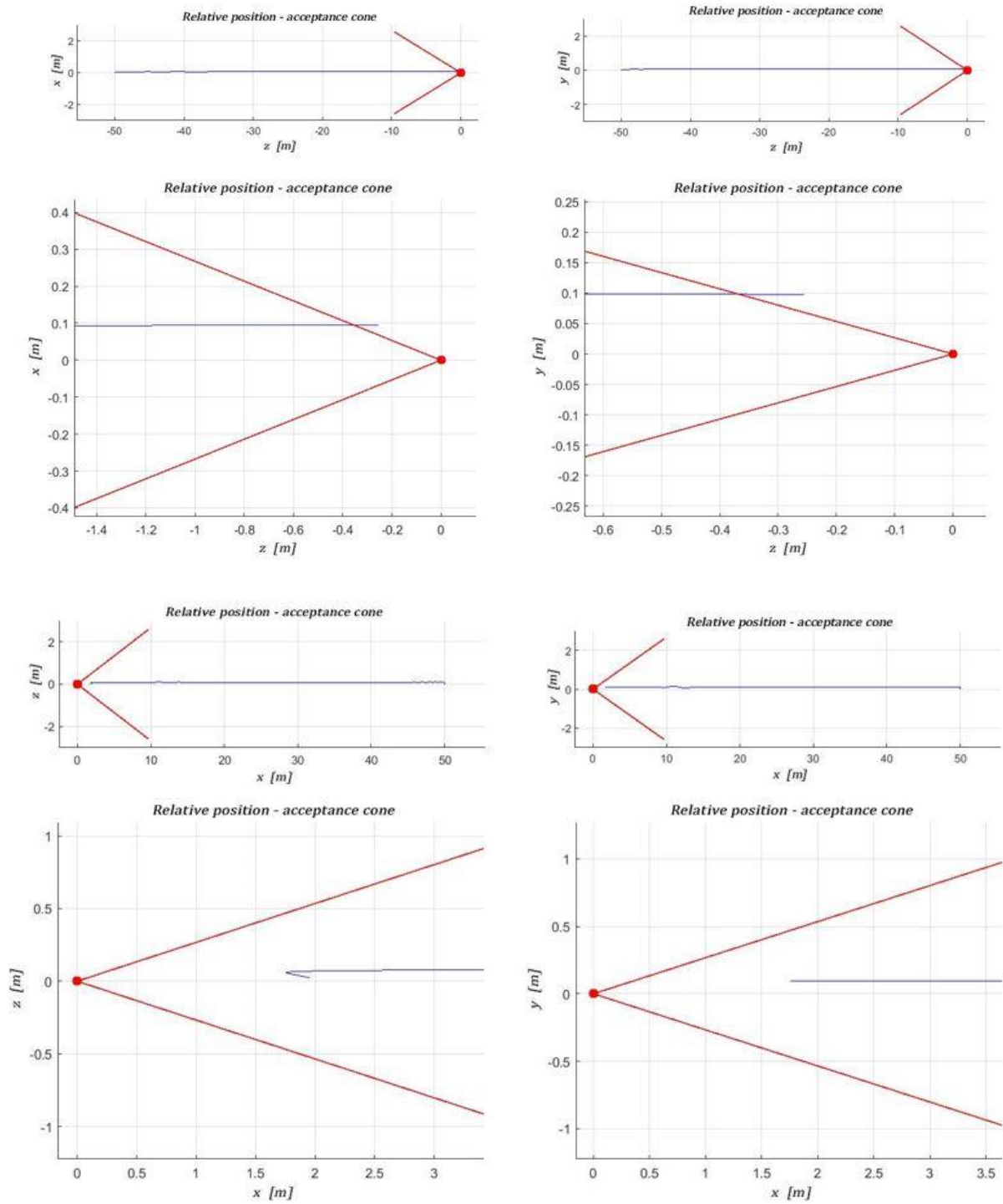


Figure 132: relative position - valve g open

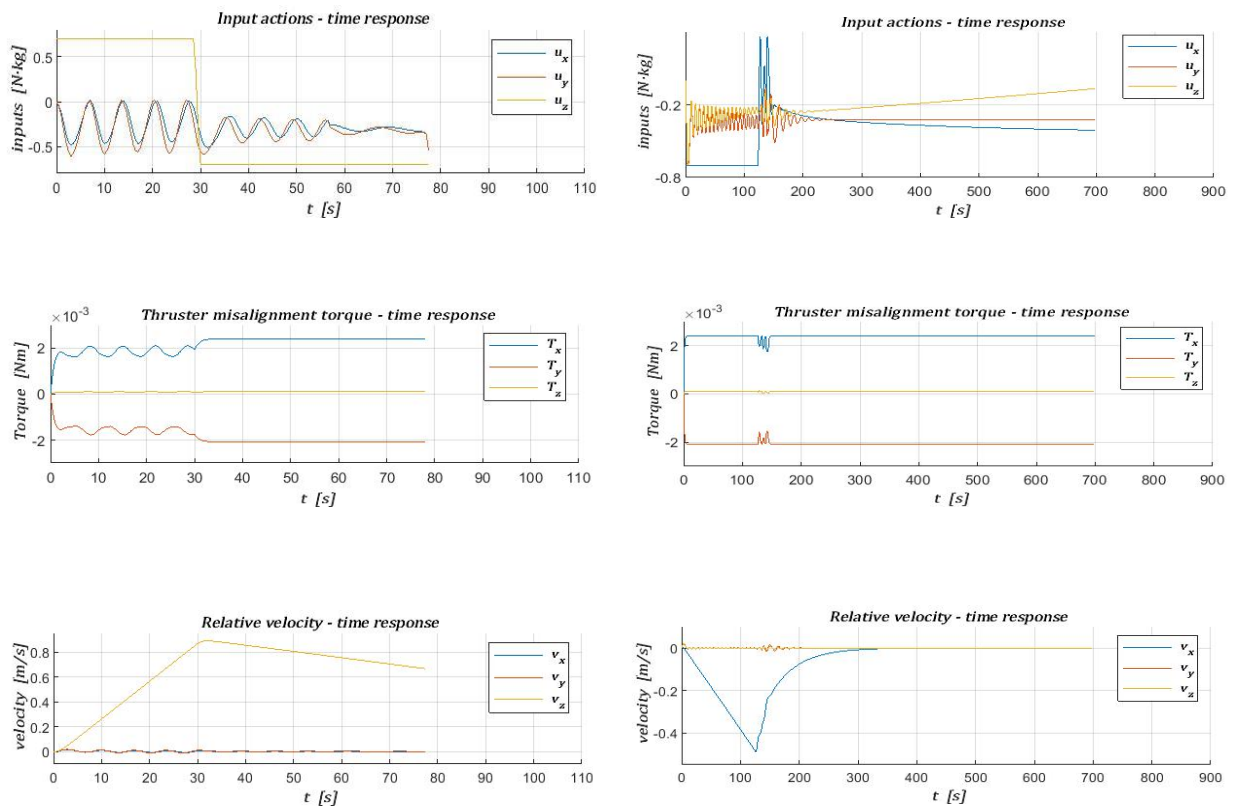


Figure 133: time responses - valve g open

In this case, plots described in Figures 132 and 133 show that this scenario is absolutely analogous to the one discussed in 4.10 (valve e open). Both manoeuvres result unsuccessful, as shown by the fact that acceptance cone constraint is not satisfied. Particular attention can be paid to time responses which, in the V-bar case, outline a short duration of the simulation (high final velocity truncated after its peak value, saturated inputs for the whole sequence). In the R-bar approach, instead, the control action tries to compensate the undesired thrust resulting from the failure without succeeding: the outcome is a too low velocity and the inability to reach the docking point.

## 4.15 Valve h closed

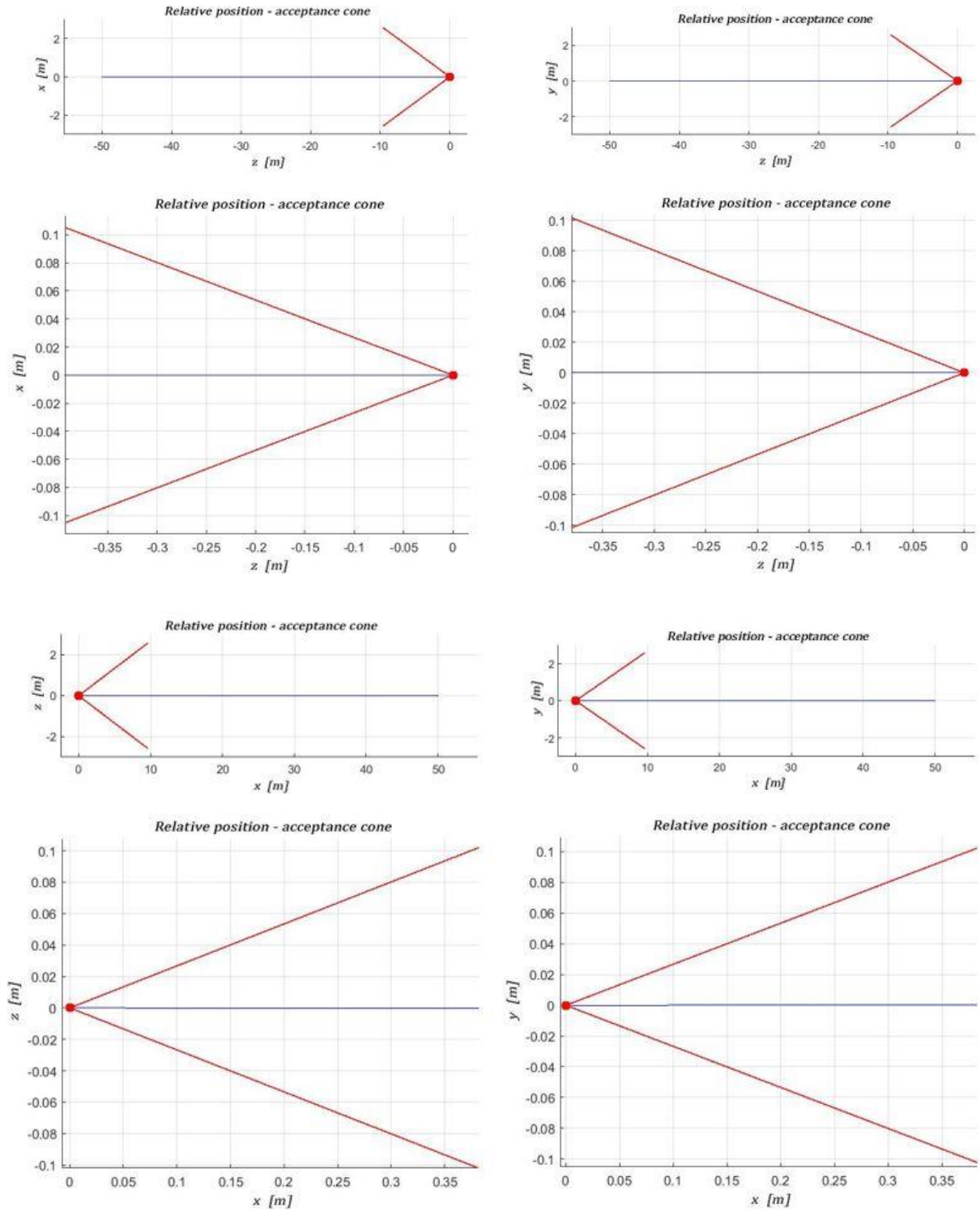


Figure 134: relative position - valve h closed

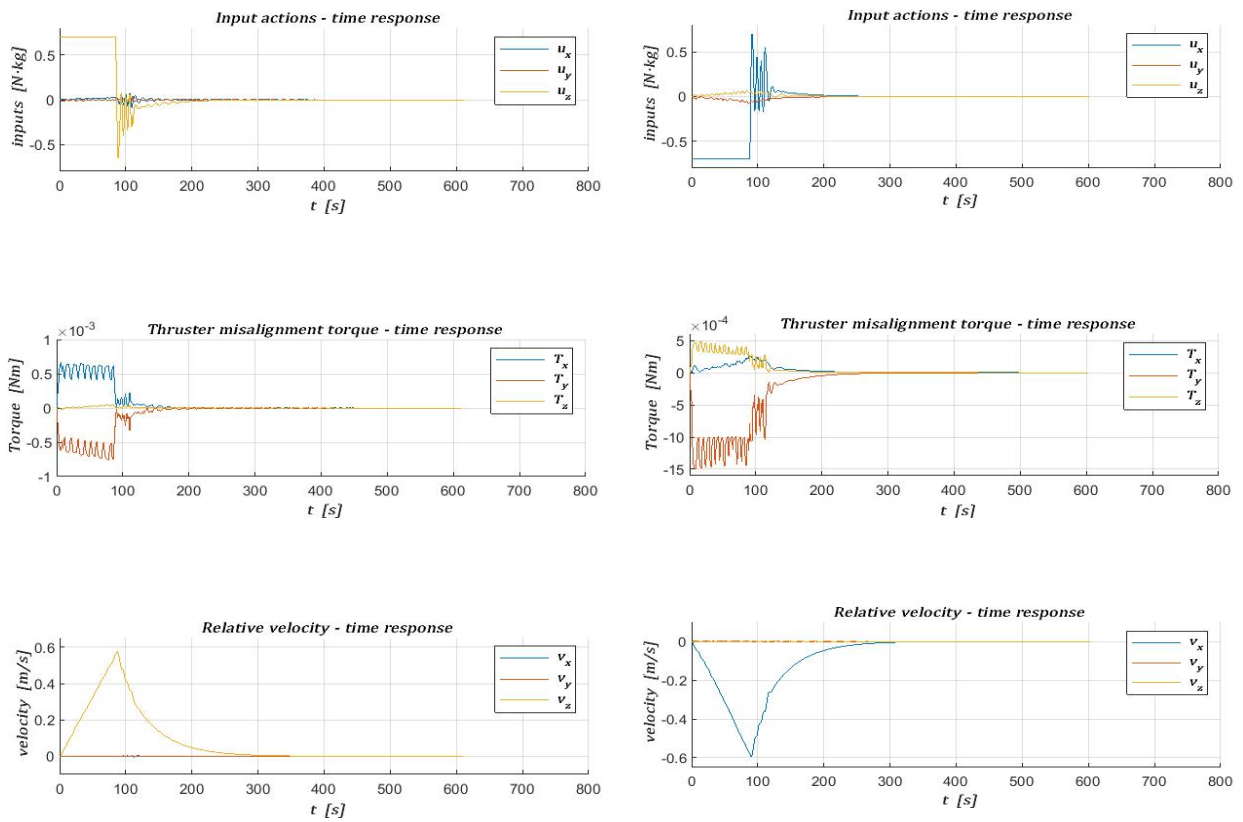


Figure 135: time responses - valve h closed

In this case, as shown by *Figure 134*, acceptance cone constraint is satisfied in both kinds of approaches. This is reflected also on the time response plot described in *Figure 135* which do not outline any anomalies with respect to the nominal case, apart from the torque produced by thruster misalignment.

## 4.16 Valve h open

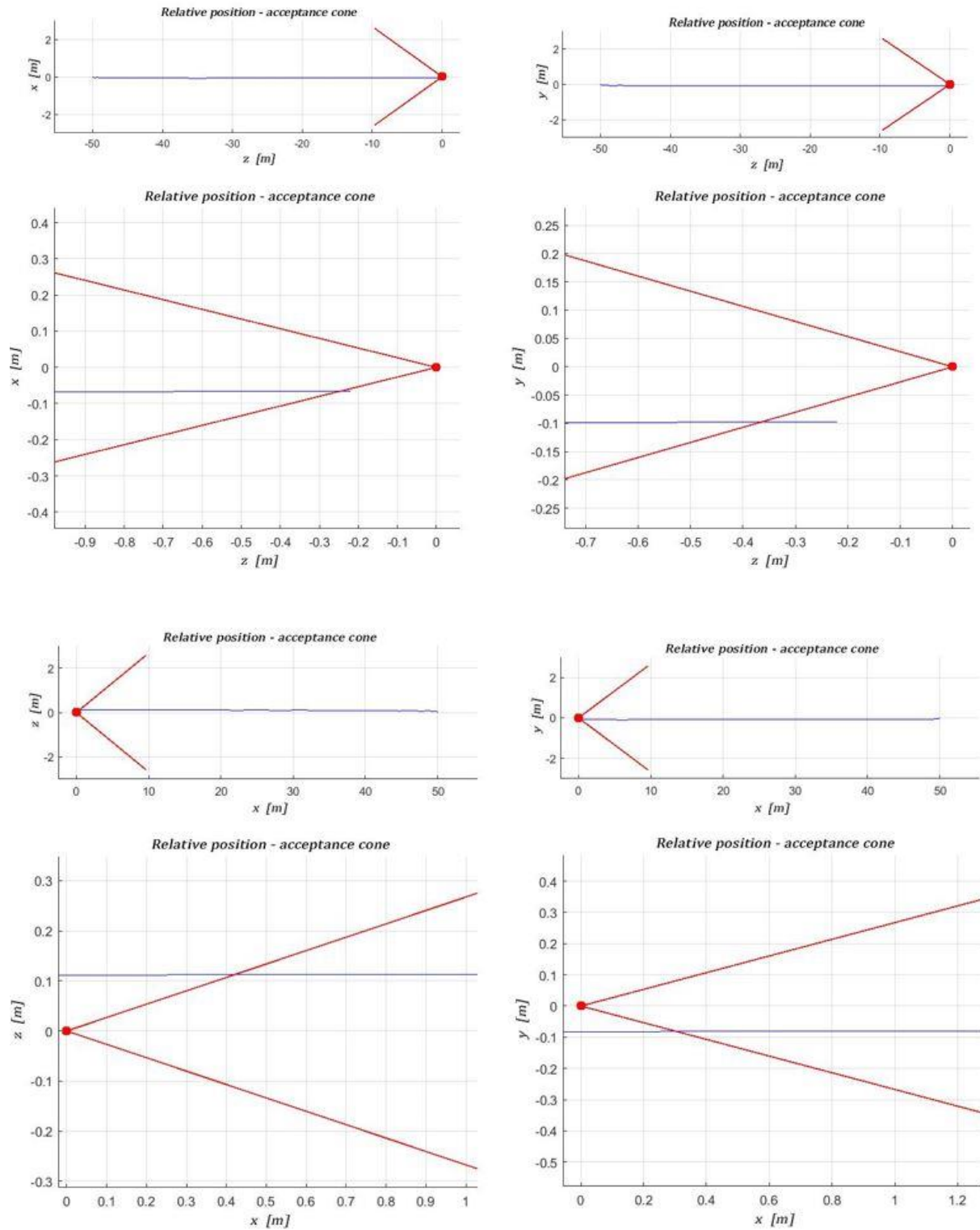


Figure 136: relative position - valve h open

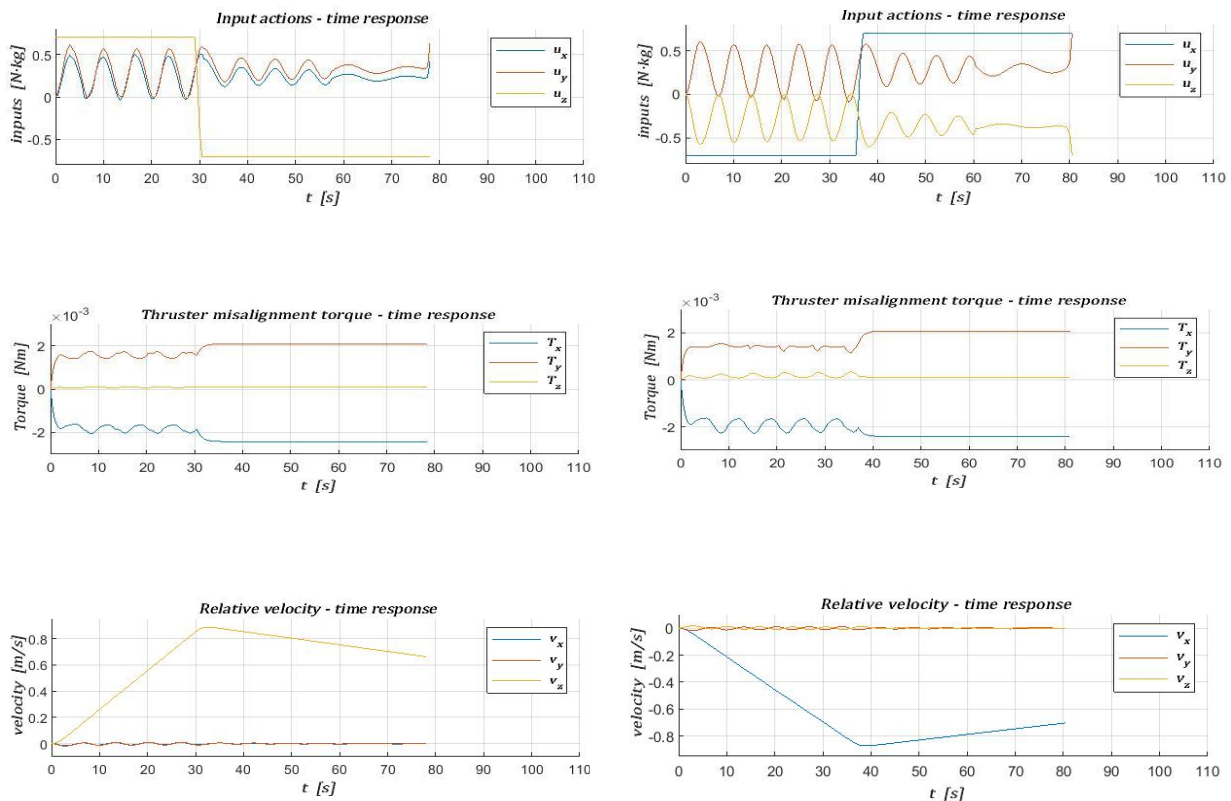


Figure 137: time responses - valve h open

In both scenarios investigated in this case, none of the manoeuvres is successful as the acceptance cone constraints are not satisfied (Figure 136). From Figure 137 it is clear how both simulations end after less than 80 seconds, causing the widely discussed problems typical of this phenomenon.

In order to sum up the outcomes of this study in off-nominal conditions, it is very clear how the failure in actuation system (in particular thrusters) is responsible of heavily affecting the success of the mission. There are some similarities in the consequences exerted on the manoeuvres across different failures: when  $a$  and  $c$  valves result faulty, the results on simulations are almost identical. The same holds for  $e$  and  $g$  valves and for the case in which  $d$  valve is fully closed and  $b$  valve is shut down as well.

In order to be able to evaluate the success rate of the simulations in each one of the investigated conditions, the following table is made:

<b>Valve</b>	<b>V-bar</b>	<b>R-bar</b>
<i>a</i> closed	Fail	Fail
<i>a</i> open	Fail	Fail
<i>b</i> closed	Fail	Success
<i>b</i> open	Fail	Fail
<i>c</i> closed	Fail	Fail
<i>c</i> open	Fail	Fail
<i>d</i> closed	Fail	Success
<i>d</i> open	Fail	Fail
<i>e</i> closed	Success	Fail
<i>e</i> open	Fail	Fail
<i>f</i> closed	Fail	Success
<i>f</i> open	Fail	Fail
<i>g</i> closed	Success	Fail
<i>g</i> open	Fail	Fail
<i>h</i> closed	Success	Success
<i>h</i> open	Fail	Fail

Table 12: success rate - off nominal conditions

## ***5. Conclusions***

A control strategy based on Model Predictive Control and on Sliding Mode Control is designed for a 12 U CubeSat involved in a Rendezvous and Docking manoeuvre. By means of a progressive refinement of the model employed for simulations, on MATLAB and Simulink, it results possible to obtain a more and more precise degree of approximation, recreating a scenario as realistic as possible thanks to disturbance modelling. The addition of further disturbing elements to the overall system is performed concurrently with adaptive tuning of controllers, in a progressive fashion, in order to gradually increase the complexity of the closed loop control system. Once concluded the design phase, the effectiveness of the final control strategy is proven.

In the following section, 20 sets of 600 total Montecarlo simulations are performed, in different scenarios, by adding weak to strong uncertainties to the initial conditions of the main parameters involved in the problem formulation. This procedure is developed for the sake of a robustness analysis, in order to take into account the most common sources of errors in the studied application. After verifying the robustness of the closed loop control system, a further refinement of the orbit controller results necessary, in order to obtain a more convenient trajectory and to avoid excessive overshoots.

In the last part of the work, an analysis of off-nominal conditions is performed, in a single failure framework concerning the propulsion system of the spacecraft, whose contingent breakdown, in most cases, would irreversibly affect the outcome of the mission.

As much as concerns nominal conditions, even in a setup including worst case scenario uncertainties and disturbances, the designed control strategy results very effective, with a 100% success rate of each performed simulation.

## 6. References

- [1] *Automated Rendezvous and Docking of Spacecraft*, Wigbert Fehse, Cambridge University Press, 2009
- [2] [www.esa.int/Enabling\\_Support/Space\\_Engineering\\_Technology/Technology\\_Cubesats](http://www.esa.int/Enabling_Support/Space_Engineering_Technology/Technology_Cubesats)
- [3] *Model predictive control system design and implementation for spacecraft rendezvous*, E.N. Hartley, P.A. Trodden, A.G. Richards, J.M. Maciejowski, Elsevier, 2012
- [4] *H-∞ and μ-Synthesis for Nanosatellites Rendezvous and Docking*, C. Pirat, F. Ankersen, R. Walker, V. Gass, IEEE, 2019
- [5] *Automated Proximity Operations Using Image-Based Relative Navigation*, L. Walker, D. Spencer, Small Satellite Conference, 2012
- [6] *Vision-Based CubeSat Closed-Loop Formation Control in Close Proximities*, F. Fahimi, De Gruyter, 2019
- [7] *Digital Control Technologies and Architectures*, Lecture notes, M. Canale
- [8] *Nonlinear Control and Aerospace Applications*, Lecture notes, C. Novara
- [9] *Chance-constrained model predictive control for spacecraft rendezvous with disturbance estimation*, F. Gavilan, R. Vazquez, E.F. Camacho, Elsevier, 2012
- [10] *Development of the Attitude Determination and Control System for a nanosatellite*, R. Mozzillo, Master's thesis, Master Degree Course in Aerospace Engineering, 2012
- [11] *Design, development and test of the control unit for a small cold-gas propulsion system*, M. Sacco, Master's thesis, Master Degree Course in Mechatronic Engineering, 2020
- [12] [simulationhub.com](http://simulationhub.com)
- [13] *Attitude Control Model for CubeSats*, J.K. Molina, V. Ayerdi, L. Zea, Latin American CubeSat Workshop, 2016
- [14] *THE NEW "DYNAMIC BEHAVIOR OF LIQUIDS IN MOVING CONTAINERS"*, T. Dodge, Southwest Research Institute, 2000
- [15] *CubeSat Slosh Dynamics and Its Effect on Precision Attitude Control for the VISORS Distributed Spacecraft Telescope Mission*, C.A. Carter, E.G. Lightsey, Master project, 2020

## 7. Appendix – STK simulations

In order to provide a better overview of the outcome of the manoeuvre, the results obtained by means of MATLAB/Simulink simulations are plotted on STK, a Multiphysics software application employed for mission analysis. The RVD procedure is plotted both for V-bar and R-bar approaches, in nominal conditions.

In *Figures 138* and *139* the RVD manoeuvre along V-bar is represented. It is clear from *Figure 138* how V-bar coincides with z-axis according to LVLH reference frame. The starting point of the manoeuvre corresponds to the one where the red caption *SROC* is found, while the trajectory described by the chaser is the one in green and appears to be a straight line fixed onto reference values, as simulation results suggest in the previous sections of this work. LVLH frame is represented in yellow and its origin corresponds with the centre of mass of Space Rider. The dashed blue lines represent the boundary of Space Rider's keep out sphere.

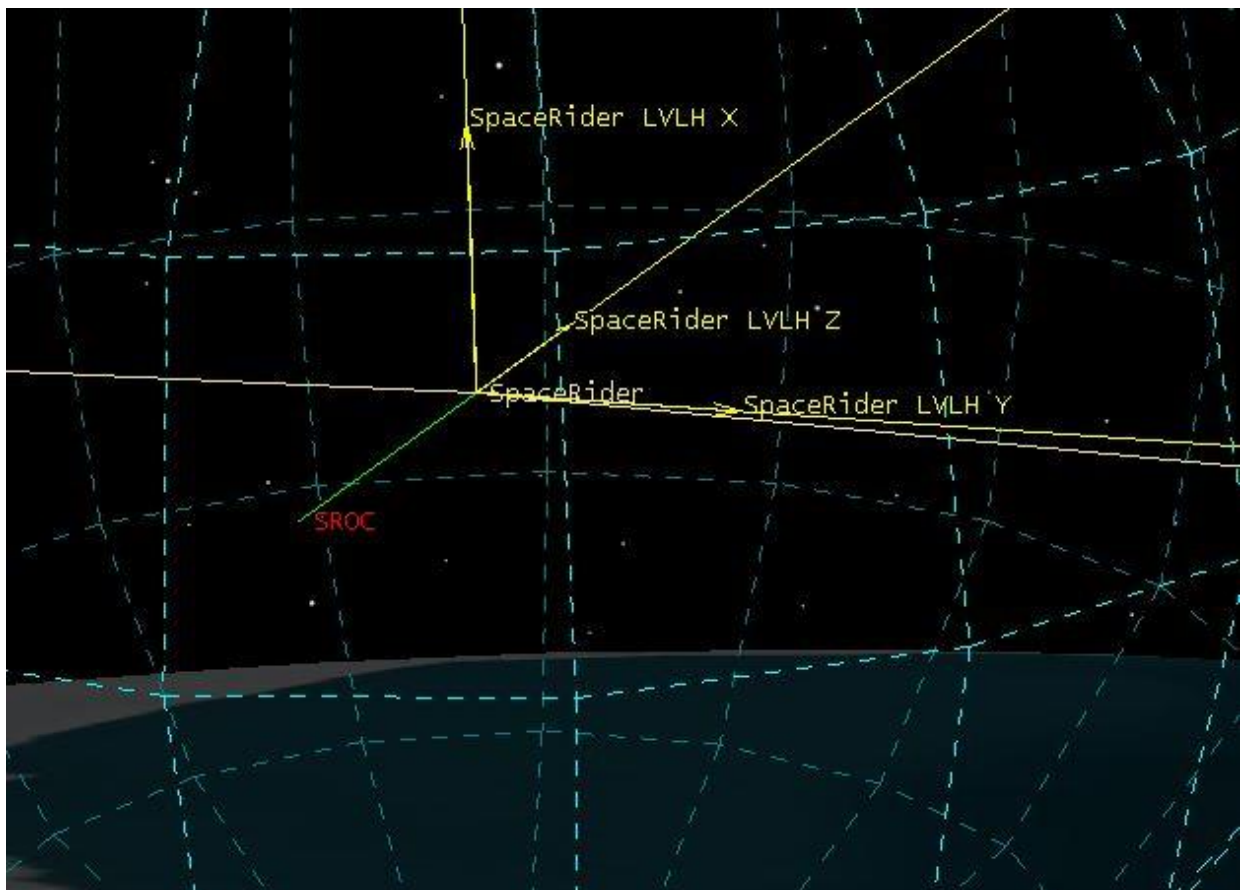


*Figure 138: V-bar approach - LVLH frame*

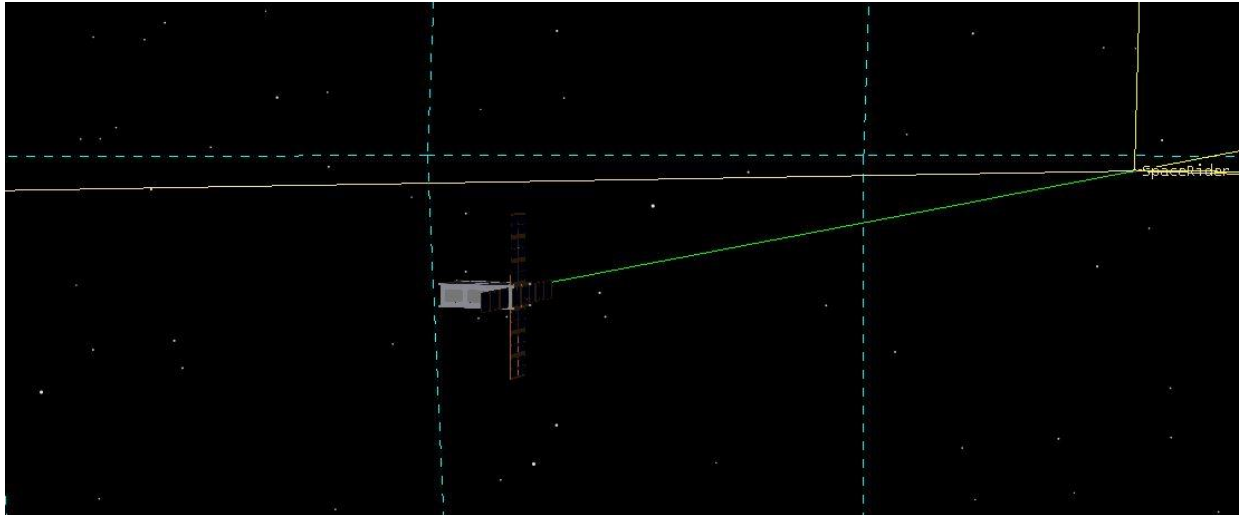


Figure 139: V-bar approach - zoom on SROC

In the following two pictures (*Figures 140 and 141*) the R-bar approach is visualized. As in the V-bar case, the trajectory has a straight-line shape and no perturbations occur along the manoeuvre.

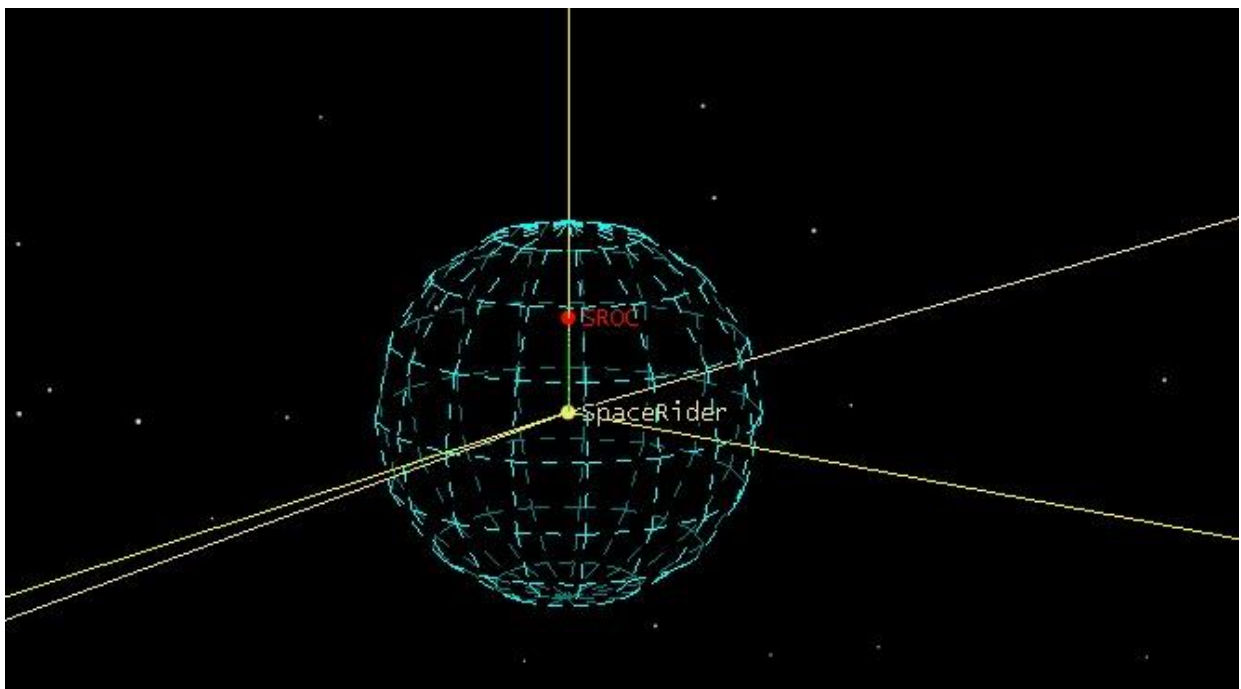


Figure 140: R-bar approach

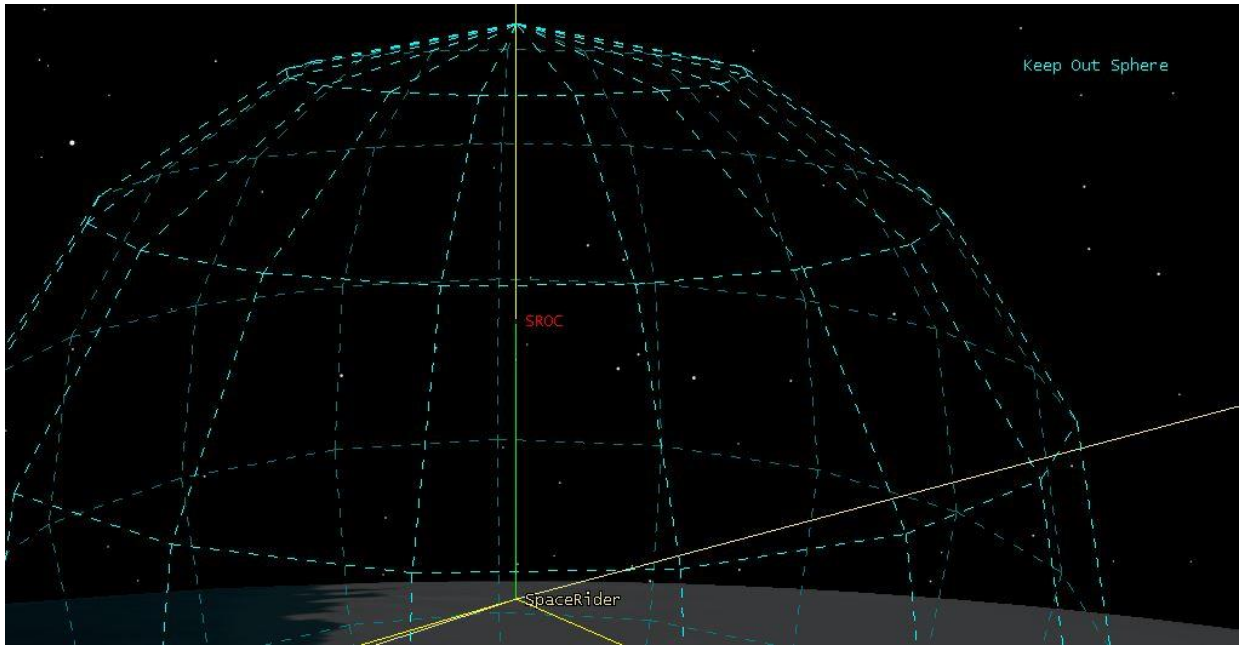


Figure 141: R-bar approach - zoom